TWO-PORE CHANNELS AND NAADP-DEPENDENT CALCIUM SIGNALLING

Peter James Calcraft

A Thesis Submitted for the Degree of PhD
at the
University of St. Andrews

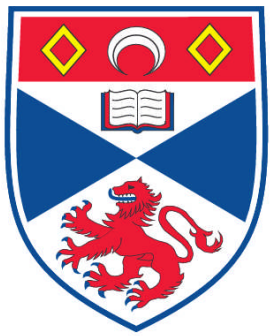

2010

Two-pore channels and NAADP-dependent calcium signalling

Peter James Calcraft

A thesis submitted to the University of St Andrews for the degree of Doctor of Philosophy

School of Biology
University of St Andrews

September 2009

Declarations

I, Peter James Calcraft, hereby certify that this thesis, which is approximately 73,000 words in length, has been written by me, that it is the record of work carried out by me and that it has not been submitted in any previous application for a higher degree.

I was admitted as a research student in September, 2005 and as a candidate for the degree of PhD in October, 2006; the higher study for which this is a record was carried out in the University of St Andrews between 2005 and 2008.

Date: Signature of candidate:

I hereby certify that the candidate has fulfilled the conditions of the Resolution and Regulations appropriate for the degree of PhD in the University of St Andrews and that the candidate is qualified to submit this thesis in application for that degree.

Date: Signature of supervisor:

In submitting this thesis to the University of St Andrews we understand that we are giving permission for it to be made available for use in accordance with the regulations of the University Library for the time being in force, subject to any copyright vested in the work not being affected thereby. We also understand that the title and the abstract will be published, and that a copy of the work may be made and supplied to any bona fide library or research worker, that my thesis will be electronically accessible for personal or research use unless exempt by award of an embargo as requested below, and that the library has the right to migrate my thesis into new electronic forms as required to ensure continued access to the thesis. We have obtained any third-party copyright permissions that may be required in order to allow such access and migration, or have requested the appropriate embargo below.

The following is an agreed request by candidate and supervisor regarding the electronic publication of this thesis:

Access to Printed copy and electronic publication of thesis through the University of St Andrews.

Date:

Signature of candidate: Signature of supervisor:

Acknowledgements

Firstly, I would like to thank Prof. Mark Evans for giving me this wonderful opportunity. Under your supervision, support and guidance the development of both skills and experience will prove to be invaluable.

I would like to thank all the people who have given me technical advice and friendship along the way. They are too numerous to name everyone but particular thanks go to Dr. Chris Wyatt, Dr. Nick Kinnear, and Dr. Jill Clark. Thanks also to the members of the Galione laboratory in Oxford, and Guida, Gloria and Abdelilah in particular for the close collaboration on the role of TPCs and for all the help I received from them.

Most important among my collaborators, has been Dr. Mike Zhu at the University of Ohio. I would therefore like to take this opportunity to acknowledge the help, support and informative discussion I have received from him, and for the opportunity he gave me to work on such an exciting project.

Thank you to all of my friends and family who have given me encouragement and support throughout my studies.

Lastly and most importantly I would like to thank my wife, Jenni. Through everything I have done your love and support has encouraged and sustained me. For that there is no end to my gratitude. Thank you.

This work was supported by the British Heart Foundation.

Abstract

Nicotinic acid adenine dinucleotide phosphate (NAADP) is a potent Ca^{2+} mobilising messenger in mammalian and non-mammalian cells. Studies on a variety of cell types suggest that NAADP evokes Ca^{2+} release from a lysosome-related store and via activation of a receptor distinct from either ryanodine receptors (RyR) or inositol 1,4,5-trisphosphate (IP_3) receptors (IP_3R). However, the identity of the NAADP receptor has, until now, remained elusive. In this thesis I have shown that NAADP-evoked Ca^{2+} release from lysosomes is underpinned by two-pore channels (TPCs), of which there are 3 subtypes, TPC1, TPC2 and TPC3. When stably over-expressed in HEK293 cells, TPC2 was found to be specifically targeted to lysosomes, while TPC1 and TPC3 were targeted to endosomes. Initial Ca^{2+} signals via TPC2, but not those via TPC1, were amplified into global Ca^{2+} waves by Ca^{2+}-induced Ca^{2+} release (CICR) from the endoplasmic reticulum (ER) via IP_3Rs. I have shown that, consistent with a role for TPCs in NAADP-mediated Ca^{2+} release, TPC2 is expressed in pulmonary arterial smooth muscle cells (PASMCs), is likely targeted to lysosomal membranes, and that TPCs also underpin NAADP-evoked Ca^{2+} signalling in this cell type. However, and in contrast to HEK293 cells, in PASMCs NAADP evokes spatially restricted Ca^{2+} bursts that are amplified into global Ca^{2+} waves by CICR from the sarcoplasmic reticulum (SR) via a subpopulation of RyRs, but not via IP_3Rs. I have demonstrated that lysosomes preferentially co-localise with RyR subtype 3 (RyR3) in the perinuclear region of PASMCs to comprise a "trigger zone" for Ca^{2+} signalling by NAADP, away from which a propagating Ca^{2+} wave may be carried by subsequent recruitment of RyR2. The identification of TPCs as a family of NAADP receptors may further our understanding of the mechanisms that confer the versatility of Ca^{2+} signalling which is required to regulate such diverse cellular functions as gene expression, fertilization, cell growth, and ultimately cell death.

Table of contents

Chapter 1: Introduction

1.1 Intracellular Ca^{2+} signalling

Ca^{2+} is a highly versatile signalling molecule capable of mediating a vast number of cellular processes including fertilization, gene expression, contraction, neurosecretion and cell death. The fact that there is such an array of Ca^{2+}-mediated cellular processes poses the following question: how can changes in the concentration of a simple divalent cation convey such information? This is not a simple case of modulating the Ca^{2+} concentration of the cytoplasm within the cell. It is now clear that Ca^{2+} signals are generated in segregated cellular compartments that determine both its site of action and the functional outcome. For example, in pancreatic β-cells the response to carbamylcholine in individual cells produced characteristic Ca^{2+} oscillations of particular amplitude, frequency, and shape (Prentki *et al.*, 1988). This led to the proposal that the spatiotemporal pattern of a given Ca^{2+} signal could provide a "fingerprint" that conveys the necessary information by which Ca^{2+} can regulate a particular cell process (Prentki *et al.*, 1988). Thus by utilizing spatiotemporal patterns of Ca^{2+} to mediate cellular processes the cell can impart the necessary information whilst avoiding the detrimental effect of universal and prolonged rises in Ca^{2+}. For example, gene expression can be modulated by variations in the Ca^{2+} signal over time in T-lymphocytes, where Ca^{2+} oscillations activate the Ca^{2+}-sensitive transcription factors NF-AT, Oct/OAP and NF-κB. However, low frequency Ca^{2+} oscillations only recruit NF-κB whereas higher frequencies recruit all 3 transcription factors, demonstrating that oscillations in Ca^{2+} mediate frequency-dependent gene expression (Dolmetsch *et al.*, 1998).

Over the last 20 years the complex mechanisms involved in Ca^{2+} signalling have begun to be unravelled. These mechanisms involve the regulation of Ca^{2+} uptake/sequestration and release/influx across the plasma membrane and the membrane of defined and multiple intracellular stores. Therefore an understanding of the mechanisms involved in the movement of Ca^{2+} across these various membranes is fundamental to resolving the means by which the cell can generate a variety of complex Ca^{2+} signals in order to regulate different Ca^{2+}-sensitive processes.

1.2 Ca^{2+} signalling across the plasma membrane

The plasma membrane is impermeable to Ca^{2+} and therefore Ca^{2+} must cross this barrier via a number of specialised protein channels and in response to a number of stimuli including depolarisation, receptor agonists and intracellular store depletion. Furthermore, in order to allow Ca^{2+} influx driven by its electrochemical gradient, the cytoplasmic Ca^{2+} is maintained at a low concentration relative to the extracellular environment and the lumen of intracellular Ca^{2+} stores. Therefore, in addition to channels mediating Ca^{2+} influx, the cell membrane also contains a number of specific pumps and transporters that actively remove Ca^{2+} from the cytoplasm.

1.2.1 Voltage-gated Ca^{2+} channels

An important pathway by which ions enter the cytoplasm via the plasma membrane is that of voltage-gated ion channels which are regulated by changes in the potential difference across the plasma membrane. Voltage-gated Ca^{2+} channels (VGCCs) are members of the family of voltage-gated ion channels which represent a superfamily of signal transduction proteins that are grouped together based on shared structural motifs. This superfamily consists of over 140 members including the voltage-gated Na^+, Ca^{2+} and K^+ channels, Ca^{2+}-activated K^+ channels and transient receptor potential (TRP) channels (Yu *et al.*, 2005). The features that determine the functionality of the members of this superfamily are ion-conductance, pore gating and pore regulation (Yu *et al.*, 2005).

VGCCs mediate Ca^{2+} influx across the plasma membrane in response to membrane depolarisation. VGCCs are comprised of a principal pore-forming subunit (α_1) and 3 auxiliary subunits (β, γ and the disulfide-linked complex $\alpha_2\delta$; (Takahashi *et al.*, 1987). VGCCs are broadly characterised into subtypes according to their pharmacological and electrophysiological properties. These subtypes include L-, T-, P/Q-, N- and R-type. L-type channels were first identified as long-lasting high-voltage-activated (HVA) channels which are sensitive to block by dihydropyridines and phenylalkylamines. Moreover, the L-type VGCC agonist BayK8644 selectively

increases the mean open time of L-type channels (Hess et al., 1984). The L-type channel was initially detected in neurons and skeletal, cardiac and smooth muscle (Hess et al 1984). However, in neurons there remained an HVA component that was insensitive to dihydropyridines. This was further divided into a ω-conotoxin sensitive component (N-type) and a slow inactivating Ca^{2+} current (P/Q-type) which was ω-conotoxin and dihydropyridine-insensitive. Furthermore, a low-voltage-activated Ca^{2+} channel was also detected, termed T-type (Fox *et al.*, 1987a; Fox *et al.*, 1987b). A current due to the R- (residual) type channel was also identified due to its resistance to dihydropyridines and the toxins used to identify the N and P/Q channels (Randall *et al.*, 1995). The pore-forming α_1 subunit determines many of the VGCC characteristics, and currently there are 10 identified mammalian α_1 subunits, for which a new classification system was required. The new nomenclature is based upon the α_1 subunit such that there are 4 genes encoding L-type channels ($Ca_v1.1$ – 1.4), 3 genes encoding the remaining HVA channels (P/Q-, N- and R-type replaced with $Ca_v2.1$, 2.2 and 2.3 respectively) and 3 genes encoding the T-type channels ($Ca_v3.1$ – 3.3) (Ertel *et al.*, 2000).

The functional multiplicity of VGCCs is dependent on the α_1 subunit as this is the pore-forming subunit and also contains the voltage sensor, gating apparatus and many sites involved in channel regulation (Catterall *et al.*, 2003). The α_1 subunit comprises 4 homologous domains each consisting of 6 transmembrane (TM) α–helices (S1-S6). The sequence also contains a membrane-reentrant loop (P-loop) which is situated between S5 and S6 of each domain repeat. The function of the P-loop is to determine the ion conductance and selectivity. Such is the degree of selectivity that, for example, a 3 amino acid residue change in the P-loop of a voltage-gated Na^+ channel results in it displaying Ca^{2+} ion selectivity (Catterall *et al.*, 2003). Negatively charged glutamate residues within the P-loops, which form the pore, are thought to determine the Ca^{2+} selectivity of the VGCCs (Yang *et al.*, 1993). The voltage sensing capability of the α-subunit is thought to be determined by the S4 section of each domain and specifically positively charged lysine and arginine residues (Dolphin, 2006). Depolarisation causes a conformational change within the protein which effectively 'opens' the pore allowing the passage of Ca^{2+} (Jones, 2003).

In addition to voltage-dependent regulation, L-type Ca^{2+} channels are also subject to regulation by a number of other factors. For example calmodulin (CaM) in

complex with Ca^{2+} (Ca^{2+}:CaM) is important in both the Ca^{2+}-dependent inactivation and facilitation of L-Type Ca^{2+} channel opening by binding to a motif within the C-terminal tail of the α_1 subunit (Zuhlke *et al.*, 1999). In addition to Ca^{2+}:CaM, phosphorylation by a number of protein kinases also regulates L-Type Ca^{2+} channels including protein kinase A, C, G (PKA, PKC and PKG) Ca^{2+}/calmodulin-dependent kinase II (CaMKII) and protein tyrosine kinases (Bers, 2002; Hudmon *et al.*, 2005; Kamp *et al.*, 2000; Keef *et al.*, 2001; McHugh *et al.*, 2000; Schroder *et al.*, 2003; Tewari *et al.*, 1997; Yagi *et al.*, 2002).

1.2.2 Voltage-independent Ca^{2+} channels

In addition to Ca^{2+} influx via VGCCs, there are a number of channels which can permit the flux of Ca^{2+} independent of a change in membrane potential. These include receptor-operated Ca^{2+} entry (ROCE) and store-operated Ca^{2+} entry (SOCE).

1.2.2.1 Receptor-operated Ca^{2+} entry

Receptor operated channels were first described in the late 1970's and are defined as plasma membrane channels that are gated by ligand binding and in a voltage-independent manner (Bolton, 1979; Van Breemen *et al.*, 1978). ROCE is mediated by an extracellular agonist either binding to a receptor in the plasma membrane (e.g. NMDA, P2X receptor) or by activating a secondary process such the G-protein coupled receptor whose heterotrimeric G-protein pathway mediates the opening of a Ca^{2+} permeable channel (e.g. α_1-adrenoceptor). One such example of ROCE was shown in arterial smooth muscle cells where ATP was shown to evoke a Ca^{2+} current via activation of P2X receptors (Benham *et al.*, 1987). The physiological importance of this ROCE mechanism has been demonstrated using $P2X_1$ knockout mice. Mesenteric arteries from these mice lost the rise in intracellular Ca^{2+} and contraction in response to neuronally released ATP (Lamont *et al.*, 2006).

ROCE is also mediated by members of the transient receptor potential (TRP) channel family of proteins. TRP channels are a diverse family of non-voltage-gated cation channels exhibiting a range of functional properties. TRPs are found in a broad

range of species and there are over 20 mammalian TRPs which are grouped into 6 subfamilies; canonical (TRPC), vanilloid (TRPV), melastatin (TRPM), ankyrin (TRPA), mucolipin (TRPML), and polycystin (TRPP) (Clapham *et al.*, 2005). All members of the TRP family have a characteristic primary structure consisting of 6 TM domains (S1-S6) and a re-entrant P-loop situated between S5 and S6. This basic structure is reminiscent of one of the 4-repeat domains of the pore forming subunit of VGCCs. Indeed, single domain channels such as TRPs form hetero- or homotetramers in order to form a functional pore (Amiri *et al.*, 2003; Kedei *et al.*, 2001). This suggests that predecessors of TRPs may have undergone 2 rounds of duplication in order to form the more complex VGCCs. However, despite this similarity to VGCCs, TRPs lack the necessary set of positively charged amino acid residues, such as arginine, within S4 required to convey voltage sensitivity (Catterall, 2000; Montell, 2005). TRP channels are non-selective with respect to Na^+ and Ca^{2+} permeability, with the exceptions of Ca^{2+}-selective TRPV5/6 and the monovalent-selective TRPM4/5 (Clapham *et al.*, 2005).

TRP channels have no unifying function, however a growing body of evidence suggests that TRPs play an important role as physiological sensors involved in vision, taste, smell, hearing, mechanosensation and thermosensation (Montell, 2005). For example, TRPV1 is gated by capsaicin and by increases in temperature from 22 °C to ~45 °C (Caterina *et al.*, 1997). Conversely, both TRPA1 and TRPM8 are activated by cold temperatures (~10 °C) and cooling compounds such as methanol and icilin (Peier *et al.*, 2002; Story *et al.*, 2003). Moreover, TRPM5 is required for sweet, bitter and umami taste signalling pathways (Zhang *et al.*, 2003). Another example of the diverse physiological role of TRPs is TRPML1 which is thought to act as a H^+ leak pathway in order to prevent over-acidification of lysosomes (Soyombo *et al.*, 2006). Of particular importance with reference to ROCE, are the members of the TRPC subfamily which have been implicated in this Ca^{2+} influx mechanism. For example, TRPC3, 6 and 7 have been shown to mediate ROCE via α_1-adrenoceptor activation or in response to increased diacylglycerol (DAG) activity (Hofmann *et al.*, 1999; Lievremont *et al.*, 2004; Thebault *et al.*, 2005).

1.2.2.2 Store-operated Ca^{2+} entry

The mechanism of SOCE was first termed 'capacitative Ca^{2+} entry' upon its proposal in 1986 (Putney, 1986), although this process was first described by Ginsborg and co-workers between 1979 and 1980 working on the cockroach salivary gland (Blackman *et al.*, 1979; Ginsborg *et al.*, 1980a; Ginsborg *et al.*, 1980b). It describes the coupling of the sarcoplasmic / endoplasmic reticulum (S / ER) store with plasma membrane channels that mediate Ca^{2+} influx in response to store emptying, such that a low luminal Ca^{2+} concentration of the ER will initiate Ca^{2+} influx across the plasma membrane in order to replenish the intracellular Ca^{2+} stores (Putney, 1986). Although much later than the observations of Ginsborg and co-workers, an endogenous SOCE current in mast cells is generally acknowledged as being the first characterised (Hoth *et al.*, 1992). This current was termed the calcium release-activated current (I_{CRAC}) and two proteins, the stromal interaction molecule (STIM1) and Orai1, have been identified as key components in SOCE. STIM1 has a single TM region which spans the ER membrane. The luminal part of STIM1 contains an EF-hand motif which is able to bind Ca^{2+} and thus act as a Ca^{2+} sensor. Upon store depletion STIM1 redistributes to puncta in close proximity to the plasma membrane (Liou *et al.*, 2005). It is proposed that STIM1 is then able to directly interact with the plasma membrane bound protein Orai1 in order to mediate Ca^{2+} influx (Hewavitharana *et al.*, 2007). Indeed, Orai has been shown to restore I_{CRAC} in SOCE deficient cells (Feske *et al.*, 2006) and when co-expressed with STIM1 form large I_{CRAC} currents (Peinelt *et al.*, 2006; Zhang *et al.*, 2006b). Some studies have suggested that Orai1 interacts with TRPCs and that this STIM1:Orai:TRPC complex mediates SOCE (Liao *et al.*, 2007). However, this suggestion has been contested by the recent finding that either STIM1 or Orai knockdown is without effect on TRPC7-mediated Ba^{2+} influx (DeHaven *et al.*, 2009). Furthermore, in HEK293 cells co-expression of STIM1 did not increase the Ca^{2+} entry activity of TRPC1, TRPC3, TRPC5 or TRPC6. Thus, Putney and colleagues concluded that STIM1 and Orai do not associate with TRPCs but rather that the agonists used in previous studies had indeed activated both ROCE and SOCE mechanisms (DeHaven *et al.*, 2009). Recently, Penna *et al.* have proposed that STIM1 interaction causes the formation of Orai1 tetramers and thus Orai forms the SOCE-associated Ca^{2+} pore (Penna *et al.*, 2008). This interaction would allow the influx of Ca^{2+} to be directed to regions of the

ER that have become depleted of Ca^{2+}. This mechanism would thus allow refilling of the depleted store in localised regions, whilst avoiding global Ca^{2+} influx. It is therefore clear that organelles are able to form close associations that allow for the coordination of localised Ca^{2+} flux, and thus add further complexity to the tight regulation of Ca^{2+} signalling within the cell.

1.2.3 The role of voltage-gated Na^+ channels

Voltage-gated Na^+ channels (Navazio *et al.*) are members of the voltage-gated ion channel superfamily that also include Ca_v channels and voltage-gated potassium channels (K_v) (Yu *et al.*, 2005). Consistent with this, Na_v channels are principally comprised of a pore-forming α-subunit which consists of 4 homologous domains of 6 TM regions (S1-S6) with a reentrant P-loop between S5 and S6 of each domain. Thus, the 4 P-loops together form a Na^+-selective pore (Yu *et al.*, 2003). There are currently 9 mammalian Na_v channels identified ($Na_v1.1$-$Na_v1.9$) which share over 50 % identity (Catterall *et al.*, 2005). Further to this Na_v channels can associate with one or more of 4 auxilliary β-subunits ($Na_v\beta_1$-$Na_v\beta_4$) (Catterall *et al.*, 2005) which modulate channel gating (Yu *et al.*, 2003). The established role of Na_v channels in excitable cells such as neurones cardiomyocytes and skeletal muscle cells is the initiation and propagation of action potentials. Upon membrane depolarisation, Na_v channels activate and subsequently inactivate within milliseconds, permitting the influx of Na^+ through the channel and into the cytoplasm resulting in further membrane depolarisation (Yu *et al.*, 2003). In contrast to excitable cells, Na_v channels were not thought to play an important role in Ca^{2+} homeostasis in non-excitable cells such as smooth muscle cells (SMCs). However, Na_v channels have been shown to enhance contractility in portal vein SMCs (Saleh *et al.*, 2005). This Na_v-dependent increase in contractility is thought to be due to stimulation of the reverse reaction of Na^+/Ca^{2+} exchanger (NCX) thus resulting in Ca^{2+} influx (Saleh *et al.*, 2005). Furthermore, in uterine SMCs, Na_v channel activation has been shown to cause subsequent opening of Ca_v1 channels that mediate SMC contraction (Saleh *et al.*, 2005).

1.2.4 K^+ channels

In addition to Ca^{2+}-mediated ion influx/efflux, a number of other channels play an important role in cellular processes including the control of membrane potential and repolarisation following, for example, an action potential. The K^+ channel superfamily are key in this respect. These represent a large family of ion channels that share selectivity for K^+ over Na^+. Included in this family are the Ca^{2+}-activated channels (K_{Ca}), inward rectifier K^+ channel (K_{ir}) and voltage-gated K^+ channel (K_v). This selectivity for K^+ is due to a conserved amino acid sequence motif (TXGYG) (Sansom *et al.*, 2002; Wray, 2004).

1.2.4.1 Ca^{2+}-activated K^+ channels

The family of Ca^{2+}-activated K^+ channels are formed by 5 subfamilies (K_{Ca}1.1-5.1) (Wei *et al.*, 2005). Of these subfamilies, there are 2 major groups that contain channels sensitive to Ca^{2+} activation. One group contains the "large-conductance" K_{Ca} channel (K_{Ca}1.1) and the second group contains the "small-conductance" K_{Ca} channels (K_{Ca}2.1-2.3) and "intermediate-conductance" channel (K_{Ca}3.1). Gating of these channels results in the efflux of K^+ and an outward current. Thus these channels can mediate hyperpolarisation or provide repolarisation in response to a prior depolarisation. K_{Ca}1.1 is activated by both voltage and an increase in intracellular Ca^{2+} concentration (Tanaka *et al.*, 1997). The channel is comprised of a pore-forming α-subunit which contains both the voltage-sensor and Ca^{2+} binding sites, and an auxiliary β-subunit which increases the Ca^{2+}-sensitivity of the channel (Cox *et al.*, 2000). However, K_{Ca}1.1 can be voltage-activated in the absence of intracellular Ca^{2+} and thus Ca^{2+} binding is thought to affect various gating kinetics such as lowering the voltage at which the channel is activated (Horrigan *et al.*, 2002). Ca^{2+} modulation of K_{Ca}1.1 is mediated by Ca^{2+} binding directly to the α-subunit at 3 Ca^{2+} binding sites (Zeng *et al.*, 2005). In contrast to K_{Ca}1.1, K_{Ca}2.1-2.3 and K_{Ca}3.1 are gated exclusively by intracellular Ca^{2+} and independent of voltage (Schumacher *et al.*, 2001). Furthermore, these channels do not bind Ca^{2+} directly but rather by a constitutively bound CaM molecule. Upon binding Ca^{2+} ions in its 2 EF-hand motifs,

CaM undergoes a conformational change which in turn causes a shift in conformation of the pore region of the channel and thus opens the pore (Schumacher *et al.*, 2001).

1.2.4.2 Voltage-gated K^+ channels

Voltage-gated K^+ channels (K_v) are structurally related to the pore-forming subunits of Ca_v. and are activated by depolarisation to allow the efflux of K^+. This results in a repolarisation of V_m. Sustained depolarisation generates a slow inactivation of the channel, thus preventing sustained channel opening and subsequent hyperpolarisation. There are currently over 30 genes that encode K_v channels (K_v1.1-12.3) which are single domain units structurally composed of 6 TM regions (S1-S6) with the characteristic P-loop between S5 and S6 (Gutman *et al.*, 2005; Korovkina *et al.*, 2002). In order to form a viable pore, K_v channels are thought to form homo- or heterotetramers with the P-loop of each subunit together forming the selectivity filter of the pore (Liman *et al.*, 1992; MacKinnon, 1991). Similar to other ion channels with the same architecture such as TRPs, this tetramer formation has led some to suggest that the 4 domain pore forming subunits of Ca_v are the product of 2 rounds of duplication of single pore domain channels such as K_v (Yu *et al.*, 2005). Similar to Ca_v channels, the tetrameric K_v channels are able to interact with ancillary β-subunits that confer various effects such as fast-inactivation (Bahring *et al.*, 2001).

1.2.4.3 Inward rectifier K^+ channels

Another channel of importance to the regulation of membrane potential is the inward rectifier potassium channel (K_{ir}). These channels are defined by having a higher conductance for K^+ moving into the cell than outwards (Sansom *et al.*, 2002). Potassium channels that share this characteristic form the K_{ir} family which is comprised of 7 subfamilies (K_{ir}1.1-7.1) (Kubo *et al.*, 2005). The 2 main suggested functions of K_{ir} are in responding to increased extracellular K^+ concentrations (Park *et al.*, 2007b) and contributing to resting V_m (Park *et al.*, 2007a). The inward flux of K^+ or rectification via K_{ir} occurs when V_m is more negative than the equilibrium potential for K^+. Therefore, as most cells resting V_m is more positive relative to the equilibrium potential of K^+, K_{ir} channels allow small outward currents (Xu *et al.*, 1999). However at more positive membrane potentials, K^+ efflux via K_{ir} is limited due to blockade of

the channel by cytoplasmic Mg^{2+} and polyamines such as spermine (Lopatin *et al.*, 1994; Matsuda *et al.*, 1987). Further modulation of K_{ir} activity is mediated by a number of cytoplasmic factors including phosphatidylinositol 4,5-bisphosphate (PIP_2), pH, ATP, phosphorylation, and heterotrimeric G proteins (Bichet *et al.*, 2003).

The structure of K_{ir} channels represents the most basic structural motif in the ion channel superfamily. They consist of 2 TM regions (M1-M2) which are homologous to the S5 and S6 regions of K_v, and therefore also incorporate the re-enterant P-loop between the two TM regions (Yu *et al.*, 2005). These subunits are also able to form a functional pore via the formation of homo or heterotetramers, further exemplifying the requirement of this common motif consisting of a 4-repeat P-loop anchored by TM regions.

1.2.5 Ca^{2+}-activated Cl^- channel

Ca^{2+} influx across the plasma membrane can have a direct depolarising effect on the cell membrane potential (V_m). In addition to these direct effects, Ca^{2+} may also affect V_m by modulating other ion channels which are also present in the plasma membrane such as the Ca^{2+}-activated Cl^- channel (CaCC). CaCCs are anion-selective channels present on the plasma membrane that are characteristically activated by increases in the intracellular Ca^{2+} concentration. These channels are activated by Ca^{2+} in a voltage-dependent manner, such that at depolarising membrane potentials CaCCs are more sensitive to activation by Ca^{2+} (Kuruma *et al.*, 2000). Such activating increases in intracellular Ca^{2+} concentration can be as a result of both Ca^{2+} release from intracellular stores and by Ca^{2+} influx via L-type Ca^{2+} channels (Wray *et al.*, 2005). Activation of CaCCs permits the efflux of Cl^- which confers an inward current and concomitant depolarisation and thereby VGCC activation. The molecular identity of CaCC has recently been identified as anoctamin 1 (ANO1; also referred to as TMEM16A) (Caputo *et al.*, 2008; Yang *et al.*, 2008). There are 10 isoforms of ANO (ANO1-10) with each sequence containing 8 TM domains and a highly conserved re-entrant pore-forming loop between TM domains 5 and 6 (Caputo *et al.*, 2008; Yang *et al.*, 2008). This loop contains 3 conserved, positively charged amino acid residues which are responsible for the channels Cl^- selectivity (Yang *et al.*, 2008). Indeed, substituting the negatively charged amino acid, glutamic acid, for the positively

charged residue arginine (Arg^{621}) resulted in an increase in cation permeability of approximately 30-fold (Yang *et al.*, 2008).

1.2.6 Removal of Ca^{2+} across the plasma membrane

In order to maintain cytoplasmic Ca^{2+} at a low (~100 nM) concentration the plasma membrane contains pumps and transporters that actively remove free Ca^{2+} ions from the cytoplasm. The plasma membrane Ca^{2+}-ATPase (PMCA) pump and the Na^{+}/Ca^{2+} exchanger (NCX) are the two major routes by which Ca^{2+} is removed from the cytoplasm across the plasma membrane.

1.2.6.1 Removal of Ca^{2+} by the plasma membrane Ca^{2+}-ATPase

The PMCA is a P-type ATPase which is ubiquitously expressed within eukaryotes and is considered to be the major Ca^{2+} transporter in the plasma membrane (Strehler *et al.*, 2001). There are 4 isoforms of PMCAs currently identified (PMCA1-4) with each isoform containing at least 6 splice variants (Strehler *et al.*, 2001). The energy obtained from the hydrolysis of 1 ATP molecule is utilised to transport 1 Ca^{2+} ion whilst allowing H^{+} into the cell. However, there is currently some debate as to the Ca^{2+}:H^{+} ratio with either a ratio of 1:1 (Di Leva *et al.*, 2008) or 1:2 (Thomas, 2009) reported. This could be significant because a ratio of 1:2 could have a greater affect on the local intracellular environment as H^{+} movement causes changes in pH and thus can affect the modulation of a number of ion channels, while a ratio of 1:1 would impact on membrane potential as it would be electrogenic. The PMCA contains 10 TM domains and 4 cytoplasmic domains. The C-terminal region contains a number of regulatory sites through which it interacts with PKA, PKC and CaM (Di Leva *et al.*, 2008; Kuo *et al.*, 1991; Preiano *et al.*, 1996). The CaM binding site is thought to interact with two sites on the main body of the pump and by doing so acts as an autoinhibitory sequence. Upon binding Ca^{2+}:CaM this domain dissociates from the main body of the pump thus alleviating its autoinhibitory effect (Di Leva *et al.*, 2008). 3 Ca^{2+} binding sites have also been identified on the C-terminal tail (Hofmann *et al.*, 1993). Two of these are thought to be constitutive binding sites with the remaining, lower affinity binding site responsible for the sequestration of Ca^{2+}.

1.2.6.2 Removal of Ca^{2+} by the Na^{+}/ Ca^{2+} exchanger

The other major mechanism of reversible Ca^{2+} extrusion by the plasma membrane is via the NCX. In physiological conditions, mammalian cells maintain intracellular Na^{+} concentration at relatively low levels relative to the extracellular environment (~10 mM and ~140 mM respectively). The NCX is therefore able to utilise the energy obtained from allowing Na^{+} ions into the cell in order to transport Ca^{2+} ions out in a ratio of 3 Na^{+}:1 Ca^{2+} (Zhang *et al.*, 2005). The NCX consists of 9 TM segments which are divided into 2 clusters of 5 and 4 TM segments. Within each of these clusters there exists α-repeat motifs which are orientated in opposing directions (Iwamoto *et al.*, 2000). These α-repeat motifs form the ion-binding pocket on each side of the membrane (Lytton, 2007). There are 3 mammalian isoforms of NCX (NCX1-3) which belong to the Ca^{2+}/cation antiporter gene superfamily (Lytton, 2007). NCX1 is ubiquitously expressed whereas NCX2 expression is limited to the brain and NCX3 has high expression within skeletal muscle with little or no expression elsewhere (Quednau *et al.*, 2004). The cellular distribution of NCX is also of particular interest as it has been shown that NCX within the plasma membrane overlies regions of the S / ER (Blaustein *et al.*, 1999; Juhaszova *et al.*, 1997). This tight association could serve to quickly remove Ca^{2+} from areas of focal release and thus contribute to the spatiotemporal pattern of Ca^{2+} signalling. Alternatively, reverse mode NCX may contribute to Ca^{2+} influx in an agonist specific manner (Syyong *et al.*, 2007).

Ca^{2+} movement across the plasma membrane is vital for the appropriate functioning of the cell and involves an array of specialised proteins (Fig. 1.1). However, it is also clear that many of the protein channels, pumps and exchangers within the plasma membrane interact with intracellular Ca^{2+} stores. These interactions can either be direct such as the coupling of the S / ER to the plasma membrane via STIM and Orai, or indirect via changes in the local Ca^{2+} concentration and/or pH.

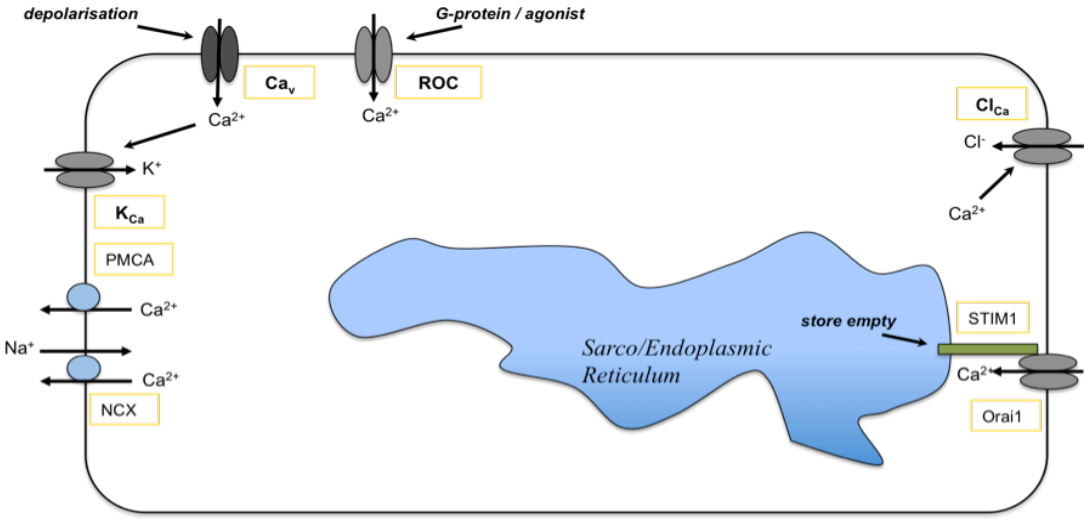

Fig. 1.1. Schematic representation of Ca^{2+} extrusion and influx mechanisms across the plasma membrane

Depicted are some of the mechanisms by which Ca^{2+} crosses the plasma membrane together with some of the ion channels that are stimulated by localised increases in intracellular Ca^{2+}. Ca_v, voltage gated Ca^{2+} channel; ROC, receptor operated channel; PMCA, plasma membrane Ca^{2+} ATPase; NCX, Na^+/Ca^{2+} exchanger; K_{Ca}, Ca^{2+}-activated K^+ channel; Cl_{Ca}, Ca^{2+}-activated Cl^- channel; STIM, stromal interaction molecule.

1.3 Ca^{2+} handling by Mitochondria

The precise role of mitochondria in Ca^{2+} homeostasis is as yet unclear. However, mitochondria are not generally considered to provide a releasable Ca^{2+} store, although there is a degree of Ca^{2+} efflux that is mediated by two ion transporters. This Ca^{2+} efflux is mediated by either a Na^+-independent mechanism which is considered to be a H^+/Ca^{2+} antiporter, or via a Na^+-dependent mechanism which is considered to be a Na^+/Ca^{2+} exchanger (Gunter *et al.*, 2004).

Despite not being recognised as a mobilisable Ca^{2+} store, mitochondria can have an important role as Ca^{2+} sinks because they are able to sequester Ca^{2+} from the cytoplasm via the mitochondrial Ca^{2+} uniporter. This route of Ca^{2+} influx is dependent upon the electrochemical potential gradient which, due to the mitochondrial respiratory chain, maintains the mitochondrial membrane potential at approximately -150 to -200 mV relative to the cytoplasm (Duchen, 2000). However, whether or not the mitochondrial Ca^{2+} uniporter is able to sequester significant Ca^{2+} in

response to agonist-mediated intracellular Ca^{2+} waves/pulses was questioned until 1995. Then a rapid mode (RaM) of calcium entry was identified by which mitochondria are able to rapidly sequester Ca^{2+} at the beginning of each Ca^{2+} pulse (Sparagna *et al.*, 1995). RaM Ca^{2+} conductivity can be up to 300-fold faster than the uniporter (Buntinas *et al.*, 2001) and therefore provides mitochondria with a method by which they can operate as high capacity Ca^{2+} sinks. For example, in the polarised pancreatic acinar cells mitochondria form a barrier around the secretory granule-rich apical pole. These mitochondria are able to rapidly sequester Ca^{2+} and in doing so stop the propagation of an IP_3-mediated Ca^{2+} wave from the apical pole to the luminal pole (Tinel *et al.*, 1999). The presence of a "mitochondrial firewall" has also been implicated in the functioning of cardiomyocytes and in motor neurones (David *et al.*, 1998; Mackenzie *et al.*, 2004). Thus the spatial organisation of mitochondria may regulate the shape of Ca^{2+} signals or compartmentalise them, and thereby determine the functional response to a given Ca^{2+} release event. In addition, an important way in which Ca^{2+} can modulate mitochondria function comes from the observation that an agonist-induced rise in the intracellular Ca^{2+} concentration is able to stimulate ATP production (Jouaville *et al.*, 1999; Robb-Gaspers *et al.*, 1998). Taken together with the observation that skeletal muscle mitochondria increase Ca^{2+} influx during contraction (Rudolf *et al.*, 2004) this process would therefore allow the stimulated cell to increase its ATP production in order to meet the increased metabolic demand. At greater concentrations Ca^{2+} is able to stimulate the mitochondrial permeability transition (MPT) and opening of the large non-selective MPT pore. The opening of this pore can cause rapid mitochondrial depolarisation and the subsequent ATP depletion can lead to cell death. Furthermore, opening of the MPT pore can also lead to the release of cytochrome C which can in turn activate the apoptotic cascade of proteolytic caspase enzymes also resulting in cell death (Bernardi, 1999). Despite not being considered as a classical releasable Ca^{2+} store, it is evident that mitochondria play an important role in Ca^{2+} homeostasis, and in particular their localisation and ability to rapidly sequester Ca^{2+} could help to shape cell type-specific Ca^{2+} signals.

1.4 Mobilisable intracellular Ca^{2+} stores

In order to achieve the array of specific spatiotemporal Ca^{2+} signals, influx of Ca^{2+} from outside the cell does not provide the sufficient level of complexity required. As a result there are a number of defined intracellular stores within the cell that can provide rapid and spatially restricted Ca^{2+} release.

1.4.1 Endoplasmic / Sarcoplasmic Reticulum

The endoplasmic reticulum (ER) is an organelle that forms an interconnected network of membrane-bound tubules and cisternae. The ER is involved in a number of functions including phospholipid synthesis and the translocation, integration, folding and modification of proteins (Voeltz *et al.*, 2002). The other important function of the ER, with respect to this thesis, is that it is considered to be the major intracellular Ca^{2+} store. The ER can be divided into two main groups, smooth ER and rough ER. Rough ER is studded with membrane bound ribosomes on its surface and is primarily involved in the synthesis of membrane and secretory proteins. Smooth ER is characterised by the absence of ribosomes and is involved, for example, in steroid synthesis and Ca^{2+} release. Within muscle cells their exists a specialized form of smooth ER known as the sarcoplasmic reticulum (SR) which is dedicated to the storage and release of Ca^{2+}. This specialised function is reflected by the fact that in longitudinal SR of striated muscle the major sequestration protein, the sarcoplasmic / endoplasmic reticulum ATPase (SERCA) pump, represents up to 90% of the total membrane protein compared to 1% with respect to the ER (Rizzuto *et al.*, 2006). As the S / ER is a releasable Ca^{2+} store, it also contains a number of proteins that are able to sequester and store Ca^{2+}, and mediate its release into the cytoplasm.

1.4.1.1 Sequestration of Ca^{2+} by the sarcoplasmic / endoplasmic reticulum Ca^{2+} ATPase

Sequestration of Ca^{2+} into the S / ER lumen is performed by the SERCA pumps. In mammals there are 3 SERCA (ATP2A1-3) genes which each encode for at least two SERCA isoforms (SERCA1a-b, SERCA2a-b, SERCA3a-f). These isoforms are

the result of alternative splicing and have varying tissue distribution. SERCA pumps are P-type ATPases characterised by the formation of an aspartyl-phosphorylated intermediate during the catalytic process. These single-subunit enzymes utilize the energy obtained from ATP hydrolysis to transport 2 Ca^{2+} ions from the cytoplasm to the ER/SR lumen in exchange for 2 H^{+} ions (Yu *et al.*, 1993). The SERCA subtypes express functional variations, for example, SERCA1 and 2a have similar affinities for Ca^{2+} whereas the affinity of SERCA2b for Ca^{2+} is approximately 2-fold greater (Lytton *et al.*, 1992; Verboomen *et al.*, 1994). SERCA3 on the other hand exhibits 3 to 4-fold lower affinity for Ca^{2+} than the other subtypes (Lytton *et al.*, 1992). This functional variability between SERCA isoforms could play an important role in the regulation of Ca^{2+} signals, and the prevalence of one or other isoform could therefore contribute to cell-type specific functions.

SERCA pumps are regulated by 2 endogenous proteins present in the SR membrane: phospholamban (PLN) and sarcolipin (SLN). PLN is a membrane spanning protein that associates with SERCA pumps and inhibits their activity by lowering the affinity of the pump for Ca^{2+} (Traaseth *et al.*, 2008). This inhibition is relieved upon phosphorylation of PLN at Ser^{16} by PKA and/or Thr^{17} by CaMKII (Wegener *et al.*, 1989). Within the SR PLN is thought to exist as an inactive homopentamer which must first depolymerise into monomers prior to interaction with and subsequent inhibition of SERCA pumps (Kimura *et al.*, 1997). SLN is also a membrane spanning protein that is homologous to PLN (Traaseth *et al.*, 2008) and, consistent with this similarity, the inhibitory effect of SLN on SERCA pump activity may be reversed via phosphorylation at Ser^{4} and Thr^{5} by serine threonine kinases (Gramolini *et al.*, 2004). Co-expression of PLN and SLN in HEK293 cells led to 'superinhibition' of SERCA1a and SERCA2a. Thus, co-expression of SLN with PLN has been proposed to cause depolymerisation of PLN into monomers, which form heterodimers with SLN resulting in subsequent superinhibition of SERCA pumps (Asahi *et al.*, 2002; Asahi *et al.*, 2003). Superinhibition of SERCA pumps may occur endogenously given that, despite varied tissue expression for both PLN and SLN, mRNA expression for both proteins has been shown to be particularly high in mouse and rat atria (Vangheluwe *et al.*, 2005).

Of significance to experimental studies is the fact that SERCA pumps may also be blocked by two potent inhibitors: thapsigargin and cyclopiazonic acid (Lytton *et al.*, 1991; Martinez-Azorin, 2004). Blockade of SERCA pumps with these inhibitors

results in the depletion of the S / ER Ca^{2+} store. Thus, these pharmacological tools can be very useful when investigating intracellular Ca^{2+} mobilising messengers and can be used to determine whether the Ca^{2+} released by these messengers is mobilised from the S / ER.

1.4.1.2 Ca^{2+} buffering proteins of the sarcoplasmic / endoplasmic reticulum

In order for the lumen to have a concentration that is not inhibitory to the SERCA pump, the S / ER contains Ca^{2+} buffering proteins (MacLennan *et al.*, 2002). The key characteristic for such proteins is to bind multiple Ca^{2+} ions with low affinity and therefore allow the organelle to effectively store Ca^{2+} (Volpe *et al.*, 1994). One such protein is calsequestrin (CSQ) which has a low affinity for Ca^{2+} (K_d 0.8 mM) and, with 700-800 nmol of Ca^{2+} per mg of protein (40-50 Ca^{2+} ions per CSQ molecule), it has a high capacity for Ca^{2+} storage (MacLennan *et al.*, 2002; Volpe *et al.*, 1994). In place of a Ca^{2+} binding site motif such as the EF-hand motif, CSQs posses a high negative charge and are thought to bind Ca^{2+} via pairs of acidic residues (Wang *et al.*, 1998). In addition to CSQ, another Ca^{2+} buffering protein, calreticulin was identified in the early 1970's (Ostwald *et al.*, 1974) and is expressed in the ER/SR of many cell types (Michalak *et al.*, 1992). Calreticulin has a low affinity (K_d 2 mM) Ca^{2+} binding domain with high capacity for Ca^{2+} binding (18 mol of Ca^{2+}/mol of protein) in the C-terminal domain. This high Ca^{2+} binding capacity is determined by a region rich in acidic amino acid residues. Calreticulin also has a high affinity (K_d 6 μM) low capacity (1.3 mol of Ca^{2+}/mol of protein) Ca^{2+} binding site in the P-domain (Baksh *et al.*, 1991; Michalak *et al.*, 1999). Both of these Ca^{2+} binding proteins allow storage of high concentrations of Ca^{2+} and with their low affinity binding sites, allow the rapid release of Ca^{2+} upon activation of Ca^{2+} release channels within the ER/SR, inositol 1,4,5-trisphosphate receptors (IP_3R) and ryanodine receptors (RyR).

1.4.2 Golgi Apparatus

The Golgi apparatus (GA) is an organelle consisting of a ribbon-like labyrinth of cisternal membranes. The GA functions as the major pathway for protein and lipid transport from the ER to the plasma membrane and other organelles. During this

process the transported proteins and lipids may undergo a number of modifications. The *cis*-Golgi is the entry face to the intermediate GA ribbon whilst the *trans*-Golgi serves as the exit surface of the GA. Both intra-Golgi transport and modifications include a number of Ca^{2+}-dependent processes (Carnell *et al.*, 1994; Oda, 1992; Porat *et al.*, 2000) and therefore the GA sequesters Ca^{2+} such that the GA cisternae Ca^{2+} content is maintained at a high concentration relative to the cytoplasm (Pezzati *et al.*, 1997). Furthermore, Ca^{2+} gradients can be formed between the *trans*- and *cis*-Golgi. For example, in pancreatic acinar cells, IP_3-mediated Ca^{2+} release via the application of acetylcholine resulted in a greater luminal Ca^{2+} concentration in the *trans*-Golgi than in the *cis*-Golgi (Dolman *et al.*, 2005). That steep Ca^{2+} gradients may be formed between *trans*- and *cis*-Golgi suggests that these different parts may have different affinities for ”released” Ca^{2+}. Due to this dependency on Ca^{2+} the GA therefore contains a number of Ca^{2+} sequestering proteins as well as Ca^{2+} release channels. In order to sequester Ca^{2+}, the *cis*- and intermediate-Golgi membrane contains SERCA pumps whereas the *trans*-Golgi membrane contains the secretory-pathway Ca^{2+}-ATPases (SPCAs) (Behne *et al.*, 2003). These Ca^{2+} pumps are encoded by two genes in humans (ATPC1 and ATPC2) and are similar to SERCAs as they are also P-type ATPases. However there are distinct differences in that they can transport Ca^{2+} or Mn^{2+} equally well, and transport 1 ion of Ca^{2+}/Mn^{2+} per ATP hydrolysis (Wei *et al.*, 2000). It has also been shown that the GA contains IP_3Rs making it a rapidly releasable Ca^{2+} store (Collado-Hilly *et al.*, 2009; Lin *et al.*, 1999) and consistent with this IP_3 was found to mobilise Ca^{2+} from GA vesicles (Surroca *et al.*, 2000). However, RyR agonists cADPR and caffeine failed to evoke Ca^{2+} release from GA vesicles suggesting that RyRs are absent from the membranes of this organelle (Surroca *et al.*, 2000). The presence of IP_3Rs therefore allow the GA to act as either a Ca^{2+} sink or as a releasable store that cooperates with other organelles (Dolman *et al.*, 2005; Vanoevelen *et al.*, 2004). However, an important consideration when determining the involvement of the GA in IP_3-mediated Ca^{2+} signalling, is that similar to SERCAs, the SPCAs are also inhibited by thapsigargin albeit with less sensitivity (Dode *et al.*, 2006; Rojas *et al.*, 2000). Thus without SPCA-specific inhibitors, distinguishing the individual contribution of these organelles in Ca^{2+} signalling could be problematic.

1.4.3 Ca^{2+} mobilisation by IP_3

Ca^{2+} mobilisation by IP_3 was first reported in the blowfly salivary gland (Berridge, 1982). This was shortly followed by the observation that IP_3 evoked Ca^{2+} release in pancreatic acinar cells (Streb *et al.*, 1983). IP_3 has since been shown to mediate intracellular Ca^{2+} release in a wide range of mammalian and non-mammalian cells, and is now regarded as the major intracellular Ca^{2+} mobilising messenger.

1.4.3.1 Synthesis and metabolism of IP_3

IP_3 signalling occurs via the activation of the multi-domain enzyme phospholipase C (PLC). Stimulation of cell-surface receptors leads to the activation of this enzyme which then catalyses the hydrolysis of the membrane phospholipid phosphatidylinositol 4,5-bisphosphate, generating 1,2-diacylglycerol (DAG) and IP_3. Initially there were 3 identifiable mammalian subtypes of PLC (β, γ, and δ) which are activated by either $G\alpha_q$ subunits of G-protein coupled receptors (GPCRs) in the case of PLC-β and PLC-δ, or in the instance of PLC-γ by tyrosine-kinase receptors (Rebecchi *et al.*, 2000). In addition, PLC-δ is also regulated by changes in the intracellular Ca^{2+} concentration (Pawelczyk, 1999). More recently, conserved regions of the PLC subtypes were used to identify 3 additional PLC subtypes: ε, η and ζ (Katan, 2005). Following its formation, IP_3 then diffuses through the cytoplasm and binds to IP_3Rs on the S / ER membrane causing the channel to open and Ca^{2+} to be released. IP_3-mediated Ca^{2+} signalling is terminated by metabolism via the action of two different enzymes. The PKC-regulated IP_3 5-phosphatase cleaves the 5-phosphate group (Majerus *et al.*, 1988) whereas the CaM-sensitive IP_3 3-kinase also terminates IP_3 signalling by the addition of a phosphate to the 3 position (Hawkins *et al.*, 1986; Takazawa *et al.*, 1990).

1.4.3.2 IP_3R subtypes

As previously mentioned, IP_3 binds to IP_3Rs on the S / ER which causes the channel moiety to open and thereby Ca^{2+} is released from the intracellular store into the cytoplasm (Berridge *et al.*, 2000). There are currently three characterised IP_3R subtypes (IP_3R-1, 2 and 3) (Blondel *et al.*, 1993) which have a tetrameric structure

with each unit comprising of 6 TM regions present in the C-terminal and an IP_3-binding site in the N-terminal region (Michikawa *et al.*, 1994; Mignery *et al.*, 1990). It is suggested that each of the 4 subunits require one molecule of IP_3 to be bound in order for the channel to open (Marchant *et al.*, 1997). The expression of the three IP_3R subtypes is not ubiquitous, as the relative contribution of each subtype to the overall expression of IP_3R varies in a tissue-dependent manner. For example, in arterial smooth muscle IP_3R-1 is the predominantly expressed subtype with little expression of IP_3R-2 and IP_3R-3 (Grayson *et al.*, 2004). Using a cell line expressing all 3 IP_3R subtypes, it was determined that these subtypes exhibit different sensitivities to IP_3 with an EC_{50} regarding Ca^{2+} release for IP_3R-2, IP_3R-1 and IP_3R-3 of 0.35, 4.7 and 18.6 μM respectively (Miyakawa *et al.*, 1999). However, in terms of IP_3 binding, IP_3R-3 bound IP_3 with significantly less affinity (K_d ~40 nM) than either IP_3R-1 or IP_3R-2 (K_d ~1 and ~2 nM respectively) (Wojcikiewicz *et al.*, 1998). The difference between the 3 IP_3R subtypes in both IP_3 binding and sensitivity to activation by IP_3 illustrates that, as with the SERCA isoforms, IP_3R subtype expression may also allow the cell to match specific protein expression to cell-type specific function. In addition to gating by IP_3, IP_3Rs are also biphasically regulated by changes in the intracellular Ca^{2+} concentration. However, as with IP_3 gating, their appears to be variation in the sensitivity of each IP_3R subtype with respect to Ca^{2+}-dependent regulation of IP_3Rs (Boehning *et al.*, 2000; Missiaen *et al.*, 1998; Miyakawa *et al.*, 1999; Taylor *et al.*, 2002). Therefore, IP_3Rs exhibit subtype-specific regulation and gating by both IP_3 and Ca^{2+}, allowing the cell and, in particular the S / ER, to tightly regulate both IP_3-mediated Ca^{2+} signals and CICR amplification of Ca^{2+} signals via IP_3Rs.

1.4.4 Ca^{2+} mobilisation by pyridine nucleotides

In addition to intracellular Ca^{2+} mobilisation by IP_3, there is a substantial body of evidence supporting the role of two pyridine nucleotides in Ca^{2+} mobilisation, cyclic adenosine diphosphate-ribose (cADPR) and nicotinic acid adenine dinucleotide phosphate (NAADP).

1.4.4.1 Ca^{2+} mobilisation by cADPR

In 1987 Lee and colleagues discovered that, in addition to IP_3, 2 pyridine nucleotides were capable of mediating Ca^{2+} release in sea urchin egg homogenate. These nucleotides were identified as β-nicotinamide adenine dinucleotide (β-NAD^+) and β-nicotinamide adenine dinucleotide phosphate (β-$NADP^+$) (Clapper *et al.*, 1987). Prior desensitisation of the homogenates with any of the 3 messengers did not inhibit further Ca^{2+} release by subsequent application of a different molecule. This illustrated that the 2 pyridine nucleotides not only mobilised Ca^{2+} by a mechanism different to that of IP_3 but also via mechanisms independent of each other (Clapper *et al.*, 1987). However, the authors also observed that β-NAD^+ mobilised Ca^{2+} after a notable delay of approximately 1-2 minutes which was absent with both IP_3 and β-$NADP^+$ mediated Ca^{2+} release (Clapper *et al.*, 1987). This delay was later demonstrated to be due to the enzymatic conversion of β-NAD^+ into an active, Ca^{2+} mobilising metabolite identified as cADPR (Lee *et al.*, 1989). Following this discovery, enzymes capable of synthesising cADPR were identified in sea urchin eggs and a number of mammalian tissues, suggesting that cADPR is a ubiquitous intracellular Ca^{2+} mobilising messenger (Koshiyama *et al.*, 1991; Lee *et al.*, 1991; Rusinko *et al.*, 1989; Walseth *et al.*, 1991).

1.4.4.2 Synthesis of cADPR

The synthesis of cADPR may be stimulated by the activation of a number of GPCR signalling pathways (Higashida, 1997). cADPR is synthesised from β-NAD^+ and this reaction is thought to be mediated by ADP-ribosyl cyclases (ARCs) which are a family of multifunctional enzymes, that exhibit a number of activities such as base-exchange, glycohydrolase and cyclase activity (Lee, 1999; Lee, 2000). The first ARC to be isolated was from the ovetestis of *Aplysia californica* (Hellmich *et al.*, 1991) and two mammalian homologues of the *Aplysia* ARC have also been identified: the type II membrane glycoprotein CD38 (Howard *et al.*, 1993; States *et al.*, 1992) and a GPI-anchored protein, CD157 (Hirata *et al.*, 1994). However investigations into the topology of the CD38 enzyme revealed that that the catalytic site is located on the extracellular face of the plasma membrane. This poses a 'topological paradox'

whereby cADPR is potentially synthesised extracellularly, only to then mobilise Ca^{2+} via interaction with its intracellularly located receptor (De Flora *et al.*, 2000). A solution to this paradox was proposed by De Flora and colleagues, basing their suggestion on the finding that β-NAD^+ can be transported outside the cell via connexin 43 hemichannels where it is then converted to cADPR, and transported back into the cell (Bruzzone *et al.*, 2001). However this process would appear to be energy inefficient and more suited to an autocrine / paracrine signalling mechanism rather than a rapid intracellular signalling system. A more probable solution is that an as yet unidentified CD38 homologue could be found on the surface of intracellular organelles. Consistent with this view, 3 ARC isoforms from the sea urchin egg, ARCα, ARCβ and ARCγ, have been cloned and characterised by Galione and co-workers (Davis *et al.*, 2008). Though not closely related to CD38 the distribution of these isoforms revealed that ARCα was ectocellular, while ARCβ and ARCγ were located within the lumen of acidic organelles and in a pattern reminiscent of the distribution of cortical granules (Davis *et al.*, 2008). It is therefore clear, that in sea urchin eggs there exists a closer coupling between the site of cADPR synthesis and its target receptor, than would be indicative of an extracellularly orientated ARC. Furthermore, in mammalian cells subpopulations of CD38 appear to be localised on the ER and nuclear membranes (Sun *et al.*, 2002; Yalcintepe *et al.*, 2005). Taken together these data suggest that future investigations may identify a mammalian equivalent of the intracellular ARCβ and ARCγ, yet with limited homology to the sea urchin isoforms. Such an enzyme that is distinct from CD38 and CD157 would therefore be capable of cADPR synthesis intracellularly and thus resolve the paradox associated with CD38 and CD157.

Some but not all ARCs are multifunctional, and it has been shown that metabolism of cADPR may be mediated by ARCs as, in addition to being able to catalyse the generation of cADPR from β-NAD^+, both CD38 and CD157 have also been shown to catalyse the hydrolysis of cADPR to ADP-ribose (Hirata *et al.*, 1994; Howard *et al.*, 1993).

1.4.4.3 cADPR-mediated Ca^{2+} mobilisation via ryanodine receptors

Ca^{2+} release by cADPR involves the regulation of RyRs present on the ER/SR. This was first demonstrated in sea urchin egg homogenates whereby caffeine and ryanodine desensitised sea urchin egg homogenate to Ca^{2+} release by cADPR but not IP_3 (Galione *et al.*, 1991; Lee *et al.*, 1993). Also, the RyR antagonist ruthenium red inhibited cADPR-mediated Ca^{2+} release (Galione *et al.*, 1991). Furthermore, it was later shown that lower, subthreshold concentrations of caffeine potentiated Ca^{2+} release by cADPR (Lee, 1993). This suggested that cADPR not only released Ca^{2+} from the same store as caffeine but also acted on the same Ca^{2+} release channels, RyRs (Lee, 1993). The role of RyRs in cADPR-mediated Ca^{2+} release has since been shown in a broad range of cell types from protozoa to mammals. In the protozoan parasite, *T. gondii* ruthenium red inhibited cADPR-mediated Ca^{2+} release but not IP_3-mediated Ca^{2+} release (Chini *et al.*, 2005). Consistent with cADPR-mediated Ca^{2+} release via RyRs in the sea urchin egg, inhibitory concentrations of ryanodine and ruthenium red block cADPR-mediated Ca^{2+} release in a number of mammalian preparations including rat brain microsomes and mesangial cells (Meszaros *et al.*, 1993; White *et al.*, 1993; Yusufi *et al.*, 2001). Furthermore, ryanodine also inhibits cADPR-mediated hyperpolarisation and dilation in rat pulmonary arterial smooth muscle cells (Boittin *et al.*, 2003), and reduced expression of the RyR subtype 3 in Jurkat T-cells results in a significant reduction in Ca^{2+} release in response to cADPR without affecting Ca^{2+} release by IP_3 (Schwarzmann *et al.*, 2002).

RyRs are large (~2000 kDa) homotetramers that regulate Ca^{2+} release from the S / ER. There are currently 3 known mammalian subtypes of RyR (RyR1, RyR2 and RyR3) which have approximately 65% amino acid homology (Hamilton, 2005). RyRs may be activated by Ca^{2+} directly or Ca^{2+} may facilitate further Ca^{2+} release via RyRs in a process known as Ca^{2+}-induced Ca^{2+} release (CICR) (Endo *et al.*, 1970). This process of CICR allows the amplification of small, localised Ca^{2+} signals into global Ca^{2+} waves via the progressive recruitment of subpopulations of RyRs. Ca^{2+} at millimolar concentrations may also inhibit RyRs and thus RyRs exhibit a bell-shaped concentration-response to cytoplasmic Ca^{2+} (Fill *et al.*, 2002). As previously mentioned, in addition to Ca^{2+} modulation of RyRs, cADPR is also an endogenous regulator that can either activate RyRs directly or facilitate CICR via RyRs by sensitising RyRs to Ca^{2+} (Galione *et al.*, 1991; Meszaros *et al.*, 1993). Further

complexity is provided by the fact that Ca^{2+} can sensitise RyRs to activation by cADPR (Panfoli *et al.*, 1999). It is therefore important to consider these combinatorial effects of cADPR and Ca^{2+} on the regulation of RyRs when investigating Ca^{2+} signals involving RyR and / or CICR (Evans *et al.*, 2005).

Despite the fact that cADPR has been shown to regulate Ca^{2+} signalling via RyRs, investigations on the mechanism of binding / regulation of RyRs by cADPR have proved inconclusive. Initial experiments regarding cADPR binding used [^{32}P]N_3-cADPR as a photoaffinity probe for cADPR binding sites. Photoaffinity labelling identified two putative cADPR binding proteins (Walseth *et al.*, 1993). These proteins of approximately 100 and 140 kDa in size are smaller than RyRs (~2000 kDa) (Hamilton, 2005) and were therefore considered to be either RyR fragments or distinct cADPR binding/accessory proteins (Walseth *et al.*, 1993). However, the former suggestion was deemed 'unlikely' by the authors as no larger labelled proteins, indicative of less fragmented sections, were detected. Furthermore, binding of cADPR to the two detected proteins was inhibited by caffeine to a differing extent, suggesting that they are separate proteins rather than resultant fragments from proteolysis of a larger protein (Walseth, et al., 1993). In recent years evidence has also been presented to suggest that FK506-binding protein 12.6 (FKBP12.6) is involved in cADPR-mediated Ca^{2+} release via RyRs. Based on studies involving microsomes from rat pancreatic islets it was proposed that FKBP12.6 normally binds to RyRs and has an inhibitory effect. Upon cADPR binding to FKBP12.6 it has been proposed that the FKBP12.6-cADPR complex dissociates from the RyR resulting in an increased open probability (Noguchi *et al.*, 1997). Similar results have also been demonstrated in other cell types including coronary arterial smooth muscle and tracheal smooth muscle (Tang *et al.*, 2002; Wang *et al.*, 2004) thus adding further support for FKBP12.6 acting as a cADPR binding protein. However, contrary to this proposal, it was observed that cADPR did not affect the binding of recombinant FKBPs to RyR3 in HEK293 cells (Bultynck *et al.*, 2001). Furthermore, it has also been demonstrated that in the sea urchin egg, antagonists of FKBP, rapamycin and FK-506, failed to inhibit [^{32}P]cADPR binding (Thomas *et al.*, 2001). Taken together, these data would suggest that either the cADPR binding site is an as yet unidentified homologue of the FKBPs or that cADPR binding to FKBP12.6 could be RyR subtype-specific.

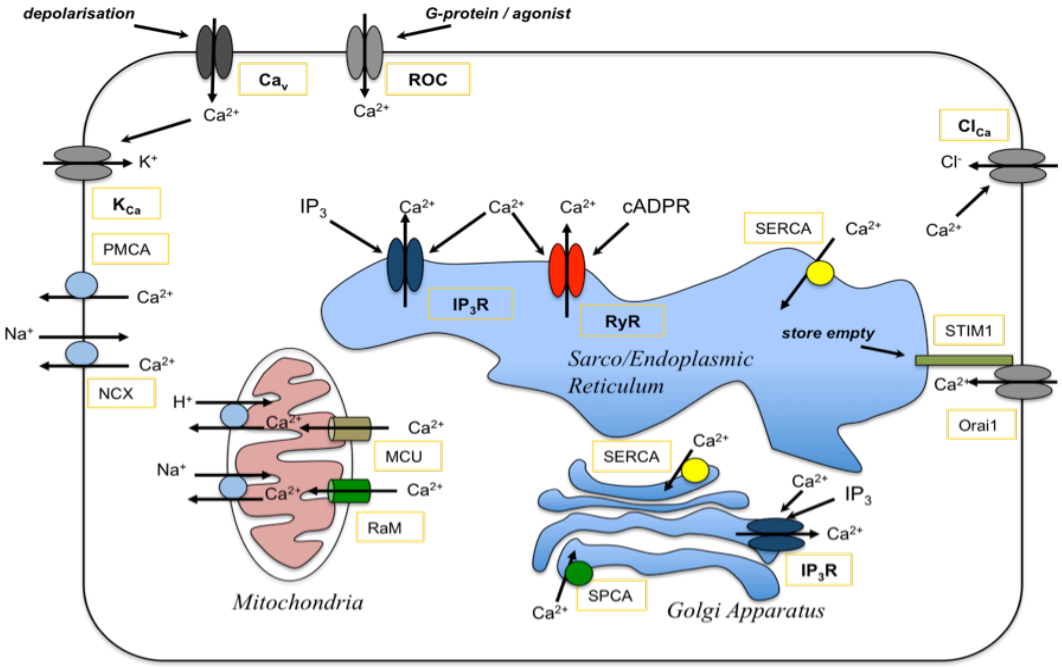

Fig. 1.2. Summary schematic representation of the mechanisms involved in Ca^{2+} extrusion/influx across the plasma membrane and sequestering/release of Ca^{2+} by intracellular Ca^{2+} stores

Depicted are some of the mechanisms by which Ca^{2+} is able cross the plasma membrane and the membranes of some of the intracellular Ca^{2+} stores. Ca_v, voltage gated Ca^{2+} channel; ROC, receptor operated channel; PMCA, plasma membrane Ca^{2+} ATPase; NCX, Na^+/Ca^{2+} exchanger; K_{Ca}, Ca^{2+}-activated K^+ channel; Cl_{Ca}, Ca^{2+}-activated Cl^- channel; STIM, stromal interaction molecule; SERCA, Sarco/endoplasmic reticulum Ca^{2+} ATPase; RyR, Ryanodine receptor; IP_3R, IP_3 receptor; SPCA, secretory pathway ATPase; MCU, mitochondrial Ca^{2+} uniporter; RaM, rapid mode of mitochondrial Ca^{2+} uptake.

1.5 NAADP-dependent Ca^{2+} signalling

In 1987 Lee and colleagues first discovered that a nicotinic acid derivative of β-nicotinamide adenine dinucleotide phosphate (β-$NADP^+$) released Ca^{2+} in sea urchin egg, and that this mechanism was independent of the IP_3- and β-NAD^+/cADPR-mediated Ca^{2+} release mechanisms (Clapper *et al.*, 1987). This Ca^{2+}-mobilising derivative was later identified as NAADP (Chini *et al.*, 1995a; Lee *et al.*, 1995). Since its discovery NAADP has been found to mobilise Ca^{2+} in a wide variety of organisms including invertebrates (Albrieux *et al.*, 1998; Chini *et al.*, 1995a; Santella *et al.*, 2000) vertebrates (Berg *et al.*, 2000; Cancela *et al.*, 1999; Chini *et al.*, 1995b; Mojzisova *et al.*, 2001; Zhang *et al.*, 2006a) and plants (Navazio *et al.*, 2000) and has

been described as the most potent Ca^{2+} mobilising agent known to date (Galione *et al.*, 2005).

1.5.1 Synthesis and metabolism of NAADP

It is widely thought that, similar to the synthesis of cADPR, NAADP is synthesised by members of the ARC family. As well as exhibiting cyclase activity necessary for cADPR synthesis, ARCs are also capable of catalysing the base-exchange reaction needed to generate NAADP (Aarhus *et al.*, 1995; Lee *et al.*, 1991). The proposed mechanism for NAADP synthesis is a base-exchange reaction via substitution of the nicotinamide group for a nicotinc acid group on β-$NADP^+$ (Aarhus *et al.,* 1995). However, this dual function of ARCs implies that NAADP synthesis is subject to the same topological paradox that is associtated with cADPR synthesis. NAADP is therefore likely to be synthesised by an as yet unidentified CD38 homologue, as mentioned previously with regard to cADPR synthesis. Recently however, work from Churchill and colleagues has shown that an enzyme present on the membrane of sea urchin sperm is capable of synthesising NAADP. Indeed, this enzyme favours base-exchange over cyclase activity and therefore does not produce measurable cADPR. This enzyme is unique from the ARC family and was termed NAADP-synthase (Vasudevan *et al.*, 2008). However, as NAADP-synthase was found to be present on the surface of the sea urchin sperm, the cellular location of this enzyme prompts similar questions regarding its functional relevance within other cell types. Nevertheless, the finding of a unique enzyme capable of NAADP synthesis adds further support to the proposal that an as yet unidentified CD38-like enzyme with an intracellularly-orientated active site, is responsible for the synthesis of NAADP necessary to support a role in intracellular signalling.

Unlike cADPR, the metabolism of NAADP is not catalysed by any of the known ARCs. However a number of common hydrolytic enzymes are responsible for the break down of this potent Ca^{2+} mobilising messenger. For example, NAADP has been shown to be metabolised to yield NAAD by cellular alkaline phosphatases (Kontani *et al.*, 1993), and the action of nucleotide pyrophosphatase yields 2'-phospho-AMP and nicotinic acid mononucleotide (De Flora *et al.*, 2000).

1.5.2 NAADP mobilises Ca^{2+} from a separate store to that mobilised by IP_3 and cADPR

Since its discovery a number of studies have been carried out in order to characterise the precise mechanism underpinning NAADP-mediated Ca^{2+} release. Importantly, NAADP has been shown to mobilise Ca^{2+} in an IP_3R- and RyR-independent manner, and from a store separate to that mobilised by IP_3 and cADPR. This was first indicated by Lee & Aarhus using Percoll density gradient centrifugation of sea urchin egg homogenate (Lee *et al.*, 1995). This technique is able to separate the homogenate into a number of fractions and their sensitivities to IP_3/cADPR/NAADP can then be assayed. Both IP_3- and cADPR-sensitive fractions co-migrated to the same two fractions. These two fractions also contained the ER marker, glucose-6-phophatase. Conversely, NAADP-sensitive fractions had a much broader distribution suggesting that this was a separate Ca^{2+} store from that mobilised by either IP_3 or cADPR (Lee *et al.*, 1995). Furthermore, cADPR antagonists (8-NH_2-cADPR, ruthenium red, and procaine) and IP_3 antagonists (heparin) had no effect on NAADP-mediated Ca^{2+} release in either the whole sea urchin egg or mircrosomes derived from homogenates of the sea urchin egg, suggesting that NAADP acts on a receptor distinct from RyRs and IP_3Rs (Chini *et al.*, 1995a; Lee *et al.*, 1995). The view that NAADP mobilises Ca^{2+} from a separate store was further supported by the finding that in sea urchin egg homogenate, depletion of the ER Ca^{2+} stores using the SERCA pump inhibitor thapsigargin was without effect on NAADP-mediated Ca^{2+} release, whereas both IP_3- and cADPR-mediated Ca^{2+} release was abolished (Genazzani *et al.*, 1996b). And this has now been confirmed in variety of mammalian cell types including PASMCs (Boittin *et al.*, 2002; Kinnear *et al.*, 2004).

In addition to the pharmacological distinction, evidence in support of a separate NAADP-mediated Ca^{2+} release mechanism has been obtained in the stratified sea urchin egg (Lee *et al.*, 2000). The process of stratification elongates sea urchin eggs by centrifugation such that cellular components can be partially separated by density. Within the stratified cells, Ca^{2+} release triggered by flash-photolysis of caged IP_3 and cADPR triggered Ca^{2+} release from the nuclear pole of the stratified egg. In marked contrast, photo-release of NAADP triggered Ca^{2+} release from the opposing distal pole of the egg (Lee *et al.*, 2000).

1.5.3 NAADP mediates Ca^{2+} release via interaction with a pharmacologically discreet receptor

Experiments have not only shown that NAADP mobilises a non-ER store but there is also a growing body of evidence to suggest that NAADP mediates its effect via interaction with a discreet NAADP receptor. As previously mentioned cADPR and IP_3 antagonists were without effect on NAADP-meditated Ca^{2+} release in both homogenates of sea urchin eggs and whole sea urchin egg suggesting that NAADP does not release Ca^{2+} via IP_3Rs or RyRs (Chini *et al.*, 1995a; Lee *et al.*, 1995). For example, in the sea urchin egg, in contrast to IP_3- and cADPR-mediated Ca^{2+} release, NAADP-mediated Ca^{2+} release was unaffected by the extravesicular Ca^{2+} concentration and by a pH change from 7.2 to 6.7 and 8.0 (Chini *et al.*, 1996; Genazzani *et al.*, 1997). This has also been confirmed in microsomes derived from mammalian cells (Yusufi *et al.*, 2002). Another unique pharmacological property of NAADP-dependent Ca^{2+} release is inhibition by L-type VGCC antagonists. In the sea urchin egg and in rat brain microsomes L-type VGCC inhibitors such as varapamil, nifedipine and diltiazem blocked NAADP-evoked Ca^{2+} release without blocking Ca^{2+} release by cADPR and IP_3 (Bak *et al.*, 1999; Genazzani *et al.*, 1996a; Genazzani *et al.*, 1997). This suggests that NAADP activates a receptor that is structurally related to L-type voltage-gated Ca^{2+} channels. That a distinct channel was involved is highlighted by the observation that the L-type VGCC agonist Bay K 8644 inhibited rather than potentiated NAADP-mediated Ca^{2+} release in sea urchin egg homogenate (Genazzani *et al.*, 1996a; Genazzani *et al.*, 1997).

Further evidence for a discreet NAADP receptor comes from the homologous desensitisation studies in sea urchin egg homogenate. Briefly, NAADP-mediated Ca^{2+} release is desensitized by sequential additions of saturating concentrations of NAADP. This inhibition by sequential additions was also exhibited by both IP_3- and cADPR-mediated Ca^{2+} mechanisms (Chini *et al.*, 1995a; Genazzani *et al.*, 1996a). However in each case desensitisation was homologous, such that desensitisation to NAADP had no effect on cADPR- or IP_3-mediated Ca^{2+} release (Chini *et al.*, 1995a; Genazzani *et al.*, 1996a). This absence of cross-desensitisation demonstrates further that each of these Ca^{2+} mobilising second messenger mediate their effects via the activation of pharmacologically distinct receptors.

The process of desensitisation to NAADP is also different. In the sea urchin egg not only does a threshold concentration of NAADP elicit release of Ca^{2+} and prevent further Ca^{2+} release by subsequent additions of NAADP for up to 11 minutes (Aarhus *et al.*, 1996), but subthreshold concentrations (1-5 nM) of NAADP block Ca^{2+} release by the later addition of a saturating concentration (0.5-1 μM) of NAADP (Aarhus *et al.*, 1996; Genazzani *et al.*, 1996a). This inactivation / desensitisation also appears to be time-dependent as preincubation of microsomes with 1 nM NAADP for 1 minute reduced subsequent NAADP-mediated Ca^{2+} release, whereas preincubation for 10 minutes resulted in complete block of release by the subsequent addition of ~1 μM NAADP (Aarhus *et al.*, 1996). In the sea urchin egg, the persistent (1500 s) self-inactivation of NAADP differs from that of IP_3 and cADPR inactivation which is transient and can be reversed within 30 minutes (Genazzani *et al.*, 1996a). In contrast to the sea urchin egg, in mammalian cells NAADP-mediated Ca^{2+} release appears to conform to a bell-shaped concentration-response curve (Berg *et al.*, 2000; Cancela *et al.*, 1999; Masgrau *et al.*, 2003). This has been shown in T-lymphocytes, pancreatic β-cells and pancreatic acinar cells, where low (nanomolar) concentrations of NAADP elicit Ca^{2+} release, whereas supra-threshold (micromolar) concentrations are ineffective (Berg *et al.*, 2000; Cancela *et al.*, 1999; Masgrau *et al.*, 2003). However, PASMCs exhibited a more variable degree of inactivation in response to intracellular dialysis of 100 μM NAADP (Boittin *et al.*, 2002). The different inactivation properties of NAADP between cell types is likely to be as a result of the variation in specific function of each cell type and possibly the nature of the NAADP receptor or regulation of the Ca^{2+} release process.

The functional role of homologous inactivation of NAADP-mediated Ca^{2+} signalling was further investigated by Churchill & Galione. In the sea urchin egg, global Ca^{2+} transients were evoked by repeated application of IP_3, cADPR or NAADP. Repeated application of either IP_3 or cADPR resulted in a gradual decrease in the peak amplitude of Ca^{2+} release. However self-inhibition was not observed when the interval between application was increased from 20 s to 120 s (Churchill *et al.*, 2001b). In contrast, repetitive NAADP stimulation resulted in a decrease in the peak Ca^{2+} released regardless of the time interval between application (Churchill *et al.*, 2001b). Furthermore, local (compartmentalised) photo-release of caged NAADP by a UV laser targeted to a subsection of a sea urchin egg blocked further release by

NAADP in that region of the cell, but was without effect on Ca^{2+} release triggered by photolysis of caged NAADP in regions of the cell distant from the initial volume in which photorelease was triggered. This localised inactivation could last for approximately 20 minutes (Churchill *et al.*, 2001b). Local IP_3 and cADPR release on the other hand, did not affect the pattern of the Ca^{2+} increase evoked by the later global release of the messenger. This not only adds further weight to the view that NAADP does not act via RyRs or IP_3Rs, but also suggests that the self-desensitisation by NAADP may confer a spatiotemporal memory with respect to Ca^{2+} release events triggered (Churchill *et al.*, 2001b).

1.5.4 NAADP mediates Ca^{2+} release via a two-pool system in sea urchin eggs

In the sea urchin egg, NAADP has been shown to evoke long-term Ca^{2+} oscillations that require CICR from the ER (Churchill *et al.*, 2001a). Thus, preincubation block of IP_3Rs with heparin or RyR-dependent Ca^{2+} release with 8-NH_2-cADPR resulted in the inhibition of the first Ca^{2+} oscillation after an initial phase of NAADP-evoked Ca^{2+} release (Churchill *et al.*, 2001a). Furthermore, depletion of ER stores by inhibition of SERCA with thapsigargin partially inhibited NAADP-induced Ca^{2+} release but did not abolish it. Importantly, however, thapsigargin inhibited the Ca^{2+} oscillations that normally followed the initial phase of Ca^{2+} release in response to photorelease of NAADP (Churchill *et al.*, 2001a). This led the authors to propose a two-pool system whereby NAADP initially mobilises Ca^{2+} from a distinct, NAADP-sensitive store which is subsequently amplified by CICR from the ER via IP_3Rs and RyRs. It was proposed, therefore, that the oscillations result from the uptake into the ER of Ca^{2+} initially released by NAADP and that this may then 'prime' the ER for subsequent Ca^{2+} release via IP_3Rs and RyRs (Churchill *et al.*, 2001a).

1.5.5 NAADP mobilises Ca^{2+} from a lysosome-related acidic Ca^{2+} store

1.5.5.1 Acidic Ca^{2+} stores

Despite the identification of the aforementioned two-pool system of NAADP-mediated Ca^{2+} release, the identity of the NAADP-sensitive store remained elusive

until 2002, when Churchill and colleagues showed that NAADP evoked Ca^{2+} release from acidic organelles called reserve granules in sea urchin eggs (Churchill *et al.*, 2002).

That acidic organelles could act as releasable Ca^{2+} stores was not widely accepted as, traditionally, lysosomes were considered to be acidic cellular compartments with the specific role of degrading both endogenous and exogenous macromolecules (Dell'Angelica *et al.*, 2000). However it was observed that lysosomes, in addition to the stores mentioned above, also contain a high luminal Ca^{2+} concentration and could thus act as a releasable Ca^{2+} store (Christensen *et al.*, 2002; Yagodin *et al.*, 1999).

The concept of a lysosomal-related, releasable Ca^{2+} store is consistent with earlier experiments which showed that Ca^{2+} release in response to pentylenetetrazole originated from dense lysosome-like granules in snail neurons (Sugaya *et al.*, 1978). Further support for a lysosome-related Ca^{2+} store came from the use of glycyl-phenalanine 2-napthylamide (GPN). GPN is a known substrate for cathepsin C which is an exopeptidase found exclusively within lysosomes. Once GPN enters the lysosome, it is broken down by cathepsin C into its constituent amino acids. These amino acids are unable to cross the lysosomal membrane and therefore their accumulation within the lumen increases the osmotic pressure until the lysosome is ruptured (Berg *et al.*, 1994; Jadot *et al.*, 1984). Addition of GPN resulted in an increase in the intracellular Ca^{2+} concentration in both mammalian and non-mammalian cells, suggesting that lysosomes may function as a Ca^{2+} store (Churchill *et al.*, 2002; Haller *et al.*, 1996; Srinivas *et al.*, 2002; Yagodin *et al.*, 1999). The process by which lysosomes sequester Ca^{2+} is not so clear. However, it appears to be dependent upon the formation of a proton gradient, which was demonstrated by the observation that the intracellular Ca^{2+} concentration of the lysosome decreased as the luminal pH increased (Christensen *et al.*, 2002). This was confirmed shortly after by the finding that 3 compounds FCCP, nigecerin and NH_3, all of which disrupt the lysosomal proton gradient, inhibited Ca^{2+} uptake into lysosome-related organelles (Churchill *et al.*, 2002) and by the finding that the vacuolar proton pump ($V\text{-}H^+$-ATPase) inhibitor bafilomycin A1 inhibited Ca^{2+} uptake into lysosomes (Christensen *et al.*, 2002). This led to the proposal that lysosome-related Ca^{2+} stores contain a $V\text{-}H^+$-ATPase which generates a proton gradient that is then utilised by a H^+/Ca^{2+}

exchanger to accumulate Ca^{2+} (Christensen *et al.*, 2002; Churchill *et al.*, 2002) (Fig.1.3).

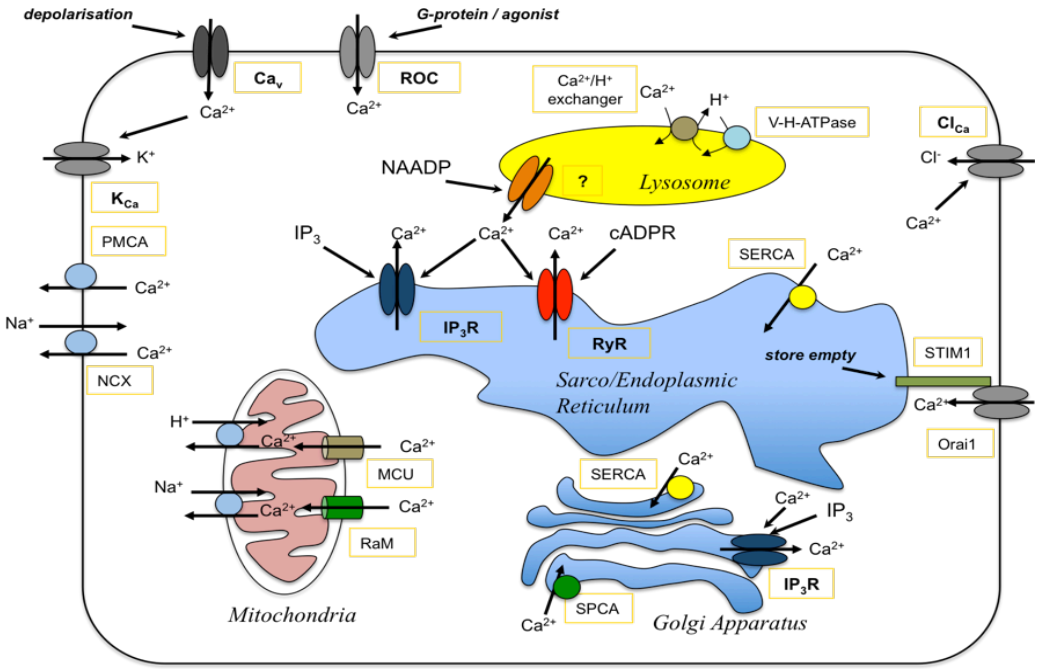

Fig. 1.3. Schematic representation of the mechanisms involved in Ca^{2+} extrusion/influx across the plasma membrane and sequestering/release of Ca^{2+} by intracellular Ca^{2+} stores including acidic organelles

Depicted are some of the mechanisms by which Ca^{2+} is able cross the plasma membrane and the membranes of organelles recognised as intracellular Ca^{2+} stores. The putative NAADP receptor is indicated by '?'. Ca_v, voltage gated Ca^{2+} channel; ROC, receptor operated channel; PMCA, plasma membrane Ca^{2+} ATPase; NCX, Na^+/Ca^{2+} exchanger; K_{Ca}, Ca^{2+}-activated K^+ channel; Cl_{Ca}, Ca^{2+}-activated Cl^- channel; STIM, stromal interaction molecule; SERCA, Sarco/endoplasmic reticulum Ca^{2+} ATPase; RyR, Ryanodine receptor; IP_3R, IP_3 receptor; SPCA, secretory pathway Ca^{2+} ATPase; MCU, mitochondrial Ca^{2+} uniporter; RaM, rapid mode of mitochondrial Ca^{2+} uptake; V-H-ATPase, vacuolar proton pump.

Similar to lysosomes, the contribution of endosomes to Ca^{2+} homeostasis has not been widely studied. However, endosomes are capable of storing Ca^{2+} with initial studies suggesting that endosomes sequester Ca^{2+} via a H^+/Ca^{2+} exchanger that is driven by a proton gradient maintained by a H^+-ATPase (Hilden *et al.*, 1989). Later reports suggest that the main mechanism by which endosomes take up Ca^{2+} is via endocytosis and that this Ca^{2+} is released over time as the endosome undergoes acidification (Gerasimenko *et al.*, 1998). Endosomes are not recognised as major releasable stores, however Ca^{2+} release is required for the fusion of endosomal

membranes after the formation of the SNARE complex (Peters *et al.*, 1998). This post-docking Ca^{2+}-dependent event is important for the fusion of early- and late-endosomal membranes and late-endosomal to lysosomal membranes (Holroyd *et al.*, 1999; Pryor *et al.*, 2000). Importantly, endosomes could be a possible additional organellar Ca^{2+} store that can be distinguished from lysosomes as, due to the specific lysosomal localisation of cathepsin C, endosomes would be unaffected by GPN (Berg *et al.*, 1994).

In fact the literature suggests that an endolysosomal Ca^{2+} store was identified as early as 1991 by Pozzan and co-workers (Fasolato *et al.*, 1991). However, little progress was made in terms of function as neither a RyR- or IP_3R-dependent Ca^{2+} release mechanism were identified and at this point in time a role of NAADP in Ca^{2+} signalling had not been suggested. However there is now a growing body of evidence that suggests that an endolysosomal Ca^{2+} store is mobilised by NAADP in a variety of cell types (Churchill *et al.*, 2002; Kinnear *et al.*, 2004; Yamasaki *et al.*, 2004; Zhang *et al.*, 2006a).

1.5.5.2 Acidic lysosome-related organelles function as NAADP-sensitive Ca^{2+} stores

A pivotal advance in the investigations on the mechanism of NAADP-dependent Ca^{2+} signalling was provided by the finding that lysis, with GPN, of reserve granules (the sea urchin egg equivalent of lysosomes) resulted in the block of NAADP-induced Ca^{2+} release, yet was without effect on Ca^{2+} release by IP_3 and cADPR. This suggested that these lysosome-related organelles functioned as a separate NAADP-sensitive store proposed as pool 1 in the two-pool system of Churchill and co-workers (Churchill *et al.*, 2002). To verify that the reserve granules could be the NAADP-sensitive store, the location of reserve granules in stratified sea urchin eggs were visualised using LysoTracker Red, a fluorescent label of acidic organelles. LysoTracker Red labelling revealed that the pole associated with NAADP-mediated Ca^{2+} release was enriched with acidic organelles whereas the opposing nuclear pole was depleted of acidic organelles (Churchill *et al.*, 2002). This is consistent with the spatial pattern of Ca^{2+} release mediated by NAADP, IP_3 and cADPR previously observed in stratified eggs (Lee *et al.*, 2000). As mentioned above with reference to lysosomes as Ca^{2+} stores, it was proposed that lysosome-related stores utilise the bafilomycin-sensitive V-H^+-ATPase pump to generate a proton

gradient which may then be utilised in turn to mediate Ca^{2+} accumulation via a H^+/Ca^{2+} exchanger. Consistent with this proposal, preincubation of sea urchin eggs with bafilomycin in order to block refilling of the acidic organelle Ca^{2+} stores, resulted in the inhibition of NAADP-mediated but not IP_3- or cADPR-mediated Ca^{2+} release (Churchill *et al.*, 2002). Given these observations and the previously proposed two-pool system, it was suggested that NAADP mediates Ca^{2+} release from a lysosome-related Ca^{2+} store which is then amplified by CICR via the ER (Churchill *et al.*, 2002) (Fig.1.3). However, a lysosome-related, NAADP-sensitive Ca^{2+} store could be a unique property of the sea urchin egg, and it therefore needed to be verified in other cell types, mammalian in particular, in which NAADP-mediated Ca^{2+} release had been identified in order to determine whether or not this was a general mechanism of Ca^{2+} signalling.

1.5.6 NAADP-mediated Ca^{2+} release in mammalian cells

Since the initial experiments showing the ability of NAADP to evoke Ca^{2+} release in sea urchin egg, NAADP has been shown to mobilise Ca^{2+} in a number of mammalian cell types including PASMCs, cerebral cortex neurons, pancreatic acinar cells, and T-lymphocytes (Bak *et al.*, 1999; Berg *et al.*, 2000; Boittin *et al.*, 2002; Brailoiu *et al.*, 2005; Cancela *et al.*, 1999; Yamasaki *et al.*, 2004). NAADP-mediated Ca^{2+} mobilisation in mammalian cells was first shown in 1999 in pancreatic acinar cells (Cancela *et al.*, 1999). These experiments identified a bell-shaped concentration-response curve in mammalian cells such that high concentrations of NAADP failed to evoke Ca^{2+} release due to desensitisation of the NAADP receptor. Importantly, it was shown that an inhibitory concentration of NAADP (100 μM) had no effect on IP_3- and cADPR-mediated Ca^{2+} release, but abolished the Ca^{2+} spiking associated with the application of the secretory hormone cholecystokinin (CCK) (Cancela *et al.*, 1999). This study verified NAADP as an important intracellular messenger in mammalian cells, and in addition suggested that CCK mediated its effects via NAADP-evoked Ca^{2+} signalling.

The bell-shaped concentration-response curve of NAADP-mediated Ca^{2+} release has also been shown in isolated PASMCs which have proved an important cell type in the development of our understanding of NAADP-mediated Ca^{2+} release in

mammalian cells (Boittin *et al.*, 2002). Evans and colleagues showed that in PASMCs intracellular dialysis of NAADP triggers a global Ca^{2+} wave and contraction (Boittin *et al.*, 2002). Furthermore, the global Ca^{2+} wave was often preceded by a spatially restricted "Ca^{2+} burst" which either declined back to basal levels or subsequently triggered a global Ca^{2+} wave. This spatially restricted Ca^{2+} burst appeared to initiate a global Ca^{2+} wave only once a given threshold for CICR from the SR was breached (threshold Ca^{2+} concentration, ~ 400 nM) (Boittin *et al.*, 2002). This was consistent with the proposed two-pool model of NAADP-mediated Ca^{2+} signalling observed in sea urchin eggs (Churchill *et al.*, 2001a) and was indicative of the presence of an NAADP-sensitive store that releases a spatially restricted Ca^{2+} burst that can then be amplified by Ca^{2+} release via RyRs and/or IP_3Rs on the SR (Boittin *et al.*, 2002). This two-pool model was confirmed by the observation that, following inhibition of RyRs by ryanodine and depletion of SR Ca^{2+} stores by the block of SERCA pumps with thapsigargin, NAADP failed to elicit global Ca^{2+} waves yet still produced spatially restricted Ca^{2+} bursts. Interestingly, blockade of IP_3Rs with xestospongin C abolished signals in response to IP_3R, but was without effect on NAADP-mediated global Ca^{2+} waves (Boittin *et al.*, 2002). Thus, it was suggested that in PASMC, NAADP mobilises Ca^{2+} from a separate store which is then amplified by Ca^{2+} release from the SR via the progressive recruitment of RyRs but not via IP_3Rs. This is not without significance, as the fact that NAADP-dependent signals may be amplified by CICR via IP_3Rs and RyRs in other cell types strongly suggests that there is inherent flexibility in the coupling process that may be utilised by different cells to generate NAADP-dependent Ca^{2+} signals with discrete spatiotemporal patterns. Furthermore, it suggests that endolysosomal Ca^{2+} stores may expand or restrict the nature of their coupling to different populations of Ca^{2+} release channels on the S / ER in a cell-specific manner.

1.5.6.1 NAADP mobilises Ca^{2+} from lysosome-related organelles in mammalian cells

Following the identification of a lysosome-related, NAADP-sensitive Ca^{2+} store in sea urchin eggs (Churchill *et al.*, 2002) the identity of the mammalian NAADP-sensitive Ca^{2+} store was investigated. Using PASMCs, Kinnear *et al*. showed that both NAADP-induced Ca^{2+} bursts and subsequent global Ca^{2+} waves were abolished by preincubation of PASMCs with bafilomycin A1 (Kinnear *et al.*, 2004).

Bafilomycin was also shown to inhibit Ca^{2+} release by flash photolysis of caged-NAADP in the pancreatic acinar cell (Yamasaki *et al.*, 2004). Furthermore, LysoTracker labelling of lysosome-related organelles in pancreatic acinar cells revealed that these organelles were localised in the apical pole, which is the region of highest NAADP sensitivity (Cancela *et al.*, 2002; Yamasaki *et al.*, 2004). LysoTracker labelling of lysosomes in PASMCs also exhibited dense clustering in a manner consistent with the spatial nature of identified, NAADP-dependent Ca^{2+} bursts. In marked contrast, LysoTracker labelling of lysosomes within pancreatic β cells showed a much more diffuse pattern which also mirrored the global nature of NAADP-mediated Ca^{2+} release observed in these cells (Yamasaki *et al.*, 2004).

Most significantly, however, depletion of acidic stores with bafilomycin has been shown to block Ca^{2+} signalling by NAADP in, for example, PASMCs (Kinnear *et al.*, 2004) and pancreatic acinar cells (Yamasaki *et al.*, 2004) and has also been shown to block, in an agonist-specific manner, Ca^{2+} signalling in response to a variety of hormones / transmitters that have been shown to increase NAADP levels in PASMCs by activation of cell surface receptors in these and other cell types.

1.5.6.2 The NAADP "trigger zone" underpins NAADP-mediated Ca^{2+} release

In order for NAADP to mediate Ca^{2+} release via a two-pool, system tight coupling must exist between the NAADP-sensitive lysosome-related store and the ER/SR. Clear evidence for such coupling was provided by the finding that LysoTracker Red-labelled lysosomes form spatially organised clusters which are in a close association with a subpopulation of RyRs in PASMCs (Kinnear *et al.*, 2004). The junctional gap between the lysosome clusters and RyRs could not be resolved by deconvolution microscopy and is likely ≤ 0.1 μm. This junction has been proposed to function as an intracellular synapse or "trigger zone" for Ca^{2+} signalling by NAADP (Fig. 1.4) (Kinnear *et al.*, 2004).

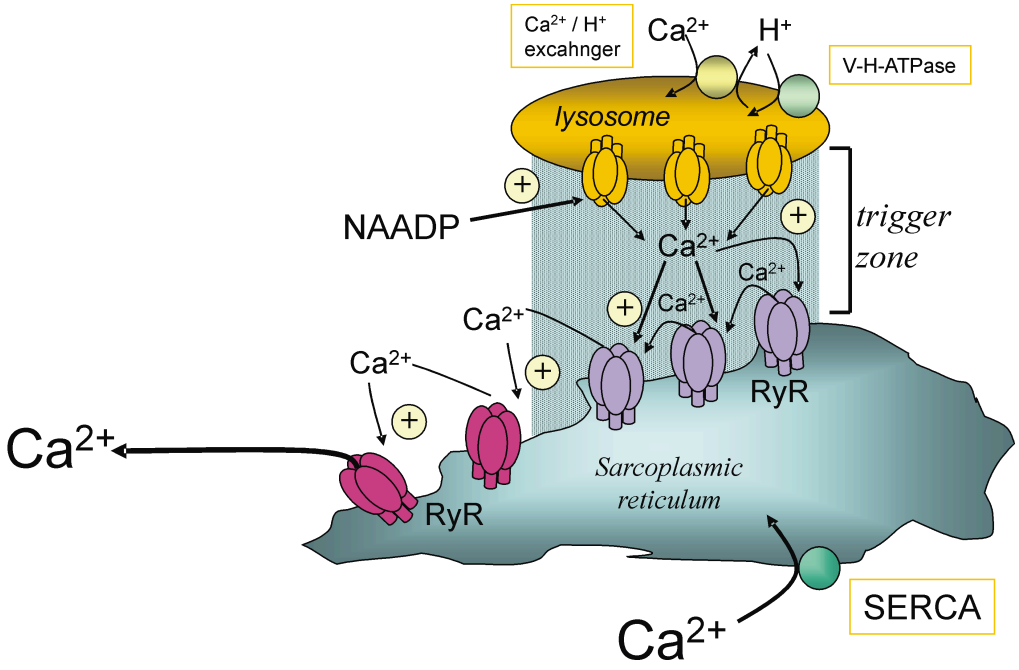

Fig. 1.4. Schematic representation of the trigger zone for Ca^{2+} release by NAADP in pulmonary arterial smooth muscle cells

The trigger zone consists of lysosomes closely opposed to ryanodine receptors (RyR) on the sarcoplasmic reticulum (SR). The lysosomes are thought to sequester Ca^{2+} via the action of the vacuolar proton pump (V-H^+-ATPase) coupled to a Ca^{2+}/H^+ exchanger. NAADP acts on putative NAADP receptors causing Ca^{2+} release into the trigger zone. If the Ca^{2+} released breaches a given threshold concentration the burst may be amplified into a global Ca^{2+} wave by Ca^{2+}-induced Ca^{2+} release (CICR) via proximal RyRs on the SR.

1.5.7 The NAADP receptor

Despite the wealth of data suggesting that NAADP not only elicits Ca^{2+} from a store separate to that of the S / ER, but also acts on its own pharmacologically distinct receptor, the molecular identity of such a receptor has remained elusive. Nevertheless, high affinity binding sites (K_d ~200 pM) have been identified in both sea urchin eggs and the mammalian brain (Billington *et al.*, 2000; Patel *et al.*, 2000a; Patel *et al.*, 2000b). NAADP binding to sea urchin egg homogenate is irreversible at physiological concentrations of K^+ which can be exploited as a tool by which NAADP receptors can be 'tagged' (Dickinson *et al.*, 2003). Protein purification studies of NAADP binding sites suggest that the NAADP receptor may be an oligomeric structure of approximately 450 kDa derived from subunits of approximately 150 kDa which is markedly different from that determined by the same

method (gel filtration) for both IP_3 and RyRs (~1000 kDa and ~2000 kDa respectively) and therefore adds further weight to the proposal that the target of NAADP is a discrete receptor (Berridge *et al.*, 2002).

However, until the NAADP receptor is identified further studies on NAADP-mediated Ca^{2+} release will remain limited. Therefore, this remains one of the key experimental objectives in the field of Ca^{2+} signalling.

1.6 Aims of this thesis

1. To determine whether ryanodine receptor subtype 1, 2 or 3, each of which is expressed in pulmonary arterial smooth muscle cells, is targeted to lysosome-sarcoplasmic reticulum junctions to comprise the trigger zone for the amplification of NAADP-induced Ca^{2+} bursts into global Ca^{2+} waves.

2. To determine whether or not a novel family of two-pore channels (TPCs) represent NAADP-gated endolysosomal calcium release channels.

3. To determine whether or not two-pore channels underpin NAADP-dependent calcium signals in pulmonary arterial smooth muscle cells.

Chapter 2: Materials and Methods

2.1 Dissection and cell isolation

2.1.1 Identification and dissection of 2nd order pulmonary arteries

Adult male Wistar rats (150-300 g) were humanely sacrificed by the Schedule 1 method of cervical dislocation (according to section 6.3 of the Home Office Code of Practice for the Humane Killing of Animals under Schedule 1 of the Animals (Scientific Procedures) Act 1986). The heart and lungs were removed *en bloc* and placed into HEPES buffered salt solution (HBSS) of the following composition (mM): 130 NaCl, 5.2 KCl, 1 $MgCl_2$, 1.7 $CaCl_2$, 10 glucose, 10 HEPES, pH 7.4, and kept on ice. Subsequent dissection was carried out under a dissection microscope (PZM, World Precision Instruments, USA) during which the tissue was bathed in cold (4 °C) HBSS. Each lobe was pinned out on a Sylgard-based dissection dish with the parietal surface facing upwards. At the point where the bronchus entered the lobe, the airway was cut open lengthways from the initial incision down the length of the lobe. Once the intrapulmonary artery was identified the airway tissue above, and the connective tissue either side of the artery was carefully removed in order to expose the artery ready for dissection. Handling the artery via a small piece of connective tissue that was left attached to the proximal end, the artery was then removed by cutting the connective tissue.

2.1.2 Isolation of pulmonary arterial smooth muscle cells

Each artery was cut open lengthways before being placed into low Ca^{2+} dissociation solution (DS) of the following composition (mM): 124 NaCl, 5 KCl, 1 $MgCl_2$, 0.5 NaH_2PO_4, 0.5 KH_2PO_4, 15 $NaHCO_3$, 0.16 $CaCl_2$, 0.5 EDTA, 10 glucose, 10 Taurine, 10 HEPES, pH 7.4, and maintained at 4°C. After 10 minutes arteries were transferred to fresh DS containing 0.5 mg/ml papain and 1 mg/ml bovine serum albumin and stored overnight at 4 °C. Papain is a cysteine protease consisting of a single polypeptide chain and has a broad substrate specificity. Contained within the

polypeptide chain are 3 residues (Cys-25, His-159 and Asn-175) that form a characteristic catalytic triad (Polgar *et al.*, 1982; Wiederanders, 2003) and it is the sulfhydryl group on the cysteine residue which is responsible for the nucleophylic attack involved in the protease activity.

The following day, 0.2 mM 1,4-Dithio-DL-thretiol (DTT) was added to the preparation in order to activate the papain, which was incubated for 1 hour at room temperature (22°C). DTT is a reducing agent that activates papain by maintaining the sulfhydryl groups present on the protease in a reduced state, thus exposing the catalytic triad to the peptide substrate. Following incubation with papain and DTT the arteries were washed 5 times in 1 ml of fresh, papain-free DS (4°C) and placed in 2 ml of fresh DS. The arteries were gently triturated using a fire-polished Pasteur pipette in order to break up tissue fragments and isolate single pulmonary arterial smooth muscle cells (PASMCs). The cell suspension was then kept at 4°C until required.

2.2 Cell culture

Human Embryonic Kidney 293 (HEK293) cells have long been used as an ideal system in which to observe the function of both stably and transiently transfected recombinant proteins. They are an ideal expression system due to the relative ease with which investigators are able to manipulate the expression of particular proteins by the incorporation of plasmid vectors (Thomas *et al.*, 2005). Of particular relevance to the experiments described in this thesis, is the reported absence of ryanodine receptor (RyR) expression in HEK293 cells (Aoyama *et al.*, 2004). This makes the HEK293 expression system particularly useful for studying candidate NAADP receptors, as one controversial proposal is that NAADP binds directly to and thereby activate RyRs (Dammermann *et al.*, 2005; Langhorst *et al.*, 2004).

I sought to use HEK293 cells to determine whether or not a novel family of two-pore ion channels functioned as NAADP receptors and Ca^{2+} release channels. To achieve this goal HEK293 cell lines were developed by my collaborator (Dr Mike Zhu, Ohio State University), which stably over-express human two-pore channel subtype 2 (hTPC2) with either a hemagglutinin (HA-) or an mCherry tag, and human

two-pore channel subtype 1 (hTPC1) with a poly-histidine tag (His_6-) or a green fluorescent protein (GFP-) tag, and chicken two-pore channel subtype 3 (cTPC3) with a GFP-tag. All cell culture was performed within a class II biological safety cabinet (Microflow, Biquell UK Ltd., UK) in order to uphold aseptic conditions.

2.2.1 Maintenance of HEK293 cells

A cryotube of HEK293 cells (either wild-type or stably over-expressing HA-hTPC2, mCherry-hTPC2, His_6-hTPC1, GFP-cTPC3 or GFP-hTPC1) containing approximately 1 x 10^6 cells was retrieved from a liquid nitrogen storage facility and rapidly thawed for approximately 2 minutes by partial submersion in a water bath set at 37 °C. Once thawed, the cell suspension was gently mixed with a pipette tip and then aliquoted into 3 T25cm^2 vent-capped tissue culture flasks. 5 ml of fresh tissue culture media (37°C) was then added to each flask. The growth media used for all cell types was Dulbecco's modified eagle medium (D-MEM; composition (mM): 0.4 glycine, 0.4 L-arginine hydrochloride, 0.2 L-Cystine 2HCl, 4 L-Glutamine, 0.2 L-histidine hydrochloride, 0.8 L-isoleucine, 0.8 L-leucine, 0.8 L-lysine hydrochloride, 0.2 L-methionine, 0.4 L-phenylalanine, 0.4 L-serine, 0.8 L-threonine, 0.08 L-tryptophan, 0.4 L-tyrosine, 0.8 L-valine, 0.029 choline chloride, 0.008 D-calcium pantothenate, 0.009 folic acid, 0.033 niacinamide, 0.02 pyridoxine hydrochloride, 0.001 riboflavin, 0.12 thiamine hydrochloride, 0.04 i-inositol, 1.8 calcium chloride, 0.00025 ferric nitrate, 0.81 magnesium sulphate, 5.33 potassium chloride, 44.0 sodium bicarbonate, 110.3 sodium chloride, 25 D-glucose, 0.04 Phenol Red) supplemented with 10% FBS, 50 units/ml penicillin, 50 μg/ml streptomycin. For cells stably over-expressing HA-hTPC2, GFP-hTPC1 or GFP-cTPC3 the growth media was additionally supplemented with 400 μg/ml geneticin G418 sulphate (G418). For cells stably over-expressing mCherry-hTPC2, or His_6-hTPC1 the growth media was additionally supplemented with 50 μg/ml Zeocin or 100 μg/ml Hygromycin B respectively.

G418 is a member of the aminoglycoside family of antibiotics and was first reported by Wagman and colleagues in 1974 (Wagman *et al.*, 1974). This antibiotic inhibits protein synthesis and subsequently causes growth inhibition in both eukaryotic and prokaryotic cells (Eustice *et al.*, 1984). Inhibition of protein synthesis

is achieved by G418 binding with, and therefore interfering with the usual ribosomal function. Zeocin is a glycopeptide antibiotic produced by *Streptomyces verticillus*. Upon entering the cell the Cu^{2+} collated to Zeocin is removed resulting in the activation of the antibiotic. Once activated, Zeocin then binds to and cleaves DNA leading to cell death (Hwang *et al.*, 2005). Hygromycin B is also a member of the aminoglycoside antibiotic family and therefore interferes with RNA recognition and subsequent protein translation (Rao *et al.*, 1983). Thus, when cells are transfected with plasmids containing the appropriate resistance gene in addition to the gene encoding the target protein, inclusion of these selection pressures in the growth media can be used to successfully select for cells expressing the desired protein.

The flasks containing the newly thawed cell suspension was gently swirled and then placed overnight in a humidified incubator (LEEC Ltd., UK) maintained at 37°C and gassed with 95% air, 5% CO_2. The following day the growth media from each flask was removed and 5 ml of fresh growth media (37°C) was added to each flask. The flasks were then returned to the incubator and the cell-line maintained by regular passaging.

All cell lines were maintained by passaging every 3-4 days at which point the cells had reached 70-90% confluency. The growth medium was removed and 1ml of Trypsin-EDTA solution was added to the flask and incubated for 3 minutes, so that the cells were no longer adherent to the base of the flask. The Trypsin-EDTA solution was then diluted to 10 ml with fresh growth medium and transferred to a 15 ml centrifuge tube. The tube was centrifuged for 3 minutes at 1000 x r.p.m. . The supernatant was removed and the pellet resuspended in 2 ml of fresh media. A 20 µl aliquot of this suspension was then used to perform a cell count. The cell suspension was thoroughly mixed with 1% trypan blue at a ratio of 1:1. 20µl of this mixture was then added via capillary action to a Hawksley haemocytometer (Hawksley, UK) with its appropriate cover slip attached. The number of viable cells occupying 0.0001 ml was then counted and the approximate number of cells/ml was calculated. The suspension was then diluted with fresh growth media such that the new flask contained 6 ml of a 1.5 - 3 x 10^5 cells/ml suspension. The flasks were then placed in the humidified incubator (37 °C, 95% air, 5% CO_2).

2.2.2 Preparation of HEK293 cells for Ca^{2+} imaging and visualisation of intracellular proteins using fluorescent labelling

Sterile 35 mm glass-bottomed tissue culture dishes (FluoroDish; World Precision Instruments, FL, USA) were prepared beforehand by coating the glass base of each dish with 1 ml of sterile 100 μg/ml poly-D-lysine hydrobromide (PDL) for 5 minutes. PDL coats the glass surface with an extracellular matrix that provides a net positive charge and therefore promotes cell attachment. For the preparation of cells for immunocytochemical labelling, glass coverslips were first sterilised by submersion in 100% ethanol for 15 minutes at room temperature. The coverslips were then placed in 30 mm sterile tissue culture dishes and PDL was added for 5 minutes. Following incubation with PDL, the excess PDL was removed and the FluoroDishes / coverslips washed with 2 ml sterile, double distilled water (dd.H_2O). The excess liquid was removed and the FluoroDishes / coverslips were allowed to dry within the safety cabinet until required.

A flask of HEK293, HA- / mCherry-hTPC2, GFP/ His_6-hTPC1 or GFP-cTPC3 cells was taken and treated with trypsin-EDTA and centrifuged as described above. Upon resuspension the cells were diluted to a seeding density of approximately 0.5 - 1.0 x 10^5 cells per ml. 2 ml of this suspension was added to either a coverslip within a 30 mm petri dish, or directly to a FluoroDish. Dishes were then incubated overnight at 37 °C, 5% CO_2.

2.2.3 Long-term storage of cells

In order to use cells of the same cell line in future experiments without using an excessive number of passages, cells were frozen and kept in a liquid nitrogen storage facility. To freeze down cells, a number of flasks were allowed to reach full confluency. Upon reaching this level, the cells were treated with trypsin-EDTA and centrifuged as described above. The supernatant was removed and the pellet re-suspended in freezing media (D-MEM, 10% FBS, 10% dimethyl sulphoxide (DMSO)). The suspension was then aliquoted by 1 ml volumes into cryotubes (Nunc, Fisher Scientific, UK) at a density of approximately 1 x 10^6 cells/ml. The tubes were transferred to an insulated container and cooled to -80 °C at an approximate rate of

1°C/min. After 24 hours the cryotubes were transferred to a liquid nitrogen store until required.

2.3 Immunocytochemistry

2.3.1 Fixation and labelling of isolated pulmonary arterial smooth muscle cells and HEK293 cells

PASMCs were isolated as described above. Glass coverslips were coated with PDL prior to fixation. 200 μl of the PASMC suspension was placed onto each coverslip and the cells were allowed to adhere for 1 hour at room temperature. Once the cells had been allowed to adhere, the coverslips were placed in cold (-20°C) methanol for 15 minutes. Methanol fixation dehydrates the cell and precipitates the proteins which are anchored to the cytoskeleton or membranes. This method quickly fixes cells but its main disadvantages are that it can lose soluble non-anchored proteins and that proteins can be denatured by the methanol. After fixation the coverslips were removed from the methanol and placed on individual stands in preparation for permeabilisation and labelling.

Transfected and non-transfected HEK293 cells were prepared for fluorescent labelling of intracellular proteins as described above. The growth medium was removed and the cells were washed twice with fresh PBS. 4 % paraformaldehyde in PBS (pH 7.4) was added and the cells incubated at 37 °C for 20 minutes. Paraformaldehyde fixes the cells by forming crosslinks between proteins. These crosslinks are methylene bridges formed between nitrogen containing side chains of basic amino acids. The main disadvantage with using paraformaldehyde is that it may autofluoresce, however this can be corrected for by appropriate background correction / subtraction. Following fixation, the fixing media was removed and the cells were again washed twice with PBS. The coverslips were removed from the dishes and placed on individual stands in preparation for permeabilisation and labelling.

In order to allow the antibodies access into the cells, the cells were permeabilised with 0.3% Triton X-100 (polyethyrene glycol mono-p-iso-octylphenyl ether) in PBS for 3 x 5 minutes at room temperature. Triton X-100 is a non-ionic

detergent which can solvate cellular membranes, forming small pores. After permeabilization, the cells were washed for 3 x 5 minutes with blocking solution (1% bovine serum albumin (BSA), 4% goat serum in PBS) at room temperature. Blocking buffer was used to minimize any non-specific binding which may occur between the antibodies and structures of no specific interest. Blocking is achieved by using a protein solution (serum) which competes for and binds to non-specific binding sites. Normally the serum used is from the species in which the secondary antibody was raised.

The cells were then incubated with the desired primary antibodies (Table 2.1) diluted to the appropriate concentration in blocking solution, overnight at 4°C. The following day, the primary antibody solution was removed, and the coverslips were washed for 3 x 5 minutes with fresh blocking solution at room temperature. After washing, the cells were then incubated with the desired fluorophore-conjugated secondary antibody (Table 2.1) diluted to the appropriate concentration with blocking solution for 2 hours in the dark at room temperature. The binding of the primary antibody and subsequent location of the protein of interest can be visualised using a fluorescent molecule. This fluorophore is conjugated to a secondary antibody which is raised to specifically bind to antibodies of the primary antibody host species. Cells were then washed with fresh PBS for 5 x 5 minutes in the dark at room temperature. The excess PBS was removed and the coverslips were mounted on microscope slides using either Gel/Mount (BioMedia) or a Mowiol (Calbiochem, Merck Chemicals Ltd., UK) based mountant of the following composition: 0.1 g/ml Mowiol, 0.25 g/ml glycerol, 0.2 M Tris, pH 8.5 containing 4'6-diamidino-2-phenylindole (DAPI; excitation 360 nm, emission 457 nm). DAPI is a fluorescent, membrane-permeable nuclear dye that predominantly binds to AT nucleotide sequences in the minor groove of DNA. Upon binding the minor groove, DAPI exhibits a large increase in fluorescent yield (Reddy *et al.*, 1999) and therefore it is very useful in visualising the nuclei of fixed cells. 15 µl of the mountant was placed on a microscope slide and the coverslip was carefully lowered on top, ensuring that no air bubbles were trapped. The mounted slides were allowed to set for 2-4 hours in the dark at room temperature and stored in the dark at 4 °C until required. Slides were viewed using the Applied Precision Deltavision imaging system or Leica TCS laser scanning confocal system.

Primary Antibody (dilution)	Secondary Antibody (dilution)	Conjugated fluorescent probe	Excitation and emission
Rabbit anti-RyR1 (1:500)	Goat anti-rabbit (1:200)	Texas Red	Ex. 555 nm Em. 617 nm
Rabbit anti-RyR2 (1:500)	Goat anti-rabbit (1:200)	Texas Red	Ex. 555 nm Em. 617 nm
Rabbit anti-RyR3 (1:500)	Goat anti-rabbit (1:200)	Texas Red	Ex. 555 nm Em. 617 nm
Mouse anti-αIgp120 (1:200)	Goat anti-mouse (1:200)	FITC	Ex. 490 nm Em. 528 nm
Rat Anti-HA (1:500)	Goat anti-rat IgG (1:200)	FITC	Ex. 490 nm Em. 528 nm
Mouse Anti-LAMP-2 (1:500)	Goat anti-mouse (1:250)	Texas Red/ Alexa-594	Ex. 555 nm/Em 617 nm Ex. 590 nm/Em 618 nm
Mouse anti-GM130 (1:250)	Rabbit anti-mouse (1:500)	Alexa-594	Ex. 590 nm Em. 618 nm
Mouse anti-cytochrome C (1:500)	Rabbit anti-mouse (1:500)	Alexa-594	Ex. 590 nm Em. 618 nm
Mouse anti-EEA1 (1:250)	Rabbit anti-mouse (1:500)	Alexa-594	Ex. 590 nm Em. 618 nm
Mouse anti-M6PR (1:500)	Rabbit anti-mouse (1:500)	Alexa-594	Ex. 590 nm Em. 618 nm
Mouse Anti-transferrin (1:500)	Rabbit anti-mouse (1:500)	Alexa-594	Ex. 590 nm Em. 618 nm
Mouse anti-PDI (1:200)	Rabbit anti-mouse (1:500)	Alexa-594	Ex. 590 nm Em. 618 nm

Table 2.1. Host species, conjugated fluorescent probes and dilution factor of the antibodies for immunocytochemical investigations

For source of antibodies see section 2.8.

2.3.2 Preparation of control slides for immunocytochemical investigations

In order for the images obtained from the fluorescently labelled intracellular proteins to be a true representation of specific binding, the background fluorescence must be corrected for. This can be done with the aid of control slides. These control slides are prepared in an identical way as the test slides, with the only exception being that the control slides are incubated overnight with blocking solution instead of with a primary antibody solution.

2.3.3 Labelling of lysosomes within isolated pulmonary arterial smooth muscle cells and HEK293 cells stably expressing HA-hTPC2 / mCherry-hTPC2

PASMCs were prepared by adding 0.5 ml of PASMC suspension to a PDL coated FluoroDish and the cells were allowed to adhere for 15 minutes at room temperature. The dish was then made up to 2 ml with fresh HBSS and washed with a further 5 x 1 ml of fresh HBSS. For HA-hTPC2 cells, the growth medium within FluoroDishes containing HA-hTPC2 cells was removed and the cells washed with 5 x 1 ml fresh HBSS. Dishes were incubated with 200 nM LysoTracker Red (excitation 577 nm, emission 590 nm) for 40 minutes in the dark at room temperature. In some experiments involving the visualisation of lysosomes, Ned-19 was also visualised. Ned-19 is a newly characterised antagonist of NAADP-mediated Ca^{2+} signalling which has also been shown to fluorescently label NAADP receptors (Naylor *et al.*, 2009). For experiments involving visualisation of Ned-19 (excitation 360 nm, emission 458 nm) labelling, 100 μM Ned-19 was added for the last 20 minutes of the incubation period for LysoTracker Red. The cells were then washed with 10 x 1 ml of HBSS and imaged using the Deltavision imaging system.

Control images for correcting the threshold for red fluorescence (590 nm) were obtained by using cells incubated with only Ned-19. The threshold was then set such that no red fluorescence was observed. Similarly, the threshold for blue fluorescence (458 nm) was obtained using cells incubated with only LysoTracker Red, and the threshold was set such that no blue fluorescence was observed. Setting these threshold levels eliminates any background fluorescence within the cell and imaging system and therefore ensures that any red or blue fluorescence measured was only due to the presence of LysoTracker Red and Ned-19, respectively. When using fluorescent compounds such as Ned-19 that do not irreversibly bind to cellular components or accumulate within organelles one would expect the fluorescent labelling to be present throughout the cell. Thus, the thresholds for fluorescent labelling were raised above that of the background threshold level in order to visualise the areas in which Ned-19 labelling was concentrated.

For mCherry-hTPC2 cells, imaging was carried out in an identical manner to that used for HA-hTPC2 cells with the exception that LysoTracker Green (excitation 504 nm, emission 511 nm) was used in place of LysoTracker Red. As mCherry-hTPC2 cells inherently exhibit red fluorescence, control images for the correction of

thresholds of red fluorescence (590 nm) were obtained using HA-hTPC2 cells prepared in parallel, and incubated with LysoTracker Green only. To obtain green (511 nm) background fluorescence levels mCherry-hTPC2 cells were incubated with LysoTracker-free HBSS.

2.4 Deconvolution microscopy

2.4.1 Visualisation of fluorescently labelled intracellular proteins in isolated pulmonary arterial smooth muscle cells and HEK293 cells

Fluorescently labelled isolated PASMCs and HEK293 cells were visualised using the Applied Precision Deltavision imaging system (Applied Precision Inc., WA, USA). The Deltavision microscope system uses Beamsplitter filters to control the wavelength of light (emitted from a 100 W mercury arc lamp) used to excite the cells. The cells were viewed using an inverted microscope (Olympus IX70) equipped with a 60X 1.4-numerical aperture oil immersion objective lens (Olympus). Images were obtained using a Photometric CH300 CCD camera. Images were collected as a series of Z sections (focal depth 0.28 μm, Z step 0.2 μm) taken through the cell at intervals 0.2 μm. This results in a stack of 2D images representing the fluorescent staining throughout the cell. Each image contains out of focus light which must be removed or resolved. The out of focus light is removed via a process called deconvolution. The Deltavision system uses constrained-iterative deconvolution which reassigns out of focus light to its original source. This method uses a series of complex algorithms which first take the raw image, and then convolve this image using the point spread function (PSF) creating a 'blurred estimate'. The PSF is a measure of how a single point source would appear if imaged by the apparatus. As light passes through the lens its path will be altered in three dimensions. The blurred estimate is then compared to the original raw image and the error is calculated which indicates the similarity between the blurred estimate and the raw image. This error calculation is then used to make a new iteration which is also compared to the original file to create another error calculation. This process is repeated until the error criterion is minimized leaving the final restored image. Following deconvolution, 3D

reconstruction and analysis was performed using Softworx (Applied Precision Inc.) and Volocity (PerkinElmer, Waltham, MA, USA) software.

2.4.2 Analysis of fluorescent labelling of intracellular proteins within isolated pulmonary arterial smooth muscle cells and HEK293 cells

Volumetric analysis of the fluorescent labelling of the cells was performed using Volocity software (Improvision, UK). In order to analyse the volume of fluorescent labelling within individual cells the resolution limit of the DeltaVision imaging system must first be considered. The imaging system can accurately resolve sources of light / labelling smaller than 0.2 μm in X-, Y- and Z-planes under optimal conditions. However, in order to introduce a margin of safety to the analysis a more conservative estimate was used. The resolution limit was set such that 0.5 μm was considered to be the smallest resolvable distance, and therefore volumes of labelling less than 0.125 μm^3 were excluded from the analysis.

2.5 Ca^{2+} imaging within isolated pulmonary artery smooth muscle cells and HEK293 cells

2.5.1 Fluorescence as a biological tool

In the experiments covered within this thesis both the Ca^{2+} imaging and the fluorescent labelling and visualisation of intracellular proteins utilises fluorescent dyes and sequence-specific antibodies conjugated to fluorescent probes. Fluorescence describes the process whereby a photon of light is emitted from a fluorophore (fluorescent molecule) as it returns from a higher energy level. Particular wavelengths of light can be absorbed by a fluorophore providing it with energy. If this energy is sufficient then an electron within the molecule will achieve a higher energy state; a process known as excitation. This excited state is relatively unstable and cannot be maintained for long. While the electron is in an excited state, it will 'drop' to an intermediate energy level due to the loss of some energy in a process known as internal conversion. After a short period of time the electron will return to

its ground (low energy) state. In doing so, the excess energy is released in the form of light. As the excited electron had dropped to an intermediate excited state prior to returning to its ground state, the emitted light will be lower in energy than the excitation wavelength. This cycle can be repeated multiple times allowing detection and visualisation of the fluorophore. These fluorophores can be used to visualise the localisation of proteins within a cell by attaching them to probes such as secondary antibodies.

Fluorophores can also be attached to ion chelating molecules to act as reporter dyes that can be used to visualise changes in ion concentrations over a period of time. Fura-2 is an example of an ion specific fluorescent indicator dye. These indicator dyes are fluorescent molecules which are attached to a structure capable of binding ions. For this reason, fluorescent Ca^{2+} indicator dyes are often derivatives of Ca^{2+} chelators such as EGTA or BAPTA (Takahashi *et al.*, 1999; Tsien, 1980). Fluorescent Ca^{2+} indicator dyes are divided into two groups based upon their mode of operation: single-wavelength intensity wavelength dyes and dual-wavelength ratiometric dyes (referred to as single wavelength and ratiometric indicators respectively). For single wavelength Ca^{2+} indicators, changes in the intracellular Ca^{2+} concentration results in a change in the intensity of the fluorescence excitation and emission spectra. For example, upon binding Ca^{2+}, fluo-3 may undergo up to a 200-fold increase in fluorescence emission (525 nm) following excitation at 506 nm (Takahashi *et al.*, 1999). Thus, an increase in Ca^{2+} is reported as an increase in the fluorescence detected when using a single excitation wavelength of light. However, there are a number of limitations associated with single wavelength indicators as the intensity of the fluorescence emission is dependent upon a number of potential variables. Firstly, the concentration of the indicator within the cell of interest will greatly affect the intensity of the signal. For example, if 2 cells of equal intracellular Ca^{2+} concentration contained different concentrations of accumulated indicator dye, a difference in Ca^{2+} concentration between the 2 cells would be reported due to the difference in emission intensity. Also, if the cell under investigation changes shape / size during the experiment due to contraction / relaxation, then the relative concentration of the indicator could change and more importantly, the distance of the emitted light will change thus affecting the intensity of the signal. Nonratiometric indicators can also be particularly susceptible to photobleaching affecting the perceived change in ion concentration. Photobleaching describes the permanent loss

of a molecules ability to fluoresce, due to covalent modification which may occur after repeated excitation. This results in a reduced intensity of fluorescent emission with time. Therefore, if a single wavelength dye undergoes photobleaching then the resultant decrease in emission intensity will be perceived as a decrease in the Ca^{2+} bound form of the indicator dye.

In contrast to single wavelength indicators, the Ca^{2+}-free and Ca^{2+} bound forms of ratiometric indicator dyes have either a common excitation wavelength (Indo-1) or dual excitation wavelengths (Fura-2), coupled to dual emission wavelengths (Indo-1) or a common emission wavelength (Fura-2). Importantly, these ratiometric dyes show differential changes in fluorescence emission due to the dual excitation/dual emission which allows for the ratiometric analysis of the output. In the example of Fura-2, increasing Ca^{2+} concentration results in increased emission when excited at 340 nm and a decrease in emission when excited at 380 nm. The resulting ratio of fluorescence at these 2 excitation wavelengths (F_{340}/F_{380}) varies as a function of Ca^{2+} concentration. Ratiometric dyes can minimise the limitations associated with single wavelength indicators, as factors unrelated to changes in Ca^{2+} concentration that alter the fluorescence intensity (e.g. alterations in cell shape/size) will equally affect the intensity of the fluorescence emitted at each excitation wavelength used, and therefore the ratio will not be altered.

For the Ca^{2+} imaging experiments described within this thesis, the ratiometric Ca^{2+} indicator dye Fura-2 was used to report changes in the intracellular Ca^{2+} concentration. This indicator was first described in 1985 (Grynkiewicz *et al.*, 1985) and, upon binding Ca^{2+}, exhibits significant shifts in the excitation spectra but little shift in the emission spectra (Fig. 2.3). The structure of Fura-2 is derived from EGTA (ethylene glycol-bis(2-aminoethylether)-tetraacetic acid) and therefore has a tetracarboxylic structure and is able to bind Ca^{2+} via interaction with 4 carboxyl groups. The aromatic amino groups present on the molecule confer the fluorescent properties of this EGTA analogue. Indeed, binding Ca^{2+} alters the electronic properties of the fluorophore thus altering the absorption spectrum. Upon binding Ca^{2+} to these binding sites the Fura-2 molecule exhibits an absorption shift from 380 nm towards 340 nm wavelengths of light. By monitoring the relative intensity of emission at 510 nm using separate excitation wavelengths of 340 nm and 380 nm and taking a ratio of the two values (340 nm/380 nm) one can determine the relative amount of Ca^{2+}-bound Fura-2 versus non-Ca^{2+}-bound Fura-2. Thus by monitoring

changes in this ratio, changes in the cytoplasmic concentration of Ca^{2+} can be detected and measured.

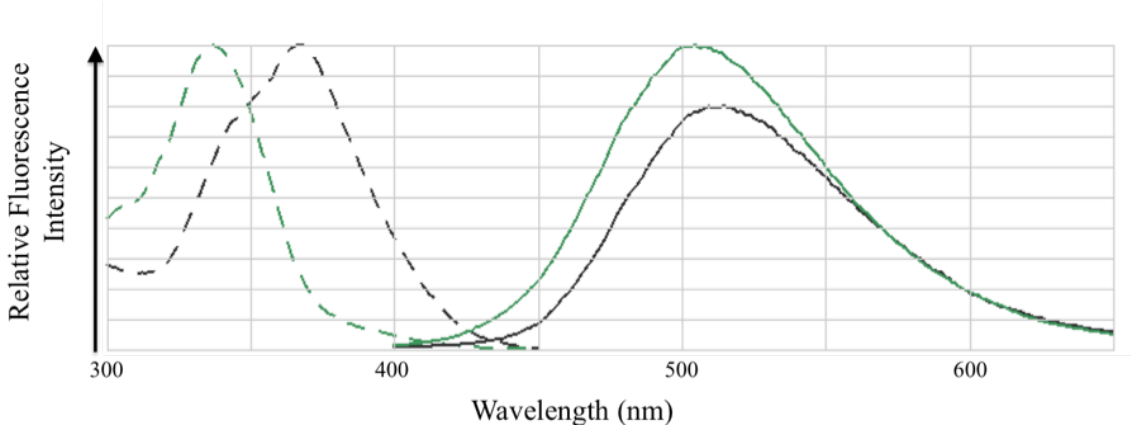

Fig. 2.3. Representative excitation and emission spectra of Fura-2

Fura-2 exhibits different spectra depending on whether it is present in its Ca^{2+}-free form (black line) or Ca^{2+}-bound form (green line). The emission spectra (solid line) remain the same whereas the excitation spectra (dashed line) of Fura-2 exhibit a leftward shift upon binding Ca^{2+}.

As previously mentioned, Fura-2 contains multiple carboxyl groups and is thus strongly negatively charged. As a result the Fura-2 molecule is unable to cross the lipid bilayer of the cell membrane without assistance. Therefore, in order to 'load' multiple cells with Fura-2 within the experimental chamber and without disrupting the cell membrane, Fura-2 is commonly combined with an acetoxymethyl (AM) ester to create Fura-2-AM. The AM ester masks the negative charge of Fura-2 and therefore the molecule can diffuse across the membrane bilayer. The Fura-2-AM ester is non-fluorescent, however once within the cell the AM ester is cleaved by esterases leaving the fluorescent form, Fura-2 within the cytoplasm.

2.5.2 Loading of HEK293 cells and isolated pulmonary arterial smooth muscle cells with the Ca^{2+} indicator dye Fura-2

For cultured cells, the growth medium of FluoroDish containing HEK293, HA-hTPC2, His_6-hTPC1 cells or HA-hTPC2 cells transfected with shRNA, was removed and the cells washed with 10 x 1 ml of fresh HBSS. 1 ml of fresh HBSS containing 5 μM Fura-2-AM was added and the dish was incubated for 30 minutes in the dark at room temperature. For PASMCs, 0.5 ml of the PASMC suspension was incubated

with 5 μM Fura-2-AM for 15 minutes in the dark at room temperature (22 °C). After this initial incubation with Fura-2-AM, the cell suspension was transferred to an experimental chamber, the bottom of which consists of a glass coverslip. The cells were incubated for a further 20 minutes in the dark at room temperature in order to allow time for the cells to adhere to the coverslip.

Following incubation with Fura-2-AM the FluoroDish/experimental chamber was washed with 10 x 1 ml of fresh HBSS, and incubated for a further 20 minutes in the dark at room temperature. The cells were washed with a further 5 x 1 ml of fresh HBSS before the FluoroDish/experimental chamber was mounted on the inverted microscope.

2.5.3 Imaging of changes in Ca^{2+} within HEK293 cells and isolated pulmonary arterial smooth muscle cells

The generation of specific excitation wavelengths of light was achieved using a TILL Photonics Polychrome II monochromator (TILL Photonics, Germany). The monochromator uses a Xenon lamp to produce white light which passes through a slit at the entrance of the monochromator. The light then reflects off of the first mirror which columnates the light, towards the diffraction grating. The diffraction grating has a highly reflective surface within which are finely etched grooves with specific spacing. When the light hits this surface the specific angles of reflection created by the grooves cause the reflected light to exhibit combinations of constructive and deconstructive patterns of interference, such that each wavelength of light is reflected at a slightly different angle. The original white light is now separated into discrete colour bands of light depending on wavelength. The light then hits the second mirror which reflects the light towards the exit slit. As the light has undergone dispersion the separate wavelengths of light diverge from the diffraction grating and continue to diverge from the second mirror. This results in only a single wavelength of light which is able to pass through the exit slit. The angle of the diffraction grating can be accurately adjusted in order to allow different wavelengths of light to exit via the exit slit. On the external side of the slit there is an optical fibre that the light can travel down to the microscope with minimal loss of intensity. At this point the light enters the fluorescence filter block whereby the light undergoes further selection of

particular wavelengths. Upon entering the filter block the excitation light passes through an emission filter. This filter only permits the passage of light that exhibit wavelengths within a specific range/band that encompasses the desired excitation wavelength. Wavelengths outwith this bandwidth are either reflected or absorbed. The light at the selected excitation wavelength is then reflected onto the experimental chamber by a dichroic mirror. Dichroic mirrors are able to reflect wavelengths of light that are below a predetermined wavelength such as the excitation wavelength, whereas light of wavelengths above this threshold such as the emission wavelength are able to pass through. The excitation light is below this threshold and therefore reflected onto the cells. The resultant emitted light is at a higher wavelength and is able to pass through the dichroic mirror. The emitted light continues through the emission filter that absorbs or reflects light outwith a narrow bandwidth (which encompasses the emission maxima), and into the detection device.

Once the desired excitation wavelengths of light have excited the Fura-2, the resultant emitted light is detected using a Hammamatsu 4480 image intensifying charge-coupled device (CCD) camera. CCD cameras allow the conversion of an analogue signal (e.g. a number of photons of light) into a digital signal which can then be analysed. It uses a photoactive region made of a layer of photodiodes on a silicon base which can be considered as an array of capacitors. When light hits and is absorbed by the photoactive layer it causes it to temporarily store this charge. The greater the number of photons that hit a given area the more electrical charge is stored by the capacitor. The capacitors then discharge their stored charge into a charge amplifier which converts the charge pulse to a voltage. The greater voltages correspond to the greater intensity of light which is converted into a number. The array is then considered as a whole by the software which allows the construction of an image with the pixels representing the corresponding area of the photoactive layer within the CCD camera. The computer software will then convert these varying voltages into a set of levels. For example, the intensity / voltage represented by each pixel is assigned a grey value based on 256 levels of grey (white through to black). Thus the CCD camera can give an accurate spatial depiction of the light intensity within a single image. The CCD camera was attached to an inverted microscope (Leica, DMIRBE). The microscope was equipped with a 40x, 1.3-numerical aperture oil immersion lens (Zeiss). The CCD camera was also coupled to an Apple

Macintosh G4 personal computer running Openlab software which was used to record and analyse the fluorescence intensity throughout each experiment.

In order to ensure that changes in the fluorescence ratio were not affected by autofluorescence within the experimental apparatus or HBSS, background subtraction was required. This was achieved by moving the lens away from the experimental chamber / dish so that the focal plane of the lens was positioned such that the cells were not in focus. Images were then captured of any emitted fluorescence (510 nm) when the chamber/dish was exposed to 340 nm and 380 nm wavelengths of light. These images represented the background fluorescence that the camera would detect during the experiment. The software would therefore subtract the corresponding intensity from each image captured during the experiment. This minimised the potential variability between multiple chambers/dishes. The Openlab software was used to control the parameters of the experiment with the imaging and recording following a pre-set automation (Written by A. M. Evans, Centre for Integrative Physiology, University of Edinburgh) which would loop until manually terminated or until it reached a pre-set number of cycles. Firstly the monochromator is triggered to generate 340 nm wavelength light and the resultant fluorescence emitted is captured by the CCD camera (exposure time 30 ms) and the image is saved. The monochromator is then switched so that it generates 380 nm wavelength of light and the resultant emitted fluorescence is again recorded by the CCD camera and the image is saved. The background fluorescence for each of the images is subtracted using the background images recorded previously. The computer then generates a ratio image by dividing the intensity of the pixels in the 340 nm image by the intensity of the corresponding pixels in the 380 nm image. This ratio image contains a grey-scale image whereby a given intensity is assigned a specific level of grey within the 256 grey-scale. The grey-scale images are then converted to a range of colours (increasing intensity represented as blue <green <yellow <orange <red) which can be used to quickly and easily visualise the changes in the Fura-2 fluorescence ratio during the experiment. This type of depiction is known as a pseudocolour representation.

2.6 Whole-cell patch clamping

Pharmacological agents such as NAADP that dissolve readily in water are often unable to diffuse across the plasma membrane. This property is useful for an intracellular signalling molecule, however observing the effect of exogenous NAADP is therefore far from straight forward. In order to deliver NAADP directly to the cytoplasm of both PASMCs and HEK293 cells the whole-cell configuration of the patch-clamp technique was used. The key characteristic of this technique is the diffusional continuity of the patch pipette solution and the cell cytoplasm (Park *et al.*, 2002).

2.6.1 Preparation and filling of patch pipettes

In this thesis, whole-cell patch-clamping was used to apply the pharmacological agent of interest by intracellular dialysis within pipette solution of the following composition: 140 mM KCl; 10 mM HEPES; 1 mM $MgCl_2$; 5 μM Fura-2 free acid, corrected to pH 7.4 with NaOH. The pipette solution was 'loaded' into a glass electrode known as a patch pipette. Patch-pipettes (2-3 MΩ resistance) were generated by 'pulling' filamented borosilicate glass capillaries (1.5 mm O.D., 0.86 mm I.D.; Harvard Apparatus, UK) using a pipette puller (pp-830, Narishige, Japan). The pp-830 pipette puller uses a two stage pull technique to produce pipettes with a consistent pipette resistance. Firstly, the glass capillary is fixed in position by screws above and below the nichrome heating coil, with the upper part fixed to the frame of the puller and the lower part attached to weights. The heating coil is then switched on to the first heat setting which heats the capillary at a focal position. As this part of the capillary heats up, the glass becomes molten and the glass is partially pulled apart by gravity pulling the weighted lower section down until it makes contact with a step. This first pull is typically over a length of 7-10 mm and produces a diameter of approximately 200 μm (Hamill *et al.*, 1981). The step physically stops the first stage in the pulling process and also switches off the heating coil thus allowing both the coil and capillary glass to cool down. The coil is then re-centred with respect to the capillary's new centre, the step is removed and the coil switched on to the second, lower heating setting. This heat also focally softens the glass and therefore allows the

weights to pull apart the glass, leaving two patch-pipettes with tips consisting of an aperture of approximately 1 μm (Hamill *et al.*, 1981).

The filled patch pipettes were mounted onto the electrode attached to the headstage. Once mounted, the pipette solution was in electrical contact with the head stage via an Ag/AgCl wire which sits within the pipette. The headstage is attached to the patch-clamp amplifier, and the amplifier kept in electrical contact with the extracellular bath solution via an Ag/AgCl bath electrode.

2.6.2 Generation of a seal and delivery of pharmacological agents

Once a cell had been identified for patching, the patch pipette was positioned above the cell of interest using a piezoelectric micromanipulator (PCS 5000 series, EXFO Burleigh, Canada). The piezoelectric micromanipulator allows smooth and stable positioning of the patch pipette within three planes. The system uses ceramic actuators that expand under the application of increasing voltages. Before a seal can be made with the cell of interest, the junction potential must be accounted for. The junction potential develops when two solutions of different ionic compositions meet at an interface. In this example, once the pipette is lowered into the experimental chamber, the bath solution and the pipette solution share an interface at the pipette aperture. This causes a junction potential to develop due to the differences in concentration and mobility of ions between the solutions. This potential can be offset by adjusting the V_{ref} on the amplifier which uses an integrator to keep the current at zero. Before making a seal the amplifier must first be set to voltage-clamp mode (V = 0 mV) with a 5 mV 'test' pulse applied with a frequency of 50 Hz and a duration of 10 ms. The pulse produces a current step with a square waveform which is observed on an oscilloscope (Fig. 2.5). The patch pipette is then lowered gradually using the micromanipulator until the patch pipette is in contact with the cell membrane. Contact with the cell can be determined using the oscilloscope whereby the increase in resistance results in a decrease in the observed current step. At this juncture, negative pressure can then be applied to the system. Negative pressure could be applied to the pipette via a length of silicon tubing that was attached to the electrode holder. The other end of the tubing was attached to a port in a 3-way stopcock. A plastic syringe was attached to another port of the stopcock to generate the negative

pressure whilst the remaining port was left free in order to release pressure from the otherwise closed system.

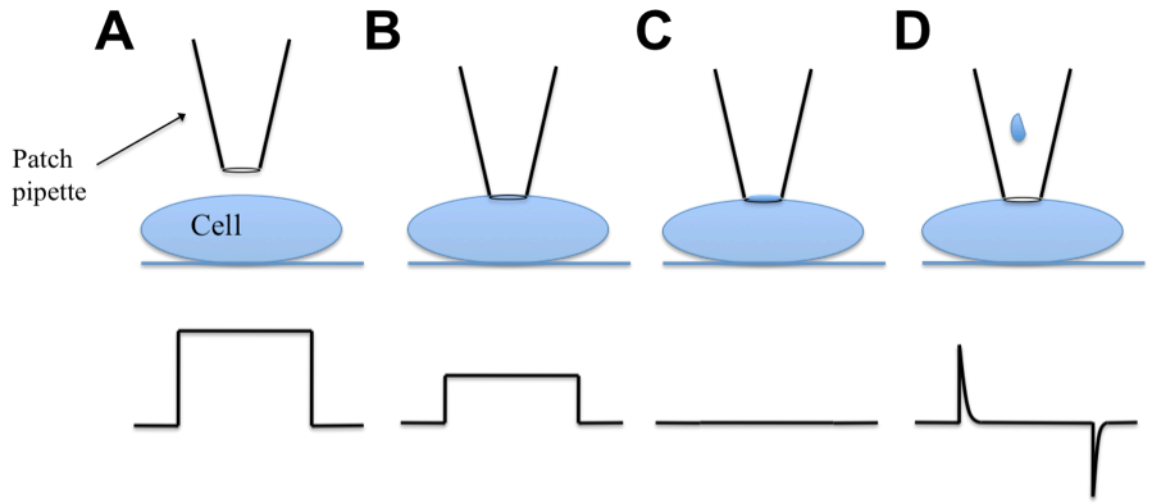

Fig. 2.5. Schematic representation of the process of intracellular dialysis of pharmacological agents via the whole-cell configuration of the patch-clamp technique

A. The upper panel shows the positioning of the patch pipette above the cell. Lower panel shows the corresponding trace shown on the oscilloscope after the application of a voltage step. **B**. The upper panel shows the patch pipette now lowered so that it is contact with the cell plasma membrane, whilst the lower panel shows the resultant decrease in the voltage step as a result of an increased resistance. **C**. Application of slight negative pressure generates a gigaseal shown in the upper panel. The lower panel shows the resultant oscilloscope trace after capacitance compensation. **D**. The upper panel represents the whole-cell configuration. Further negative pressure results in the removal of the patch of membrane immediately beneath the patch pipette. The lower panel shows the oscilloscope trace with whole-cell configuration producing characteristic capacitance transients.

Application of negative pressure results in an improved seal and increased electrode resistance resulting in a further reduction in the current step observed on the oscilloscope. This was monitored until a gigaohm (GΩ) seal was obtained with additional negative pressure applied if required. With a 10 GΩ seal the pipette and the membrane will be less than 1 nm apart (Hamill *et al.*, 1981). After forming a GΩ seal, capacity transients caused by stray pipette capacitance to the bath, are compensated for by adjusting the fast and slow capacitance compensation facilities on the integrator unit of the amplifier. Further suction was then applied in order to rupture the patch of membrane covered by the pipette's aperture. Rupture of the patch is indicated by the sudden appearance of large capacity transients due to whole-cell capacitance. This is termed 'break-in'. Upon break-in the NAADP within the

pipette solution is able to dialyse into the cell and the resultant changes in the intracellular Ca^{2+} concentration was viewed using Fura-2 fluorescence ratio imaging. For all experiments involving the whole-cell configuration of the patch-clamp technique, the seal resistance was ≥ 2 GΩ, and the series resistance and pipette resistance were ≤ 10 MΩ and ≤ 3 MΩ respectively.

NAADP and IP_3 were delivered to individual cells using the whole-cell configuration of the patch-clamp technique and in current-clamp mode (PASMC; I = 0) or voltage-clamp mode (HEK293 cells; V = -40 mV), using a CV 203BU headstage (Axon Instruments, Molecular Devices, USA) attached to an axopatch 200B integrating patch-clamp unit (Axon Instruments, Molecular Devices, USA).

2.6.3 Extracellular application of pharmacological agents

In Ca^{2+} imaging experiments in both PASMC and HEK293 cells, caffeine or carbachol (CCh) were added towards the end of the record in order to determine whether the cells were responsive to intracellular Ca^{2+} release via RyRs or IP_3Rs respectively. As both caffeine and CCh are cell membrane permeant, these compounds were applied extracellularly. Also, is some of the experiments within this thesis, cells were pre-incubated with the antagonists, bafilomycin A1, thapsigargin, dantrolene and Ned-19. These compounds are also cell permeable and were therefore applied extracellularly.

2.7 Radioligand binding assay

2.7.1 Preparation of sea urchin egg homogenate for use in radioligand binding assay

For both the determination of NAADP binding to TPC2 and the subsequent competition of [^{32}P]NAADP binding to TPC2 by Ned-19, homogenate was used from sea urchin egg, HA-hTPC2 cells and mouse liver. Sea urchin egg homogenate had been prepared prior to the radioligand binding experiments by my collaborators Professor Antony Galione, Dr Margarida Ruas and Dr Xiaotong Cheng. Briefly, eggs

were harvested from *Lytechinus pictus* (*L. pictus*) and *Strongylocentrotus puratus* (*S. puratus*) by injection with 0.5 M KCl and collected in ASW (artificial sea water: 435 mM NaCl; 40 mM MgCl; 15 mM $MgSO_4$; 11 mM $CaCl_2$; 10 mM KCl; 2.5 mM $NaHCO_3$ and 20 mM Tris base, pH 8.0). The eggs were then washed by centrifugation at 800 *g* in the following number of solutions: Ca^{2+}-free ASW with EGTA (twice), Ca^{2+}-free ASW (twice), and then washed in gluconate intracellular-like medium (Glu-IM) with the following composition (mM): 250 *N*-methyl-d-glucamine, 250 potassium gluconate, 20 Hepes, 1 $MgCl_2$ (pH 7.2). Cells were then homogenized with a glass Dounce tissue homogeniser in intracellular medium with the following additions: 2 mM ATP, 20 mM phosphocreatine, 20 U/ml creatine phosphokinase, 50 μg/ml leupeptin (EDTA-free cocktail), 20 μg/ml aprotinin, and 100 μg/ml soya bean trypsin inhibitor. The cortical granules were then removed by centrifugation at 13,000 *g* for 10 s at 4 °C and the supernatant was removed and stored at -80 °C until required.

2.7.2 Preparation of mouse liver homogenate for use in radioligand binding assay

Mouse liver homogenate had been prepared prior to the radioligand binding experiments by my collaborators Professor Antony Galione, Dr Margarida Ruas and Dr Xiaotong Cheng. Briefly, mouse liver tissue was dissected from C57/BL6 mice and was homogenised at 4 °C using an UltraTurax homogeniser in binding medium of the following composition: 20 mM HEPES, 1 mM EDTA (pH 7.2) and supplemented with a protease inhibitor cocktail (Roche). The membranes were then washed twice by centrifugation at 20,000 *g* for 10 minutes and the supernatant was removed and stored at -80 °C until required.

2.7.3 Preparation of wild-type HEK293 and HA-hTPC2 expressing cell homogenates for use in radioligand binding assay

In order to determine whether over-expression on hTPC2 in HEK293 cells resulted in an increase in NAADP binding and whether Ned-19 competes with NAADP for TPC2 binding, homogenates were prepared prior to binding experiments. 24 petri dishes (150 mm) containing either HA-hTPC2 or wild-type HEK293 cells

(90-100% confluency) were used in order to generate a suitable amount of protein. The cell culture medium was discarded and the cells washed once with cold (4°C) PBS. Each petri dish was then placed on ice and a small amount of fresh cold PBS was added and the cells scraped into the PBS before being collected into centrifuge tubes. The cell solution was centrifuged at 1500 *g* for 3 minutes at 4 °C. Following centrifugation, the supernatant was removed and the cells were resuspended in cold hypotonic buffer of the following composition: 20 mM HEPES, 1 mM EDTA, 1 mM PMSF, pH 7.2 . The suspension was then incubated for 30 minutes at 4°C, and the cells homogenised with 15 strokes from a glass Dounce tissue homogeniser and the homogenate centrifuged at 1500 *g* for 3 minutes at 4°C. The supernatant was removed and retained and the pellet, containing the unbroken cells and nuclei was discarded. The supernatant was centrifuged at 10,0000 *g* for 1 hour at 4°C. The supernatant was removed and the pellet resuspended in fresh cold hypotonic buffer and the new suspension was incubated for 1 hour at 4 °C. Following this, the suspension was centrifuged again at 10,0000 *g* for 1 hour at 4 °C. The supernatant was removed and the pellet was finally resuspended in fresh cold hypotonic buffer using a needle and syringe to ensure that the pellet had been fully and uniformly resuspended. The protein concentration was then determined using a BCA protein assay. The remaining homogenate was aliquoted, snap frozen in liquid nitrogen and stored at -80°C until required.

2.7.4 BCA protein assay for the determination of protein concentration

In order to use membrane homogenates in radioligand binding experiments, the protein concentration of the homogenates must first be determined. This can be done by comparing the samples against a set of known standards which, for the purpose of this experiment was BSA. Protein concentration was determined by the bicinchoninic acid (BCA) protein assay using the following manufacturers protocol (Sigma-Aldrich, Dorset, UK). This assay utilises a reaction whereby Cu^{2+} can be reduced by proteins to form Cu^{1+} in alkaline conditions. This reduction can be mediated by cysteine, tryptophan and tyrosine residues, and the peptide bond. The greater the reduction of the Cu^{2+} ions, the higher the protein concentration. The BCA forms a blue/purple coloured complex with the reduced Cu^{1+} in alkaline conditions, which has an

absorption maxima of 562 nm. Therefore with higher protein concentrations the solution will be less blue / purple and more green in colour. 8 parts of each of the protein standards (0-2000 μg/ml in duplicate) were mixed with 1 part of the BCA working reagent (containing 0.08 % copper sulphate pentahydrate) in a 96-well plate. In addition to the standards, the HEK293 cell homogenate (diluted 20-fold) was also mixed in the same proportions with the BCA working solution. The plate was then incubated for 30 minutes at 37°C. The absorbance of each sample was then measured at 562 nm and a standard curve constructed using Graphpad Prism analysis software using the results obtained from the protein standards. Using this standard curve, the protein concentration of the homogenate could be determined by interpolation. This was then adjusted according to the initial dilution factor and the value obtained used to ensure the appropriate amount of protein was used for the radioligand binding assay.

2.7.5 Preparation of [^{32}P]NAADP for use in radioligand binding assay

[^{32}P]NAADP can be synthesised via a two-step process as described previously (Patel *et al.*, 2000a). The first reaction was to synthesise [^{32}P]NADP from [^{32}P]NAD. This was done by incubating [^{32}P]NAD with 0.5 U/ml human NAD kinase, 5 mM MgATP and 100 mM HEPES for 1 h at room temperature. After this 100 mM nicotinic acid and 1 μg/ml ADP-ribosyl cyclase were added to the reaction chamber and the mixture was incubated for a further 1 h at room temperature in order to allow for the second synthesis phase to occur. The final mixture was separated by running it through a high pressure liquid chromatography (HPLC) column. Separation was achieved using an anion-exchange column packed with AGMP1 (Bio-Rad, UK). Elution was performed at a flow rate of 1 ml/minute using an increasing gradient of trifluoroacetic acid (TFA) as described previously (Patel *et al.*, 2000a). The [^{32}P]NAADP fraction was then stored at 4 °C until required.

2.7.6 Radioligand competition binding assay

In order to show NAADP binding in membranes prepared from sea urchin egg, HEK293 cells expressing/not-expressing HA-hTPC and mouse liver homogenates, a

competition assay was performed whereby NAADP at increasing concentrations can compete with and therefore reduce the amount of [^{32}P]NAADP binding to the homogenate. Firstly, 25 μl of NAADP (in DMSO) in a range of concentrations was added to each tube. 175 μl of homogenate was then added and allowed to incubate for 1 hour at room temperature, 50 μl of [^{32}P]NAADP added ([^{32}P]NAADP final concentration, 0.2 nM) making a final volume of 250 μl, before incubation of the preparation for a further hour at room temperature in order to allow binding to reach equilibrium. The bound [^{32}P]NAADP was trapped using Whatman GF/B filter papers that were placed in a Brandel Cell Harvester. The tubes were washed 3 times with Glu-IM (3 x 1 ml). The filter papers were then collected and the amount of [^{32}P]NAADP retained was determined either by Cerenkov spectrometry or by storage phosphor screen autoradiography.

For Cerenkov spectrometry the filters are placed in scintillation vials containing 10 ml H_2O and the relative amount of [^{32}P]NAADP retained within each vial was determined using a scintillation counter.

For storage phosphor screen autoradiography filter papers were wrapped in cling film and then placed in an exposure cassette. A storage phosphor screen (GE Healthcare) was then placed atop the filters and the cassette closed. The screen was then exposed for 2 hours, and scanned using a Typhoon 9400 scanner (GE Healthcare: scanning at 633 nm) at a resolution of 100 μm. The resulting image was quantified using IamgeQuant (GE Healthcare). Analysis of radioactivity levels by the storage phosphor screen system has been utilised previously as part of the [^{32}P]NAADP binding assay (Lewis *et al.*, 2007). As its name suggests the screen will 'store' a record of the sample which can then be imaged using known wavelengths. The screen contains crystals of BaFBR:Eu^{2+} and, upon exposure to radiation, the Eu^{2+} is oxidised to Eu^{3+} and the BaFBr is reduced to $BaFBr^{-}$. The oxidised/reduced ions remain in this state following the subsequent removal of the screen from the sample filters. This energy is then released when the screen is excited by the appropriate wavelength of light. The Typhoon scanner will scan the screen with a wavelength of 633 nm, and as a result 390 nm wavelength light is emitted which is allowed through the band-pass filter and is detected and measured by the detector. The intensity of this light is directly proportional to the level of radioactivity in the sample, and is transformed by the scanner into a grey scale image, with the areas

containing the higher intensity of emitted 390 nm light represented by the darker pixels. The image can then be analysed to determine the relative amount of radioactivity in each sample using densitometry analysis (ImageQuant software, Amersham Biosciences, UK). In order to compare this technique to scintillation counting, Lewis *et al.* generated a standard displacement curve with NAADP in sea urchin egg homogenate which was then analyzed by the Typhoon scanner and by the scintillation counter. The resultant standard curves were identical and therefore validated the use of phosphor storage screens to report radioactivity of a given sample (Lewis et al., 2007).

2.7.7 Radioligand competition binding assay to determine whether Ned-19 inhibits [^{32}P]NAADP binding to TPC2

In order to further validate Ned-19 as a competitive and specific antagonist of NAADP, an assay was performed to determine if increasing concentrations of Ned-19 could displace [^{32}P]NAADP binding in a competitive manner. Firstly, 25 μl of Ned-19 (in DMSO) in a range of concentrations was added to each tube. 175 μl of sea urchin egg homogenate or HA-hTPC2 cell homogenate was then added and allowed to incubate for 1 hour at room temperature, 50 μl of [^{32}P]NAADP added ([^{32}P]NAADP final concentration, 0.2 nM) making a final volume of 250 μl, and the preparation incubated for a further hour at room temperature. The bound [^{32}P]NAADP was trapped using Whatman GF/B filter papers that were placed in a Brandel Cell Harvester. The tubes were washed 3 times with Glu-IM (3 x 1 ml) as described previously. The filter papers were then collected and the amount of [^{32}P]NAADP retained was determined either by Cerenkov spectrometry or by storage phosphor screen autoradiography.

Radioligand binding data were analysed using Prism analysis software (GraphPad Software Inc., USA). Goodness of fit was assessed using the R^2 value calculated using the following formula: $R^2 = 1.0 - (SS_{reg} / SS_{tot})$, where SS_{reg} is the sum of squares of the vertical distance of each point from the best fit line, and SS_{tot} is the sum of squares of the vertical distance of each point from the mean *y* value.

2.8 Drugs and chemicals

Fura-2-AM, Fura-2 pentapotassium salt, DAPI, LysoTracker Red, LysoTracker Green, DMEM, Opti-MEM, FBS, Trypsin-EDTA, Zeocin, Geneticin G418 sulphate, and Penicillin/Streptomycin were obtained from Invitrogen/Molecular probes (Invitrogen Ltd., USA). GeneJammer transfection reagent was obtained from Stratagene (Agilent Technologies, USA). Bafilomycin A1 and anti-M6PR antibody was obtained from Calbiochem (Merck, Germany). Ned-19 was a kind gift from Dr. Grant Churchill. Anti-RyR antibodies were a kind gift from Prof. Sidney Fleischer. Anti-Igp120 antibody was a kind gift from Prof. Paul Luzio. Mouse anti-LAMP-2 antibody was obtained from the Developmental Studies Hybridoma Bank (University of Iowa, USA). Anti-HA antibody was obtained from Roche (UK). Anti-transferrin and anti-PDI antibodies were obtained from Abcam (UK). Anti-GM130 and anti-EEA1 antibodies were obtained from BD biosciences (USA). Anti-cytochrome C antibody was obtained from Zymed (USA). Texas Red-conjugated secondary antibodies were obtained from Jackson ImmunoResearch (USA). Alexa594-conjugated secondary antibodies were obtained from molecular probes (Invitrogen, UK). [^{32}P]NAD was a kind gift from Prof. Antony Galione. All other compounds were obtained from Sigma-Aldrich (UK).

2.9 Statistical analysis

Where appropriate the data presented within this thesis are represented by the mean and standard error of the mean (S.E.M. ±) for '*n*' experiments. For comparing groups and determining statistical significance, analyses were carried out using a student's *t* test or one-way analysis of variance with a Bonferroni post hoc test using the InStat3 statistical software (GraphPad Software Inc., USA). Differences between groups were considered statistically significant if $P \leq 0.05$.

Chapter 3: Lysosomes co-localise with ryanodine receptor subtype 3 to form a trigger zone for Ca^{2+} signalling by NAADP in rat pulmonary arterial smooth muscle

3.1 Introduction

Since its discovery, NAADP has been shown to potently mobilise Ca^{2+} in a number of cell types and via a complex two-pool release mechanism (Boittin *et al.*, 2002; Churchill *et al.*, 2001a; Churchill *et al.*, 2002; Kinnear *et al.*, 2004; Zhang *et al.*, 2006b). It is clear that in PASMCs, NAADP initiates global Ca^{2+} waves in an all-or-none manner by triggering Ca^{2+} release from acidic lysosome-related Ca^{2+} stores that is subsequently amplified by CICR from the SR via the progressive recruitment of ryanodine receptors (RyRs) (Boittin *et al.*, 2002; Kinnear *et al.*, 2004). That NAADP selectively mobilises Ca^{2+} from a lysosome-related Ca^{2+} store was shown using bafilomycin A1 (Kinnear *et al.*, 2004). Bafilomycin depletes lysosome-related Ca^{2+} stores by inhibiting the V-H^+-ATPase pump and was found to abolish NAADP-mediated Ca^{2+} release in PASMCs but not RyR- or IP_3R-dependent Ca^{2+} release from the SR (Kinnear *et al.*, 2004). Furthermore, depletion of SR Ca^{2+} stores by block of sarcoplasmic / endoplasmic reticulum Ca^{2+} ATPase (SERCA) pumps with thapsigargin and blockade of RyRs with ryanodine, respectively, occluded global Ca^{2+} waves, but not spatially restricted Ca^{2+} bursts from lysosomes (Boittin *et al.*, 2002; Kinnear *et al.*, 2004).

An additional observation of some interest was that NAADP-dependent Ca^{2+} bursts from lysosomes either declined back to basal levels without inducing CICR, or breached a given threshold for the initiation of a global Ca^{2+} wave by CICR from the SR via RyRs. In this respect, an important observation was that LysoTracker Red labelled lysosomes formed dense clusters in PASMCs, consistent with the spatially restricted nature of the Ca^{2+} bursts evoked by NAADP (Kinnear *et al.*, 2004). Strikingly, these dense clusters of lysosomes were closely associated with a sub-

population of BODIPY-ryanodine labelled RyRs. Moreover, the separation between these closely associated RyRs and lysosomes was beyond the limit of the resolution of deconvolution microscopy (< 100 nm) i.e. they appeared to form a true junction (Kinnear *et al.*, 2004). Indeed, this separation is consistent with the junctional gap required for other organellar junctions such as between the S / ER and mitochondria, and the S / ER and the plasma membrane which measure 15-50 nm and 15-30 nm respectively (Poburko *et al.*, 2004). The small separation between RyRs and lysosomes is therefore indicative of the presence of lysosome-SR junctions akin to a synapse for Ca^{2+} signalling by NAADP, and this structure was proposed to be a "trigger zone" for initiation of global Ca^{2+} waves in response to NAADP. This proposal is entirely consistent with the two-pool mechanism of Ca^{2+} signalling by NAADP and with the all-or-none manner in which NAADP triggers global Ca^{2+} waves (Boittin *et al.*, 2002). This finding is all the more intriguing given that all 3 RyR subtypes are expressed in vascular smooth muscle (Neylon *et al.*, 1995; Yang *et al.*, 2005). I therefore sought to determine whether or not a particular RyR subtype was targeted to the lysosome-SR junctions.

3.2 Methods

In order to investigate the lysosome-SR junction each element must first be visualised. This was achieved using antibodies raised against specific sequences of each protein. Lysosomes within acutely isolated PASMCs were visualised using the GM10 antibody raised against the lysosomal glycoprotein antigen αIgp120 (a kind gift from Professor Paul Luzio). Previously, αIgp120 has been shown to be almost exclusively expressed on lysosomal membranes with little or no expression on the plasma membrane, Golgi apparatus, or endosomes (Lewis et al., 1985). The anti-αIgp120 antibody was in turn visualised using a goat anti-mouse secondary antibody conjugated to the fluorescent molecule FITC (excitation 490 nm, emission 528 nm). RyR subtypes were visualised using antibodies raised against specific sequences within each subtype (RyR1, residues 4681-4700; RyR2, 1344-1365; RyR3, 4326-4336) and were a kind gift from Professor Sidney Fleischer. Importantly, these anti-bodies have been shown to bind specifically to sequences of either RyR1 (Lesh *et al.*,

1993), RyR2 (Jeyakumar *et al.*, 2001) or RyR3 (Jeyakumar *et al.*, 1998). RyR subtype labelling was in turn visualised using a secondary goat anti-rabbit antibody conjugated to the fluorescent molecule Texas Red (excitation 555 nm, emission 617 nm). The conjugated fluorescent probes Texas Red and FITC are suitable to be used simultaneously to co-label cells, as their excitation and emission spectra exhibit little overlap and therefore, excitation of one fluorophore will not cause the erroneous excitation and subsequent erroneous emission from the other. Co-labelling of the PASMCs thus allowed for the analysis of areas in which both αIgp120 and RyR subtype labelling coincided, and therefore indicates areas of co-localisation between lysosomes and a particular RyR subtype.

Importantly, fluorescence owing to specific binding of the fluorophore-conjugated secondary antibody to the primary antibody must be distinguished from any background fluorescence due to non-specific binding of the primary antibody or inherent fluorescence within the slide/apparatus. This was achieved using paired control slides which were generated using the method described in Chapter 2. Briefly, control slides were prepared in the same way as test slides but the primary antibody solution was replaced with blocking solution during the initial incubation. In these control slides any of the fluorophore-conjugated secondary antibody that binds to elements within the cell is non-specific. Therefore, one can determine the level of background fluorescence, and effectively subtract/remove this from the images obtained from the test slides and thus ensure that the remaining fluorescence in due to specific labelling of the primary antibody.

The labelled proteins within isolated PASMCs were visualised using the Applied Precision Deltavision imaging system. The cells were viewed using an inverted microscope (Olympus IX70) equipped with a 60x 1.4-numerical aperture oil immersion objective lens (Olympus) and images were obtained using a Photometric CH300 CCD camera. A series (30-40) of Z sections (focal depth 0.28 μm, interval step 0.2 μm) taken through the cell were obtained in the form of a Z stack of 2D images. The out of focus light was removed by the imaging system using constrained-iterative deconvolution and a 3D image was generated as described in chapter 2.

Each image was adjusted to remove background fluorescence which was achieved using the control slides described above. The control slides were imaged to

determine the intensity of the fluorescence obtained from non-specific binding of the secondary fluorophore-conjugated antibody. When the threshold intensity level was raised such that no fluorescence was observed, this was determined as the background fluorescence threshold for that fluorescent probe. For all subsequent test cells, the threshold was raised to this level such that all fluorescence below this intensity threshold was excluded, thus ensuring that the observed fluorescence was solely due to specific labelling of the desired protein.

Following deconvolution, volumetric analysis of RyR and αIgp120 labelling and co-localisation between the two elements was performed using Volocity software (PerkinElmer, Waltham, MA, USA). First, in order to determine the degree of RyR and lysosomal labelling within the whole cell and sub-cellular regions of isolated PASMCs, a model was required that could be applied to each cell for analysis. The model developed consists of the whole cell and 3 sub-cellular regions termed the 'perinuclear region', the 'extra-perinuclear region', and the 'sub-plasmalemmal region' (Fig. 3.1).

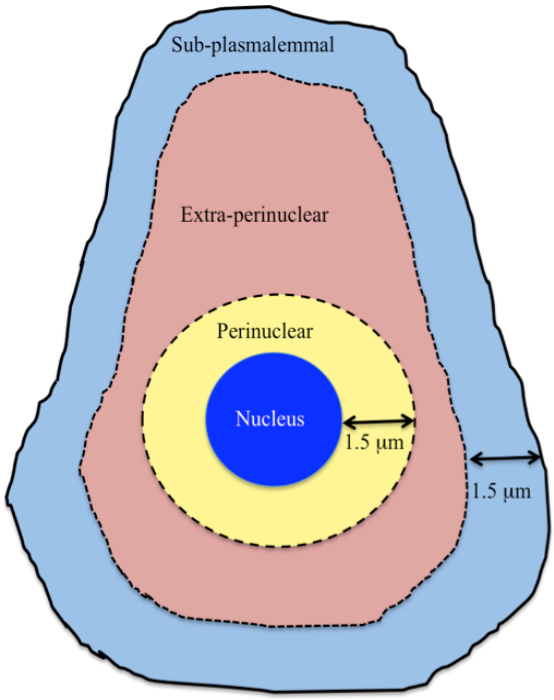

Fig. 3.1. Schematic representation of the subdivision of regions within isolated pulmonary arterial smooth muscle cells

Isolated cells were divided into three regions, namely the perinuclear (yellow), extra-perinuclear (pink), and sub-plasmalemmal (light blue) regions. The perinuclear region was determined as the volume of cytoplasm within 1.5 µm of the DAPI labelled nucleus (dark blue). The sub-plasmalemmal region was determined as the volume of cytoplasm within 1.5 µm of the plasma membrane. The extra-perinuclear region was determined as being the remaining volume of cytoplasm that resides between the sub-plasmalemmal and perinuclear regions.

Analysis of the distribution of labelling across these regional volumes of cells was

then carried out using Volocity software. This was achieved using 3D reconstructions of deconvolved Z sections (focal depth 0.28 μm, Z step 0.2 μm) taken through each cell selected for study and in the following manner:

1. The total cell volume was measured by drawing a 3D region of interest (ROI) around the perimeter of the cell. The resultant template was termed the 'whole cell mask'.
2. A 3D ROI was then drawn around the perimeter of the DAPI labelled nucleus and the nuclear volume measured.
3. A third ROI was drawn at a distance of 1.5 μm from the perimeter of the DAPI labelled nucleus. The perinuclear volume was then determined by subtracting the nuclear volume from the volume contained within this ROI, and termed the 'perinuclear mask'
4. The sub-plasmalemmal volume was then determined by drawing a further 3D ROI 1.5 μm from the intracellular face of the plasma membrane. The volume within this ROI was then subtracted from the volume of the whole cell to provide the sub-plasmalemmal 'mask'.
5. Finally, the extra-perinuclear region was determined by subtracting the nuclear, perinuclear, and sub-plasmalemmal volume from the total cell volume. The extra-perinuclear volume being equal to the remaining volume.
6. Note, in individual cells where regions of the plasma membrane were ≤ 3 μm from the nucleus, the total distance between the nucleus and plasma membrane was measured, and a 3D ROI drawn at half this distance. Thus, allowing for no extra-perinuclear volume at this point.

These defined masks were used as templates, such that the volume of labelling/co-localisation was determined for each region but with all labelling occupying a space outside the given regional template excluded. The thresholds for each fluorescent probe used (known as a channel) were set to exclude background fluorescence leaving 3D elements of labelling that are of an intensity above that of the background threshold. Volocity is then able to measure the volume of these remaining fluorescent elements. First, the desired mask is applied to the cell such that only fluorescent elements that are within this volume are measured. The number of

voxels (3D pixels) that each element of labelling occupies within the mask is measured and the number of voxels is then converted into an SI unit (μm^3) value. The volume of each element is recorded and the total volume of labelling summated. This process was repeated for each fluorescent channel and for each regional mask.

For assessing the volume of co-localisation between αIgp120 and RyR subtype labelling, the software merged / overlaid the masks relating to the 2 fluorescent channels used. The number of voxels occupied by both RyR and αIgp120 labelling in the merged mask was then determined and the corresponding μm^3 values calculated.

In order to analyse the volume of individual elements the resolution limit of the Deltavision imaging system must first be considered. Under carefully controlled "optimal" experimental conditions, the Deltavision imaging system used in these investigations is able to accurately resolve elements of labelling smaller than 0.2 μm in size. However, these precisely controlled conditions cannot be duplicated under my experimental conditions. Therefore, in these analyses, I set a more conservative value on the limit of resolution. To this end, I included only those volumes of labelling measuring at least 0.5 μm in the X-, Y- and Z-planes (volume 0.125 μm^3) with any element of labelling smaller than this excluded from consideration.

As expected, the total volume of the PASMCs imaged and each of the 3 subdivided regions varied between region type and between individual cells. Therefore, in order to allow for direct comparison of labelling across the 3 regions and between individual cells, labelling was expressed as a density. This was achieved by dividing the volume occupied by fluorescent labelling (μm^3) for a given protein by the total volume of that particular region (μm^3). Thus, data are presented as the mean ± S.E.M. of the density of labelling (μm^3 per μm^3).

3.3 Results

3.3.1 Examination of the spatial distribution of lysosomal labelling in isolated pulmonary arterial smooth muscle cells

3.3.1.1 Lysosomes are predominantly localised to the perinuclear region of isolated pulmonary arterial smooth muscle cells

In experiments carried out in association with Dr. Nicholas Kinnear the distribution of lysosomes within acutely isolated PASMCs was visualised using the GM10 antibody raised against the lysosomal glycoprotein antigen αIgp120. 3D reconstructions of deconvolved Z-sections taken through isolated PASMCs, revealed that αIgp120 labelling formed tight clusters. Fig. 3.2A*a* shows a transmitted light image of an exemplar cell and (*b*) the distribution of labelling for αIgp120 (green) relative to the DAPI labelled nucleus in a deconvolved Z-section (focal depth 0.28 μm) taken through the cell and corrected to remove background fluorescence determined from matched control slides. As mentioned above, in these and all subsequent analyses only those volumes of labelling measuring ≥ 0.5 μm in the X-, Y- and Z-planes (volume 0.125 μm^3) were included in the analysis. Fig. 3.2A*c* shows the distribution of labelling for αIgp120 (green) relative to the DAPI labelled nucleus in a 3D reconstruction of a series of deconvolved Z-sections (focal depth 0.28 μm, Z step 0.2 μm). Fig. 3.2A*d* shows a 3D representation of the position of each individual volume of labelling ≥ 0.125 μm^3 coloured to denote whether it was registered in the perinuclear (orange), extra-perinuclear (pink) or subplasmalemmal (light blue) region. Even visual consideration of the distribution of αIgp120 labelling here strongly suggests that the majority was concentrated in the perinuclear region of the cell.

In order to quantify the spatial distribution of αIgp120 labelling within PASMCs, the cells were divided into 3 regions (perinuclear, extra-perinuclear, sub-plasmalemmal) as described above (Fig. 3.1). To this end, the volume of labelling in each region was divided by the volume represented by the respective region, thus providing a density of labelling (μm^3 of labelling per μm^3 volume of region). This therefore allowed direct comparison of αIgp120 labelling between different regions within individual cells and between all the cells analysed.

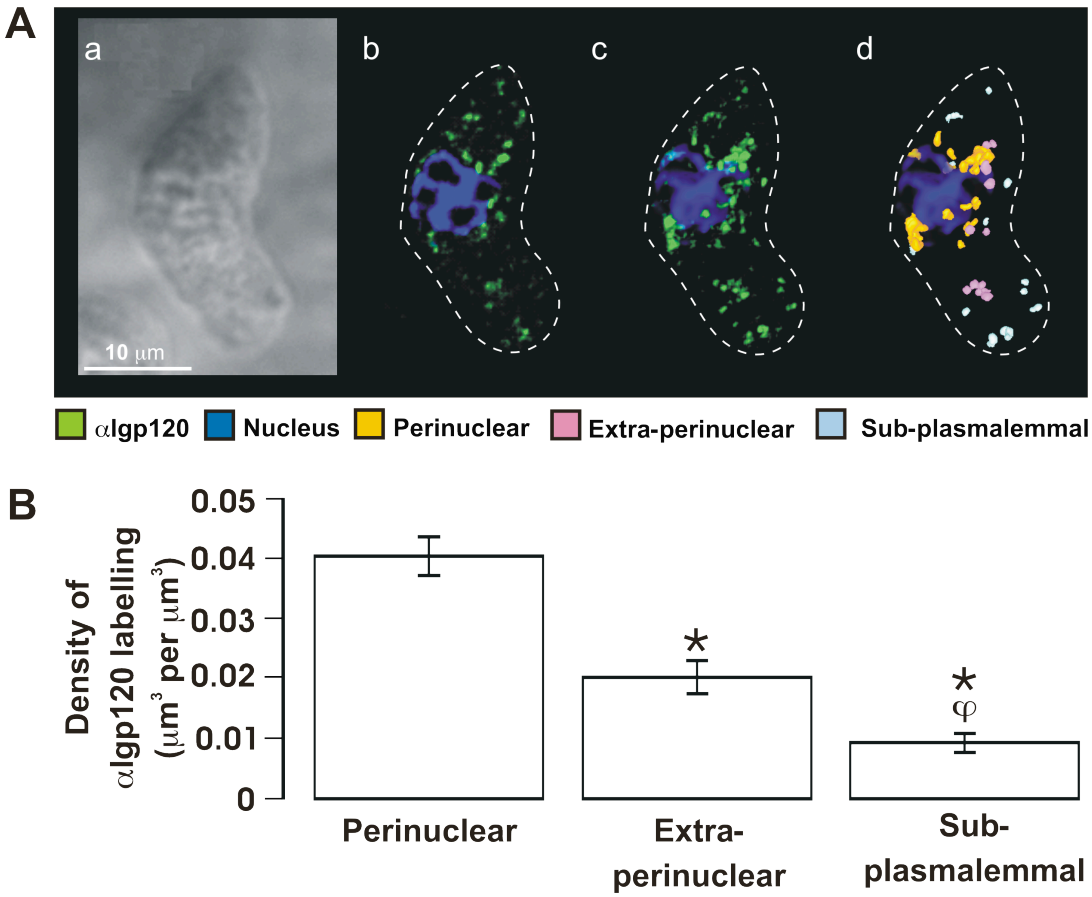

Fig. 3.2. Cellular distribution of αIgp120-labelled lysosomes within isolated pulmonary arterial smooth muscle cells

A*a* Transmitted light image of the isolated PASMC imaged. **A***b* Deconvolved Z-section (focal depth 0.28 μm) taken through the cell showing the distribution of αIgp120 labelling (green) in relation to the nucleus of the cell (dark blue) and plasma membrane (dotted line). **A***c* 3D reconstruction of a series of Z-sections taken through the cell shown in panel a (Z step 0.2 μm) showing the spatial distribution of αIgp120 labelling (green) in relation to the plasma membrane (dotted line) and nucleus (dark blue). **A***d* shows a 3D reconstruction as shown in panel *b*, with the individual αIgp120 labelling coloured according to region; perinuclear region (orange) extra-perinuclear region (pink) and sub-plasmalemmal region (light blue). **B** Bar chart showing the density of αIgp120 labelling in each region (μm^3 per μm^3; mean ± S.E.M.) across all the PASMCs studied (n = 35). * indicates a statistically significant difference (P<0.05) when compared to the density of αIgp120 labelling in the perinuclear region, whereas φ indicates a statistically significant difference (P<0.05) when compared to the density of αIgp120 labelling in the extra-perinuclear region.

Fig. 3.2B shows the mean (± S.E.M.) density of αIgp120 labelling in each region of the subdivided PASMCs imaged. The density of αIgp120 labelling across

these 3 regions was non-uniform, with a predominance of labelling within the perinuclear region. The density of αIgp120 labelling declined markedly from a peak value of 0.04 ± 0.003 μm^3 per μm^3 within the perinuclear region (*n* = 35; Appendix, Table 3.3), to 0.02 ± 0.003 μm^3 per μm^3 in the extra-perinuclear region (*n* = 35; Appendix 1, Table 3.4) and still further to as little as 0.01 ± 0.002 μm^3 per μm^3 in the sub-plasmalemmal region (*n* = 35 Fig. 3.2B; Appendix 1, Table 3.5). When comparing the sub-plasmalemmal or extra-perinuclear regions to the perinuclear region, these differences were significant ($P < 0.05$). Across all PASMCs studied, lysosomal labelling in the perinuclear region represented 56 ± 3 % (n = 35) of all lysosomal labelling, despite the perinuclear region only representing 31 ± 1 % (n = 35) of the whole cell volume (Appendix 1, Table 3.6). Clearly, therefore, lysosomes are primarily located within the perinuclear region of the cell.

3.3.1.2 Lysosomes cluster preferentially in the perinuclear region of isolated pulmonary arterial smooth muscle cells

Further analysis was then carried out to determine whether or not there was significant clustering of lysosomes and if so, within which region. Here I measured the volume of each individual element of labelling, which included as one element all elements of labelling separated by a distance below the resolution of the deconvolution microscopy used here (< 100 nm). Thus, larger volumes of αIgp120 labelling would indicate a greater degree of clustering. The bar chart in Fig. 3.3 shows that the mean volume of labelling was highest in the perinuclear region measuring 0.76 ± 0.06 μm^3 (n = 35; Appendix 1, Table 3.3), and declined to 0.62 ± 0.09 μm^3 (n = 35; Appendix 1, Table 3.4) in the extra-perinuclear region and then still further to 0.31 ± 0.03 μm^3 (n = 35; Appendix 1, Table 3.5) in the sub-plasmalemmal region of the cell. Thus, it is evident that lysosomes form dense clusters within the perinuclear region of the cell and in a manner consistent with previous reports from this laboratory in which clustering of LysoTracker Red labelled lysosomes was identified in living cells (Kinnear *et al.*, 2004). In each case the clustering mirrors the spatially restricted nature of NAADP-mediated Ca^{2+} bursts observed in PASMCs (Boittin *et al.*, 2002; Kinnear *et al.*, 2004). Fig. 3.4 shows an example of this clustering of lysosomes and the resultant spatially restricted Ca^{2+} burst in response to

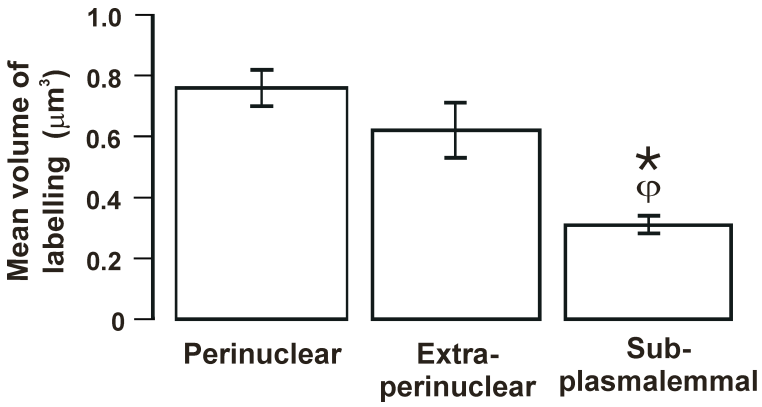

Fig. 3.3. Lysosomes are preferentially clustered in the perinuclar region of pulmonary arterial smooth muscle cells

Bar chart showing the mean volume of individual elements of αIgp120 labelling in each region (μm^3; mean ± S.E.M.) across all the PASMCs studied (n = 35). * indicates a statistically significant difference (P<0.05) when compared to the mean volume of αIgp120 labelling in the perinuclear region, whereas φ indicates a statistically significant difference (P<0.05) when compared to the mean volume of αIgp120 labelling in the extra-perinuclear region.

NAADP. Fig. 3.4A*a* shows a transmitted light image of an example cell and (*b*) the corresponding 3D reconstruction of a series of deconvolved Z-sections (focal depth 0.28 μm, Z step 0.2 μm) showing the distribution of clusters of LysoTracker Red (excitation 568 nm, emission 590 nm) within the cell. Fig. 3.4B shows the Fura-2 fluorescence ratio recorded in a different cell showing a Ca^{2+} burst (indicated by the white arrow) elicited by intracellular dialysis of NAADP (10 nM). This is also consistent with previous observations of αIgp120 labelling of lysosomes within rat kidney fibroblastic cells, that found small punctate labelling throughout the cytoplasm but which was concentrated in the perinuclear region (Reaves *et al.*, 1996)

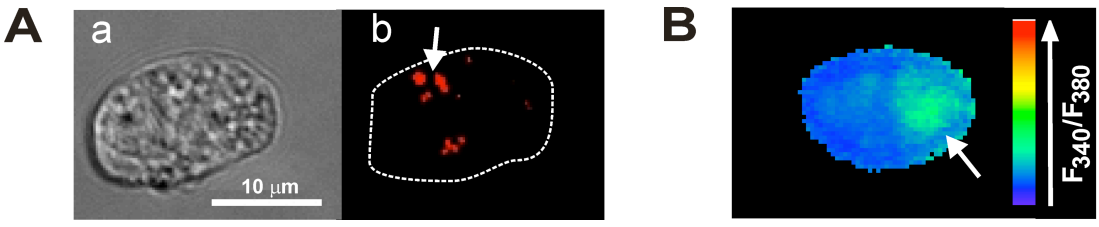

Fig. 3.4. Lysosomes form clusters in pulmonary arterial smooth muscle cells

A*a* Transmitted light image of the isolated PASMC imaged. **A***b* 3D reconstruction of a series of Z-sections taken through the cell shown in panel *a* (Z step 0.2 μm) showing the spatial distribution of LysoTracker Red fluorescence in relation to the plasma membrane (dotted line). A cluster of LysoTracker labelling is indicated by the white arrow. **B** A pseudocolour image of the Fura-2 fluorescence ratio recorded in a different cell showing a spatially restricted Ca^{2+} burst (indicated by the white arrow) in response to the intracellular dialysis of 10 nM NAADP.

3.3.2 Ryanodine receptor subtypes 1, 2, and 3 are differentially distributed within isolated pulmonary arterial smooth muscle cells

Having established that lysosomes are not uniformly distributed throughout individual isolated PASMCs, the spatial distribution of RyR subtypes was then examined. 3D reconstructions of deconvolved Z-sections taken through isolated PASMCs labelled for each RyR subtype, revealed that RyR subtype labelling was not uniformly distributed throughout the cytoplasm and that each RyR subtype exhibited a different spatial distribution "profile".

3.3.2.1 Ryanodine receptor subtype 3 is predominantly targeted to the perinuclear region of isolated pulmonary arterial smooth muscle cells

Fig. 3.5A shows the distribution of RyR3 within an example cell. For this, and the subsequent analysis of RyR1 and RyR2 distribution within PASMCs (Fig. 3.5B-C) the panels represent the following: (*a*) shows a transmitted light image of an exemplar cell; (*b*) shows the distribution of labelling for each RyR subtype (red) relative to the DAPI labelled nucleus in a deconvolved Z-section (focal depth 0.28 μm) taken through the cell; (*c*) A 3D reconstruction of a series of deconvolved Z-sections (focal depth 0.28 μm, Z step 0.2 μm) showing the distribution of labelling for RyR (red) relative to the DAPI labelled nucleus; (*d*) shows a 3D representation with the position of each individual volume of labelling (≥ 0.125 μm^3) coloured to denote its location in the perinuclear (orange), extra-perinuclear (pink) and sub-plasmalemmal (light blue) region. Visual assessment of the distribution of RyR3 within isolated PASMCs (Fig. 3.5A), suggests that RyR3 labelling formed clusters that were predominantly found in the perinuclear region, consistent with the distribution of lysosomes. Fig. 3.6 shows the mean (± S.E.M.) density of RyR labelling for each RyR subtype within each region of the cells studied. The perinuclear predominance of RyR3 labelling shown in Fig. 3.5A is reflected in the mean density of RyR3 labelling in each of the 3 regions (Fig. 3.6), which was approximately 4-fold greater in the perinuclear region (0.072 ± 0.008 μm^3 per μm^3, n = 11; Appendix 1, Table 3.16) when compared to the extra-perinuclear region (0.019 ± 0.005 μm^3 per μm^3; n = 11; Appendix 1, Table 3.17) and approximately 14-fold

greater than that observed in the sub-plasmalemmal region (0.005 ± 0.001 μm^3 per μm^3; *n* = 11; Appendix 1, Table 3.18). Thus, similar to the spatial distribution of αIgp120-labelled lysosomes, RyR3 is preferentially targeted to the perinuclear region of PASMCs.

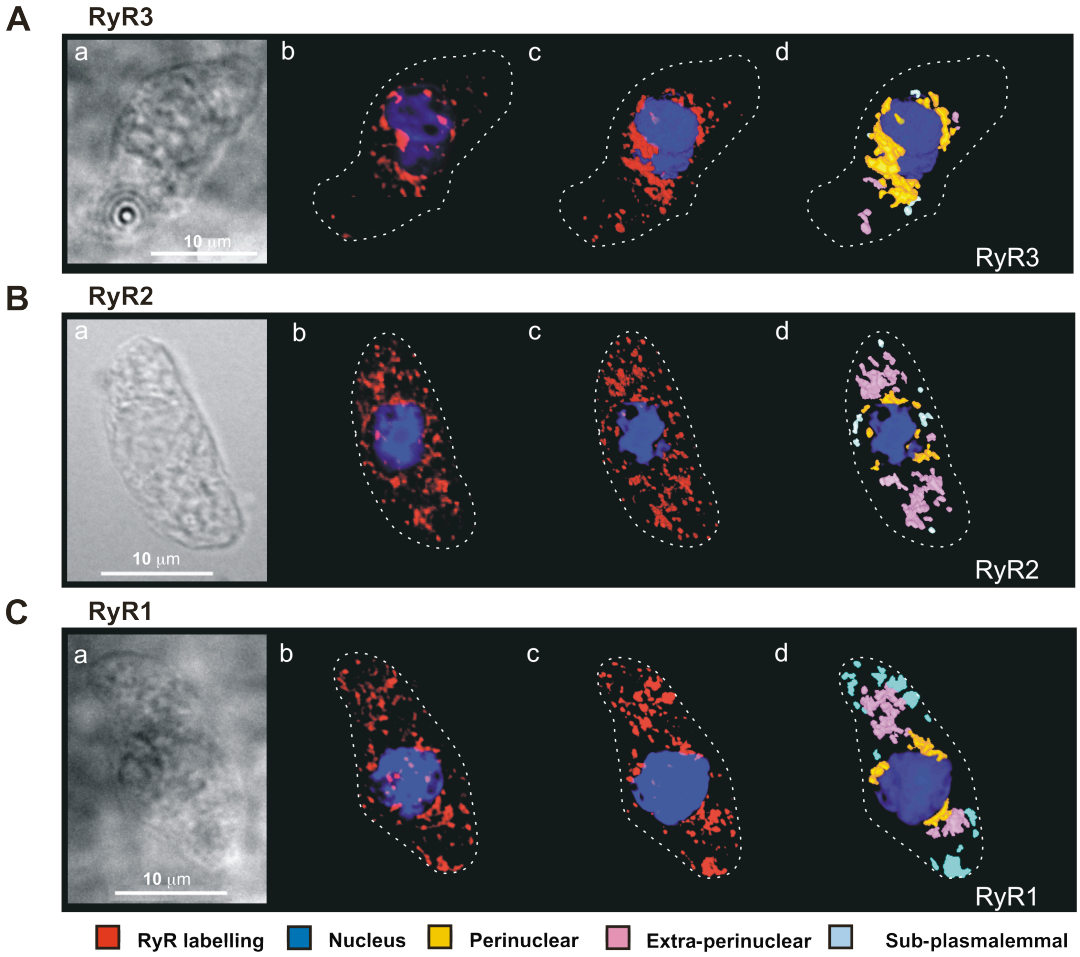

Fig. 3.5. All 3 ryanodine receptor subtypes exhibit different regional distribution within pulmonary arterial smooth muscle cells

Example cells showing the cellular distribution of RyR-labelling are shown for RyR1 (**A**), RyR2 (**B**), and RyR3 (**C**). In each case the panels show the following: Panel *a* shows a transmitted light image of the isolated PASMC imaged; Panel *b* shows a deconvolved Z-section (focal depth 0.28 μm) taken through the cell showing the distribution of RyR subtype labelling (red) in relation to the nucleus of the cell (dark blue) and plasma membrane (dotted line); Panel *c* shows a 3D reconstruction of a series of Z-sections taken through the cell shown in panel *a* showing the spatial distribution of the RyR subtype (red) in relation to the plasma membrane (dotted line) and nucleus (dark blue); Panel *d* shows a 3D reconstruction with the individual RyR subtype labelling coloured according to region; perinuclear region (orange) extra-perinuclear region (pink) and sub-plasmalemmal region (light blue).

3.3.2.2 Ryanodine receptor subtype 2 is predominantly targeted to the extra-perinuclear region of isolated pulmonary arterial smooth muscle cells

In marked contrast to RyR3, RyR2 labelling was predominantly targeted to the extra-perinuclear region of isolated PASMCs. Fig. 3.5B*b* shows the distribution of RyR2 labelling (red) relative to the DAPI labelled nucleus (blue) in the exemplar isolated PASMC (*a*). Fig. 3.5B*c* shows a 3D reconstruction of a series of deconvolved Z-sections (focal depth 0.28 μm, Z step 0.2 μm) showing the distribution of RyR2 labelling (red) relative to the DAPI labelled nucleus (blue), whereas panel *d* shows the 3D representation with the position of each individual volume of labelling (≥ 0.125 μm^3) coloured to denote its location in the perinuclear (orange), extra-perinuclear (pink) and sub-plasmalemmal (light blue) region within the isolated PASMC. Visual consideration of the distribution of RyR2 labelling here suggests that the majority of labelling was localised to the extra-perinuclear region of the cell. Consistent with this apparent distribution, comparison of the density of RyR2 labelling in each region (Fig. 3.6) reveals that RyR2 labelling in the extra-perinuclear region (0.065 ± 0.009 μm^3 per μm^3, n = 14; Appendix 1, Table 3.13) was approximately 2-fold greater than in the perinuclear region (0.039 ± 0.002 μm^3 per μm^3; Appendix 1, Table 3.12) and approximately 6-fold greater than was measured in the sub-plasmalemmal region (0.011 ± 0.002 μm^3 per μm^3; Appendix 1, Table 3.14). These data suggest that although it is found in all 3 regions of the cell the distribution of RyR2, in contrast to lysosomes and RyR3, is preferentially targeted to the extra-perinuclear region.

3.3.2.3 Ryanodine receptor subtype 1 is uniformly distributed within isolated pulmonary arterial smooth muscle cells

RyR3 and RyR2 appear to be predominantly targeted to the perinuclear and extra-perinuclear regions respectively. Conversely, RyR1 appears to have a different spatial distribution than either RyR3 or RyR2 within PASMCs. Fig. 3.5C*b* shows the distribution of RyR1 labelling (red) relative to the DAPI labelled nucleus (blue) in the exemplar isolated PASMC (*a*). Fig. 3.5C*c* shows a 3D reconstruction of a series of deconvolved Z-sections (focal depth 0.28 μm, Z step 0.2 μm) showing the distribution

of RyR1 labelling (red) relative to the DAPI labelled nucleus (blue), whereas panel *d* shows the 3D representation with the position of each individual volume of labelling (≥ 0.125 μm^3) coloured to denote its location in the perinuclear (orange), extra-perinuclear (pink) and sub-plasmalemmal (light blue) region within the isolated PASMC. This reveals that the distribution of RyR1 is relatively uniform across all 3 regions of isolated PASMCs (Fig. 3.3A). Thus, Fig. 3.6 shows that RyR1 labelling in the perinuclear region (0.041 ± 0.007 μm^3 per μm^3, n = 10; Appendix 1, Table 3.8) is not significantly different from labelling in the extra-perinuclear region (0.025 ± 0.005 μm^3 per μm^3; Appendix 1, Table 3.9) or the sub-plasmalemmal region (0.031 ± 0.005 μm^3 per μm^3; Appendix 1, Table 3.10).

3.3.2.4 Each ryanodine receptor subtype exhibits a different distribution profile

For clarity of consideration the bar chart shown in Fig. 3.6 compares the relative density of each RyR subtype labelling within each region of PASMCs. Fig. 3.6 confirms that within these cells RyRs exhibit subtype-specific distribution "profiles" (Fig. 3.6). Comparison of the regional distribution of each RyR subtype supports the conclusions above, such that within the perinuclear region, RyR3 is the predominant subtype, with an approximately 2-fold greater density of labelling (0.072 ± 0.008 μm^3 per μm^3, n = 11; Appendix 1, Table 3.16) than for either RyR2 (0.039 ± 0.002 μm^3 per μm^3, n = 14; Appendix 1, Table 3.12) or RyR1 (0.041 ± 0.007 μm^3 per μm^3, n = 10; Appendix 1, Table 3.8). In contrast, RyR2 labelling predominates within the extra-perinuclear region (0.065 ± 0.009 μm^3 per μm^3, n = 14; Appendix 1, Table 3.13), with an approximately 3-fold greater density of labelling than for either RyR3 (0.019 ± 0.005 μm^3 per μm^3, n = 11; Appendix 1, Table 3.17) or RyR1 (0.025 ± 0.005 μm^3 per μm^3, n = 10; Appendix 1, Table 3.9). Within the sub-plasmalemmal region, due to its uniform distribution, RyR1 appears to be the predominate subtype with an approximately 3-fold greater density of labelling (0.031 ± 0.005 μm^3 per μm^3, n = 10; Appendix 1, Table 3.10) than RyR2 (0.011 ± 0.002 μm^3 per μm^3, n = 14; Appendix 1, Table 3.14) and 6-fold greater density of labelling than observed for RyR3 (0.005 ± 0.001 μm^3 per μm^3, n = 11; Appendix 1, Table 3.18).

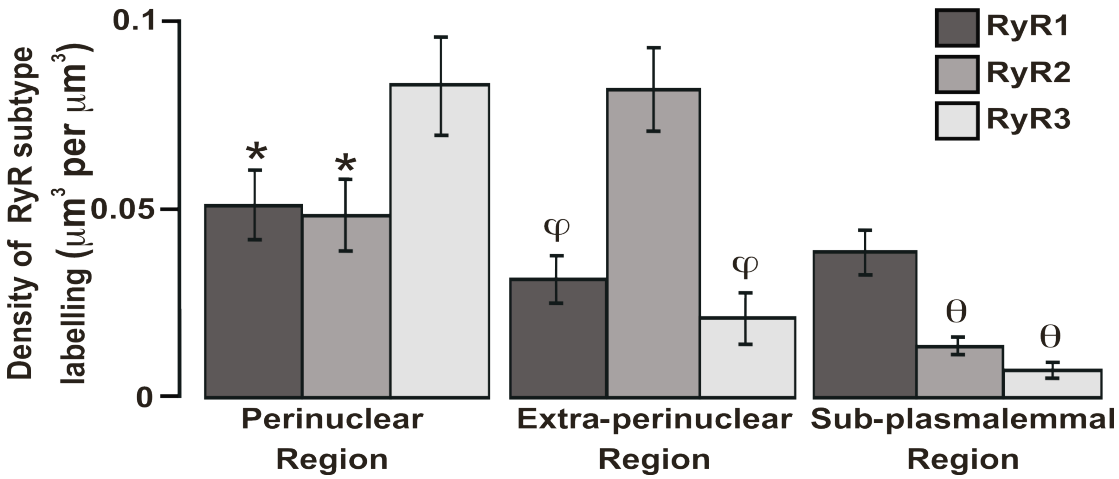

Fig. 3.6. Summary of ryanodine receptor subtype distribution within isolated pulmonary arterial smooth muscle cells

Bar chart showing the density of RyR labelling (μm^3 per μm^3; mean ± S.E.M.) for each RyR subtype within the 3 designated regions of sub-divided PASMCs. The charts are grouped by region in order to show the predominance of particular subtypes within a given region. * indicates a statistically significant difference ($P < 0.05$) when compared to the RyR3 labelling in the perinuclear region. φ indicates a statistically significant difference ($P < 0.05$) when compared to the density of RyR2 labelling in the extra-perinuclear region. θ indicates a statistically significant difference ($P < 0.05$) when compared to the density of RyR1 labelling in the sub-plasmalemmal region (RyR1 $n = 10$; RyR2 $n = 14$; RyR3 $n = 11$).

3.3.2.5 Ryanodine receptor subtype 3 preferentially clusters in the perinuclear region of isolated pulmonary arterial smooth muscle cells

As with the lysosomal labelling, further analysis was carried out to determine whether any of the RyR subtypes exhibit a greater propensity to form clusters and, if so, whether these clusters are present in any particular region of PASMCs. The mean volume of individual elements of RyR subtype labelling within each region of the cells studied was therefore compared, as a larger mean volume would be indicative of a greater degree of clustering. Fig. 3.7 shows that the mean volume of distinct elements of RyR3 labelling within the perinuclear region was 2.40 ± 0.33 μm^3 (n = 11; Appendix 1, Table 3.16) which was significantly greater than was observed in either the extra-perinuclear (0.72 ± 0.15 μm^3, n = 11; $P < 0.05$; Appendix 1, Table 3.17) or sub-plasmalemmal (0.47 ± 0.11 μm^3, n = 11; $P < 0.05$; Appendix 1, Table

3.18) regions of PASMCs. Therefore, it would appear that RyR3 clusters, similar to lysosomal clusters, are preferentially targeted to the perinuclear region in PASMCs.

Fig. 3.7 also shows that examination of the mean volume of individual elements of RyR2 labelling revealed a greater degree of RyR2 clustering in the extra-perinuclear region (1.60 ± 0.30 μm^3, n = 11; Appendix 1, Table 3.13) when compared to the perinuclear region (0.97 ± 0.15 μm^3, n = 11; Appendix 1, Table 3.12), though this difference was not deemed statistically significant ($P > 0.05$). However, the mean volume of RyR2 labelling declined significantly in the sub-plasmalemmal region (0.46 ± 0.06 μm^3, n = 11; $P < 0.05$; Appendix 1, Table 3.14) when compared to either the perinuclear or extra-perinuclear regions. Thus, in contrast to RyR3 and lysosomes, RyR2 clusters appear to be preferentially targeted to the extra-perinuclear region of PASMCs.

Comparison of the mean volume of individual elements of RyR1 labelling (Fig. 3.7) revealed that there was little difference in the degree of RyR1 clustering between the perinuclear (1.04 ± 0.27 μm^3, n = 11; Appendix 1, Table 3.8), the extra-perinuclear (0.71 ± 0.21 μm^3, n = 11; Appendix 1, Table 3.9), and the sub-plasmalemmal regions (0.53 ± 0.08 μm^3, n = 11; Appendix 1, Table 3.10). Thus, consistent with the relatively uniform regional density of RyR1 labelling, RyR1 does not appear to cluster preferentially within any given region of PASMCs.

Comparison of the mean volumes of individual elements of RyR subtype labelling in Fig. 3.7 demonstrates that RyR3 forms dense clusters in the perinuclear region of PASMCs. This was evident from the finding that RyR3 exhibits a 2-fold greater mean volume of labelling (2.40 ± 0.33 μm^3, n = 11; Appendix 1, Table 3.16) in the perinuclear region than either RyR1 (1.04 ± 0.27 μm^3, n = 11; $P < 0.05$; Appendix 1, Table 3.8) or RyR2 (0.97 ± 0.15 μm^3, n = 11; $P < 0.05$; Appendix 1, Table 3.12). By mean volume, there is also evidence for clustering of RyR2 in the extra-perinuclear region (1.60 ± 0.30 μm^3, n = 11; Appendix 1, Table 3.9) which was approximately 2-fold greater within this region than exhibited by either RyR1 (0.71 ± 0.21 μm^3, n = 11; $P < 0.05$; Appendix 1, Table 3.9) or RyR3 (0.72 ± 0.15 μm^3, n = 11; $P < 0.05$; Appendix 1, Table 3.17). However this is approximately 1.5-fold less than the mean volume of labelling exhibited by RyR3 in the perinuclear region, further demonstrating the preferential localisation of RyR3 clusters in the perinuclear region of PASMCs.

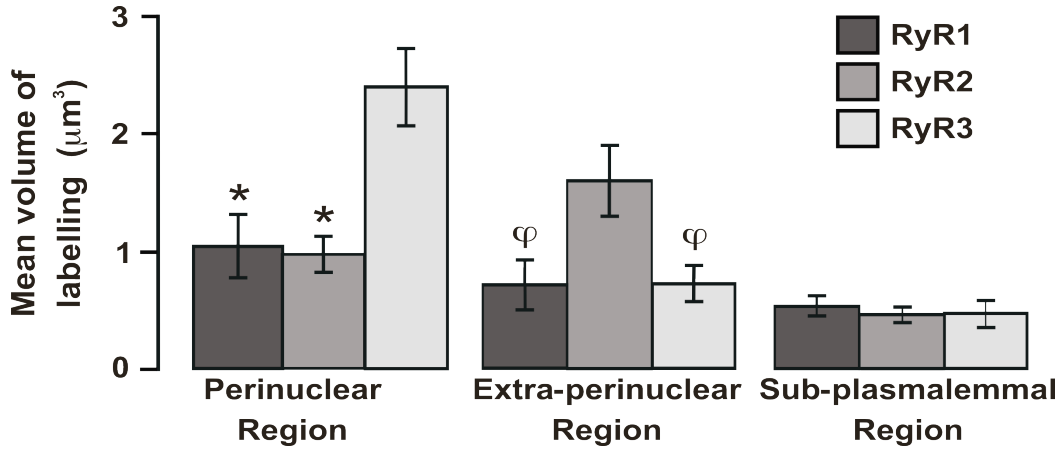

Fig. 3.7. Ryanodine receptor subtype 3 preferentially cluster in the perinuclar region of pulmonary arterial smooth muscle cells

Bar chart showing the mean volume of individual elements of RyR subtype labelling in each region (μm^3; mean ± S.E.M.) across all the PASMCs studied (RyR1, n = 10; RyR2 n = 14; RyR3 n = 11). * indicates a statistically significant difference (P<0.05) when compared to the mean volume of RyR3 labelling in the perinuclear region. φ indicates a statistically significant difference (P < 0.05) when compared to mean volume of RyR2 labelling in the extra-perinuclear region.

3.3.3 Examination of the co-localisation between lysosomes and each ryanodine receptor subtype in isolated pulmonary arterial smooth muscle cells

From the analysis of the distribution profiles of RyR subtypes and αIgp120 labelling, perhaps the most striking observation is that dense clusters of both αIgp120 and RyR3 labelling were found within the perinuclear region of PASMCs. The similar distribution profiles of both αIgp120 and RyR3 labelling would suggest that lysosomes may couple with a specific subtype of RyRs, namely RyR3. With this in mind, the co-localisation between each RyR subtype and lysosomes within isolated PASMCs was investigated. This was achieved by analysing the total density, and the regional distribution of co-localisation between labelling for αIgp120 and each RyR subtype.

3.3.3.1 Lysosomes preferentially co-localise with ryanodine receptor subtype 3 in isolated pulmonary arterial smooth muscle cells.

RyR3 showed significantly greater co-localisation with αIgp120 labelling than either RyR1 or RyR2. This is consistent with the observed distribution of both

αIgp120 and RyR3, which are both predominantly localised in the perinuclear region. Example cells co-labelled for αIgp120 and either RyR3, RyR2 or RyR1 are shown in Fig. 3.8A, B and C respectively. In each example panel *a* shows a transmitted light image of an exemplar cell and panel *b* shows the distribution of labelling for αIgp120 (green) relative to the DAPI labelled nucleus (blue) in a 3D reconstruction of a series of deconvolved Z-sections (focal depth 0.28 μm, Z step 0.2 μm). Panel *c* shows another 3D reconstruction of deconvolved Z-section in the same cell representing the distribution of labelling for the given RyR subtype (red) relative to the DAPI labelled nucleus. To visualise areas of co-localisation Z-sections were superimposed resulting in a deconvolved Z-section showing the distribution of RyR subtype (red), αIgp120 (green) and areas of co-localisation visualised in yellow, shown in panel *d*. Panel *e* shows a 3D reconstruction of the superimposed deconvolved Z-sections showing the distribution of labelling for the given RyR subtype (red), αIgp120 (green) and co-localisation between the two labels (yellow) relative to the DAPI labelled nucleus. In order to allow for visualisation of the position of co-localisation between αIgp120 and a given RyR subtype, panel *f* shows the distribution of each individual element of co-localisation (yellow) in a 3D reconstruction of deconvolved Z-sections with non-co-localised elements of αIgp120 and RyR-labelling removed.

Visual comparison of the cells presented in Fig. 3.8 would suggest that although αIgp120 co-localises with all RyR subtypes, there is a greater degree of co-localisation with RyR3 than with either RyR2 or RyR1. This is further illustrated in Fig. 3.9A which shows the mean (± S.E.M.) density of co-localisation between αIgp120 and each RyR subtype across the entire cell volume of the PASMCs examined (*i.e.* no regional subdivision). RyR3 showed a significantly greater density of co-localisation with αIgp120 (0.006 ± 0.0006 μm^3 per μm^3, $n = 11$; Appendix 1, Table 3.27) when compared to either RyR2 (0.0034 ± 0.0007 μm^3 per μm^3; $n = 14$; $P < 0.05$; Appendix 1, Table 3.23) or RyR1 (0.0031 ± 0.0007 μm^3 per μm^3, $n = 10$; $P < 0.05$; Appendix 1, Table 3.19). This 2-fold greater density of co-localisation of RyR3 with αIgp120 provides further confirmation that lysosomes preferentially co-localise with RyR3 in PASMCs. This is also evident from the fact that within the whole cell, RyR3 was found to co-localise with 26 ± 3 % ($n = 11$; Appendix 1, Table 3.31) of the total volume of lysosome labelling, whereas labelling for RyR2 and RyR1 co-

localised with only 16 ± 2 % (n = 10; Appendix 1, Table 3.31) and 15 ± 3 % (n = 14; Appendix 1, Table 3.31) of the total volume of lysosomal labelling respectively.

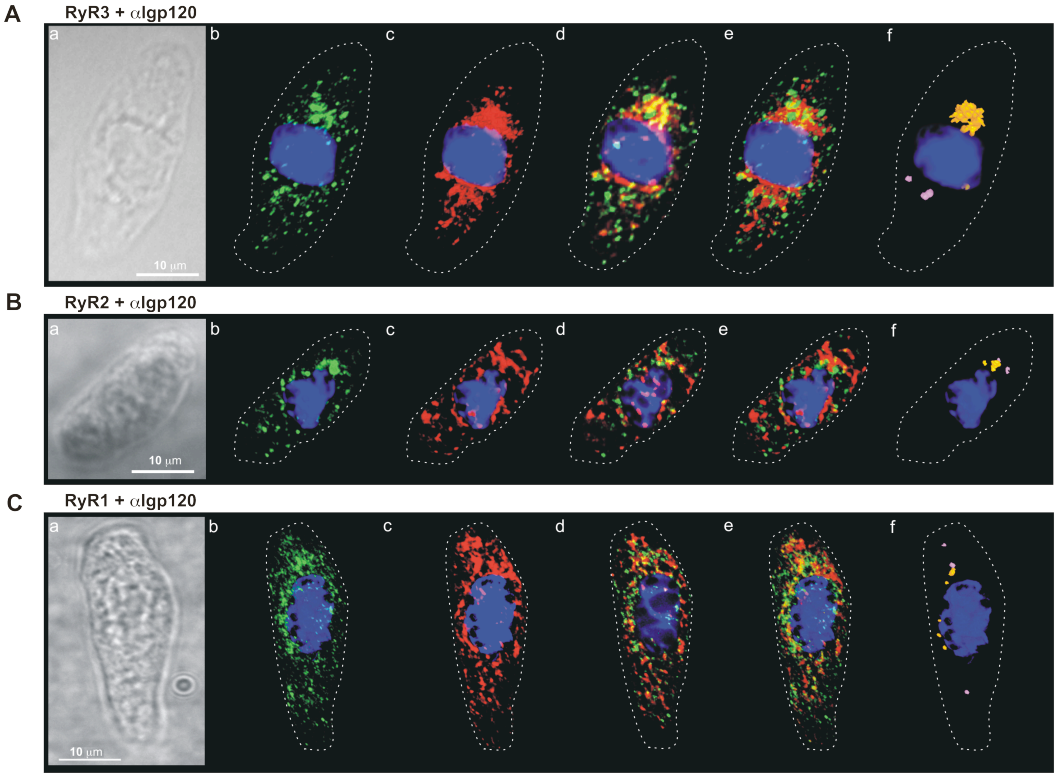

Fig. 3.8. Lysosomes preferentially co-localise with ryanodine receptor subtype 3 within isolated pulmonary arterial smooth muscle cells

Example cells showing the degree and spatial distribution of co-localisation between αIgp120 labelling and labelling of RyR3 (**A**), RyR2 (**B**), and RyR1 (**C**). In each case the panels show the following: Panel *a* shows a transmitted light image of the isolated PASMC imaged; Panel *b* shows a 3D reconstruction of a series of deconvolved Z-sections (Z step 0.2 μm) taken through the cell shown in panel *a* showing the spatial distribution of αIgp120-labelled lysosomes (green) in relation to the plasma membrane (dotted line) and nucleus (dark blue); Panel *c* shows a 3D reconstruction of deconvolved Z-sections showing the distribution of RyR labelling (red) in relation to the plasma membrane and nucleus as indicated in panel *b*; Panel *d* shows a deconvolved Z-section (focal depth 0.28 μm) taken through the PASMC showing the distribution of labelling for αIgp120, the given RyR subtype and the co-localisation between the two in relation to the nucleus of the cell (dark blue) and the plasma membrane, with areas of co-localisation shown in yellow; Panel *e* shows a 3D representation of RyR subtype and αIgp120 labelling (red and green respectively); Panel *f* is a 3D reconstruction showing individual volumes of co-localisation between αIgp120 and a given RyR subtype.

The preferential co-localisation of lysosomes with RyR3 is further demonstrated in Fig. 3.9B, which shows the Pearson product-moment correlation coefficient values for the co-localisation between αIgp120 and each RyR subtype. This coefficient

value (ranging from -1 to 1) is an indication of the strength of association between two continuous variables. Fig. 3.9B shows that the co-localisation between αIgp120 and RyR3 had a significantly greater correlation (0.26 ± 0.01, n = 11; Appendix 1, Table 3.27) than observed for either RyR2 and αIgp120 labelling (0.18 ± 0.01, n = 14; $P < 0.05$; Appendix 1, Table 3.23) or RyR1 and αIgp120 labelling (0.16 ± 0.01, n = 10; $P < 0.05$; Appendix 1, Table 3.19). It is important to note, that the Pearson product-moment correlation coefficient value is a measure of the correlation in the whole cell and not focussed on any particular region. Therefore, despite the greater degree of correlation between αIgp120 and RyR3 than for either RyR2 or RyR1, this is likely to be an underestimate of the degree of correlation between αIgp120 and RyR3 in the perinuclear region. The greater Pearson coefficient values, together with the greater density of co-localisation across the entire cell volume does, however, provide further evidence in support of the proposal that lysosomes preferentially co-localise with RyR3 in PASMCs.

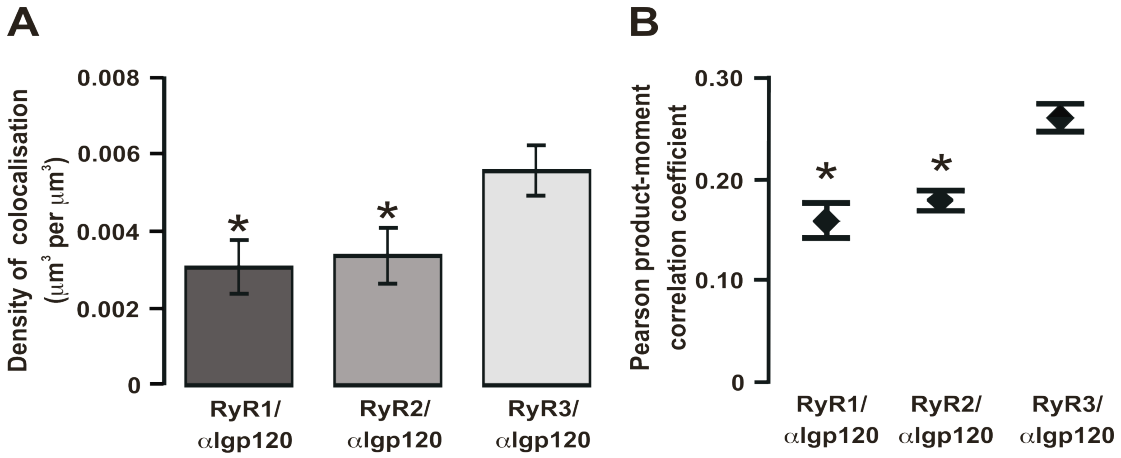

Fig. 3.9. Co-localisation is greater in cells co-labelled for RyR3 than those co-labelled for RyR2 and RyR1

A Bar chart showing the density of co-localisation (μm³ per μm³; mean ± S.E.M.) between αIgp120 labelling and each RyR subtype within the whole cell volume. **B** The Pearson product-moment correlation coefficient for each RyR subtype indicating linear dependence (mean ± S.E.M.). * indicates a statistically significant difference ($P < 0.05$) when compared to the RyR3/αIgp120 co-localisation density or Pearson correlation coefficient (RyR1, n = 10; RyR2, n = 14; RyR3, n = 11).

3.3.4 Examination of the regional distribution of co-localisation between lysosomes and each ryanodine receptor subtype in isolated pulmonary arterial smooth muscle cells

The initial comparison of αIgp120 co-localisation with each RyR subtype suggests that αIgp120 preferentially co-localises with RyR3 (Fig. 3.8, Fig. 3.9). Furthermore, visual comparison of αIgp120-labelled cells co-labelled for RyR1, RyR2 or RyR3 strongly suggests that the majority of co-localisation was concentrated in the perinuclear region of the cell (Fig. 3.8). However, further analysis of the intracellular distribution of co-localisation between αIgp120 and each RyR subtype was required in order to determine whether co-localisation is localised to any particular region of PASMCs. Fig. 3.10 shows the mean (± S.E.M.) density of co-localisation between αIgp120 labelling and labelling for each RyR subtype within each region of the cells studied.

3.3.4.1 Lysosomes preferentially co-localise with ryanodine receptor subtype 3 in the perinuclear region of isolated pulmonary arterial smooth muscle cells

Comparing the density of co-localisation across the 3 regions it appears that αIgp120 not only preferentially co-localises with RyR3, but in addition this co-localisation is preferentially targeted to a particular region of the cell. Fig. 3.10 shows that the density of co-localisation between αIgp120 and RyR3 was greatest in the perinuclear region (0.012 ± 0.002 μm^3 per μm^3, n = 11; Appendix 1, Table 3.28), which was approximately 4-fold greater than in the extra-perinuclear region (0.003 ± 0.001 μm^3 per μm^3, n = 11; $P < 0.05$; Appendix 1, Table 3.29) and 60-fold greater than in the sub-plasmalemmal region (0.0002 ± 0.0002 μm^3 per μm^3, n = 11; $P < 0.05$; Appendix 1, Table 3.30). Moreover, 41 ± 6 % of the total volume of lysosomal labelling in the perinuclear region was co-localised with RyR3 (n = 11, Appendix 1, Table 3.32). This is in marked contrast to the extra-perinuclear region and sub-plasmalemmal regions, in which only 17 ± 7 % and 2 ± 1 % (n = 11, Appendix 1, Table 3.32), respectively, of the lysosomal labelling was co-localised with RyR3.

Importantly, Fig. 3.10 also shows that the density of co-localisation between RyR3 and αIgp120 in the perinuclear region (0.012 ± 0.002 μm^3 per μm^3, n = 11;

Appendix 1, Table 3.28) was significantly greater than the density of co-localisation in the perinuclear region of cells co-labelled for αIgp120 and either RyR2 (0.0064 ± 0.0010 μm^3 per μm^3, n = 14; P<0.05; Appendix 1, Table 3.24) or RyR1 (0.0057 ± 0.0015 μm^3 per μm^3, n = 10; P<0.05; Appendix 1, Table 3.20). This is consistent with the distribution profiles exhibited by both αIgp120 and RyR3 labelling and suggests that lysosomes preferentially co-localise with RyR3 in the perinuclear region of PASMCs.

3.3.4.2 Co-localisation of lysosomes with each ryanodine receptor subtype in the extra-perinuclear region of isolated pulmonary arterial smooth muscle cells

In contrast to the perinuclear region, Fig. 3.10 also shows that within the extra-perinuclear region there was no significant difference in the density of co-localisation between cells co-labelled for RyR3 and αIgp120 (0.0033 ± 0.0012, n = 11; Appendix 1, Table 3.29) and either RyR2 and αIgp120 (0.0053 ± 0.0018, n = 14, Appendix 1, Table 3.25) or RyR1 and αIgp120 (0.0027 ± 0.0009, n = 10; Appendix 1, Table 3.21). Although there was a greater degree of co-localisation between RyR2 and lysosomes, the difference between the each of the RyR subtypes was not statistically significant. Given the predominance of RyR2 within the extra-perinuclear region, one might expect a significant difference in the degree of co-localisation of lysosomes with this RyR subtype. The absence of any significant difference would therefore suggest that within this region, lysosomes do not preferentially co-localise with a particular RyR subtype. The greater degree of co-localisation of RyR2 with lysosomes is likely to be due to the greater density of RyR2 labelling when compared to RyR1 or RyR3 (Fig. 3.6) and therefore the coincidence of αIgp120 and RyR2 labelling occurring within a given area would be greater than for either RyR1 or RyR3. Given the marked decline in RyR3 labelling between the perinuclear and extra-perinuclear regions, this would indicate that there is a high degree of co-localisation of lysosomes and RyR3 relative to RyR1 or RyR2.

3.3.4.3 Co-localisation of lysosomes with each ryanodine receptor subtype in the sub-plasmalemmal region of isolated pulmonary arterial smooth muscle cells

Fig. 3.10 also shows that there was little or no co-localisation between αIgp120 and any of the 3 RyR subtypes in the sub-plasmalemmal region. Furthermore, similar to the extra-perinuclear region, there was no significant difference in the density of co-localisation between the 3 RyR subtypes and αIgp120 in the sub-plasmalemmal region, with cells co-labelled for RyR3 and αIgp120 measuring 0.0002 ± 0.00015 μm^3 per μm^3 (n = 11; Appendix 1, Table 3.30) compared to cells co-labelled for αIgp120 and either RyR2 or RyR1 measuring 0.0005 ± 0.0002 μm^3 per μm^3 (n = 14; Appendix 1, Table 3.26) and 0.0011 ± 0.0003 μm^3 per μm^3 (n = 10; Appendix 1, Table 3.22) respectively.

Thus, it would appear that lysosomes not only co-localise preferentially with RyR3, but they are also spatially localised such that this co-localisation is predominantly found in the perinuclear region of PASMCs. This is consistent with the predominance of perinuclear localisation observed in both RyR3 and αIgp120 labelling.

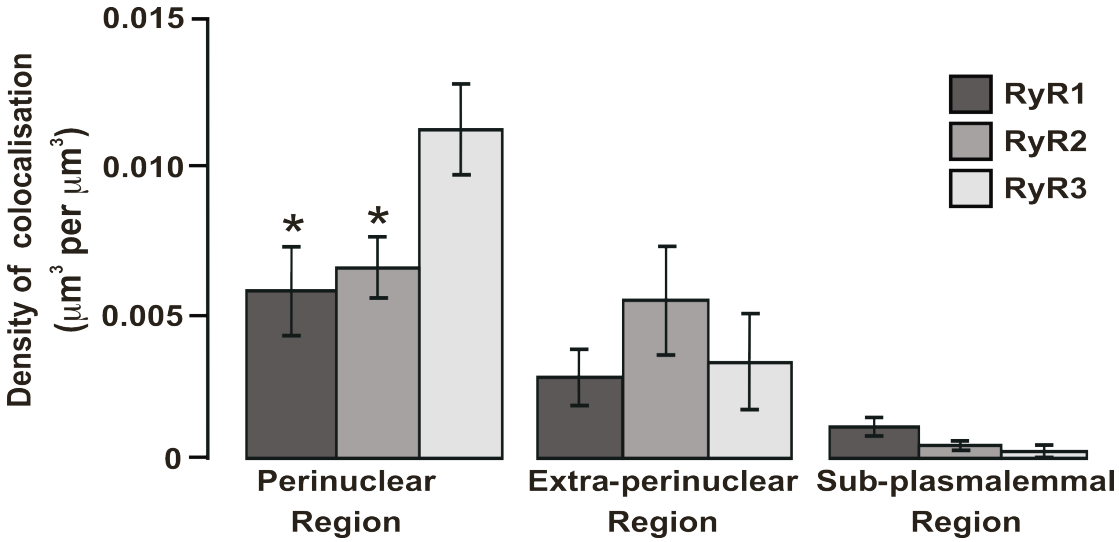

Fig. 3.10. Lysosomes preferentially co-localise with ryanodine receptor subtype 3 in the perinuclear region of pulmonary arterial smooth muscle cells

Bar chart showing the density of co-localisation between αIgp120 labelling and each RyR subtype (μm^3 per μm^3; mean ± S.E.M.) within all 3 of the designated regions of subdivided PASMCs. * indicates a statistically significant difference (P < 0.05) when compared to the RyR3 labelling in the perinuclear region (RyR1, n = 10; RyR2, n = 14; RyR3, n = 11).

3.3.4.4 Lysosomes preferentially cluster with ryanodine receptor subtype 3 in the perinuclear region of isolated pulmonary arterial smooth muscle cells

In addition to the density of co-localisation between αIgp120 and each RyR subtype, the mean (± S.E.M.) volume of individual elements of co-localisation was also examined. Fig. 3.11 shows that the mean volume of co-localisation between RyR3 and αIgp120 was approximately 2-fold and 20-fold greater in the perinuclear region (0.81 ± 0.15 μm^3, n = 11; Appendix 1, Table 3.28) than in the extra-perinuclear (0.35 ± 0.08 μm^3, n = 11; $P < 0.05$; Appendix 1, Table 3.29) and sub-plasmalemmal (0.04 ± 0.02 μm^3, n = 11; $P < 0.05$; Appendix 1, Table 3.30) regions respectively. Furthermore, in the perinuclear region, the mean volume of co-localisation between RyR3 and αIgp120 was 3-fold and 2-fold greater than the mean volume of co-localisation between αIgp120 and either RyR1 (0.30 ± 0.03 μm^3, n = 10; $P < 0.05$; Appendix 1, Table 3.20), or RyR2 (0.38 ± 0.04 μm^3, n = 14; $P < 0.05$; Appendix 1, Table 3.24) in the same region (Fig. 3.11).

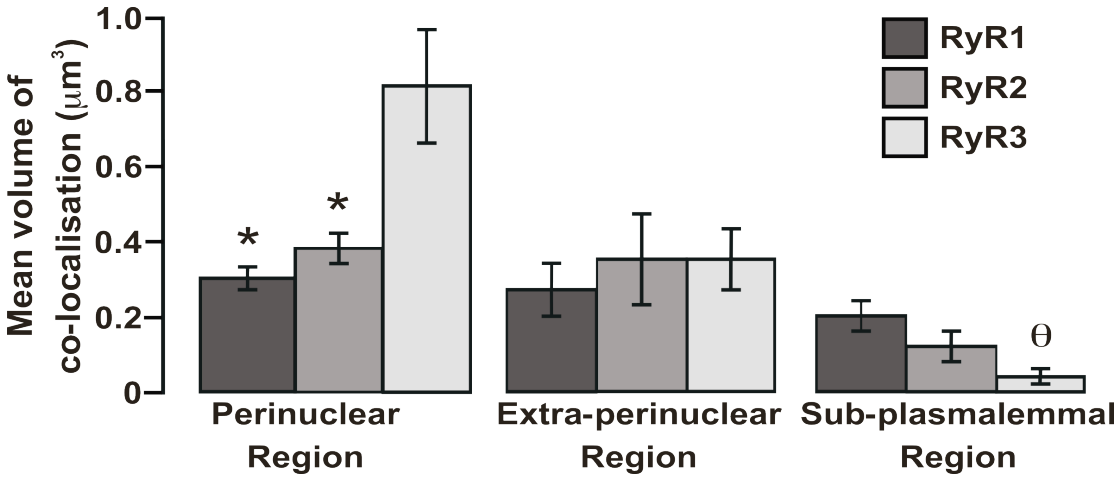

Fig. 3.11. Lysosome clusters preferentially co-localise with clusters of ryanodine receptor 3 in the perinuclar region of pulmonary arterial smooth muscle cells

Bar chart showing the mean volume of individual elements of co-localisation within each region (μm^3; mean ± S.E.M.) between αIgp120 and each RyR subtype across all the PASMCs studied (RyR1, n = 10; RyR2 n = 14; RyR3 n = 11). * indicates a statistically significant difference ($P < 0.05$) when compared to the mean volume of co-localisation between αIgp120 and RyR3 labelling in the perinuclear region. θ indicates a statistically significant difference ($P < 0.05$) when compared to mean volume of co-localisation between αIgp120 and RyR1 labelling in the sub-plasmalemmal region.

Greater volumes of individual elements of co-localisation are indicative of a greater degree of clustering and therefore, the data presented in Fig. 3.11 is consistent with the greatest density of co-localisation occurring between RyR3 and αIgp120 in the perinuclear region of PASMCs. Taken together these data strongly suggest that, not only do lysosomal clusters preferentially co-localise with clusters of RyR3, but also these lysosome-RyR3 clusters are targeted to the perinuclear region of PASMCs.

3.3.4.5 The density of ryanodine receptor subtype and lysosomal labelling was equal across all isolated pulmonary arterial smooth muscle cells studied

It is worth noting that the significant difference in co-localisation between αIgp120 and the 3 RyR subtypes is not due to unequal labelling of either αIgp120 or RyR across the cells examined. This is demonstrated in Fig. 3.12 which shows that there is no significant difference in the density of αIgp120 labelling in cells co-labelled for either RyR3 (0.023 ± 0.002 μm^3 per μm^3, n = 11; Appendix 1, Table 3.33) RyR2 (0.021 ± 0.0017 μm^3 per μm^3, n = 14; Appendix 1, Table 3.33) or RyR1 (0.019 ± 0.0035 μm^3 per μm^3, n = 10; Appendix 1, Table 3.33).

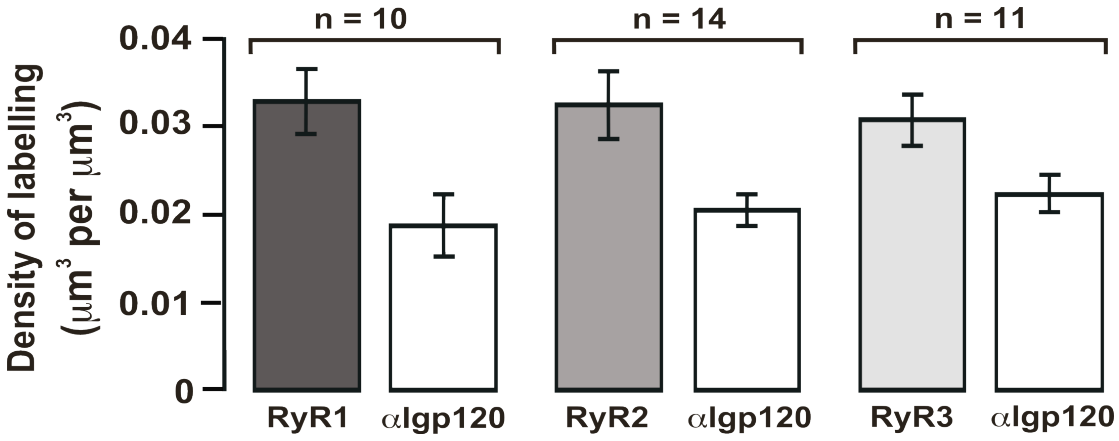

Fig. 3.12. Differences in co-localisation is not due to unequal antibody labelling between RyR subtypes.

Bar chart showing the density of labelling (μm^3 per μm^3; mean ± S.E.M.) for both αIgp120 and RyR subtype within the whole cell volume. αIgp120 labelling was divided according to the RyR subtype with which it was co-labelled.

Similarly Fig. 3.12 shows that there was no significant difference in the whole cell density of RyR3 (0.032 ± 0.0028 μm^3 per μm^3, n = 11; Appendix 1, Table 3.33)

RyR2 (0.0328 ± 0.0038 μm^3 per μm^3, n = 14; Appendix 1, Table 3.33) or RyR1 labelling (0.032 ± 0.004 μm^3 per μm^3, n = 10; Appendix 1, Table 3.33). Thus, with equal total labelling across the cells, the preferential co-localisation of αIgp120 with RyR3 suggests that, in PASMCs RyR3 forms a close association with clusters of lysosomes.

3.3.5 Inhibition of ryanodine receptor subtypes 1 and 3 by dantrolene abolishes global Ca^{2+} waves but not Ca^{2+} bursts in response to NAADP

The data presented thus far suggest that lysosomes are predominantly localised in the perinuclear region of isolated PASMCs. Labelling of RyR subtypes revealed that RyR3 is the predominant subtype within this region. Furthermore, measurement of the density of co-localisation between αIgp120 and individual RyR subtypes revealed that the greatest degree of co-localisation was in the following order: RyR3 >> RyR2 ≥ RyR1 suggesting that lysosomes and RyR3 form a trigger zone for Ca^{2+} signalling by NAADP. To further verify this proposal, the effect on NAADP-mediated Ca^{2+} release by selectively blocking RyR1 and RyR3 with dantrolene was examined. Dantrolene selectively blocks Ca^{2+} release via RyR3 and RyR1 but is without effect on RyR2 (Zhao *et al.*, 2001). Thus, the rank order of co-localisation between lysosomes and the 3 subtypes (RyR3 >> RyR2 ≥ RyR1) offered the opportunity to determine whether or not RyR3 underpinned the amplification of NAADP-mediated Ca^{2+} bursts into global Ca^{2+} waves.

The effect of dantrolene on Ca^{2+} transients triggered by intracellular dialysis from a patch pipette of NAADP (10 nM) was studied in the whole-cell configuration of the patch clamp technique and under current clamp conditions (I = 0), with changes in the intracellular Ca^{2+} concentration reported by the Fura-2 fluorescence ratio (F_{340}/F_{380}). An exemplar record is shown in Fig. 3.13A. The upper panel shows a series of pseudocolour images of the Fura-2 fluorescence ratio recorded in an isolated PASMC during the intracellular dialysis of 10 nM NAADP, with the record of the Fura-2 fluorescence ratio against time shown in the bottom panel. Intracellular dialysis of 10 nM NAADP induced spatially restricted Ca^{2+} bursts (indicated by the white arrow in Fig. 3.13A, Image 2) which either returned to basal levels or proceeded and then triggered a global Ca^{2+} wave. The mean Fura-2 fluorescence ratio

(± S.E.M.) increased from a basal level of 0.51 ± 0.05 to a peak of 1.42 ± 0.21 before returning to baseline (n = 5).

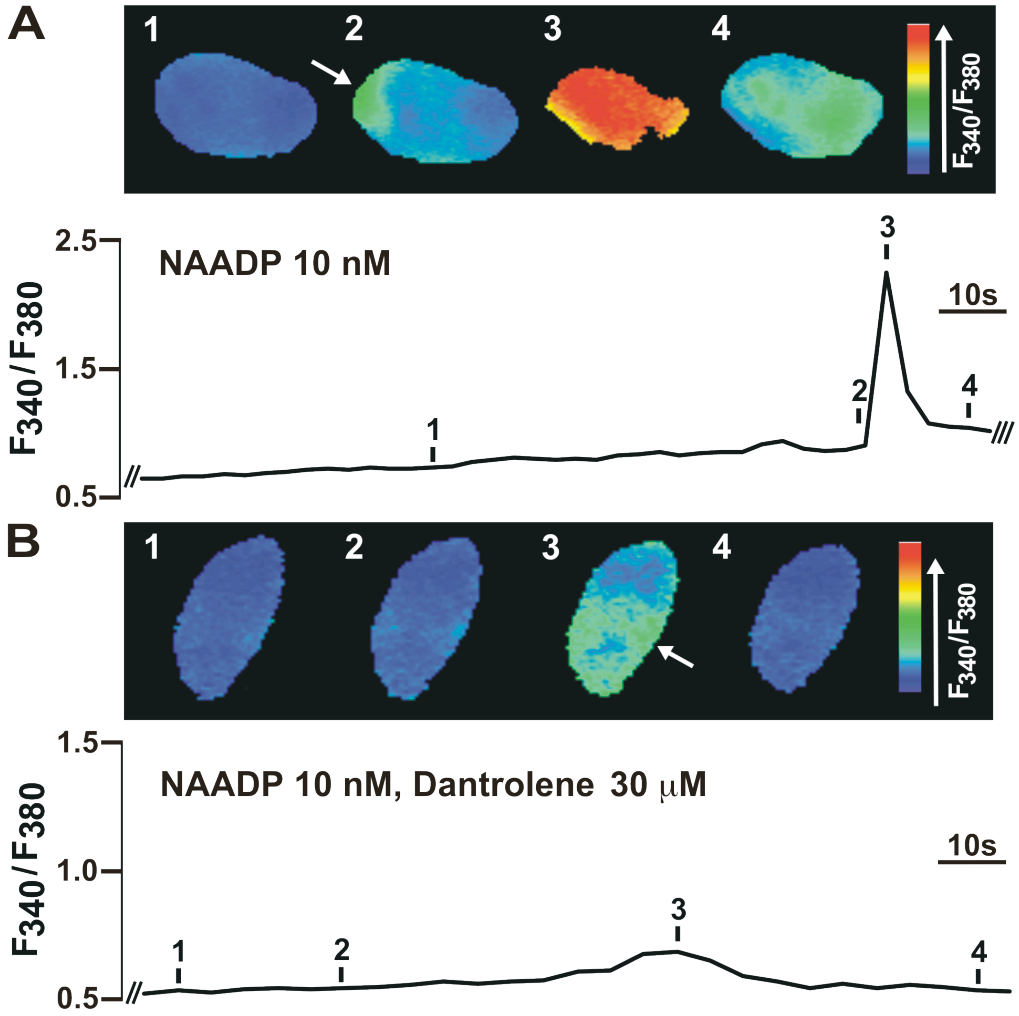

Fig. 3.13. Dantrolene inhibits the NAADP-evoked global Ca^{2+} wave in pulmonary arterial smooth muscle cells

A Top panel, series of pseudocolour images of the Fura-2 fluorescence ratio recorded in an isolated PASMC during the intracellular dialysis of 10 nM NAADP. NAADP evokes a Ca^{2+} burst indicated by the white arrow (image 2) which precedes a global Ca^{2+} wave. Bottom panel, corresponding record of the Fura-2 fluorescence ratio against time for the cell imaged in the top panel. Access to the cytosol via the formation of the whole-cell configuration is indicated by the two bars at the beginning of the record. Note, the loss of a GΩ seal is indicated at the end of the record by three bars. **B** Top panel, series of pseudocolour images of the Fura-2 fluorescence ratio recorded in an isolate PASMC during the intracellular dialysis of 10 nM NAADP following the preincubation (15 min) with 30 μM dantrolene. Dantrolene inhibited the global Ca^{2+} wave but not the localised Ca^{2+} bursts (indicated in image 3 by the white arrow) in response to NAADP. Bottom panel, corresponding record of the Fura-2 fluorescence ratio against time for the cell imaged in the top panel.

Following preincubation (15 min) of PASMCs with 30 μM dantrolene, intracellular dialysis of 10 nM NAADP failed to induce a global Ca^{2+} wave. However, dantrolene did not inhibit NAADP-induced Ca^{2+} bursts. Fig. 3.13B shows one such record. The upper panel shows a series of pseudocolour images in which the NAADP-induced Ca^{2+} burst is indicated (white arrow, image 3) with the record of the Fura-2 fluorescence ratio against time shown in the lower panel. In the presence of dantrolene the change in the Fura-2 fluorescence ratio was markedly attenuated, increasing from a basal level of 0.55 ± 0.03 to a peak of only 0.83 ± 0.05 (n = 6). The bar chart in Figure 3.14 shows that the mean change in the Fura-2 fluorescence ratio triggered by NAADP was markedly decreased from 0.91 ± 0.2 in the absence of dantrolene (n = 5; Appendix 1, Table 3.34) to 0.28 ± 0.03 (n = 6, P < 0.05; Fig 3.13; Appendix 1, Table 3.35) in the presence of dantrolene (30 μM). The fact that dantrolene abolished the global Ca^{2+} wave but not the preceding Ca^{2+} burst triggered by NAADP is consistent with the effect of blocking all RyRs with ryanodine and of depleting SR Ca^{2+} stores with thapsigargin (Boittin *et al.*, 2002). When taken together these data therefore support the proposal that RyR3 is a pre-requisite for the amplification of NAADP-induced Ca^{2+} bursts into global Ca^{2+} waves. Thus, it is likely that RyR3, but not RyR1 or RyR2 is targeted to lysosome-SR junctions to comprise a trigger zone for Ca^{2+} signalling by NAADP.

3.3.5.1 Dantrolene is without effect on ionomycin-induced Ca^{2+} influx in pulmonary arterial smooth muscle cells

A previous report has suggested that dantrolene may inhibit the fluorescence reporting capability of Fura-2 (Nohmi *et al.*, 1991). Therefore, it was important to determine whether or not dantrolene, when applied to PASMCs, compromised the ability of Fura-2 to reliably report changes in intracellular Ca^{2+}. To this end I investigated the effects of dantrolene on the ability of the ionophore ionomycin to raise the intracellular Ca^{2+} concentration in PASMCs. Application of ionomycin (1 μM) induced an increase in the Fura-2 fluorescence ratio from 0.43 ± 0.02 to 0.74 ± 0.05 in the absence, and from 0.42 ± 0.01 to 0.78 ± 0.05 in the presence of 30 μM dantrolene. The bar chart in Fig. 3.14 shows the mean (± S.E.M.) change in the fluorescence ratio in response to ionomycin (1 μM) in the absence (0.31 ± 0.04, n =

11; Appendix 1, Table 3.36) and following pre-incubation (15 minutes) with 30 μM dantrolene (0.36 ± 0.05, *n* = 12; Fig. 3.14; Appendix 1, Table 3.36). These data show quite clearly that dantrolene was without effect on the change in the Fura-2 fluorescence ratio resulting from ionomycin-induced Ca^{2+} influx, in marked contrast to its inhibitory effect on Ca^{2+} signalling by NAADP. It is unlikely, therefore, that dantrolene compromises the ability of Fura-2 to report changes in intracellular Ca^{2+} concentration under the conditions of my experiments.

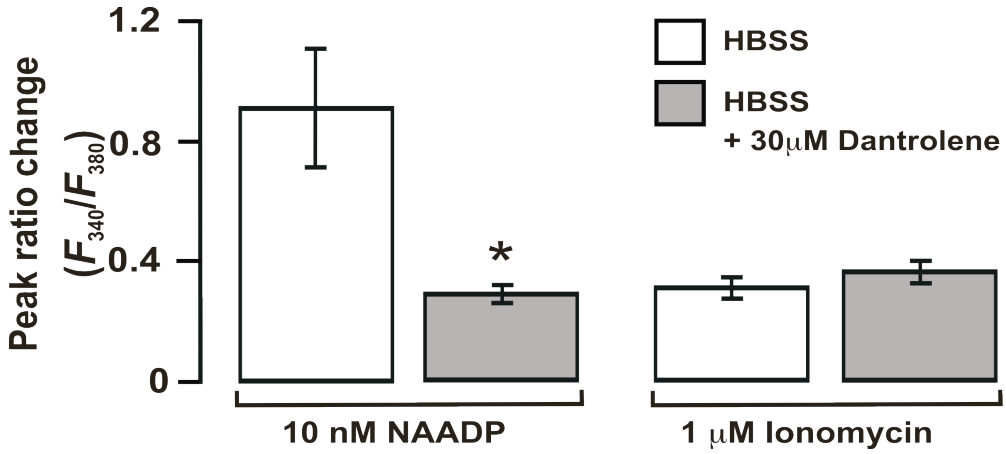

Fig. 3.14. Dantrolene inhibits the global Ca^{2+} release in response to NAADP but not ionomycin in pulmonary arterial smooth muscle cells

Bar chart showing the peak change in the Fura-2 fluorescence ratio (mean ± S.E.M.) recorded in PASMCs in response to either the intracellular dialysis of NAADP (10 nM) or extracellular application of ionomycin (1 mM). The response to NAADP and ionomycin were recorded in either the absence (white box; NAADP *n* = 5; ionomycin *n* = 11) or presence of 30 μM dantrolene (grey box; NAADP *n* = 6; ionomycin *n* = 12). * indicates a statistically significant difference ($P < 0.05$) when compared to the peak change in fluorescence ratio in response to 10 nM NAADP in the absence of 30 μM dantrolene.

3.4 Discussion

The data presented in this chapter provide further evidence in support of a two-pool mechanism for NAADP-dependent Ca^{2+} signalling in pulmonary arterial smooth muscle cells (Boittin *et al.*, 2002; Churchill *et al.*, 2001a). These data also strongly suggest that this two-pool mechanism is dependent upon lysosomal clusters that preferentially co-localise with SR regions to which a subpopulation of RyRs, namely

RyR3, is targeted to form a trigger zone for Ca^{2+} signalling by NAADP within the perinuclear region of PASMCs.

3.4.1 Lysosomes are predominantly localised in the perinuclear region of pulmonary arterial smooth muscle cells.

Visualisation of lysosomes with the lysosomal marker aIgp120 revealed that these organelles were present throughout the cytoplasm of PASMCs. However, the cellular distribution of lysosomes labelled with aIgp120 was clearly non-uniform, with the majority of labelling present within the perinuclear region of PASMCs. Indeed, the density of lysosomal labelling in the perinuclear region was approximately 2-fold and 4-fold greater than that observed in the extra-perinuclear and subplasmalemmal regions, respectively. Furthermore, lysosomes appeared to form dense clusters within the perinuclear region, whereas outside this region a more diffuse labelling pattern was observed. This is reflected in the mean volume of individual elements of lysosomal labelling (which included as one all elements of labelling separated by a distance below the resolution of the deconvolution microscopy used here, < 100 nm). This was greatest in the perinuclear region and declined in the extra-perinuclear region, and further still in the subplasmalemmal region. It would appear, therefore, that lysosomes form dense clusters within the perinuclear region of the cell. This is consistent with previous reports in which LysoTracker Red labelled lysosomes were shown to form dense clusters in PASMCs (Kinnear *et al.*, 2004). Furthermore, this clustering mirrored the spatially restricted nature of the NAADP-mediated Ca^{2+} bursts observed in PASMCs, which has been proposed to be due to the mobilisation by NAADP of lysosome-related Ca^{2+} stores (Boittin *et al.*, 2002; Kinnear *et al.*, 2004) as illustrated in Fig. 3.4. It is notable, therefore, that there have been reports of lysosome clusters in the perinuclear region of other mammalian cells such as mouse fibroblasts (Falcon-Perez *et al.*, 2005) a rat kidney fibroblast cell line (Reaves *et al.*, 1996) and the COS-7 cell line (Matsushita *et al.*, 2004).

3.4.2 Ryanodine receptor subtypes exhibit different spatial distributions

In an identical method used for the analysis of lysosomal labelling, examination of the distribution of RyR subtypes 1, 2 and 3 revealed that, despite a similar density of labelling in PASMCs, each subtype exhibited quite different patterns of spatial organisation.

3.4.2.1 Ryanodine receptor subtype 3 is predominantly targeted to the perinuclear region of isolated pulmonary arterial smooth muscle cells

Analogous to the distribution of lysosomes, RyR3 exhibited a highly polarised spatial distribution, with the greatest density of RyR3 labelling localised to the perinuclear region. The density of labelling in this region was found to be approximately 4-fold greater than in the extra-perinuclear region and 14-fold greater than in the sub-plasmalemmal region. Moreover RyR3 was found to be the predominant RyR subtype within the perinuclear region, with a 2-fold greater density of labelling than for either RyR1 or RyR2. Furthermore, the mean volume of individual elements of RyR3 labelling was greatest within the perinuclear region and declined 3-fold and 5-fold in the extra-perinuclear and sub-plasmalemmal region, respectively. The mean volume of individual elements of RyR3 labelling was also 2-fold greater than was observed for either RyR1 or RyR2. Therefore, RyR3 exhibits a high degree of clustering within the perinuclear region of PASMCs, and such extensive clustering was not observed for either RyR1 or RyR2. That RyR3 is the predominant subtype found in the perinuclear region of PASMCs and declines in density outside of this region may indicate that RyR3 performs a highly specialised function within this region of the cell.

3.4.2.2 Ryanodine receptor subtype 2 is predominantly localised to the extra-perinuclear region of isolated pulmonary arterial smooth muscle cells

In marked contrast to the immediate decline of RyR3 labelling outside the perinuclear region, the density of RyR2 labelling increased significantly between the perinuclear and the extra-perinuclear region. Thus, RyR2 labelling in the extra-perinuclear region was 2-fold and 6-fold greater than was observed in the perinuclear

and sub-plasmalemmal region respectively. Such a concentration of RyR2 labelling within the extra-perinuclear region was also reflected in the mean volume of individual elements of labelling. This was approximately 2-fold greater than that observed in the perinuclear region, and 3-fold greater than the sub-plasmalemmal region. It seems likely, therefore that RyR2 may form clusters preferentially within this region. Not only was RyR2 labelling concentrated in the extra-perinuclear region, but it would also appear that it is the predominant RyR subtype within this region. This was confirmed by the fact that that the density of RyR2 labelling was 3-fold greater within this region than for either RyR1 or RyR3. Moreover the mean volume of labelling was 2-fold greater than was observed for RyR1 and RyR3. Together these suggest that RyR2 is the predominant subtype within this region and this may inform on its role with respect to Ca^{2+} signalling in pulmonary arterial smooth muscle cells (see below).

3.4.2.3 Ryanodine receptor subtype 1 is the predominant subtype present in the sub-plasmalemmal region of isolated pulmonary arterial smooth muscle cells

In contrast to both RyR3 and RyR2, RyR1 was uniformly distributed throughout the cell with no significant difference in the density of labelling between all 3 regions. Due to this even distribution profile, RyR1 would appear to be the predominant RyR subtype present in the sub-plasmalemmal region, with a 3-fold and 6-fold greater density of labelling than for RyR2 and RyR3, respectively. This suggests that RyR1 may play a significant role with respect to Ca^{2+} signalling between the SR and the plasma membrane and may therefore couple to Ca^{2+}-activated ion channels in the plasma membrane, such as the large-conductance Ca^{2+}-activated potassium channels ($K_{Ca}1.1$). RyR1 may therefore be the RyR subtype responsible for Ca^{2+} release from "peripheral" SR that, via the activation of $K_{Ca}1.1$, underpins cADPR-mediated hyperpolarisation of PASMCs and dilation of pulmonary arteries in response to the activation of adenylyl cyclase by G-protein coupled receptors (Boittin *et al.*, 2003). This possibility is highlighted by findings in other cell types that suggest that RyR1 may form a close association with and therefore modulate the activity of the plasma membrane-bound TRPC3 (Woo *et al.*, 2008).

The above data suggest that within each region of the subdivided PASMCs studied there exists a predominant RyR subtype, with RyR3, RyR2 and RyR1 being

the foremost subtype in the perinuclear, extra-perinuclear and sub-plasmalemmal regions, respectively.

3.4.3 Lysosomes preferentially co-localise with ryanodine receptor subtype 3 in the perinuclear region to comprise a trigger zone for Ca^{2+} signalling by NAADP

3.4.3.1 Lysosomes predominantly co-localise with ryanodine receptor 3 in the perinuclear region of pulmonary arterial smooth muscle cells

Despite there being no cell-to-cell variation in the density of labelling for aIgp120 or either of the RyR subtypes, the density of co-localisation between αIgp120 and RyR within the whole cell was approximately 2-fold greater than for either RyR1 or RyR2. This suggests that lysosomes preferentially co-localise with RyR3. However, analysis of co-localisation between αIgp120 and each RyR subtype by region of the cell was required in order to provide further insight into the components that underpin the mechanism of NAADP-mediated Ca^{2+} signalling in PASMCs.

Within the perinuclear region, 41 % of all lysosomal labelling co-localised with RyR3 compared with 17 % and 2 % in the extra-perinuclear and sub-plasmalemmal regions, respectively. This produced a density of co-localisation in the perinuclear region that was 4-fold greater than was observed in the extra-perinuclear region and 60-fold greater than observed in the sub-plasmalemmal region. In marked contrast to RyR3, only 13 % of lysosomal labelling co-localised with either RyR2 or RyR1 respectively in the perinuclear region. That lysosomes may associate with RyR1 and RyR2 to a lesser degree than with RyR3 in this region was also reflected in the fact that the density of co-localisation between aIgp120 and either RyR2 or RyR1 was 2-fold lower than for RyR3. Moreover, the mean volume of individual elements of co-localisation between RyR3 and lysosomal labelling was 2-fold and 20-fold greater in the perinuclear region than in the extra-perinuclear and sub-plasmalemmal regions, respectively. Furthermore, the mean volume of co-localisation between RyR3 and lysosomes was 2-fold greater than for either RyR2 or RyR1 in the perinuclear region.

When taken together with the above, these data suggest that lysosomes primarily cluster within the perinuclear region of PASMCs and that these clusters

preferentially co-localise with RyR3 and provides a rank order of co-localisation of: RyR3 >> RyR2 ≥ RyR1. It would appear, therefore, that lysosomes and RyR3 are held in a close association in PASMCs and thereby comprise a trigger zone for Ca^{2+} signalling by NAADP.

3.4.3.2 Dantrolene inhibits NAADP-induced global Ca^{2+} waves but not Ca^{2+} bursts in isolated pulmonary arterial smooth muscle cells

In order to functionally confirm that lysosomes co-localise with RyR3 to form a trigger zone for NAADP-dependent Ca^{2+} signalling, dantrolene was used to distinguish between RyR2 and RyR3 / RyR1. Intracellular dialysis of 10 nM NAADP into isolated PASMCs resulted in global Ca^{2+} waves. These waves were the result of Ca^{2+} bursts that breached the threshold for, and were subsequently amplified by CICR via RyRs as described in previous reports (Boittin *et al.*, 2002). Pre-incubation with dantrolene resulted in the inhibition of NAADP-mediated global Ca^{2+} waves. However, in the presence of dantrolene Ca^{2+} bursts were still observed, suggesting that dantrolene was not inhibiting NAADP-mediated Ca^{2+} release from lysosomes but rather the initial amplification process via CICR. That Ca^{2+} bursts were observed in the presence of dantrolene without initiation of a global Ca^{2+} wave was reminiscent of the effect of both ryanodine and thapsigargin on NAADP-mediated Ca^{2+} release in PASMCs (Boittin *et al.*, 2002). The effect of dantrolene is therefore consistent with the immunocytochemical data presented above, in that it supports the view that NAADP-mediated Ca^{2+} bursts from lysosomes are initially amplified by CICR from the SR via RyR3. This first step is pivotal to the amplification of spatially restricted Ca^{2+} bursts into global Ca^{2+} waves, but the onward propagation into a global Ca^{2+} wave may be more complex.

3.4.4 Why might ryanodine receptor subtype 3 be specifically targeted to lysosome-SR junctions?

Clearly, my data suggest that lysosomes and RyR3 comprise a trigger zone for Ca^{2+} signalling by NAADP. However, it is important to ask why this association may be RyR subtype specific. One potential factor that could be of relevance in this respect is that of identified variations in the regulation of each RyR subtype by Ca^{2+}.

The threshold for activation of RyR1, RyR2 and RyR3 by cytoplasmic Ca^{2+} concentration is approximately 100 nM for all 3 subtypes (Chen *et al.*, 1997a; Chen *et al.*, 1997b; Li *et al.*, 2001). However, of particular note is that the estimated EC_{50} for RyR2 and RyR3 differ significantly with half maximal activation at ~250 nM and ~400 nM for RyR2 and RyR3, respectively (Chen *et al.*, 1997b; Li *et al.*, 2001). The higher level of half maximal activation by Ca^{2+} exhibited by RyR3 allows for a higher "margin of safety" with respect to amplification of initial NAADP-mediated Ca^{2+} bursts via CICR. For example, the higher threshold for activation by CICR of RyR3 when compared to RyR2 could reduce the possibility of false amplification of subthreshold Ca^{2+} release events within the lysosome-SR junction.

In addition to the EC_{50}, the mean channel open time versus the cytoplasmic Ca^{2+} concentration for each RyR subtype is different. The mean open time for RyR2 and RyR3 are similar and each exhibit a ~10-fold increase in mean open time over their activation range. By contrast, the mean open time for RyR1 is much lower and only increases 2-fold over the range of Ca^{2+} concentration that confers channel activation (Chen *et al.*, 1997b; Li *et al.*, 2001). Furthermore, the observed open probability (P_o) versus cytoplasmic Ca^{2+} concentration curves for each subtype show that RyR3 exhibits a greater increase in the P_o (0-1) than does RyR2 (0-0.9) and even more so than for RyR1 (0-0.2) which exhibits little gain in P_o with increasing Ca^{2+} concentration (Chen *et al.*, 1997b; Li *et al.*, 2001). Thus, of the 3 RyR subtypes RyR3 would provide the greatest degree of amplification of Ca^{2+} bursts from lysosome-related Ca^{2+} stores.

A further factor that may be of significance is the sensitivity of each RyR to inactivation by Ca^{2+}, which also varies between each of the RyR subtypes. The IC_{50} for RyR3 is 3 mM, which may be significantly less sensitive to inactivation than RyR2 (IC_{50} = 2mM). Nevertheless, both RyR3 and RyR2 activity have been observed at Ca^{2+} concentrations > 10 mM (Chen *et al.*, 1997b; Li *et al.*, 2001). In contrast, RyR1 is inactivated by Ca^{2+} within the μM range and can be completely inactivated at 1 mM Ca^{2+} (Chen *et al.*, 1997b). The far greater sensitivity of RyR1 to inactivation by Ca^{2+} may also explain, in part, the reduced gain in P_o for RyR1 relative to RyR2 and RyR3. It is clear, therefore, that RyR1 would be poorly suited to a role in the amplification of Ca^{2+} bursts within lysosome-SR junctions as it would

likely be inactivated at the high Ca^{2+} concentrations reached within the junctional space upon release of Ca^{2+} bursts from the lysosome-related stores.

With the aforementioned facts considered, it is clear that RyR3 would provide a greater margin of safety with respect to the amplification of Ca^{2+} bursts within lysosome-SR junctions. Moreover, once the threshold for CICR via RyR3 is breached, RyR3 would offer the greatest potential amplification via CICR and its relative insensitivity to inactivation by high (mM) Ca^{2+} concentrations would limit the possibility of failure with respect to amplification of received Ca^{2+} signals. It is also possible, therefore, that the targeting of RyR3 to lysosome-SR junctions may be key to the all-or-none manner in which NAADP-induced Ca^{2+} bursts trigger global Ca^{2+} waves. However, the density of RyR3 labelling declines markedly outside the perinuclear region and this fact does not suggest that RyR3 is key to the development of a propagating and global Ca^{2+} wave.

3.4.5 How may a propagating global Ca^{2+} wave be precipitated following amplification of Ca^{2+} bursts by ryanodine receptor subtype 3 within lysosome-SR junctions?

Following amplification of NAADP-mediated Ca^{2+} bursts a propagating, global Ca^{2+} wave must arise from the lysosome-SR junction. However, the density of RyR3 labelling declines by approximately 4-fold between the perinuclear region and the extra-perinuclear region, and there is a 14-fold decline in the density of RyR3 labeling from the perinuclear region to the sub-plasmalemmal region. This polarised distribution suggests that RyR3 is unlikely to play a role in signal propagation beyond the perinuclear region after the initial amplification process has occurred.

In marked contrast to what was observed with RyR3, the density of RyR2 labelling increased markedly (2-fold) within the extraperinuclear region of the cell when compared to the perinuclear region, but decreased 6-fold in the sub-plasmalemmal region relative to the extra-perinuclear region. Furthermore, RyR2 was found to be the predominant subtype within the extra-perinuclear region with a ~3-fold greater density of labelling than for either RyR1 or RyR3. This distribution in itself suggests that RyR2 rather than RyR1, may function to carry a propagating Ca^{2+} wave away from lysosome-SR junctions, and this suggestion is supported by consideration of the properties of RyR regulation by Ca^{2+}. Thus, RyR2 has a lower

EC_{50} for CICR than RyR3 and is less sensitive to inactivation by Ca^{2+} than RyR1. Therefore, RyR2 would ensure that, once a Ca^{2+} wave has been initially amplified by RyR3, propagation by CICR would be less prone to failure. Thus the functional properties of RyR2 lend it well to a role in the propagation of a global Ca^{2+} wave away from lysosome-SR junctions, in much the same way as RyR2 supports the propagating wave initiated by CICR in response to voltage-gated Ca^{2+} influx in cardiac muscle (Macgregor *et al.*, 2007).

In conclusion, lysosomes form junctional complexes with regions of the SR containing a high density of RyR3 to comprise a trigger zone for Ca^{2+} signalling by NAADP. Within this trigger zone NAADP-dependent Ca^{2+} bursts are amplified in an all-or-none manner by CICR via RyR3. Thereafter, a propagating global Ca^{2+} wave could be developed by subsequent recruitment of RyR2 by CICR as this amplified signal exits lysosome-SR junctions (Fig. 3.15).

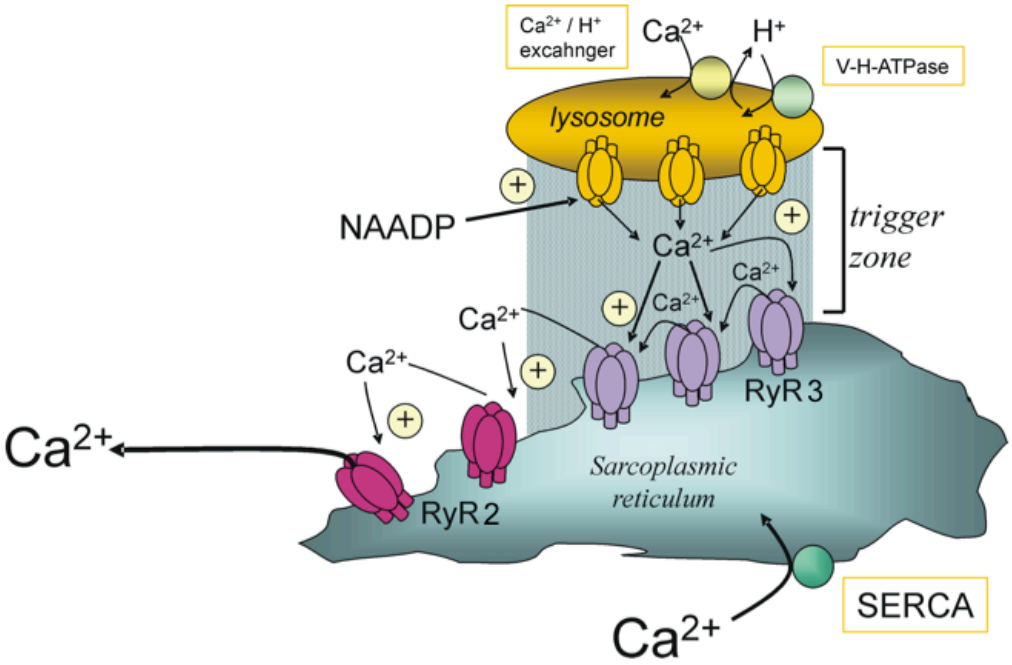

Fig. 3.15. Schematic representation of the trigger zone for Ca^{2+} signalling by NAADP in pulmonary arterial smooth muscle cells

The trigger zone comprises lysosomes closely opposed to RyR3 on the SR. NAADP evokes Ca^{2+} bursts from the lysosomes which are then amplified by Ca^{2+}-induced Ca^{2+} release (CICR) via RyR3. The propagating global Ca^{2+} wave is likely amplified beyond the lysosome-SR junctions by further CICR via RyR2.

Chapter 4: Two-pore channels are targeted to endosomes and lysosomes and mobilise Ca^{2+} in response to NAADP

4.1 Introduction

In Chapter 3 my studies developed from the original observation that lysosomes form junctional complexes with the sarcoplasmic reticulum (SR) in pulmonary arterial smooth muscle cells (PASMCs) to comprise a trigger zone for Ca^{2+} signalling by NAADP. I not only provided further support for the presence of lysosome-SR junctions but also confirmed that these junctions may be formed in a manner that confers selective regulation of a subpopulation of ryanodine receptors (RyR), namely RyR3. The identification of such junctional complexes supports the view that NAADP mobilises Ca^{2+} from a lysosome-related acidic organelle that is then amplified by Ca^{2+}-induced Ca^{2+} release (CICR) from the sarco / endoplasmic reticulum (S / ER) (Churchill *et al.*, 2002; Kinnear *et al.*, 2004; Yamasaki *et al.*, 2004; Zhang *et al.*, 2006b) and may, given that the initial phase of Ca^{2+} release can prove difficult to resolve, explain why others have concluded that NAADP directly activates RyRs (Dammermann *et al.*, 2005; Hohenegger *et al.*, 2002). It is becoming increasingly clear, therefore, that NAADP mobilises Ca^{2+} from lysosomes in an IP_3R- and RyR-independent manner via the activation of its own receptor.

4.1.1 Transient receptor potential mucolipin 1 and NAADP-dependent Ca^{2+} signalling

Recently it was proposed that the lysosome-bound transient receptor potential mucolipin 1 (TRPML1) functioned as the molecular target of NAADP (Zhang *et al.*, 2008). In this study using lipid bilayers, blockade of TRPML1 with anti-TRPML1 antibodies was shown to block NAADP-induced activation of lysosomal Ca^{2+} channels (Zhang *et al.*, 2008). However, others have shown that membranes derived from normal rat kidney (NRK) cells over-expressing TRPML1 exhibit no increase in

[^{32}P]NAADP binding, and that TRPML1 channel activity was not increased by the addition of NAADP in *Xenopus* oocytes expressing TRPML1 (Pryor *et al.*, 2006). Thus, there is significant evidence contrary to the view that TRPML1 is an NAADP-sensitive Ca^{2+} release channel and this point is emphasised by the finding that the antibody used by Zhang and co-workers to label / block TRPML1 has been shown to label elements within TRPML1 null cells suggesting that it is non-selective (Prof. Antony Galione, *personal correspondence*). That TRPML1 may not represent an NAADP-activated Ca^{2+} release channel, is also suggested by two independent studies that identify TRPML1 not as a Ca^{2+} permeable channel, but as either a Fe^{2+} (Dong *et al.*, 2008) or a H^{+} release channel in lysosome membranes (Soyombo *et al.*, 2006). Despite extensive investigations, therefore, the identity of the NAADP receptor remains elusive.

4.1.2 Two-pore channels

4.1.2.1 Identification of two-pore channels as novel members of the voltage-gated cation channel superfamily

In 2000 the two-pore channel subtype 1 (TPC1; gene name *TPCN1*) was first cloned and identified as a novel two-domain channel (Ishibashi *et al.*, 2000). The protein, deduced from screening the rat kidney cDNA library, was reported as being 819 amino acid residues with a calculated molecular weight of 94.6 kDa (Ishibashi *et al.*, 2000). Mammalian TPCs are comprised of 12 transmembrane (TM) α-helices containing 2 homologous domains of 6 TM α-helices (S1-S6) and a re-entrant P-loop incorporated between S5 and S6 of each domain (Fig. 4.1A). Their characteristic structure indicates that TPCs are new members of a family of proteins belonging to the superfamily of voltage-gated cation channels, which is composed of over 140 members that are related by both structural and functional motifs (Yu *et al.*, 2005). The P-loop is one of the important functional elements of this ion channel superfamily and is thought to sit within the pore and contribute towards ion conductance and ion selectivity (Yu *et al.*, 2005). As previously stated, the pore-forming subunits of voltage-gated sodium (Na_v) and calcium (Ca_v) channels have 4 domains whereas single-domain proteins such as TRP channels function as tetramers. Single-domain

proteins are therefore thought to have undergone two rounds of duplication in order to develop the necessary number of domains required to provide the pore region consistent with that conferred to Na_v and Ca_v channels. This led Ishibashi *et al*. to suggest that TPCs could be the intermediate product of the 2 rounds of duplication (Ishibashi *et al.*, 2000). Therefore, their structure would likely suggest that TPCs form dimers with each subunit contributing 2 P-loops. Thus upon the formation of a dimer, 4 P-loops come together to form a functional pore (Fig. 4.1A).

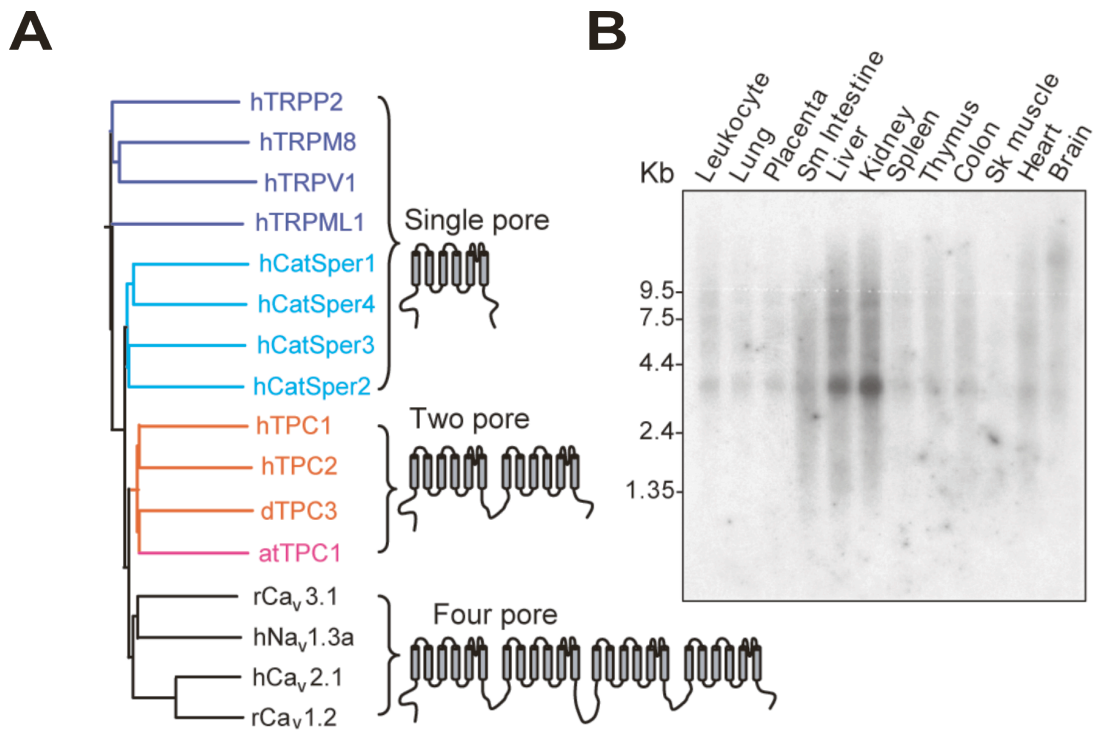

Fig. 4.1. Two-pore channels share structural similarity with single-pore and four-pore domain channels and exhibit a wide tissue distribution

A Comparison of the phylogenetic relationship between TPC subtypes and both single-pore and four-pore domain channels suggesting that TPCs may form an intermediate stage between the two rounds of duplication that separate these two gene families. Abbreviations used: at, *Arabidopsis thaliana*; Ca_V, voltage-gated Ca^{2+} channel; d, dog; h, human; Na_V, voltage-gated Na^+ channel; r, rat. **B** Northern blot analysis of TPC2 expression in human tissues showing that TPC2 exhibits a wide tissue distribution with abundant expression in liver and kidney in particular. This figure was kindly provided by Mike Zhu.

The structural similarity of TPC1 to Ca_v channels led Ishibashi *et al.* to postulate that TPC1 would be a membrane bound, voltage-gated cation channel (Ishibashi *et al.*, 2000). However, xenopus oocytes injected with TPC1 cRNA

showed no significant difference in membrane currents from the background currents recorded in control cells. Also, isotopic studies with the same cells failed to show any significant Na^+ or Ca^{2+} uptake from the extracellular media. Furthermore Chinese hamster ovary cells (CHOs) expressing TPC1 also failed to demonstrate membrane currents significantly above background (Ishibashi *et al.*, 2000). These data led the authors to suggest that TPCs may need additional proteins for either effective processing and delivery to the membrane, or for the formation of a functional pore. A further suggestion by Ishibashi *et* al. was that TPCs may require something other than voltage for appropriate gating of the pore. Lastly, the authors suggested that the cellular distribution of the TPC1 protein must be determined in order to establish whether or not TPC1 is targeted to membranes other than the plasma membrane (Ishibashi et al., 2000). This point is most pertinent to the question of the molecular identity of the NAADP receptor, as this would reasonably be expected to be present on the membranes of lysosome-related organelles.

Following the identification of TPC1 in the rat, plant TPC1 was first identified and cloned from *Arabidopsis* and was termed AtTPC1 (Furuichi *et al.*, 2001). The AtTPC1 protein is 733 amino acid residues in length with an estimated molecular weight of approximately 85 kDa and, similar to rat TPC1 has a predicted 12 TM structure divided into two domains of 6 TM regions each (Furuichi *et al.*, 2001). AtTPC1 expression rescued the Ca^{2+} uptake activity in the yeast mutant *cch*1 (Furuichi *et al.*, 2001) and also, sugar-induced luminescence, acting as an indicator for increased cytoplasmic Ca^{2+} in *Arabidopsis* leaves, was enhanced by over expression of AtTPC1 and was suppressed by expression of antisense AtTPC1 (Furuichi *et al.*, 2001). In 2005, Sanders and colleagues used a GFP-TPC1 fusion protein to show that AtTPC1 is expressed on membranes distinct from the plasma membrane, and is associated with the vacuolar membrane (Peiter *et al.*, 2005). Using TPC1 over-expressing cells they then determined that AtTPC1 has a role in the development of the cytoplasmic Ca^{2+}-dependent slow vacuolar channel current, which is responsible for Ca^{2+}-dependent Ca^{2+}-release from intracellular vacuoles of plant cells (Peiter *et al.*, 2005). Further confirmation of plant TPC1 functioning as a cation channel present on the vacuolar membrane was provided by Dietrich and colleagues, though the authors suggest that plant TPC1 is a vacuolar Ca^{2+}-gated Ca^{2+} release channel (Kawano *et al.*, 2004; Ranf *et al.*, 2008). That plant TPC1 may be activated in response to Ca^{2+} is not inconsistent with its structure, as a notable difference

between plant TPC1 and mammalian TPCs is the presence of EF-hands on plant TPC1 (Ranf *et al.*, 2008). The ability of EF-hands to bind Ca^{2+} would thus provide plant TPC1 with a degree of Ca^{2+}-sensitivity. Therefore, investigations using plant cell types have shown that plant TPC1 is involved in intracellular Ca^{2+} signalling and, of particular importance to the present study, that plant TPC1 is located on the membrane of vacuoles rather than the plasma membrane (Fig. 4.2) (Furuichi *et al.*, 2001; Kawano *et al.*, 2004; Peiter *et al.*, 2005; Ranf *et al.*, 2008).

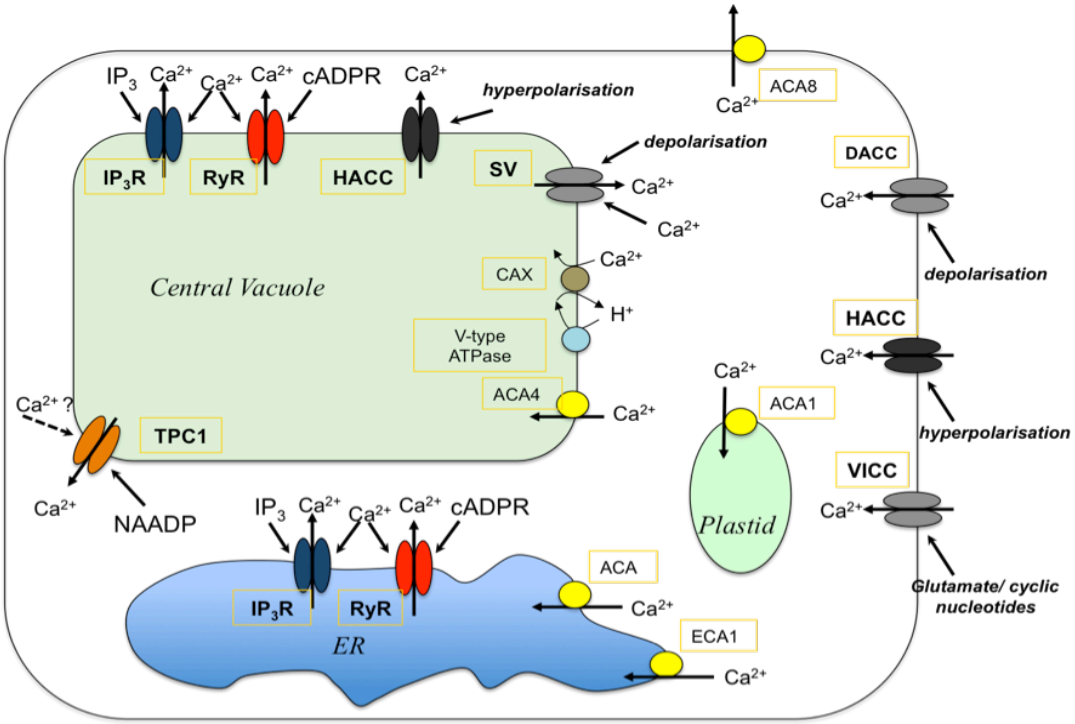

Fig. 4.2. Schematic representation of the major Ca^{2+} signalling pathways in an *Arabidopsis thaliana* cell

Depicted are some of the mechanisms by which Ca^{2+} is able cross the plasma membrane and some of the major Ca^{2+} storing organelles including the central vacuole, plastids and the ER. Ca^{2+} is sequestered into organelles or removed across the cell membrane by autoinhibited Ca^{2+} ATPases (Pacaud *et al.*). Ca^{2+} influx may occur via depolarisation-activated Ca^{2+} channels (DACC), hyperpolarisation-activated Ca^{2+} channels (HACC), and voltage-independent Ca^{2+} channels (VICC). The ER also sequesters Ca^{2+} via the ER-type Ca^{2+} ATPase (ECA) and may be mobilised via activation of RyRs and IP_3Rs. The large Ca^{2+}-storing central vacuole sequesters Ca^{2+} via ACA and the action of the Ca^{2+}/H^+ antiporter (CAX) coupled to a V-type ATPase. Ca^{2+} may be mobilised from the vacuole via the activation of IP_3Rs, RyRs, HACCs, the slow-activating vacuolar channel (SV) and the plant two-pore channel (TPC1).

4.1.2.2 Two-pore channels are expressed in a broad range of species and exhibit an extensive mammalian tissue distribution

3 subtypes of TPC have been identified in the animal kingdom (TPC1, TPC2 and TPC3) and one subtype in plants (plant TPC1; also known as AtTPC1). However, it is important to note that plant TPC1 shows low sequence homology to either animal TPC1, TPC2 or TPC3, and is considered to be a plant counterpart to all animal TPCs and not exclusively comparable to animal TPC1. That plant TPC1 is distantly related to all 3 animal subtypes is exemplified by comparison of the conserved TM regions with ≤ 30 % amino acid sequence homology shared with the 3 animal TPC subtypes, which are also equally distant from each other. Fig. 4.3 shows the phylogenetic tree generated from all known TPC sequences. This shows that all 3 TPCs are present in sea urchins and most vertebrates. However, TPC3 appears to be absent in primates and some rodents (e.g. mice and rats; Fig. 4.3). Such a broad species distribution including both animal and plant kingdoms suggests that the genes encoding these proteins are from a common / ancient gene family, further supporting the notion that TPCs present an intermediate between the 6-TM structured channels such as TRPs and the 4-repeat, 24-TM pore forming subunits of, for example, Na_v and Ca_v. Not only do TPCs exhibit a broad species distribution but they also appear to have an extensive tissue distribution. Analysis of TPC2 tissue expression by Northern blot shows that TPC2 mRNA is present in most human tissues, including the cardiovascular system, with a particularly high level of expression in the liver and kidney (Fig. 4.1B), very similar to the tissue distribution of TPC1 in rat (Ishibashi *et al.*, 2000). The broad range of tissue expression observed with TPC1 and TPC2 in mammals suggests a potentially important role for TPCs in cell function within the animal kingdom.

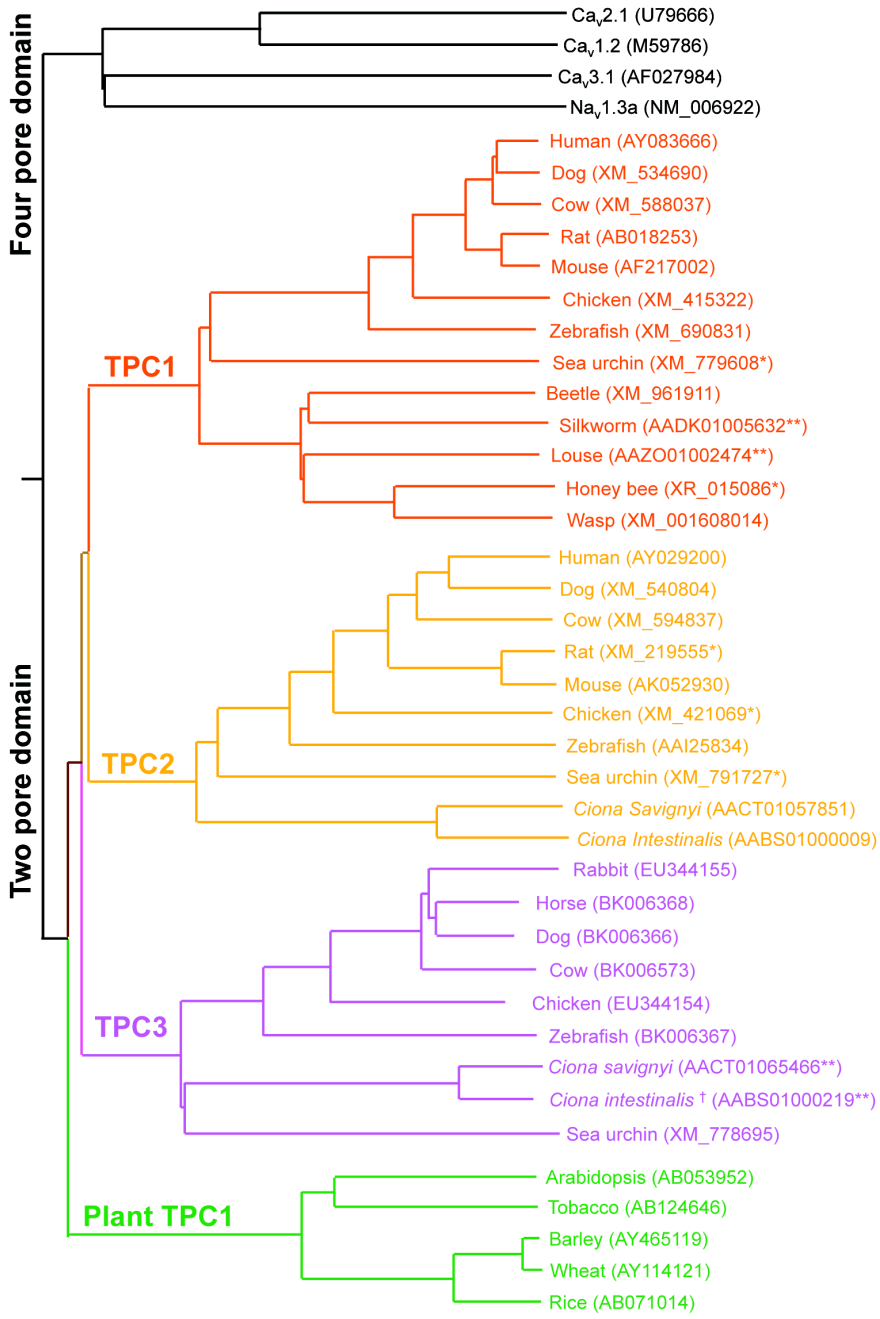

Fig. 4.3. Comparison of TPCs from multiple species

Comparison of the phylogenetic relationship between known TPC sequences plotted and aligned by my collaborator Dr. Mike Zhu using ClusterW (http://align.genome.jp) and plotted using a Neighbour-Joining algorithm. Representative sequences for the third and fourth TM domains of the pore-forming subunits of family members of Ca_V and Na_V channels are also included for comparison. GenBank accession numbers are shown in parentheses. * Indicates that corrections were made to these sequences based on multi-sequence alignments and splice donor and acceptor sites in genomic sequences. ** Indicates that sequence was assembled from genomic sequences. † Indicates that this sequence was previously designated as Ci-TPC1 (Okamura *et al.*, 2005).

4.1.3 Are two-pore channels candidates for the NAADP receptor?

Despite the lack of functional data available for TPCs, a number of characteristics exhibited by these channels lend them to further investigation as putative NAADP receptors. For example, the similarity of these channels to VGCCs is consistent with previous reports that NAADP-mediated Ca^{2+} release is inhibited by both L-type Ca^{2+} channel agonists and antagonists (both phenylalkylamines and dihydropyridines) (Genazzani *et al.*, 1996a; Genazzani *et al.*, 1997). In addition to its structure, the reported size of human TPC1 and plant TPC1 of 94.6 and 85 kDa, respectively, are both similar to the reported size (150 kDa) of NAADP binding sites isolated by protein purification studies from sea urchin egg homogenate (Berridge et al., 2002). There is indirect evidence, therefore, that TPCs may be the molecular target of NAADP. Furthermore, animal TPCs are present in many of the species from which cells have been shown to exhibit NAADP-dependent Ca^{2+} signals, including sea urchin, rat, mouse, rabbit, dog, cow and human (Bak *et al.*, 2001; Cancela *et al.*, 1999; Chini *et al.*, 1995a; Lee *et al.*, 1995; Mojzisova *et al.*, 2001; Zhang *et al.*, 2006b). Moreover, the ubiquitous tissue expression of mammalian TPCs is consistent with the finding that NAADP has been shown to mediate Ca^{2+} signalling in a wide variety of tissues including heart, brain, endocrine, exocrine, and smooth muscle (Bak *et al.*, 2001; Bak *et al.*, 1999; Boittin *et al.*, 2002; Cancela *et al.*, 1999; Chini *et al.*, 2002; Mitchell *et al.*, 2003). This further emphasises the fact that TPCs may play an important role in Ca^{2+} homeostasis in animal cells and, of particular importance, may function as the NAADP receptor. The vacuolar location of plant TPC1 is also consistent with the proposal that TPCs may be involved in NAADP-mediated Ca^{2+} release from lysosome-related organellar stores. In this chapter I therefore sought to determine whether or not TPCs function as NAADP receptors.

4.2 Methods

The experiments included in this chapter use HEK293 cells stably over-expressing human TPC1 (hTPC1), human TPC2 (hTPC2) or chicken TPC3 (cTPC3) which were generated for me by my collaborator Mike Zhu by incorporating the

cDNA into the following vectors: TPC1 cDNA was placed in a pIREShyg2 vector (BD Biosciences); TPC2 cDNA was placed in a pIRESneo vector (BD Biosciences); and TPC3 cDNA was placed in a pEGFPC3 (BD Biosciences). HEK293 cells were transfected with the vectors using Lipofectamine 2000 (Invitrogen) following the manufacturer's protocol. In order to allow for studies on the cellular location of TPCs the cDNA of each subtype was attached with an tag such that the cDNA for *TPC1* was attached to a His_6-tag (C terminus), *TPC2* with an HA epitope or mCherry-tag (N terminus) and *TPC3* with a GFP-tag (N-terminus). Tissue culture and maintenance of the created cell lines was carried out as described above (Chapter 2).

4.2.1 shRNA-mediated knockdown of two-pore channel subtype 2 in HEK293 cells

In order to verify that the NAADP-mediated Ca^{2+} transient observed in HA-hTPC2 cells was due to the over-expression of hTPC2, sequence-specific short hairpin RNA (shRNA) was used in order to knockdown / knockout hTPC2 protein expression. 4 plasmids encoding anti-hTPC2 shRNA and an mRFP reporter were designed and prepared by my collaborators, Professor Jianjie Ma and Dr. Zui Pan.

RNA interference (RNAi) is a form of gene regulation that occurs post-transcriptionally. It was first observed in 1998 when double stranded RNA (dsRNA) selectively abolished the twitching phenotype of *Caenorhabditis elegans* when injected directly into the body (Fire *et al.*, 1998). This led the way for investigations involving the silencing of functional genes by exogenous application of dsRNA. RNAi can be achieved by incorporating DNA encoding shRNA into an expression vector. When this sequence is expressed, the resultant RNA consists of a sense and anti-sense strand which, due to its own complementarity, associates with itself by forming a hairpin structure that is able to interact with both the target mRNA and the cell machinery capable of mediating RNAi.

The 4 shRNA probes used in these experiments were targeted to specific sequences of hTPC2 (Fig. 4.4, Table 4.1) and were annealed to the *Bam*H1 and *Eco*RI restriction sites of the pSIREN-DNR plasmid (Clontech, CA, USA). Each probe contained a sequence encoding a mRFP reporter protein. The presence of the mRFP reporter allowed for the visual determination of successful shRNA transfection. To maximise the success of shRNA mediated knockdown/knockout of hTPC2, the 4 probes were mixed in equal proportions and treated as a single solution for subsequent

experiments. It is important to note that the process of transfection of a plasmid into the cells could adversely affect protein expression/synthesis in cells. Thus, in order to discern whether the knockdown of hTPC2 was due to the shRNA rather than the transfection process, a control plasmid containing scrambled shRNA was also used in parallel to the test plasmids (Table 4.1). The effect of shRNA-mediated knockout / knockdown of hTPC2 expression in HA-hTPC2 cells was characterised using Ca^{2+} imaging. However, the ability of shRNA against hTPC2 to reduce hTPC2 expression was first verified using both Western blot and immunocytochemical labelling of intracellular proteins. When verifying the shRNA by Western blot, the level of β-actin in each sample was used as a further control. If the transfection process does not adversely affect protein expression / synthesis one would expect, therefore, the level of β-actin in shRNA-transfected cells to be similar to non-transfected cells.

```
MAEPQAESEP  LLGGARGGGG  DWPAGLTTYR  SIQVGPGAAA  RWDLCIDQAV  VFIEDAIQYR   60
SINHRVDASS  MWLYRRYYSN  VCQRTLSFTI  FLILFLAFIE  TPSSLTSTAD  VRYRAAPWEP  120
PCGLTESVEV  LCLLVFAADL  SVKGYLFGWA  HFQKNLWLLG  YLVVLVVSLV  DWTVSLSLVC  180
HEPLRIRRLL  RPFFLLQNSS  MMKKTLKCIR  WSLPEMASVG  LLLAIHLCLF  TMFGMLLFAG  240
GKQDDGQDRE  RLTYFQNLPE  SLTSLLVLLT  TANNPDVMIP  AYSKNRAYAI  FFIVFTVIGS  300
LFLMNLLTAI  IYSQFRGYLM  KSLQTSLFRR  RLGTRAAFEV  LSSMVGEGGA  FPQAVGVKPQ  360
NLLQVLQKVQ  LDSSHKQAMM  EKVRSYGSVL  LSAEEFQKLF  NELDRSVVKE  HPPRPEYQSP  420
FLQSAQFLFG  HYYFDYLGNL  IALANLVSIC  VFLVLDADVL  PAERDDFILG  ILNCVFIVYY  480
LLEMLLKVFA  LGLRGYLSYP  SNVFDGLLTV  VLLVLEISTL  AVYRLPHPGW  RPEMVGLLSL  540
WDMTRMLNML  IVFRFLRIIP  SMKPMAVVAS  TVLGLVQNMR  AFGGILVVVY  YVFAIIGINL  600
FRGVIVALPG  NSSLAPANGS  APCGSFEQLE  YWANNFDDFA  AALVTLWNLM  VVNNWQVFLD  660
AYRRYSGPWS  KIYFVLWWLV  SSVIWVNLFL  ALILENFLHK  WDPRSHLQPL  AGTPEATYQM  720
TVELLFRDIL  EEPEEDELTE  RLSQHPHLWL  CR                               752
```

Fig. 4.4. Amino acid sequence for human two-pore channel subtype 2

The amino acid sequence of human TPC2 (hTPC2). The predicted transmembrane and P-loop regions are highlighted in yellow and cyan respectively. The 4 amino acid sequences corresponding to the mRNA sequences against which the 4 shRNA probes are targeted, are indicated by red italics.

Name of Probe	Nucleotide number	Nucleotide sequence
Si-hTPC2 A	216-238	GCTTTACCGACGGTATTACTCGA
Si-hTPC2 B	585-608	GCTGCAGAACTCCTCTATGATGAA
Si-hTPC2 C	923-945	GCAGCCATCATCTACAGTCAGTTC
Si-hTPC2 D	1556-1578	GCTCTGGCTGTGTACCGATTGCCA
Control		GATCCGTGCGCTGCTGGTGCCA-ACTTCAAGAGATTTTTTGCTAGCG

Table 4.1. Name and nucleotide sequence of the shRNA probes used in studies involving RNA interference.

4.2.1.1 shRNA transfection of HEK293 cells

Cells were prepared 24 hours prior to shRNA transfection. For Ca^{2+} imaging experiments and verification by Western blot, transfection was carried out in FluoroDishes and 60 mm sterile petri dishes respectively. These were prepared beforehand as described above. For verification by fluorescent labelling, shRNA transfection was carried out using cells seeded onto poly-D-lysine coated coverslips placed within sterile 30 mm tissue culture dishes as described in Chapter 2.

HA-hTPC2 cells were transfected with the shRNA plasmids using the transfection agent GeneJammer (Stratagene, Ailent Technologies, CA, USA). The quantities of reagents used varied according to the number of dishes that were to be transfected. Therefore the following method describes the transfection of 1 dish of HA-hTPC2 cells and was scaled up as appropriate: 94 μl of sterile, serum-free, antibiotic-free D-MEM (Opti-MEM; at room temperature) was transferred to a polystyrene tube. 6 μl of GeneJammer transfection reagent was pipetted directly into the serum-free media and the solution was gently mixed with the pipette tip before being incubated for 5 minutes at room temperature (22°C). 2 μl of the shRNA plasmid solution (1 μg/μl) was then added to the solution and mixed gently with the pipette tip. This solution was then incubated for 30 minutes at room temperature.

GeneJammer is a polyamine based transfection reagent that is positively charged. Due to their polarity, polyamines are able to bind effectively to nucleic acids, which are negatively charged, in solution. Upon binding to the shRNA plasmid

in solution, particles are formed in which the plasmid is surrounded by the positively charged polyamine molecules. This then allows the plasmid/polyamine particle to interact with the negatively charged plasma membrane of the cell. Following this interaction it is thought that the plasmid / polyamine particles are internalized by the cell via endocytosis (Kanatani *et al.*, 2006; Orth *et al.*, 2008).

A previously prepared dish containing HA-hTPC2 cells was taken and the growth media was removed and replaced with 900 μl of fresh growth media. Following the incubation of the GeneJammer transfection reagent with the shRNA plasmid, 100 μl of this transfection mixture was added drop-wise and the dish was gently mixed. The dish was incubated for 8 hours at 37°C, 5% CO_2. A further 1 ml of fresh growth media was then added and the dish was returned to the incubator whereby it was incubated for a further 3-4 days.

4.2.2 Determination of shRNA-mediated knockdown of two-pore channel subtype 2 in HEK293 cells by use of Western blot

4.2.2.1 Lysis of cells and preparation of protein samples

HA-hTPC2 cells were prepared and transfected with shRNA prior to lysis, as described above. The media was removed and each dish was washed twice with fresh sterile PBS (2 ml). The cells were lysed using Radio Immunoprecipitation Assay (RIPA) buffer of the following composition: 150 mM NaCl, 20 mM Na_3PO_4, 50 mM NaF, 2 mM EDTA, 0.1% SDS, 1% Na deoxycholate, 1% Triton X-100, 1:100 dilution Protease Inhibitor Cocktail (Sigma P8340), pH 7.2. 100 μl of fresh RIPA buffer was added to each dish and the cells were incubated for 30 minutes at 4 °C. The cells were thoroughly scraped and collected at one area at the base of the dish. The solution was collected and aliquoted into sterile 0.5 ml ependorf tubes and then centrifuged at 14,000 r.p.m. for 15 minutes at 4 °C. The supernatant was collected, the protein concentration determined and the remaining samples were stored at -80 °C until required.

4.2.2.2 Determination of protein concentration by Bradford assay

The Bradford assay was first described in 1976 (Bradford, 1976) and is established as a quick and inexpensive assay for determining protein concentrations. The assay utilises the characteristic of Coomassie Brilliant Blue G-250 whereby the absorbance maximum shifts from 470 nm to 595 nm upon binding to protein. This is achieved by interactions with amino acid residues of the protein that serve to stabilize the anionic form of the dye. The anionic form has an absorbance maximum of 595 nm whereas the unbound cationic form of the dye has an absorbance maximum of 470 nm. The assay is then read in a spectrophotometer at a wavelength of 595 nm which indicates the level of bound dye within the solution. By comparing the protein samples of unknown concentration with known standards, the concentration of the samples can be determined.

A

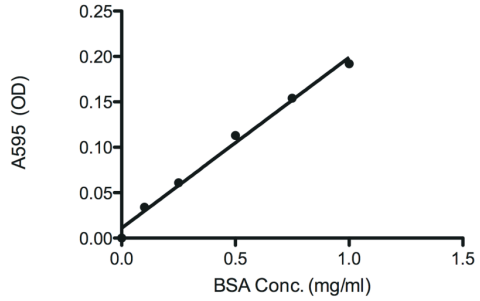

B

BSA conc. (mg/ml)	A_{595} (OD)	Sample Protein conc. (mg/ml)
0.00	0.000	
0.10	0.034	
0.25	0.061	
0.50	0.113	
0.75	0.154	
1.00	0.192	
	0.082	***0.378***
	0.100	***0.474***

Fig. 4.5. Example BSA standard curve used for interpolating the protein concentration of 2 unknown samples

A Example of the standard curve generated by plotting the absorbance at 595 nm against the protein concentration of the BSA standards. Standard curve was generated using linear regression. **B** Corresponding table of the values for the absorbance (595 nm) for the BSA protein standards. The values obtained for the samples were interpolated using the standard curve to estimate the protein concentration of each sample (bold italics).

The protein standards were prepared in dd.H_2O from a stock of BSA 1.45 mg/ml and consisted of the following concentrations (mg protein/ml): 0, 0.1, 0.25, 0.5, 0.75, 1, and 1.45. Appropriate volumes (10 μl) of each protein sample and standard was added to separate plastic cuvettes. 2 ml of Bradford reagent (Coomassie brilliant blue G-250, 95 % ethanol and

85 % orthophosphoric acid) was added to each cuvette and the solution was mixed and the cuvettes were incubated at room temperature for 10 minutes. Each cuvette was then placed into the spectrophotometer (CE 393 Digital Grating Spectrophotometer, Cecil Instruments Ltd., UK) and the absorption at 595 nm was measured. The readings from the protein standards were used to generate a standard curve of protein concentrations (Fig. 4.5), from which the concentration of the samples was determined using the interpolation function of the Prism analysis software (GraphPad Software Inc., USA).

4.2.2.3 SDS-polyacrylamide gel electrophoresis

Sodium dodecyl sulphate (SDS) polyacrylamide gel electrophoresis (SDS-PAGE) is a process whereby proteins migrate towards an anode at various velocities through a polacrylamide gel in response to an applied electric field. Importantly with SDS-PAGE, proteins have varying migratory velocities due to different molecular weight. Polyacrylamide gels consist of a porous matrix that provides resistance to protein migration depending upon their size, such that low molecular weight proteins can migrate at a faster rate. SDS is an anionic detergent which denatures the proteins and binds to them and therefore, the overall charge of the protein becomes highly negative. The denatured protein is no longer able to maintain its secondary / tertiary structure and so is reduced to a negatively charged 'rod' shape or random coil configuration. SDS binds to peptides with a constant weight ratio and so the charge is uniform along its length. Therefore the intrinsic charge of the peptide is insignificant to the overall charge inferred by the SDS-peptide complex and thus charge is proportional to the molecular weight of the protein.

For the experiments covered in this thesis, a discontinuous gel electrophoresis system was used. This system uses two gels: a stacking gel (pH 6.8) and a resolving gel (pH 8.8). The stacking gel contains much larger, non-restrictive pores than the resolving gel, which results in the protein samples becoming concentrated at the stacking/resolving gel interface leading to a greater resolution. The resolving gel is made first with the stacking gel formed on top of the resolving gel once the latter has set. The gels are made by co-polymerisation of acrylamide and bis-acrylamide. This polymerisation relies upon the generation of free radicals and is initiated by the addition of TEMED to the reaction mixture. TEMED is a tertiary amine base which

is added in order to catalyze the formation of free radicals from ammonium persulfate (APS). These free radicals add an unpaired electron to an acrylamide monomer effectively creating an acrylamide free radical. This activated monomer is then able to react with a non-activated monomer and thus initiate the polymerisation reaction. The polymers can be cross-linked by units of bis-acrylamide which forms a gel-like mesh with the characteristic pores. Proteins were resolved using a 10 % gel (10 % acrylamide, 0.375 M Tris, 0.1 % w/v SDS, 0.05 % w/v APS and 0.05 % TEMED) which was poured into Novex gel cassettes (Invitrogen, UK). dd.H_2O was carefully poured on top and the gel allowed to set for 30-40 minutes. Once the polymerisation reaction was completed the overlaid H_2O was discarded and any unpolymerised gel was removed by washing with fresh dd.H_2O. The stacking gel (4.2 % acrylamide, 0.375 M Tris, 0.1 % w/v SDS, 0.05 % w/v APS and 0.05 % TEMED) was then poured on top of the resolving gel and a 10-well comb was inserted to create the wells within the stacking gel. The gel was then allowed to set for 30 minutes.

The protein samples were mixed with Laemmli buffer containing SDS, β-mercaptoethanol, glycerol and bromophenol blue. The β-mercaptoethanol reduces the disulfide bonds within the protein, which is then further reduced by the SDS as described previously. The glycerol increases the sample density so that it will layer in the wells, and bromophenol blue is a dye that will allow the migration of the sample to be tracked visually. The cassette was then placed and run in an XCell *surelock* Mini-Cell system (Invitrogen, UK). 5 μl of Precision Plus Protein standards (Bio-Rad, UK) were loaded into a free well. The gels were run for 30 minutes at 50 V and then at 125 V for approximately 2 hours.

4.2.2.4 Immunoblotting

In order to detect and visualise protein bands, they must first be transferred onto a nitrocellulose membrane. Once the protein bands had migrated sufficiently, the SDS-PAGE gels were removed from the cassettes and placed into transfer buffer (42.9 mM Tris, 38.9 glycine, 0.038 % w/v SDS, 20 % methanol. Grade 1F electrode filter paper and Hybond ECL nitrocellulose membranes were cut so that they would match the shape of the gel and then pre-soaked in transfer buffer along with blotting pads. A piece of filter paper was placed on the bottom of the transfer stack on top of

which the gel was placed. The pre-soaked nitrocellulose membrane was placed on top of the gel followed by a further piece of filter paper. The stack was then placed in an XCell II blot module Mini Cell system (Invitrogen, UK), with 2 pre-soaked blotting pads placed on each side of the stack. The module was orientated such that the gel faced the cathode whereas the nitrocellulose membrane faced the anode. As a result the proteins would move towards the anode and subsequently transfer to the membrane. The gels were blotted for 1.5 hours at 25 V.

4.2.2.5 Immunodetection (by ECL)

After the immunoblotting was complete the membranes were carefully removed from the stack and placed in blocking buffer (20 mM Tris base, 150 mM NaCl, 0.1 % Tween 20, 5 % non-fat milk powder, pH 7.5) for 1 hour at room temperature. This is to ensure that any regions of the membrane that have not bound sample protein are 'blocked' by binding constituents of the blocking buffer. This prevents non-specific binding of the antibody to the membrane. The membranes were then washed with TBST (20 mM Tris base, 150 mM NaCl, 0.1 % Tween 20, pH 7.5) 3 x 10 minutes. The primary anti-HA or anti-βactin antibody was diluted (1:1000) in 1 % blocking buffer (20 mM Tris base, 150 mM NaCl, 0.1 % Tween 20, 1 % non-fat powder milk, pH 7.5). The membrane was then incubated with the primary antibody solution overnight at 4°C. The following day the membrane was washed 3 x 10 minutes with TBST in order to remove any unbound primary antibody. The secondary horseradish peroxidase (HRP)-conjugated anti-rat or anti-mouse antibodies (when anti-HA and anti-βactin primary antibodies were used respectively) were diluted to 1:1000 in 1 % blocking buffer. The membrane was then incubated with the secondary antibody solution for 2 hours at room temperature. Following this incubation period, the membrane was washed 3 x 10 minutes with TBST. The binding of the primary antibody and subsequent location of the protein of interest was detected using a chemiluminescence detection system which utilises an HRP substrate, luminol. This substrate is oxidised by HRP and when the excited electron returns to its normal energy state a photon of light is emitted (maximum wavelength 428 nm). These photons can be detected upon exposure to ECL Hyperfilm (Amersham, UK). The regions of primary antibody binding will have a high concentration of HRP present

and therefore the light emitted from this area will be significantly enhanced. The membrane was incubated with a 1:1 mixture of ECL Western blotting detection Reagents 1 and 2 (Amersham Bioscience, UK) for 1 minute at room temperature. The Reagent mixture was removed and the membrane was placed in an exposure cassette. A sheet of ECL Hyperfilm (Amersham, UK) was placed on top of the membrane in a dark room, the cassette was closed and the film exposed for 30-120 seconds. The film was then developed using RG fixer and developer (Photon Imaging Systems Ltd., UK).

4.2.3 Flash photolysis of caged NAADP

In order to confirm the biphasic pattern of NAADP-evoked Ca^{2+} release in HEK293 cells stably over-expressing HA-hTPC2 flash photolysis experiments were carried out by Dr. Abdelilah Arredouani (University of Oxford). Briefly, HA-hTPC2 cells, seeded onto poly-D-lysine coated FluoroDishes, were bathed in a bath solution of the following composition: 130 mM NaCl, 5.2 mM KCl, 1 mM $MgCl_2$, 10 mM glucose, and 10 mM HEPES (pH 7.4). The pipette solution contained the following: 140 mM KCl, 1 mM $MgCl_2$, 10 mM HEPES and 0.1 mM Fluo3 pentapotassium (pH 7.2). 10 μM caged-NAADP was then added to the pipette solution. For the experiments requiring IP_3R antagonism, heparin (200 μg/ml) was added to the pipette solution. Cells were held at -40 mV in the whole-cell configuration of the patch-clamp technique. The caged-NAADP was photolysed using several ultraviolet flashes (each 10 ms in duration) generated using a XF-10 arc lamp (HI-TECH Scientific). The resultant change in the intracellular Ca^{2+} concentration was reported using Fluo3 fluorescence (excitation 490 nm, emission 530 nm) monitored by a photomultiplier tube.

4.3 Results

4.3.1 Two-pore channels are targeted to endosomes and lysosomes

4.3.1.1 Two-pore channel subtype 2 is specifically targeted to lysosomes

As NAADP is known to mobilise Ca^{2+} from acidic lysosome-related organelles (Churchill *et al.*, 2002; Kinnear *et al.*, 2004; Yamasaki *et al.*, 2004; Zhang *et al.*, 2004), one would expect a putative NAADP receptor to be targeted, possibly exclusively, to the membranes of these acidic organelles. In collaboration with Dr. Mike Zhu I therefore examined the intracellular localisation of TPCs and their co-localisation with various organellar markers.

Fig 4.6A shows a 3D reconstruction of a series of deconvolved Z-sections (focal depth 0.28 μm, Z step 0.2 μm) taken through a HEK293 cell stably expressing mCherry-tagged (excitation 587 nm, emission 610 nm) hTPC2 which had been pre-incubated (40 minutes) with LysoTracker Green (200 nM; excitation 504 nm, emission 511 nm). Panel A*a* shows a transmitted light image of the cell under study, with subsequent panels showing the distribution of (*b*) mCherry fluorescence labelling (red), (*c*) LysoTracker Green fluorescent labelling (green), (*d*) a merged image of (*b*) and (*c*). Panel (*e*) reveals the areas of co-localisation (yellow) between mCherry and LysoTracker Green labelling. Visual inspection of these images alone strongly suggests that TPC2 is targeted to the membranes of acidic organelles. Further analysis added weight to this viewpoint, as the density of co-localisation between mCherry-TPC2 and LysoTracker Green was 0.0033 ± 0.0012 μm^3 per μm^3 (n = 6; Fig. 4.7A; Appendix 2, Table 4.2) and accounted for 26 ± 5 % and 24 ± 6 % of the total volume of mCherry and LysoTracker Green labelling, respectively. Furthermore, the Pearson product-moment correlation coefficient value for mCherry-hTPC2 and LysoTracker Green labelling was 0.30 ± 0.06 (n = 6; Fig. 4.7B; Appendix 2, Table 4.2). This illustrates that there is a strong linear correlation between mCherry-hTPC2 and LysoTracker Green staining and suggests that TPC2 is targeted to acidic organelles.

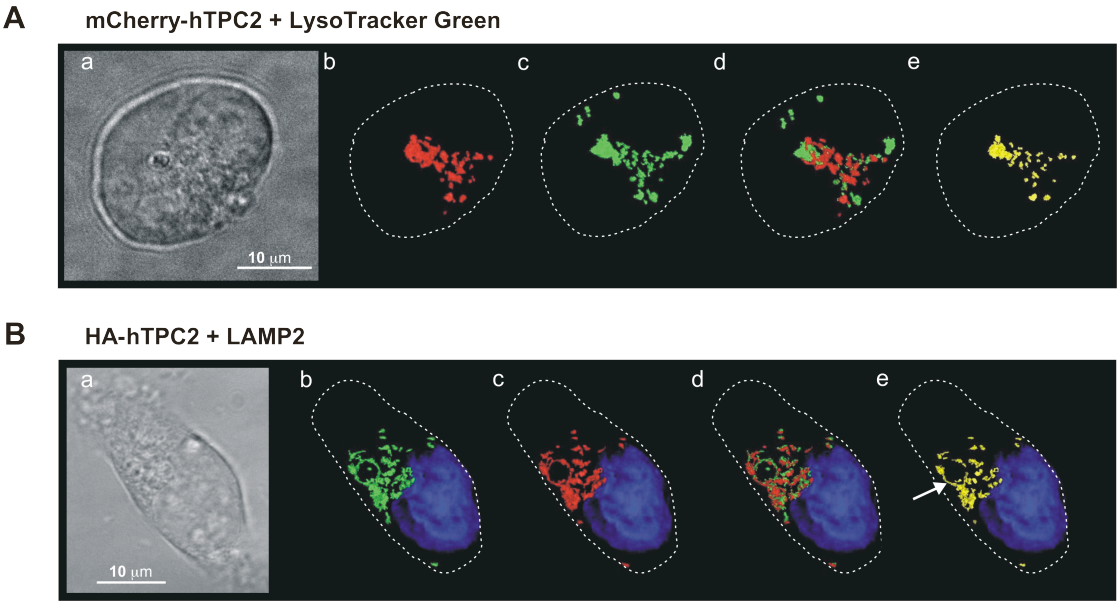

Fig. 4.6. TPC2 is targeted to lysosomes in HA-TPC2 and mCherry-TPC2 cells.

A Example cell showing the co-localisation between mCherry labelled hTPC2 (red; excitation 587 nm, emission 610 nm) and lysosomes labelled with LysoTracker Green (green; excitation 504 nm, emission 511 nm). Panel *a* shows a transmitted light image of the isolated mCherry-hTPC2 cell imaged; Panel *b* shows a 3D reconstruction of a series of deconvolved Z-sections taken through the cell shown in panel *a* showing the distribution of mCherry-tagged (red) hTPC2 in relation to the plasma membrane (dotted line); Panel *c* shows a 3D reconstruction of deconvolved Z-sections showing the distribution of LysoTracker Green labelling (green) in relation to the plasma membrane as indicated in panel *b*; Panel *d* shows a 3D representation of mCherry-hTPC2 and LysoTracker Green labelling (red and green respectively); Panel *e* is a 3D reconstruction showing individual elements of co-localisation between hTPC2 and LysoTracker Green. **B** Example cell showing the co-localisation between FITC labelled hTPC2 (green; excitation 490 nm, emission 528 nm) and LAMP2 labelling (red; excitation 555 nm, emission 617 nm). Panel *a* shows a transmitted light image of the isolated HA-hTPC2 cell imaged; Panel *b* shows a 3D reconstruction of a series of deconvolved Z-sections taken through the cell shown in panel *a* showing the distribution of HA-tagged hTPC2 (green) in relation to the nucleus (dark blue) plasma membrane (dotted line); Panel *c* shows a 3D reconstruction of deconvolved Z-sections showing the distribution of LAMP2 labelling (red) in relation to the nucleus and plasma membrane as indicated in panel *b*; Panel *d* shows a 3D representation of HA-hTPC2 and LAMP2 labelling (green and red respectively); Panel *e* is a 3D reconstruction showing individual volumes of co-localisation between hTPC2 and LAMP2 labelled lysosomes. Both elements appear to co-localise around a large vesicular structure highlighted in Panel *e* by the white arrow.

This apparent targeting of TPC2 to acidic organelles is entirely consistent with the proposed location of the NAADP receptors, and such specific targeting was confirmed by studies on the co-localisation of TPC2 with labelling for lysosomes

using antibodies specific for lysosome-associated membrane protein 2 (LAMP2). Fig. 4.6B shows a 3D reconstruction of a series of deconvolved Z-sections (focal depth 0.28 μm, Z step 0.2 μm) taken through a HEK293 cell stably expressing HA-hTPC2 that had been labelled for HA and LAMP2. Panel B*a* shows a transmitted light image of the cell under study and (*b*) shows the distribution of labelling for HA-hTPC2 (green) relative to the DAPI labelled nucleus (blue) whereas (*c*) shows the distribution of LAMP2 labelling (red). Panel (*d*) shows the merged image of (*b*) and (*c*), and (*e*) shows the areas of the cell in which HA-hTPC2 and LAMP2 labelling co-localised (yellow). From visual consideration of these images it is clear that TPC2 co-localises with LAMP2-labelled lysosomes and provides support for the view that TPC2 is targeted to acidic organelles. This is further highlighted by the clear co-localisation between LAMP2 and TPC2 around a large vesicular structure as shown in Fig. 4.6B*e* (highlighted by the white arrow). Moreover, consideration of LAMP2 labelling with respect to the DAPI-labelled nucleus shows that, similar to PASMCs (Chapter 3), lysosomes appear to cluster in the perinuclear region of HEK293 cells. Across the whole cell the density of co-localisation between HA-hTPC2 and LAMP2 labelling was 0.0068 ± 0.0008 μm^3 per μm^3 (n = 7; Fig. 4.7A; Appendix 2, Table 4.4) which was significantly greater when compared to the co-localisation between LysoTracker Green and mCherry-hTPC2 (0.0033 ± 0.0012 μm^3 per μm^3, n = 6; P<0.05). Furthermore the volume of HA-hTPC2/LAMP2 co-localisation represented 51 ± 2 % and 63 ± 4 % of the total volume of HA-hTPC2 and LAMP2 labelling, respectively. This greater degree of co-localisation was also reflected in the Pearson product-moment correlation coefficient value which measured 0.64 ± 0.01 (n = 7; Fig. 4.7B; Appendix 2, Table 4.4) which was also greater than observed for mCherry-hTPC2 and LysoTracker Green labelling (0.30 ± 0.06, n = 6; P<0.05).

These data highlight the important distinction between the two methods of lysosomal labelling. LysoTracker consists of a fluorophore attached to a weak base that accumulates in the lumen of acidic organelles. Conversely, LAMP2 is a membrane-bound protein present on the lysosomal membrane. Therefore, an ion channel targeted to lysosomal membranes would be expected to exhibit greater overlapping distribution with LAMP2 than with LysoTracker Green.

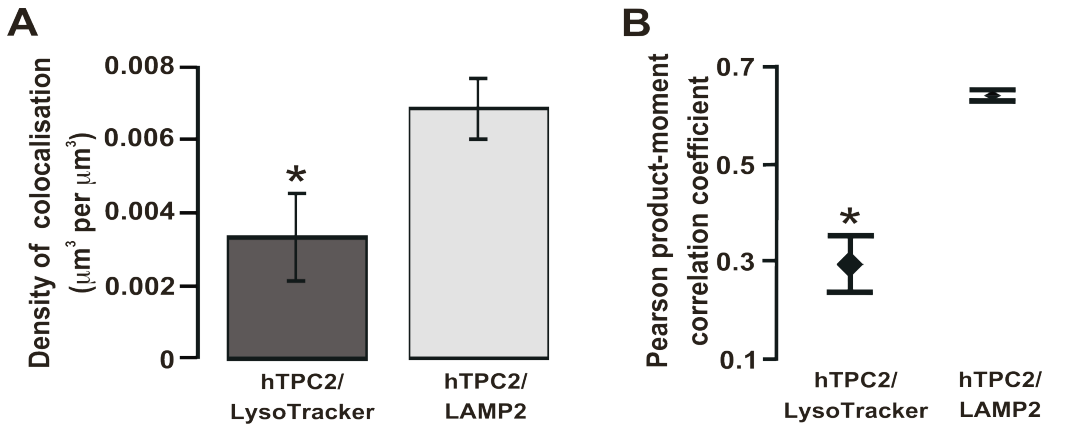

Fig. 4.7. TPC2 co-localisation is greater with lysosomes labelled with LAMP2 than with LysoTracker Green

A Bar chart showing the density of co-localisation (μm^3 per μm^3; mean ± S.E.M.) between hTPC2 and either LysoTracker or LAMP2 labelling. **B** The Pearson product-moment correlation coefficient for TPC2 and either LysoTracker labelled- or LAMP2-labelled lysosomes, indicating linear dependence (mean ± S.E.M.). * indicates a statistically significant difference ($P<0.05$) when compared to the hTPC2/LAMP2 co-localisation density or Pearson correlation coefficient (LysoTracker $n = 6$; LAMP2 $n = 7$).

The apparent targeting of TPC2 to acidic organelles is entirely consistent with the proposed location of the NAADP receptors, and such specific targeting was confirmed by higher resolution confocal imaging studies (in collaboration with Dr. Mike Zhu, see Calcraft *et al.,* 2009 for methods) on the co-localisation of TPC2 with labels for a variety of intracellular organelles. Fig. 4.8A shows single Z-sections taken through HEK293 cells stably expressing HA-hTPC2 and labelled with sequence specific antibodies for HA and LAMP2. Panel *a* shows a transmitted light image of the cell under study and (*b*) shows the distribution of HA-hTPC2 (green) and (*c*) the distribution of LAMP2 (red). Panel *d* shows the merged image of (*b*) and (*c*) with areas of co-localisation shown as yellow. Visual consideration of these images shows that, consistent with the deconvolution microscopy data (Fig. 4.6), TPC2 appears to co-localise with lysosomes. Furthermore, the Pearson product-moment correlation coefficient value for HA and LAMP2 labelling was 0.906 ± 0.003 ($n = 5$; Appendix 2, Table 4.5). Such a high coefficient value (i.e. close to +1) demonstrates that a strong linear correlation exists between HA-hTPC2 and LAMP2 labelling and thus further demonstrates that TPC2 is targeted to the membranes of lysosomes.

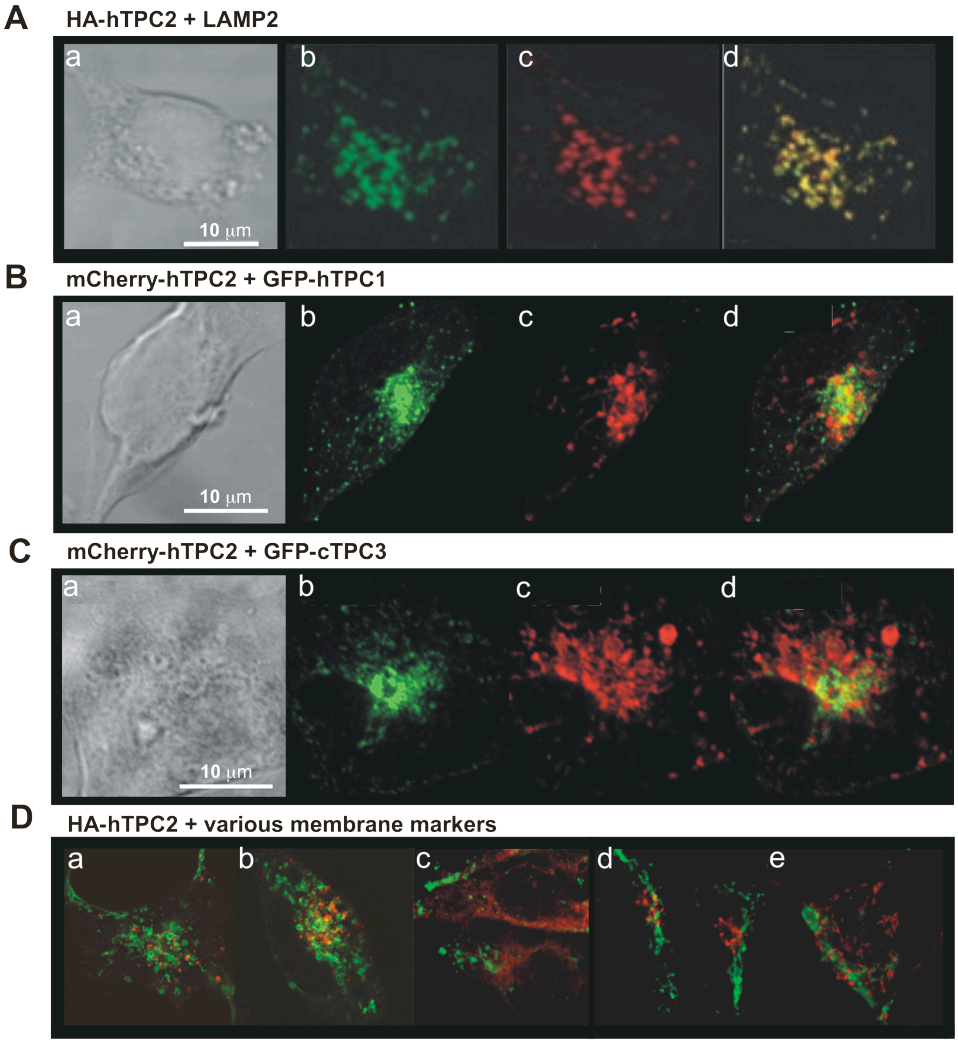

Fig. 4.8. TPC2 is targeted to lysosomal membranes

A Example cell showing the co-localisation between FITC labelled (excitation 490 nm, emission 528 nm) HA-hTPC2 (green) and Alexa 594-labelled (excitation 590 nm, emission 617 nm) LAMP2 (red). Panel *a* shows a transmitted light image of the isolated HA-hTPC2 cell imaged; Panel *b* shows a single Z section showing the distribution of HA-hTPC2 (green). Panel *c* shows a single Z-section showing the distribution of LAMP2 (red). Panel *d* shows a merged image of panels *b* and *c* revealing areas of co-localisation between the 2 labels (yellow). **B,C** Example cells showing the degree of co-localisation between mCherry-tagged (excitation 587 nm, emission 610 nm) hTPC2 and GFP-tagged (excitation 489 nm, emission 510 nm) hTPC1 (**B**) or cTPC3 (**C**). In each case Panel *a* shows a transmitted light image of the cell imaged. Panel *b* shows a single Z-section, showing the distribution of either GFP-hTPC1 (green) or GFP-cTPC3. Panel *c* shows a single Z-section, showing the distribution of mCherry-hTPC2 (red). Panel *d* is a merged image of panels *b* and *c* showing areas of co-localisation (yellow). **D** Example cells showing merged images indicating co-localisation between FITC labelled HA-hTPC2 (green) and the following selected organelle markers visualised with Alexa 594-conjugated secondary antibody: Panel *a*, EEA1; labelling of early endosomes; Panel *b*, M6PR labelling of late endosomes; Panel *c*, PDI labelling of ER; Panel *d*, GM130 labelling of Golgi apparatus; Panel *e*, CytC labelling of mitochondria.

Fig. 4.8B and Fig. 4.8C show single Z-sections taken through HEK293 cells stably expressing mCherry-tagged (excitation 587 nm, emission 610 nm) hTPC2 and either GFP-tagged (excitation 489 nm, emission 510 nm) hTPC1 or GFP-cTPC3 respectively. In each case, panel *a* shows a transmitted light image of the cell under study and (*b*) shows the distribution of GFP-hTPC1 (A*b*) or GFP-cTPC3 (B*b*) (green) and (*c*) the distribution of mCherry fluorescence (red). Panel *d* shows the merged image of (*b*) and (*c*) with areas of co-localisation shown as yellow. These images show that TPC2 does not appear to co-localise with either TPC1 or TPC3. Therefore, TPC1 and TPC3 may be targeted to the membranes of organelles other than lysosomes. Fig. 4.8D shows merged single Z-sections taken through HEK293 cells expressing HA-hTPC2 and labels for various intracellular organelles. In each cell the green labelling indicates the distribution of HA-hTPC2, with red labelling identifying the distribution of the following: (*a*) early endosomes, early endosome marker 1 (EEA1); (*b*) late endosomes, manose-6-phosphate receptor (M6PR); (*c*) ER, protein disulphide isomerase (PDI); (*d*) Golgi apparatus, Golgi matrix protein (GM130); (*e*) mitochondria, cytochrome C. These images show that there is little or no co-localisation between hTPC2 and these organelles, adding further support to the view that TPC2 is specifically targeted to lysosomal membranes.

4.3.1.2 Two-pore channel subtypes 1 and 3 are targeted to endosomes and other unidentified organelles

That TPC2 does not appear to co-localise with either TPC1 or TPC3 suggests that each TPC subtype may be targeted to different organelles and this was confirmed by further co-localisation analysis.

Fig. 4.9A shows single Z-sections taken through an exemplar HEK293 cell stably expressing GFP-tagged (excitation 489 nm, emission 510 nm) hTPC1 that had been fixed and labelled for LAMP2 and visualised via an Alexa-594 (excitation 590 nm, emission 610 nm) conjugated secondary antibody. Panel (*a*) shows a transmitted light image of the cell under study and subsequently shows the distribution of (*b*) GFP fluorescence labelling (green), (*c*) LAMP2 labelling (red), (*d*) a merged image of (*b*) and (*c*) with areas of co-localisation indicated (yellow). Similarly Fig. 4.9B shows single Z-sections taken through an exemplar HEK293 cell expressing GFP-hTPC1

labelled for transferrin and visualised using an Alexa-594 secondary antibody. Panel (*a*) shows a transmitted light image of the cell under study and subsequently shows the distribution of (*b*) GFP fluorescence labelling of hTPC1 (green), (*c*) transferrin labelling (red), (*d*) a merged image of (*b*) and (*c*) with areas of co-localisation indicated (yellow). Fig. 4.9C-D reveal the cellular distribution of cTPC3 with Fig. 4.19C showing single Z-sections taken through a HEK293 cell stably expressing GFP-cTPC3 that had been fixed and labelled for LAMP2 and visualised via an Alexa-594 conjugated secondary antibody. Panel (*a*) shows a transmitted light image of the cell under study and subsequently shows the distribution of (*b*) GFP fluorescence (green), (*c*) LAMP2 labelling (red), (*d*) a merged image of (*b*) and (*c*) with areas of co-localisation indicated (yellow). Similarly Fig. 4.9D shows single Z-sections taken through an exemplar HEK293 cell expressing GFP-cTPC3 labelled for M6PR and visualised using an Alexa-594 secondary antibody. Panel (*a*) shows a transmitted light image of the cell under study and subsequently shows the distribution of (*b*) GFP fluorescence labelling of hTPC1 (green), (*c*) M6PR labelling (red), (*d*) a merged image of (*b*) and (*c*) with areas of co-localisation indicated (yellow). Visual consideration of these images reveals that, in marked contrast to hTPC2, both hTPC1 and cTPC3 exhibited little or no co-localisation with LAMP2-labelling of lysosomes. This is consistent with the images presented in Fig. 4.8A and Fig. 4.8B which show that there was little or no co-localisation between hTPC2 and either hTPC1 or cTPC3 and suggests that, in contrast to TPC2, these subtypes are targeted to organelles other than lysosomes. Indeed, Fig. 4.9B and Fig. 4.9D shows that there was a high degree of co-localisation between hTPC1 and transferrin-labelled early endosomes, and between cTPC3 and M6PR-labelled late endosomes. It is important to note that the TPC1 and TPC3 did not exhibit a complete co-labelling with either transferrin or M6PR respectively, and therefore these TPC subtypes may also be targeted to the membranes of as yet unidentified intracellular organelles.

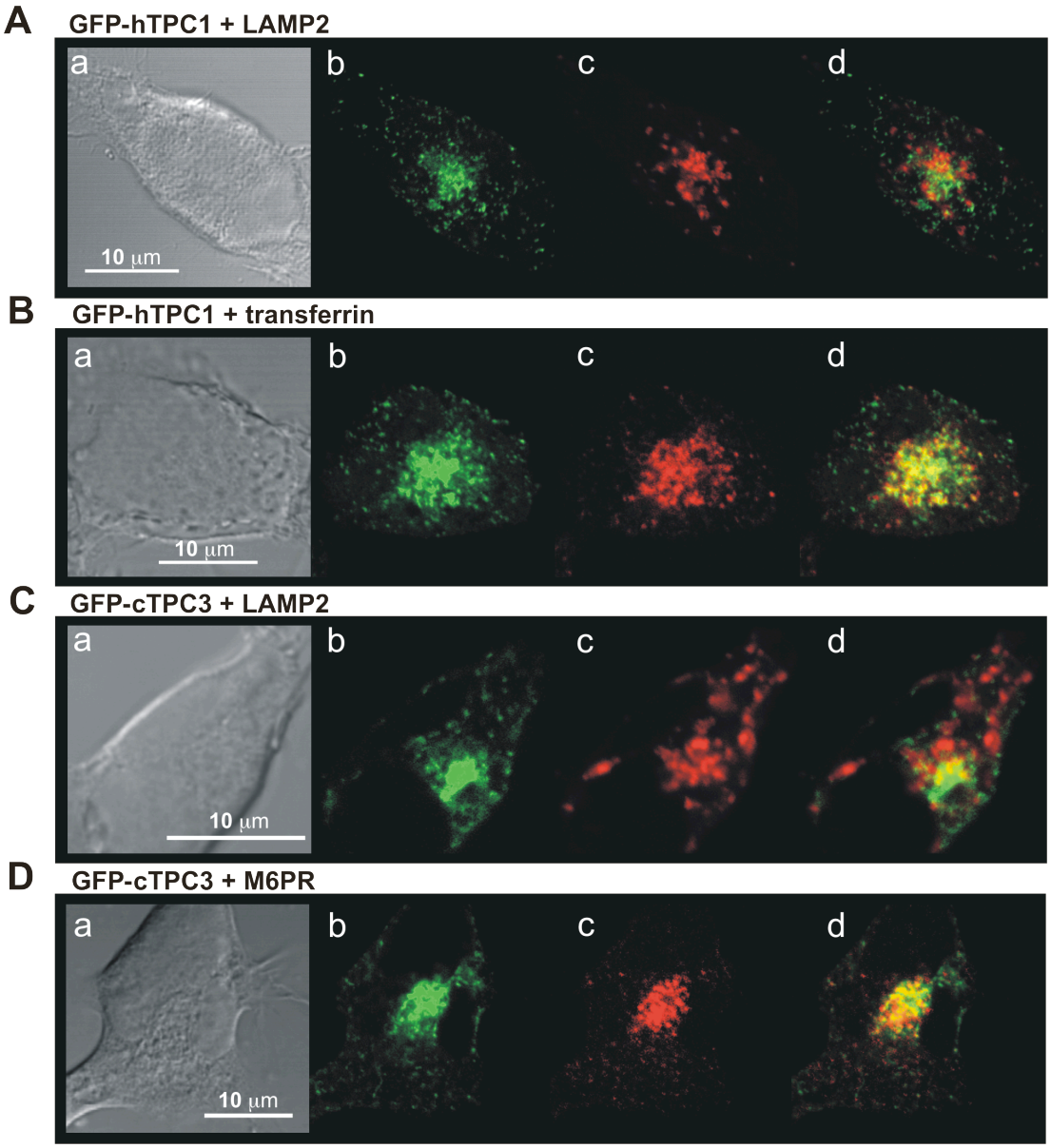

Fig. 4.9. TPC1 and TPC3 are targeted to the membranes of endosomes

A, B Example cells showing the degree of co-localisation between GFP-tagged (excitation 489 nm, emission 510 nm) hTPC1 and either LAMP2-labelled lysosomes (**A**) or transferrin-labelled early endosomes (**B**) visualised via an Alexa-594 conjugated secondary antibody (excitation 590 nm, emission 618 nm). In each case, Panel *a* shows a transmitted light image of an exemplar cell. Panel *b* shows a single Z-section, showing the distribution of GFP-hTPC1 (green). Panel *c* shows a single Z-section, showing the distribution of either LAMP2 (**A**) or transferrin (**B**) (red). Panel *d* is a merged image of panels *b* and *c* showing areas of co-localisation (yellow). **C**, **D** Example cells showing the degree of co-localisation between GFP-cTPC3 and either LAMP2-labelled lysosomes (**C**) or M6PR-labelled late endosomes (**D**) visualised via an Alexa-594 conjugated secondary antibody. In each case, Panel *a* shows a transmitted light image of an exemplar cell. Panel *b* shows a single Z-section, showing the distribution of GFP-cTPC3 (green). Panel *c* shows a single Z-section, showing the distribution of either LAMP2 (**C**) or M6PR (**D**) (red). Panel *d* is a merged image of panels *b* and *c* showing areas of co-localisation (yellow).

Furthermore, the Pearson product-moment correlation coefficient value for LAMP2 and either GFP-hTPC1 or GFP-cTPC3 was 0.590 ± 0.039 (n = 9) and 0.538 ± 0.028 (n = 6) respectively (Appendix 4, Table 4.5). These are significantly lower than the correlation coefficient obtained using the same method for HA-hTPC2 and LAMP2 (0.906 ± 0.003; n = 5) and suggest that in contrast to TPC2, TPC1 and TPC3 are not specifically targeted to lysosomes. Moreover, the Pearson product-moment correlation coefficient value for GFP-hTPC1 and transferrin was 0.590 ± 0.026 (n = 8; Appendix 4, Table 4.5), and for GFP-cTPC3 and M6PR was 0.485 ± 0.024 (n = 2; Appendix 4, Table 4.5). These values are also significantly lower than the correlation between TPC2 and LAMP2 and thus further suggests that although TPC1 and TPC3 appear to co-localise with early and late endosomes respectively, they may also be targeted to the membranes of as yet unidentified intracellular organelles.

That TPC2 is targeted specifically to lysosomes and TPC1 and TPC3 are targeted to endosomes is consistent with the previously reported vacuolar location of plant TPC1 (Peiter *et al.*, 2005) and further indicates a potential role for TPCs in intracellular Ca^{2+} signalling. Furthermore the specific lysosomal location of TPC2 would make this an ideal candidate receptor for Ca^{2+} signalling by NAADP.

4.3.2 [^{32}P]NAADP binds to two-pore channel subtype 2 with two binding affinities

The localisation of TPC2 to lysosomes shown above, and their similarity to Ca_v supports the view that TPC2 may represent the NAADP receptor. To this end I, in collaboration with Dr. Margarida Ruas and Dr. Xiaotong Cheng (See Chapter 5 also), investigated whether [^{32}P]NAADP bound to TPC2, and whether over-expression of hTPC2 in HEK293 cells resulted in increased [^{32}P]NAADP binding. Fig. 4.10A shows a comparison of the maximal specific binding of [^{32}P]NAADP in membranes prepared from either HEK293 cells or HA-hTPC2 cells. This shows that stable over-expression of hTPC2 in HEK293 cells resulted in a 3-fold increase in [^{32}P]NAADP binding in membranes with TPC2 enriched membranes exhibiting 338.0 ± 25.9 % of the maximal specific binding in wild-type cells (Appendix 2, Table 4.6). This increase in the specific binding of [^{32}P]NAADP strongly suggests that TPC2 is capable of binding NAADP. This is of particular significance as TRPML1, which has been previously proposed to be an NAADP receptor, showed no increase in [^{32}P]NAADP binding when over-expressed in NRK cells (Pryor *et al.*, 2006). Fig.

4.10B and C shows a ligand competition assay using membranes prepared from HA-hTPC2 cells (B) and mouse liver (C). The liver was selected for comparison of endogenous binding sites as this tissue type was shown to have the highest level of TPC2 mRNA expression by Northern blot analysis (Fig. 4.1B). In these ligand binding assays (carried out by Dr. Xiaotong Cheng alone / in my absence) the affinity of NAADP for recombinant hTPC2 and endogenous NAADP binding sites in mouse liver was determined via analysis of the competitive binding between 0.2 nM [^{32}P]NAADP and a range of concentrations (1 pM to 1 mM) of unlabelled NAADP. Fig. 4.10B shows that the hTPC2-containing membranes derived from HA-hTPC2 cells exhibit two NAADP binding affinities with the goodness of fit determined by the R^2 value (based on the sum of squares; Chapter 2) with dissociation constants (K_d) of 5.0 ± 4.2 nM and 7.2 ± 0.8 μM (mean ± S.E.M.; n = 3; Appendix 2, Table 4.7). This binding curve closely resembled the resultant curve obtained from competitive displacement of [^{32}P]NAADP using mouse liver membranes which also exhibited 2 affinities with K_d values of 6.6 ± 3.5 nM and 4.6 ± 2.4 μM (n = 4; Fig. 4.10C; Appendix 2, Table 4.9). Thus, hTPC2 exhibits similar binding characteristics to endogenous mammalian NAADP binding sites derived from liver, which is also notable because this tissue displayed the highest density of TPC2 expression by Northern blot analysis. Furthermore, the high-affinity binding site is comparable with previous values reported in other mammalian preparations such as the heart and brain (Bak *et al.*, 2001; Masgrau *et al.*, 2003; Patel *et al.*, 2000b) and high affinity binding sites identified in sea urchin egg homogenates (Billington *et al.*, 2000; Patel *et al.*, 2000a). The identification of 2 [^{32}P]NAADP binding affinities in both HA-hTPC2 cells and mouse liver homogenates is consistent with previous reports on a pancreatic β-cell line (MIN6) which also exhibited 2 [^{32}P]NAADP binding sites with K_d values of 130 ± 31 nM and 12 ± 0.6 μM (Masgrau *et al.*, 2003). The presence of two NAADP binding sites has also been proposed in sea urchin eggs (Patel, 2004).

In marked contrast, the precursor of NAADP, β-NADP$^+$ showed only low-affinity binding with a K_d of 10.3 ± 3.1 μM in HA-hTPC2 cells (n = 3; Fig. 4.10B; Appendix 2, Table 4.8) and 4.5 ± 2.3 μM in mouse liver membranes (n = 4; Fig. 4.10C; Appendix 2, Table 4.9). Such a low affinity is expected as β-NADP$^+$ does not mobilise Ca^{2+} from lysosome-related stores and therefore would not be expected to bind to a putative NAADP receptor with the same affinity as NAADP. This low

affinity of β-NADP$^+$ relative to NAADP binding is also consistent with previous reports in the rabbit heart and in sea urchin egg (Bak *et al.*, 2001; Patel *et al.*, 2000a). Indeed, it is possible that the binding observed may reflect contamination of β-NADP$^+$ preparations with NAADP as previously suggested and reported (Lee *et al.*, 1995; Patel *et al.*, 2000a).

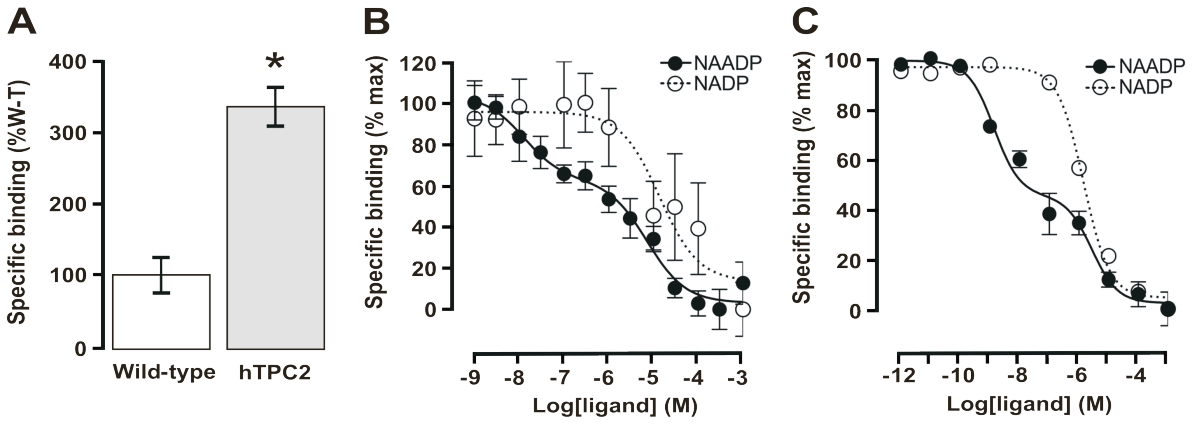

Fig. 4.10. [^{32}P]NAADP binds to TPC2 in membranes prepared from HA-hTPC2 cells

A Specific binding for membranes prepared from wild-type HEK293 cells (W-T) and HA-hTPC2 cells. * indicates a statistically significant difference (P<0.05) when compared to the mean maximal specific binding obtained from membranes prepared from wild-type HEK293 cells (n = 3). **B** Displacement of [^{32}P]NAADP binding from the total membrane prepared from HA-hTPC2 cells reveals that NAADP binds to TPC2 with 2 affinities. Displacement with NAADP produced a K_{d1} of 5.0 ± 4.2 nM and a K_{d2} of 7.2 ± 0.8 μM (n = 4), and displacement with NADP produced a K_d of 10.3 ± 3.1 μM (n = 4). **C** Displacement of [^{32}P]NAADP binding from the total membrane was prepared from mouse liver reveals that NAADP binds to TPC2 with 2 affinities. Displacement with NAADP produced a K_{d1} of 6.6 ± 3.5 nM and a K_{d2} of 4.6 ± 2.4 μM (n = 3), and displacement with NADP produced a K_d of 4.5 ± 3.3 μM (n = 3).

Over-expression of HA-hTPC2 in HEK293 cells resulted in a significant increase in [^{32}P]NAADP binding and strongly suggests that NAADP binds to TPC2. That NAADP binds to TPC2 via both a low and high affinity site may, at least in part, provide for a mechanism to explain the bell-shaped concentration-response curve observed with respect to NAADP-induced Ca^{2+} signals in mammalian preparations (Berg *et al.*, 2000; Cancela *et al.*, 1999; Masgrau *et al.*, 2003) and also the unique inactivation properties observed sea urchin eggs. However, in sea urchin egg low sub-threshold concentrations of NAADP desensitise / inactivate the receptor to subsequent activation by maximal NAADP concentrations, whereas higher

concentrations activate the receptor (Aarhus *et al.*, 1996; Dickinson *et al.*, 2003; Genazzani *et al.*, 1996a). In the mammalian system it is speculated that the significance of these findings may be that NAADP activates its receptor by binding to the low affinity binding site, and when the concentration of NAADP is sufficiently high, occupancy of the low affinity site would additionally confer "self-inactivation" of the NAADP-receptor complex.

Together these data show that TPC2 exhibits the key characteristics of NAADP binding sites previously observed in mammalian cells and thus provides further support for the proposal that TPC2 may function as an NAADP receptor.

4.3.3 NAADP mobilises Ca^{2+} in HEK293 cells that stably over-express two-pore channel subtype 2

Having established that NAADP binds to hTPC2 with two affinities and that hTPC2 is targeted to lysosomal membranes when over-expressed in HEK293 cells, I sought to determine whether NAADP was able to mobilise Ca^{2+} via hTPC2. In order to achieve this NAADP (100 pM to 1 mM) was applied intracellularly into HEK293 cells stably over-expressing HA-hTPC2 by dialysis from a patch pipette in the whole-cell configuration of the patch-clamp technique and under voltage-clamp conditions (V = -40 mV) to ensure inactivation of any voltage-activated Ca^{2+}currents, with resultant changes in the intracellular Ca^{2+} concentration reported by the Fura-2 fluorescence ratio (F_{340}/F_{380}). A representative record showing the response to intracellular dialysis of 10 nM NAADP in a HA-hTPC2 expressing HEK293 cell is shown in Fig. 4.11A. The upper panel shows a series of pseudocolour images of the cell in question that are representative of the F_{340}/F_{380} ratio recorded at the time points labelled on the record of the F_{340}/F_{380} ratio against time shown in the lower panel. Clearly, a global Ca^{2+} wave is triggered with a peak change in the F_{340}/F_{380} ratio of 0.92 ± 0.14 (n = 44; Appendix 2, Table 4.10).

In marked contrast to the Ca^{2+} transient evoked by intracellular dialysis of 10 nM NAADP, no such Ca^{2+} signal was observed when NAADP was omitted from the pipette solution (n = 14; Fig. 4.11B; Appendix 2, Table 4.11), consistent with the Ca^{2+} wave being triggered in response to intracellular dialysis of NAADP rather than being representative of an artefact of the process of intracellular dialysis *per se*.

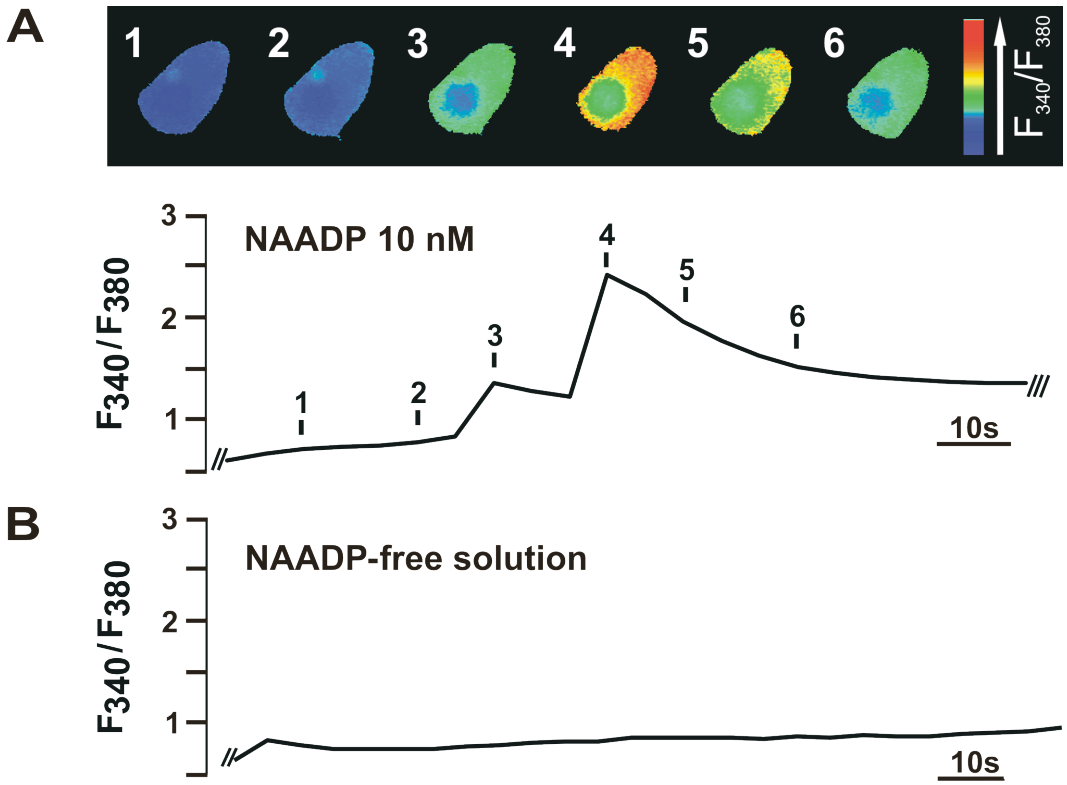

Fig. 4.11. NAADP evokes global Ca^{2+} transients in HA-hTPC2 cells

A Top panel, series of pseudocolour images of the Fura-2 fluorescence ratio (F_{340}/F_{380}) recorded in an HA-hTPC2 cell during the intracellular dialysis of 10 nM NAADP. NAADP evokes a global Ca^{2+} transient. Bottom panel, corresponding record of the F_{340}/F_{380} ratio against time for the cell imaged in the top panel. For this, and the subsequent record, access to the cytoplasm via the formation of the whole-cell configuration is indicated by the two bars at the beginning of the record, and the loss of a GΩ seal is indicated at the end of the record by three bars. **B** Record of the F_{340}/F_{380} ratio against time recorded in an HA-hTPC2 cell during the intracellular dialysis of NAADP-free pipette solution.

Closer inspection of the NAADP-mediated Ca^{2+} transients in cells over-expressing HA-hTPC2 reveals that the pattern of Ca^{2+} release elicited was biphasic, and therefore reminiscent of the two-pool mechanism of Ca^{2+} release by NAADP observed in PASMC, whereby NAADP evokes Ca^{2+} bursts that either return to basal levels or precede and then trigger a global Ca^{2+} wave by CICR from the SR via RyRs (Boittin *et al.*, 2002). With respect to the biphasic nature of NAADP-dependent Ca^{2+} signals in HA-hTPC2 expressing HEK293 cells, Fig. 4.12A-C shows that there was marked cell-to-cell variation. The initial "shoulder" or "pacemaker phase" of the Ca^{2+} transient identified in Fig. 4.11A was not always observed, as in some cells only a monophasic Ca^{2+} transient was observed (Fig. 12A). This is most likely due to the fact that the speed of coupling (see below) can vary and thereby, on occasion, limit

the capacity of the imaging system to discriminate between the two phases of Ca^{2+} release observed in other records. A further variation observed is shown in Fig. 4.12B in which a much smaller initial rise in Ca^{2+}, or "shoulder" precedes a global Ca^{2+} transient. Finally, Fig. 4.13C shows that a large (>0.5 ratio units) initial phase preceded a large, global Ca^{2+} transient of the secondary phase. However, closer inspection reveals that this large initial phase occurs at a higher resting Ca^{2+} concentration. Thus, it is possible that the cytoplasmic concentration may alter the magnitude of Ca^{2+} release in response to NAADP during both the initial "shoulder" and the secondary amplification phase.

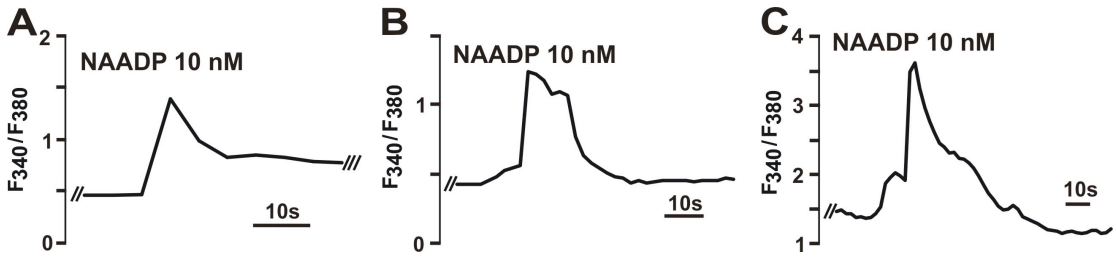

Fig. 4.12. NAADP evokes varied Ca^{2+} transients in HEK293 cells expressing HA-hTPC2

Example records showing the Fura-2 fluorescence ratio against time recorded in HA-hTPC2 cells in response to intracellular dialysis of 10 nM NAADP. The observed initial phase of the response was varied and an example of each is highlighted in the following panels: no clearly discernable initial phase (**A**); a small initial phase (**B**); a large initial phase (>0.5 ratio units) prior to a secondary phase (**C**). For all records, access to the cytoplasm via the formation of the whole-cell configuration is indicated by the two bars at the beginning of the record and the loss of a GΩ seal is indicated at the end of the record by three bars.

Of equal importance to my studies was the finding, that intracellular dialysis of 10 nM NAADP into wild-type HEK293 cells failed to evoke a significant change in the Fura-2 fluorescence ratio relative to basal levels recorded before or immediately after entering the whole-cell configuration (n = 15; Fig. 4.13A; Appendix 2, Table 4.12). This is despite the fact that my collaborator, Dr Mike Zhu, cloned TPC2 from HEK293 cells that must, therefore, exhibit endogenous expression of this channel. In light of this fact I determined the effect of increasing the NAADP concentration applied via the patch pipette 100-fold to 1 μM. Fig. 4.13B shows an exemplar record, with pseudocolour images shown in the upper panel and the record of the F_{340}/F_{380} ratio shown in the lower panel and inset at an expanded scale. Close inspection of the pseudocolour images identified (white arrow) a small, spatially restricted Ca^{2+}

transient, with similar events being observed in 3 out of 5 cells studied. This resulted in a mean peak change in the F_{340}/F_{380} ratio of 0.19 ± 0.04 (n = 5; Appendix 2, Table 4.13).

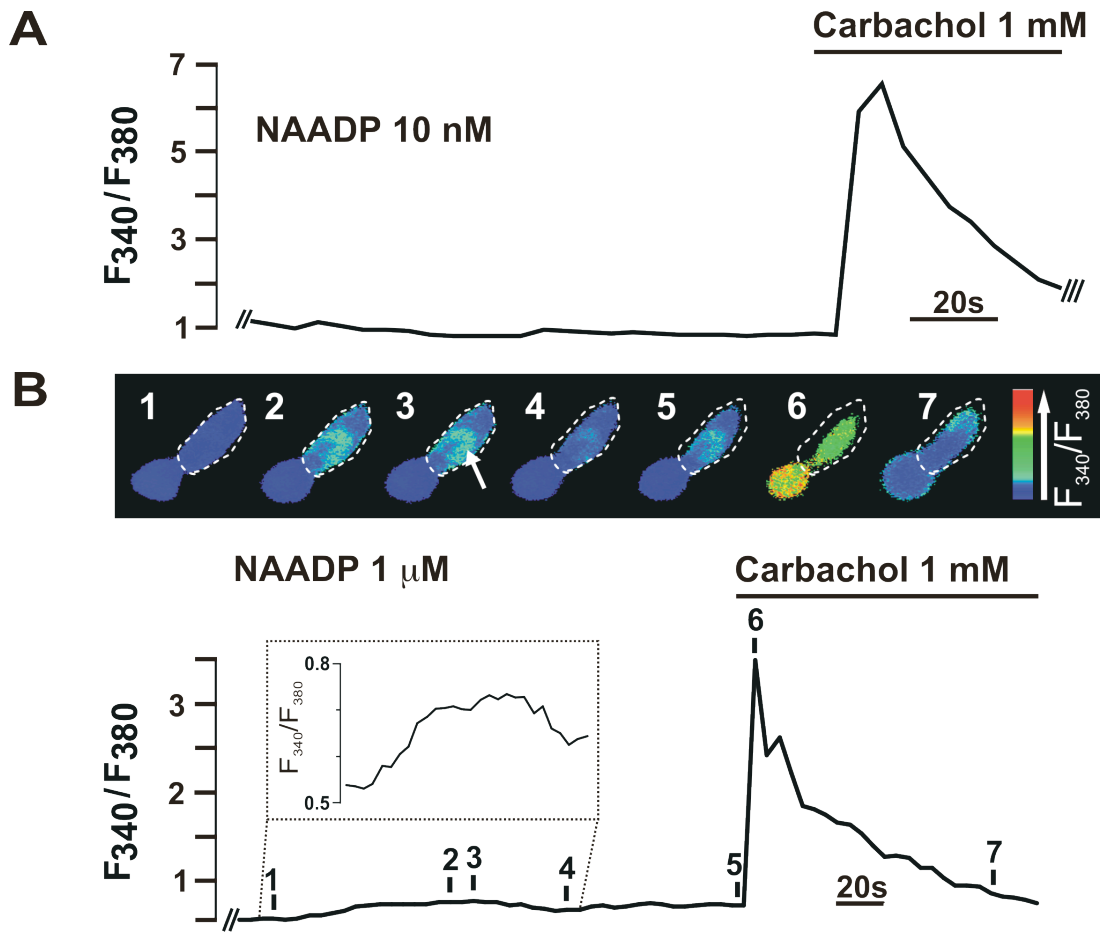

Fig. 4.13. NAADP may evoke spatially restricted Ca^{2+} transients but not does not evoke global Ca^{2+} transients in wild-type HEK293 cells

A Record of the Fura-2 fluorescence ratio (F_{340}/F_{380}) against time recorded in a wild-type HEK293 cell during the intracellular dialysis of 10 nM NAADP. For this, and the subsequent record, access to the cytoplasm via the formation of the whole-cell configuration is indicated by the two bars at the beginning of the record and the loss of a GΩ seal is indicated at the end of the record by three bars. **B** Top panel, series of pseudocolour images of the F_{340}/F_{380} ratio recorded in a wild-type HEK293 cell during the intracellular dialysis of 1 μM NAADP. At this concentration NAADP evokes spatially restricted Ca^{2+} transients indicated by the white arrow. Bottom panel, corresponding record of the F_{340}/F_{380} ratio against time for the cell imaged in the top panel. Inset, spatially restricted Ca^{2+} transients are evoked by 1 μM NAADP.

That 1 μM NAADP was required to evoke small, spatially restricted Ca^{2+} transients in wild-type HEK293 cells suggests that the endogenous level of TPC2

expression may be less than required for the initiation of global Ca^{2+} waves. This view is supported by comparison of the mean change in the F_{340}/F_{380} ratio in both HA-hTPC2 cells and wild-type HEK293 cells (Fig. 4.14). This confirms the binding data presented above whereby over-expression of hTPC2 in HEK293 cells resulted in a 3-fold increase in [^{32}P]NAADP binding and by the lack of clear specific binding in wild-type HEK293 cells. Consistent with this, Dr. Mike Zhu has demonstrated by real time Q-RT-PCR that mRNA levels are ≤ 1,000 times lower in wild-type HEK293 cells when compared to cells that stably over-express hTPC2 (see Calcraft *et al.*, 2009 – supplementary data).

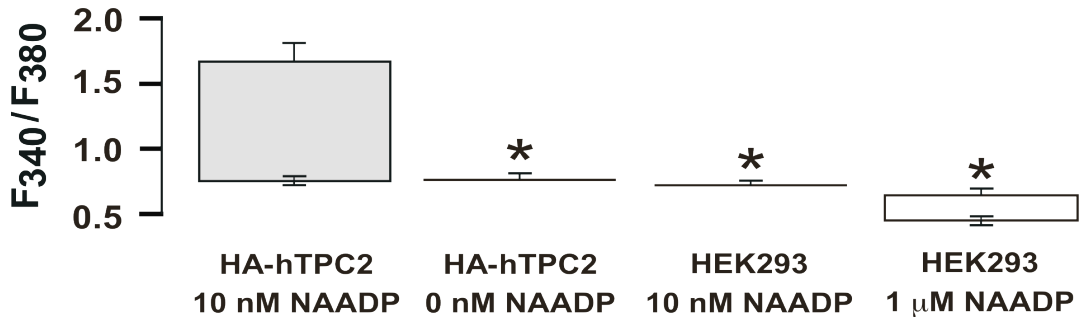

Fig. 4.14. Comparison of the change in the Fura-2 fluorescence ratio resulting from intracellular dialysis of NAADP in HA-hTPC2 and wild-type HEK293 cells

Bar chart showing the mean change in the Fura-2 fluorescence ratio (F_{340}/F_{380}) recorded in HA-hTPC2 cells in response to 10 nM (n = 44) and 0 nM (n = 14) NAADP, and wild-type HEK293 cells in response to dialysis of 10 nM (n = 15) or 1 μM (n = 5) NAADP. The columns are presented as the basal level (mean ± S.E.M.) to the peak change in the F_{340}/F_{380} ratio (mean ± S.E.M.). When no discernable change in the ratio beyond basal levels was observed, data are presented as a line representing the mean basal level (mean ± S.E.M.). * indicates a statistically significant difference (P < 0.05) when compared to the peak change in fluorescence ratio in response to 10 nM NAADP in HA-hTPC2 cells.

4.3.4 NAADP-dependent Ca^{2+} release exhibits a bell-shaped concentration-response curve in HEK293 cells over-expressing two-pore channel subtype 2

The data presented above show that NAADP (10 nM) evokes a global Ca^{2+} transient in HEK293 cells over-expressing HA-hTPC2 but not in non-transfected (wild-type) HEK293 cells, suggesting that NAADP evokes Ca^{2+} release via the activation of hTPC2. I therefore sought to further characterise this channel by determining whether hTPC2 exhibits similar functional characteristics to those

previously observed in mammalian cells. One such characteristic is the bell-shaped concentration-response curve, whereby intracellular dialysis of concentrations of NAADP that are considerably higher than the threshold for initiation of Ca^{2+} release result in a failure of NAADP-induced Ca^{2+} release, which has been proposed to be due to homologous desensitization (Berg *et al.*, 2000; Boittin *et al.*, 2002; Cancela *et al.*, 1999; Masgrau *et al.*, 2003).

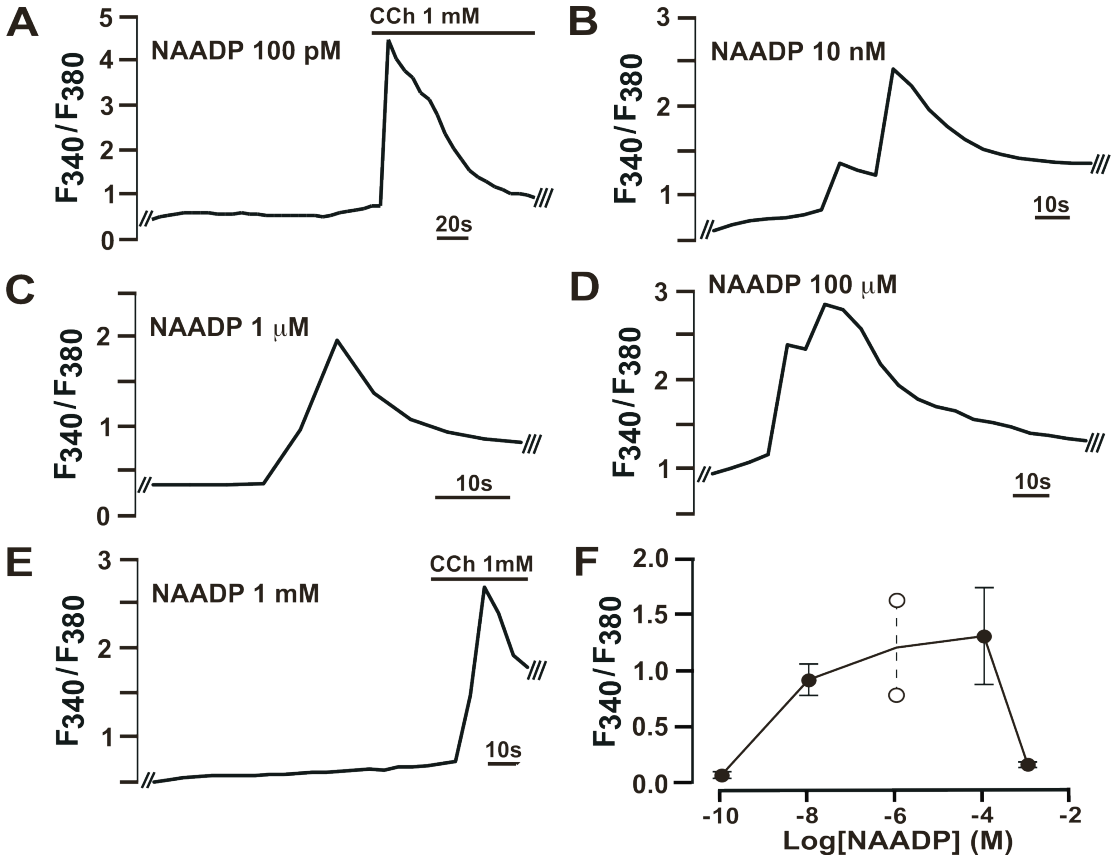

Fig. 4.15. TPC2 exhibits a bell-shaped concentration-response curve to NAADP in HA-hTPC2 cells

Example records showing the Fura-2 fluorescence ratio (F_{340}/F_{380}) against time recorded in HA-hTPC2 cells in response to intracellular dialysis of NAADP at the following concentrations: 100 pM (**A**); 10 nM (**B**); 1 μM (**C**); 100 μM (**D**); 1 mM (**E**). Access to the cytoplasm via the formation of the whole-cell configuration is indicated by the two bars at the beginning of the record. Note, the loss of a GΩ seal is indicated at the end of the record by three bars. When no transient in response to NAADP was observed, 1 mM carbachol (CCh) was added extracellularly. **F** Curve showing the mean (± S.E.M) of the peak change in the Fura-2 fluorescence ratio plotted against the log concentration of NAADP in the patch pipette, recorded in HA-hTPC2 cells in response to dialysis of NAADP at the following concentrations: 100 pM (n = 4), 10 nM (n = 44), 1 μM (n = 2), 100 μM (n = 11), and 1 mM (n = 10). Note, for n = 2 the range is plotted as indicated by the unfilled circles joined by a dashed line.

Fig. 4.15A shows a representative record of the F_{340}/F_{380} ratio against time recorded in an HA-hTPC2 expressing cell during intracellular dialysis of 100 pM NAADP. This figure shows that, as observed during intracellular dialysis of NAADP-free pipette solution, 100 pM NAADP failed to evoke a global Ca^{2+} wave (0.074 ± 0.004; n = 4; P<0.05; Appendix 2, Table 4.14). As 10 nM NAADP evoked global Ca^{2+} transients in HA-hTPC2 cells (Fig. 4.15B) this would suggest that the threshold for activation of hTPC2 by NAADP is within the nanomolar concentration range. This is consistent with the radioligand binding data which revealed a high affinity binding site with a K_d value of 5.0 ± 4.2 nM. That TPC2 is activated within the nanomolar concentration range is also consistent with the previously reported level of activation observed in both mammalian and non-mammalian preparations including sea urchin egg, pancreatic acinar cells, T-lymphocytes, pancreatic β-cells and PASMC (Berg *et al.*, 2000; Boittin *et al.*, 2002; Cancela *et al.*, 1999; Lee *et al.*, 1995; Masgrau *et al.*, 2003). Intracellular dialysis of either 1 μM or 100 μM also evoked large Ca^{2+} transients, reported as an increase in the F_{340}/F_{380} ratio of 1.21 ± 0.42 (n = 2; Fig. 4.15C; Appendix 2, Table 4.15) and 1.31 ± 0.43 (n = 11; Fig. 4.15D; Appendix 2, Table 4.16) respectively. The mean peak change in the F_{340}/F_{380} ratio increased as the concentration of NAADP was increased from 10 nM to 100 μM, although this difference is not considered statistically significant. In marked contrast, intracellular dialysis of 1 mM NAADP failed to induce a Ca^{2+} transient (n = 10; P<0.05; Fig. 4.15E; Appendix 2, Table 4.17). This is consistent with previous reports on NAADP-dependent Ca^{2+} signalling in a variety of cell types and is indicative of self-inactivation / desensitisation of the Ca^{2+} release process. Importantly, 1 mM NAADP did not inhibit global Ca^{2+} signals triggered by 1 mM carbachol (CCh; Fig. 4.15E) which mediates Ca^{2+} signals via IP_3-dependent mechanisms. Thus, desensitisation by NAADP of Ca^{2+} signalling via hTPC2 appears to be homologous. This is consistent with observations in other mammalian cells whereby low (nanomolar) concentrations of NAADP elicit Ca^{2+} release, whereas supra-maximal (micromolar) concentrations are ineffective (Berg *et al.*, 2000; Cancela *et al.*, 1999; Masgrau *et al.*, 2003). The inactivation / desensitisation of hTPC2 by high concentrations of NAADP may well be conferred by the low affinity binding site identified above (Fig. 4.10) i.e. occupation of the high-affinity binding site likely confers channel activation whereas occupation of the low-affinity binding site likely

confers inactivation. Fig. 4.15F shows the concentration-response curve for intracellular dialysis of NAADP (100 pM to 1 mM) into HA-hTPC2 expressing cells, which exhibits a bell-shaped profile consistent with that observed in a variety of mammalian preparations (Berg *et al.*, 2000; Cancela *et al.*, 1999; Masgrau *et al.*, 2003).

4.3.5 The concentration delay kinetics for intracellular dialysis of NAADP

During the intracellular dialysis of 10 nM NAADP into HA-hTPC2 cells, when a clear point of initiation was observed, the average time to the initiation of the Ca^{2+} transient was 28.2 ± 3.3 s (n = 22; Appendix 2, Table 4.18) after the whole-cell configuration was achieved. The time taken for diffusional equilibrium between the patch pipette and the cell to become established varies according to size of molecule. In 1988 Pusch and Neher provided a model to calculate the diffusion coefficient of a given molecule used in the whole-cell configuration of the patch-clamp technique (Eqn. 4.1) (Pusch *et al.*, 1988):

$$\tau = (0.6 \pm 0.17) \cdot R_s \cdot M_r^{1/3} \qquad \text{(Eqn. 4.1)}$$

where τ is the diffusion coefficient (seconds), R_s the series resistance (MΩ), and M_r is the molecular mass. Using the formula presented in Eqn. 4.1 and assuming the maximal series resistance of 10 MΩ and the relative molecular mass of NAADP to be 744, the diffusional time constant for NAADP is 54.4 ± 15.4 s. This constant can then be inserted into the formula presented in Eqn. 4.2 to determine the relative concentration of NAADP in the cell compared to the patch pipette at a given time:

$$c_{(t)} = c_{(p)} - c_{(1)} \cdot \exp^{(-t/\tau)} \qquad \text{(Eqn. 4.2)}$$

where the relative concentration of NAADP in the cell at a given time t is c_t, c_p is the constant concentration inside the pipette, τ is the diffusional time constant (seconds), and c_1 is the concentration determined by $c_p - c_{(t = 0)}$. For these experiments the resting concentration of NAADP in the cell is assumed to be 0 and therefore $c_{(1)} = c_{(p)}$.

Fig. 4.16A shows the relative concentration of NAADP in the cell, based upon the values obtained using Eqn. 4.2. From this curve, it is evident that at the average

time to the initiation of the response to 10 nM NAADP (28.2 ± 3.3 s), the concentration of NAADP in the cell would be approximately 4 nM. This is consistent with previous reports in PASMCs which have shown that 10 nM NAADP evoked global Ca^{2+} waves whereas concentrations ≤ 2 nM failed to initiate global Ca^{2+} waves (Boittin *et al.*, 2002). These data provide further indirect confirmation that the Ca^{2+} transient observed in HA-hTPC2 cells in response to intracellular dialysis of 10 nM NAADP is as a direct response to the intracellular dialysis of NAADP.

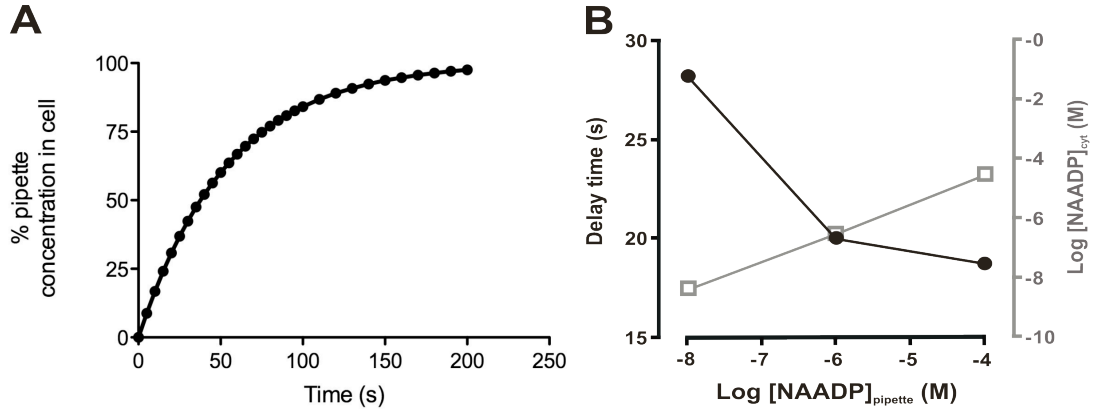

Fig. 4.16. Concentration-delay kinetics for the intracellular dialysis of NAADP

A Graph showing the relative concentration of NAADP in the cell compared to the constant concentration present in the patch-pipette (%) against time (seconds) following the formation of the whole-cell configuration. Calculations have been performed using the formulae presented in Eqns. 4.1 and 4.2. **B** Graph showing the mean delay time (seconds) to the initiation of the NAADP-mediated Ca^{2+} transient versus the log concentration of NAADP in the patch pipette (black circles, left y-axis). Also plotted is the predicted log concentration of NAADP in the cell ($[NAADP]_{cyt}$) at the time of the initiation of the NAADP-mediated Ca^{2+} transient, plotted against the log of each concentration tested (gray squares, right y-axis). The predicted concentration was calculated using the formulae presented in Eqns. 4.1 and 4.2.

In addition to 10 nM NAADP, intracellular dialysis of 1 μM and 100 μM NAADP evoked global Ca^{2+} transients in HEK293 cells stably expressing HA-hTPC2, with the average time delay to the initiation of the Ca^{2+} transient measuring 20 ± 5.0 s (n = 2; Appendix 2, Table 4.18) and 18.8 ± 2.8 (n = 4; Appendix 2, Table 4.17) respectively. Fig. 4.16B shows the delay time for the initiation of the peak Ca^{2+} transient for each concentration of NAADP used. This clearly shows that the delay time for the initiation of the NAADP-evoked Ca^{2+} transient is reduced when the concentration of NAADP in the patch pipette is increased. Fig. 4.16 also shows the

predicted concentration of NAADP in the cell at the time of initiation of the Ca^{2+} transient for each concentration of NAADP ($[NAADP]_{pipette}$) examined. If the diffusion of NAADP were to conform exactly to the model proposed by Pusch and Neher the predicted concentration at the point of initiation should be equal for each concentration of NAADP examined. However, Fig. 4.16B shows that there is some deviation from this model (from 4 nM, 308 nM to 29 μM corresponding to a pipette concentration of 10 nM, 1 μM and 100 μM respectively). This may be due to a number of factors that are not taken into account in the concentration-delay kinetic (Eqn. 4.2). For example, the rate of NAADP metabolism within the cytoplasm or the non-uniform distribution of lysosomal clusters within the cell (Chapter 3) would affect the perceived rate of NAADP diffusion. Moreover, the mechanism of NAADP-mediated Ca^{2+} release via TPC2 may be complicated by the requirement for time-dependent interactions with accessory proteins or phosphorylation of the channel. Thus, this model of diffusion is an indication of the diffusional delay and should therefore be used as a guide only. Nevertheless, that the delay time to the initiation of the Ca^{2+} transient is inversely proportional to the concentration of NAADP in the pipette, suggests that the diffusion of NAADP conforms approximately to the proposal that there is an associated concentration-delay kinetic when using intracellular dialysis (Pusch *et al.*, 1988) and therefore further suggests that the Ca^{2+} transient observed in HA-hTPC2 cells at each concentration (10 nM, 1 μM and 100 μM) of NAADP is as a direct response to the intracellular dialysis of NAADP.

4.3.6 NAADP mobilises Ca^{2+} from lysosome-related acidic organelles via two-pore channel subtype 2

As mentioned previously, NAADP has previously been shown to mobilise Ca^{2+} from lysosome-related acidic organelles in mammalian and non-mammalian cells (Churchill *et al.*, 2002; Kinnear *et al.*, 2004). One of the primary indicators of this fact in both the sea urchin egg and mammalian cells was the finding that pre-incubation with bafilomycin A1, a vacuolar H^+ pump (V-H^+-ATPase) inhibitor, can deplete lysosomal Ca^{2+} stores and thereby block subsequent Ca^{2+} release in response to NAADP (Churchill *et al.*, 2002; Kinnear *et al.*, 2004). As mentioned previously,

through analysis of hTPC2 co-localisation with LysoTracker and LAMP2 I have shown that hTPC2 is preferentially targeted to lysosomes in HEK293 cells. Therefore, one would expect bafilomycin to confer block of NAADP-dependent Ca^{2+} signalling via hTPC2. I therefore investigated the effect of bafilomycin on NAADP-mediated Ca^{2+} release in HA-hTPC2 expressing cells.

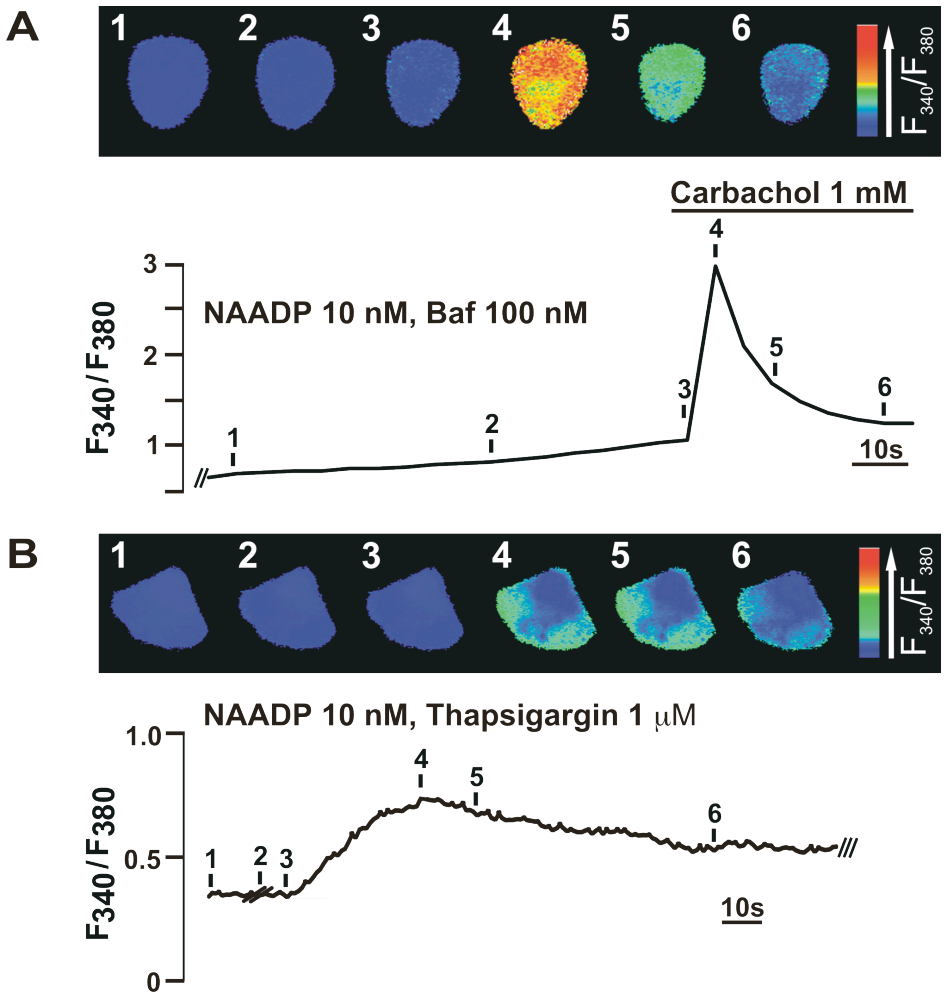

Fig. 4.17. NAADP-mediated Ca^{2+} release is inhibited fully by bafilomycin and partially by thapsigargin

A Top panel, series of pseudocolour images of the Fura-2 fluorescence ratio (F_{340}/F_{380}) recorded in an HA-hTPC2 cell pre-incubated (45 min) with 100 nM bafilomycin A1 (baf) during the intracellular dialysis of 10 nM NAADP. Bottom panel, corresponding record of the F_{340}/F_{380} ratio against time for the cell imaged in the top panel. For this and the subsequent record access to the cytoplasm via the formation of the whole-cell configuration is indicated by the two bars at the beginning of the record. **B** Top panel, series of pseudocolour images of the F_{340}/F_{380} ratio recorded in an HA-hTPC2 cell pre-incubated (30 min) with thapsigargin (1 μM) during the intracellular dialysis of 10 nM NAADP. Bottom panel, corresponding record of the F_{340}/F_{380} ratio against time for the cell imaged in the top panel. The loss of a GΩ seal is indicated at the end of the record by three bars.

Following pre-incubation (45 minutes) of HA-hTPC2 expressing cells with 100 nM bafilomycin, 10 nM NAADP failed to evoke a global Ca^{2+} transient (n = 11; Fig. 4.17A; Appendix 2, Table 4.19) and thus, no increase in the Fura-2 fluorescence ratio above basal levels was observed. However, pre-incubation with 100 nM bafilomycin did not inhibit Ca^{2+} transients evoked by the application of 1 mM CCh. This suggests that bafilomycin depletes the lysosomal, NAADP-releasable Ca^{2+} store without affecting the ability of IP_3 to evoke Ca^{2+} release from the ER. This therefore shows that NAADP-dependent Ca^{2+} signalling via hTPC2 exhibits a similar pharmacology to that observed with respect to NAADP-mediated Ca^{2+} release in other preparations (Churchill *et al.*, 2002; Kinnear *et al.*, 2004; Yamasaki *et al.*, 2004) and suggests that the observed Ca^{2+} release is dependent upon an acidic lysosome-related Ca^{2+} store that is maintained, in part, by the activity of a V-H^+-ATPase. This is consistent with the fact that hTPC2 is targeted to lysosomes and with previous studies on a range of cells that demonstrate that NAADP releases Ca^{2+} from a bafilomycin-sensitive, lysosome-related acidic Ca^{2+} store and not from the ER (Brailoiu *et al.*, 2005; Churchill *et al.*, 2002; Kinnear *et al.*, 2004; Yamasaki *et al.*, 2004; Zhang *et al.*, 2006a).

In marked contrast, depletion of ER Ca^{2+} stores with a SERCA pump inhibitor, thapsigargin, resulted in partial inhibition of NAADP-mediated Ca^{2+} release in HA-hTPC2 expressing cells. Thus, following pre-incubation (30 mins) of HA-hTPC2 expressing cells with 1 μM thapsigargin, relatively small, spatially restricted Ca^{2+} signals were evoked by NAADP but the larger, global Ca^{2+} transient was not observed (Fig. 4.17B). Thus, the increase in the Fura-2 fluorescence ratio measured only 0.23 ± 0.06 (Fig. 4.18; n = 5; Appendix 2, Table 4.20). As expected, this is significantly lower than the change in the Fura-2 fluorescence ratio observed in HA-hTPC2 expressing cells in the absence of thapsigargin (P<0.05; Fig. 4.18) and is indicative of residual lysosomal Ca^{2+} release. This suggests that a functional ER is not required for the initiation of NAADP-mediated Ca^{2+} release but that the ER is a prerequisite for subsequent amplification of the initial phase of NAADP-dependent Ca^{2+} release into a global Ca^{2+} transient. This is consistent with observations in other cell types such as sea urchin eggs, PASMCs and pancreatic acinar cells where NAADP-dependent Ca^{2+} release couples to the ER by CICR via RyRs and / or IP_3Rs (Cancela *et al.*, 1999; Cancela *et al.*, 2000; Churchill *et al.*, 2001a). Given that

HEK293 cells do not express high levels of RyRs (Aoyama *et al.*, 2004) it is therefore most likely that, in the absence of thapsigargin, NAADP-mediated Ca^{2+} release is amplified into a global Ca^{2+} transient by CICR from the ER via the progressive recruitment of IP_3Rs.

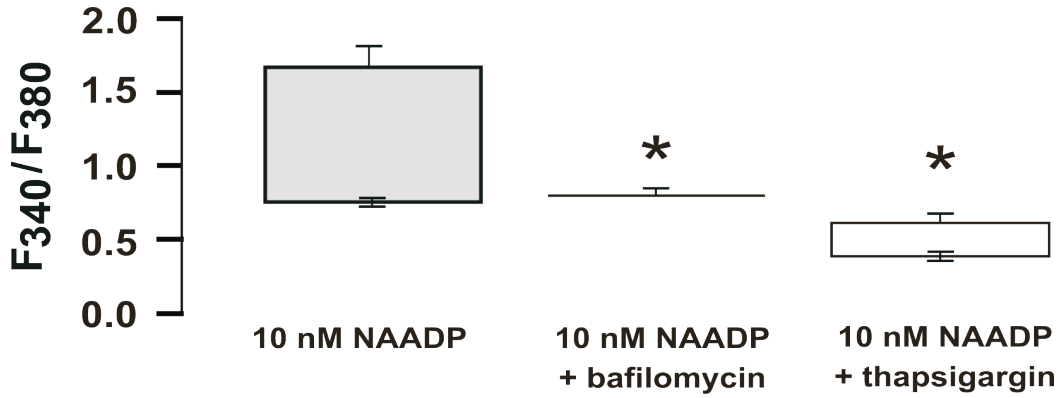

Fig. 4.18. Comparison of the effect of thapsigargin and bafilomycin on NAADP-mediated Ca^{2+} release in HA-hTPC2 cells

Bar chart comparing the mean change in the F_{340}/F_{380} ratio in response to dialysis of 10 nM NAADP recorded in HA-hTPC2 cells either in the absence of antagonists (n = 44) or pre-incubated with thapsigargin (n = 5) or bafilomycin A1 (n = 11). The columns are presented as the basal level (mean ± S.E.M.) to the peak change in the Fura-2 fluorescence ratio (mean ± S.E.M.). When no discernable change in the ratio beyond basal levels was observed, data are presented as a line representing the mean basal level (mean ± S.E.M.) * indicates a statistically significant difference (P<0.05) when compared to the peak change in F_{340}/F_{380} ratio in response to 10 nM NAADP in HA-hTPC2 cells.

In order to confirm the requirement of IP_3Rs for amplification of NAADP-mediated Ca^{2+} bursts in HEK293 cells a specific IP_3R antagonist was required. Xestospongin C is a specific IP_3R antagonist and has previously been shown to inhibit IP_3-mediated Ca^{2+} release in pulmonary arterial smooth muscle (Boittin *et al.*, 2002). However, in HEK293 cells stably expressing HA-hTPC2, NAADP-evoked Ca^{2+} release appeared to remain unaffected in the presence of xestospongin C although it blocked Ca^{2+} release in response to CCh (not shown). There was no clear explanation for this contrary observation. Nevertheless, studies using a different IP_3R antagonist, heparin, resolves this discrepancy. Like NAADP heparin is unable to cross the plasma membrane and must be introduced into the cytoplasm via a patch pipette. However, given that heparin would be co-dialysed with NAADP, one could not

guarantee that heparin would block IP_3Rs prior to NAADP-evoked Ca^{2+} release via TPCs. Consequently, heparin was co-dialysed into the cell with caged-NAADP and allowed to equilibrate prior to the application of NAADP. Following this, NAADP may be released via flash photolysis of the caged-NAADP. My experimental apparatus was not able to perform flash photolysis and therefore these experiments were carried out by Dr. Abdelilah Arredouani (University of Oxford) as described above (see Methods). Fig. 4.19A shows a representative record of the Fluo3 fluorescence against time in response to the photorelease of NAADP in an HA-hTPC2 expressing HEK293 cell. As observed during the intracellular dialysis of NAADP in HA-HEK293 expressing cells, photorelease of NAADP triggered a global Ca^{2+} transient which appeared to be biphasic (n = 6). In marked contrast, inclusion of heparin (200 μg/ml) in the pipette solution resulted in the inhibition of the second phase of the NAADP-evoked Ca^{2+} transient but not the first (Fig. 4.19B; n = 5). This effect was similar to that observed during intracellular dialysis of NAADP in HA-hTPC2 cells in the presence of thapsigargin (Fig. 4.17B). Together these records demonstrate that in HEK293 cells NAADP-mediated Ca^{2+} release is amplified by CICR from the ER via IP_3Rs.

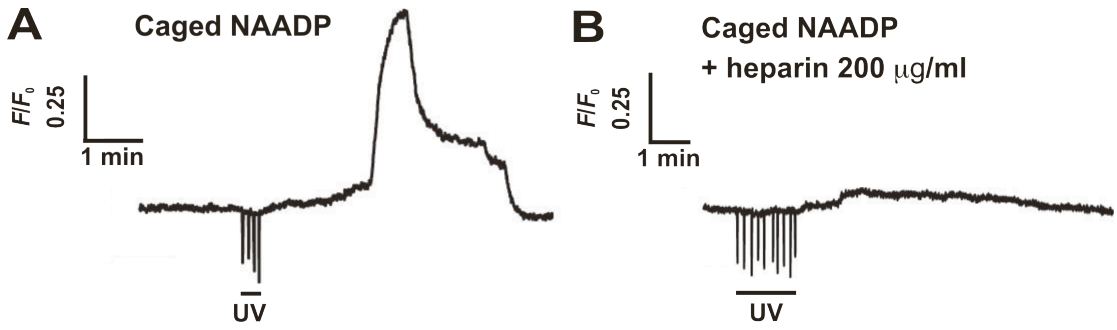

Fig. 4.19. Effect of photoreleased NAADP in HEK293 cells expressing hTPC2

A Record of the Fluo-3 fluorescence (F/F_0) against time recorded in an HA-hTPC2 cell during the photorelease of caged NAADP (10 μM). For this and the subsequent record, release of NAADP was evoked by flash photolysis of caged NAADP by ultraviolet (UV) irradiation. **B** Record of the F/F_0 recorded in an HA-hTPC2 cell pre-incubated with heparin (200 μg/ml) during the photorelease of caged NAADP (10 μM).

4.3.7 Knockdown of two-pore channel subtype 2 expression by shRNA blocks NAADP-dependent Ca^{2+} signalling

In order to confirm that NAADP-dependent Ca^{2+} transients observed in HA-hTPC2 expressing cells were dependent on hTPC2, transfection of shRNA (see Methods) against hTPC2 was used to knockdown hTPC2 expression.

The presence of HA-hTPC2 protein in lysates of HA-hTPC2 expressing cells was determined by Western blot after transfection of cells with either shRNA against hTPC2 or a scrambled shRNA control, using an anti-HA antibody to identify HA-hTPC2. Fig. 4.20 shows a representative blot probed with sequence-specific antibodies raised against HA. In protein obtained from control cells, a clear band was present that corresponded to a protein of approximately 100 kDa. However, in cells transfected with shRNA against hTPC2 this band appeared to be markedly reduced. As expected, in the lane loaded with protein obtained from wild-type HEK293 cells, there was no band corresponding to HA-hTPC2. When the cells were re-probed for β-actin, the corresponding band (~40 kDa) appeared to be of equal intensity across all lanes (Fig. 4.20) indicating that any difference between the level of HA-hTPC2 detected is not due to unequal protein loading but rather the reduced expression of hTPC2 resulting from transfection of shRNA against hTPC2.

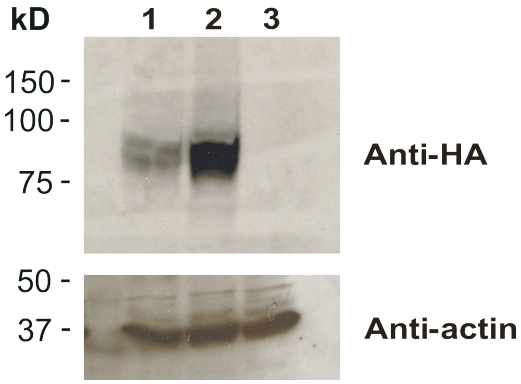

Fig. 4.20. Effective knockdown of hTPC2 expression in HA-hTPC2 cells

Top panel shows the labelling with specific antibody for the HA tag present on hTPC2 immunoblotted against homogenate protein samples obtained from either HA-hTPC2 cells transfected with shRNA against hTPC2 (lane 1) HA-hTPC2 cells transfected with scrambled shRNA (lane 2) or wild-type HEK293 cells (lane 3). Lower panel shows the labelling when the blot was re-probed with a specific antibody against β-actin.

However, it is worth noting that the transfection efficiency was not complete (~70%) resulting in a reduction of, rather than complete abolition of hTPC expression. The knockdown of hTPC2 in HA-hTPC2 cells by shRNA was therefore verified using immunocytochemical labelling of the HA-tag. Both shRNA transfected HA-hTPC2 cells and untransfected HA-hTPC2 cells were labelled with a specific

antibody raised against HA, as described previously. This labelling was visualised using a secondary FITC-conjugated antibody. Cells that were successfully transfected with shRNA were identified by the presence of fluorescence corresponding to the expression of the mRFP reporter gene present within the pSIREN-DNR plasmid. Fig. 4.21A shows a representative 3D reconstruction of a series of deconvolved Z-sections taken through an HA-hTPC2 cell labelled for HA. This image shows that these cells present extensive and widespread HA-hTPC2 labelling (green). When HA-hTPC2 cells were transfected with shRNA against hTPC2, successful transfection was indicated by the presence of mRFP (red; Fig 4.21B) and in all cells expressing mRFP the level of HA-hTPC2 labelling was virtually abolished.

Comparison of the density of HA-labelling (Fig. 4.21C) revealed that incubation with shRNA significantly reduced the density of HA-labelling in HA-hTPC2 cells by approximately 8-fold from 0.038 ± 0.009 μm^3 per μm^3 (n = 4; Appendix 2, Table 4.21) to 0.0050 ± 0.0025 μm^3 per μm^3 (n = 6; P<0.05; Appendix 2, Table 4.22). This significant reduction in HA-hTPC2 labelling is consistent with the reduced expression observed in the homogenates when assessed by Western blot (Fig. 4.20) and suggests that the sequence specific shRNA against hTPC2 is effective in reducing the expression of HA-hTPC2 in HEK293 cells. Importantly, it is likely that this 8-fold reduction reduces TPC2 expression to below the expression level observed in wild-type HEK293 cells, which exhibit 3-fold less [^{32}P]NAADP binding when compared to cells stably over-expressing HA-hTPC2 (Fig. 4.10A) and importantly undetectable levels of specific binding. However, it is important to note that the transfection efficiency, determined by the number of cells expressing mRFP, was approximately 70 %. This is consistent with the greatly reduced yet incomplete knockdown of HA-hTPC2 protein observed in the Western blot. This therefore implies that the presence of the mRFP reporter dye is a requirement for the selection of cells that have been transfected with shRNA, and therefore for cells in which an ~8-fold decrease in the density of HA-hTPC2 cells has been achieved. Therefore, mRFP was used to identify cells for whole-cell patch clamp experiments on the effect of shRNA on NAADP-dependent Ca^{2+} signalling via TPC2.

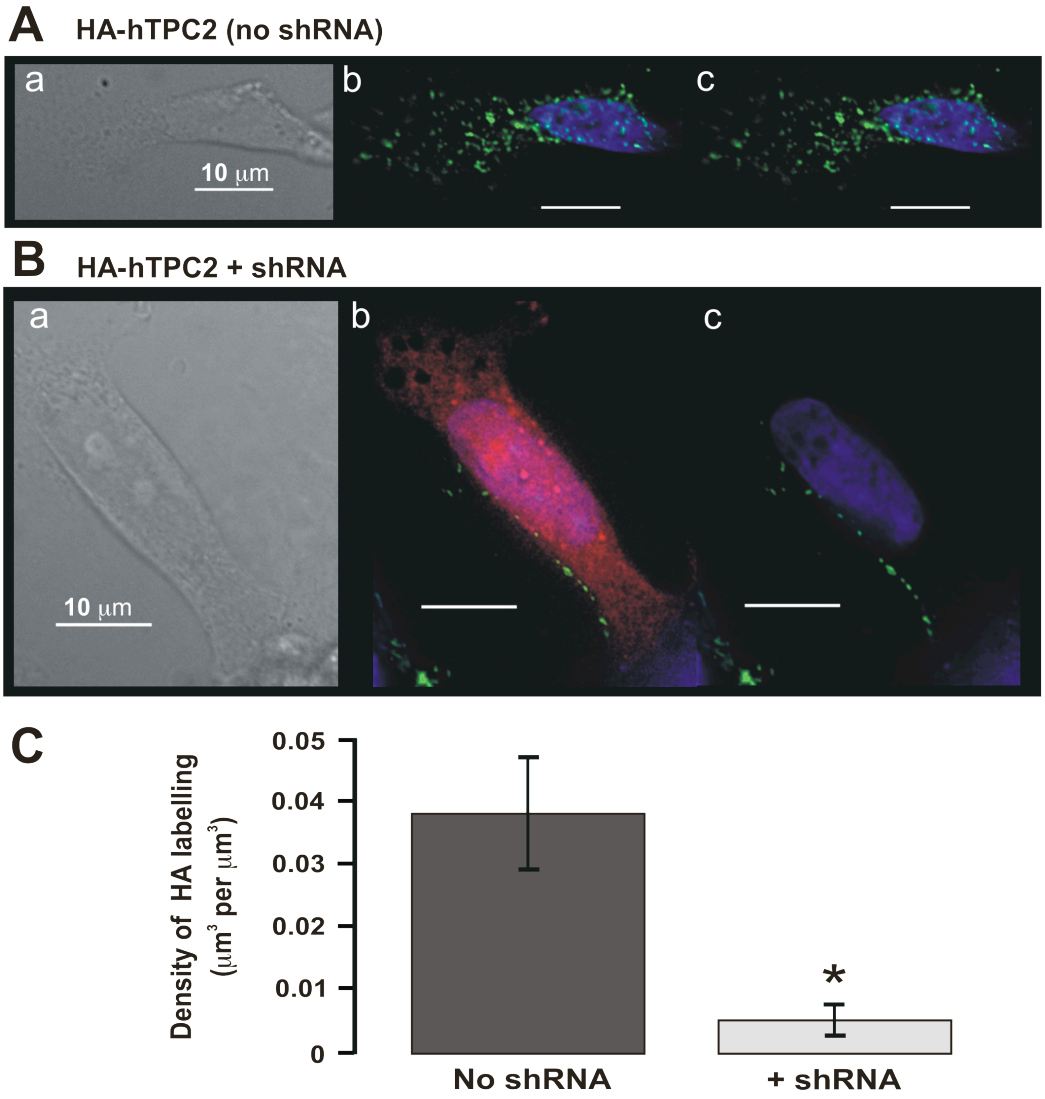

Fig. 4.21. shRNA reduces expression of HA-hTPC2 in HEK293 cells

Example cells showing the degree of HA-hTPC2 labelling in HA-hTPC2 cells (**A**) and HA-hTPC2 cells transfected with shRNA (**B**). In each case the panels show the following: Panel *a* shows a transmitted light image of the isolated HA-hTPC2 cell imaged; Panel *b* shows a 3D reconstruction of a series of deconvolved Z-sections taken through the cell shown in panel *a* showing the distribution of HA labelling (green) and the presence of mRFP (red) indicating successful shRNA transfection, relative to the nucleus (dark blue); Panel *c* shows a 3D reconstruction of deconvolved Z-sections as shown in panel *b*, showing the distribution of HA labelling relative to the nucleus (dark blue). **C** Bar chart comparing the density of HA labelling (μm^3 per μm^3; mean ± S.E.M.) within the whole cell volume of HA-hTPC2 control cells (n = 4) and HA-hTPC2 cells transfected with shRNA (n = 6). * indicates a statistically significant difference (P<0.05) when compared to the HA labelling density of HA-hTPC2 control cells.

Having verified that shRNA against hTPC2 was effective in reducing hTPC2 expression in HA-hTPC2 cells, I next investigated the effect of shRNA-mediated

hTPC2 knockdown on the response to intracellular dialysis of 10 nM NAADP. The resultant change in the intracellular Ca^{2+} concentration was reported by changes in the Fura-2 fluorescence ratio. Importantly, only cells that were seen to express mRFP, observed via a RFP Alpha Vivid filter, were selected for patching.

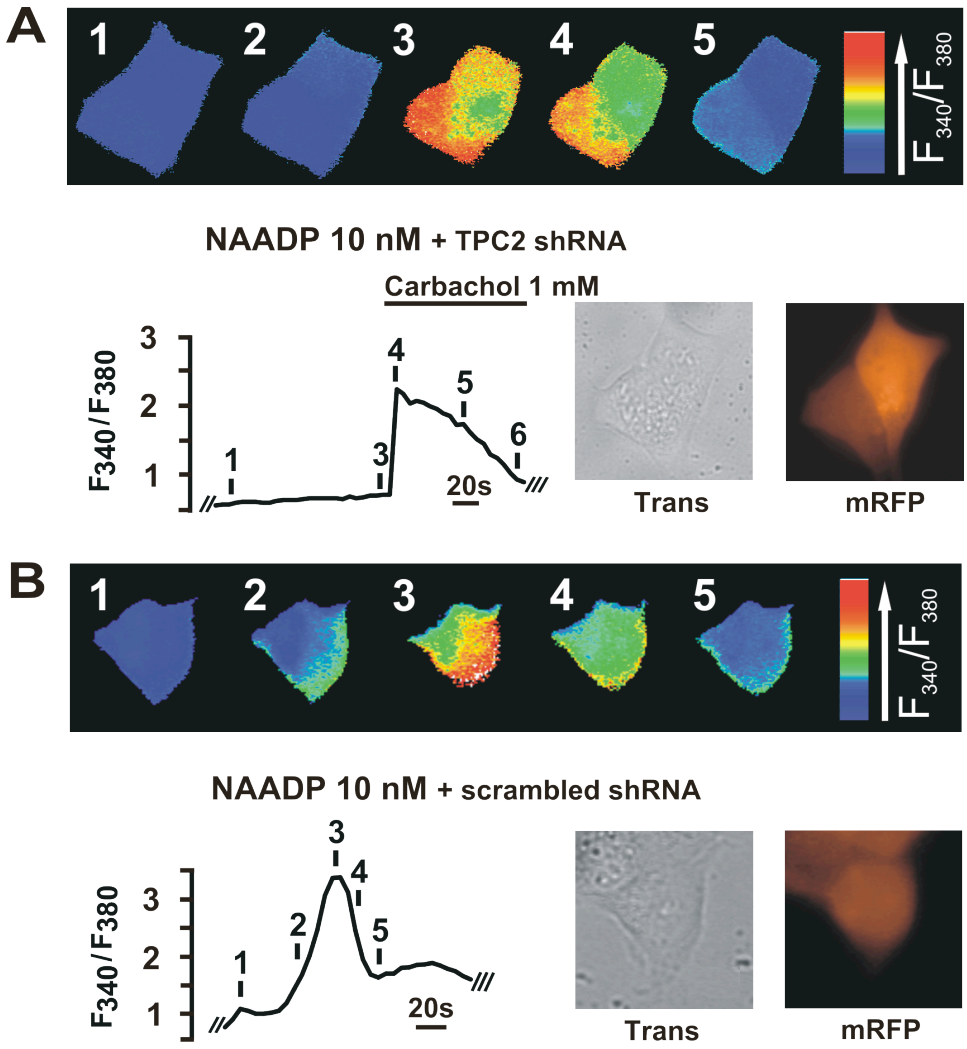

Fig. 4.22. shRNA against TPC2 abolishes NAADP-mediated Ca^{2+} transients in HA-hTPC2 cells

Example records of the response to intracellular dialysis of 10 nM NAADP in HA-hTPC2 cells transfected with either shRNA against TPC2 (**A**) scrambled shRNA (**B**). In both cases the panels contain the following: Top panel, series of pseudocolour images of the Fura-2 fluorescence ratio (F_{340}/F_{380}) recorded in HA-hTPC2 cells during the intracellular dialysis of 10 nM NAADP; Bottom left panel, corresponding record of the F_{340}/F_{380} ratio against time for the cell imaged in the top panel. Access to the cytoplasm via the formation of the whole-cell configuration is indicated by the two bars at the beginning of the record and the loss of a GΩ seal is indicated at the end of the record by three bars; Bottom right panel, the transmission light image (Trans) and image of mRFP labelling (mRFP) within the selected cell verifying successful transfection.

A representative record showing the effect of pre-incubation (72-96 hours) with shRNA against hTPC2 on NAADP-mediated Ca^{2+} release is shown in Fig 4.22A. The upper panel shows a series of pseudocolour images of the Fura-2 fluorescence ratio recorded during the intracellular dialysis of 10 nM NAADP, with the record of the Fura-2 fluorescence ratio against time shown in the bottom left panel. The bottom right panel shows the transmission light image and the corresponding image of mRFP labelling. Transfection of hTPC2 expressing cells with shRNA abolished Ca^{2+} signalling in response to 10 nM NAADP, with no change in the Fura-2 fluorescence ratio above basal levels evident (n = 10; P<0.05; Fig. 4.23C; Appendix 2, Table 2.24). In marked contrast, HA-hTPC2 cells transfected with scrambled shRNA exhibited Ca^{2+} transients in response to intracellular dialysis of 10 nM NAADP, with a peak change in the Fura-2 fluorescence ratio of 1.15 ± 0.4 (n = 6; Fig. 4.22B; Appendix 2, Table 4.23) that was not significantly different to control hTPC2 expressing cells (0.92 ± 0.14; n = 44; Fig. 4.23). I can conclude therefore, that shRNA knockdown of hTPC2 was effective in cells that stably over-expressed hTPC2 and that knockdown of hTPC2 blocked Ca^{2+} signalling induced by intracellular dialysis of 10 nM NAADP. Thus NAADP mediates Ca^{2+} signals in a manner that is dependent on the expression of hTPC2.

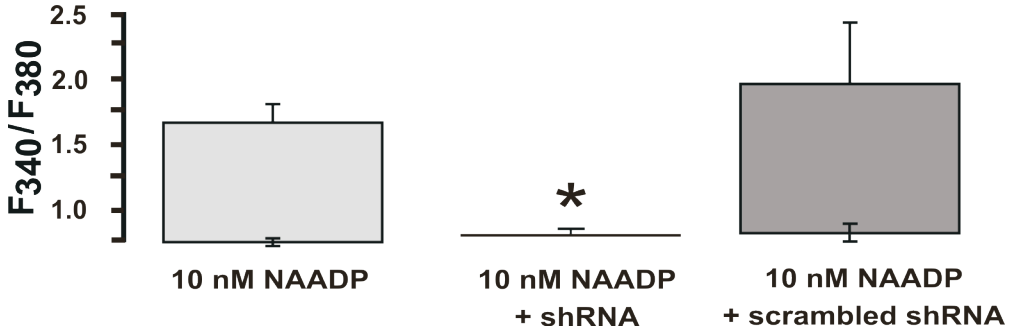

Fig. 4.23. shRNA against TPC2 but not scrambled shRNA abolishes NAADP-mediated Ca^{2+} transients in HA-hTPC2 cells

Bar chart comparing the mean change in F_{340}/F_{380} ratio recorded in shRNA transfected (n = 10), scrambled shRNA transfected (n = 6) and non-transfected (n = 44) HA-hTPC2 cells in response to dialysis of 10 nM NAADP. The columns are presented as the basal level (mean ± S.E.M.) to the peak change in the F_{340}/F_{380} ratio (mean ± S.E.M.). When no discernable change in the ratio beyond basal levels was observed, data are presented as a line representing the mean basal level (mean ± S.E.M.) * indicates a statistically significant difference (P<0.05) when compared to the peak change in F_{340}/F_{380} ratio in response to 10 nM NAADP in HA-hTPC2 cells.

4.3.8 NAADP evokes Ca^{2+} bursts but not global Ca^{2+} transients in HEK293 cells that stably over-express two-pore channel subtype 1

TPC1 is also ubiquitously expressed in primates (including humans), rats and mice and is targeted to endosomes which, like lysosomes, may represent acidic, Ca^{2+} storing organelles (Gerasimenko *et al.*, 1998; Hilden *et al.*, 1989). Therefore I sought to determine whether or not NAADP could mediate Ca^{2+} signals in HEK293 cells that stably over-express His_6-hTPC1. As for studies on hTPC2, this was achieved by intracellular dialysis of 10 nM NAADP via a patch-pipette, in the whole-cell configuration of the patch-clamp technique and under voltage-clamp conditions (V = -40 mV). Resultant changes in the intracellular Ca^{2+} concentration were once again reported by changes in the Fura-2 fluorescence ratio.

Fig. 4.24 shows a representative record of the effect of intracellular dialysis of 10 nM NAADP on the Fura-2 fluorescence ratio in a His_6-hTPC1 expressing cell. The upper panel shows a series of pseudocolour images, with the lower panel showing the corresponding record of the Fura-2 fluorescence ratio against time; inset shows record on an expanded scale. Clearly, intracellular dialysis of 10 nM NAADP evoked small, spatially restricted Ca^{2+} transients, and this was observed in 3 out of 4 cells studied. These Ca^{2+} release events did not spread throughout the entirety of the cell and resulted in a mean peak change in the Fura-2 fluorescence ratio of 0.35 ± 0.09 (n = 4; Appendix 2, Table 4.25). These spatially restricted Ca^{2+} transients were reminiscent of the response to 10 nM NAADP observed in hTPC2 expressing cells following pre-incubation with thapsigargin, and of the response of wild-type HEK293 cells to a higher concentration of NAADP (1 μM; Fig. 4.15). As TPC1 appeared to be primarily targeted to endosomes, these data suggest that 10 nM NAADP mediates Ca^{2+} release from endosomes via TPC1 in a manner that is unable to breach the threshold for amplification by CICR via IP_3Rs on the ER. The spatially restricted nature of release via hTPC1 is consistent with the spatially restricted distribution of hTPC1 and the endosomes to which this channel subtype is targeted, as shown in the immunofluorescence images presented above (Fig. 4.19). These findings therefore suggest that endosomes / TPC1 do not allow for efficient coupling to ER Ca^{2+} release mechanisms in HEK293 cells. Nonetheless, these findings suggest that TPC1 may

also mediate Ca^{2+} signals in response to NAADP and that TPCs may therefore represent a family of NAADP receptors.

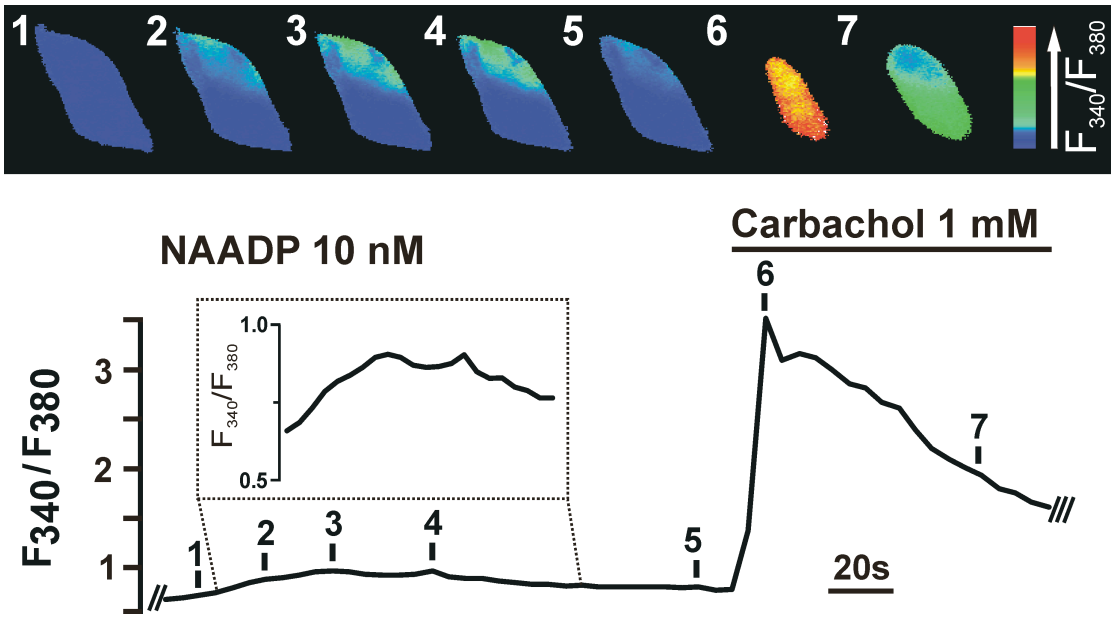

Fig. 4.24. His_6-hTPC1 cells exhibit spatially restricted Ca^{2+} transients in response to 10 nM NAADP

Top panel, series of pseudocolour images of the Fura-2 fluorescence ratio recorded in an His_6-hTPC1 cell during the intracellular dialysis of 10 nM NAADP. NAADP evoked spatially restricted Ca^{2+} transients that did not spread throughout the whole cell. Bottom panel, corresponding record of the Fura-2 fluorescence ratio against time for the cell imaged in the top panel. Access to the cytoplasm via the formation of the whole-cell configuration is indicated by the two bars at the beginning of the record. Note, the loss of a GΩ seal is indicated at the end of the record by three bars. Inset, spatially restricted Ca^{2+} transients are evoked by 10 nM NAADP. Similar observations were made in 3 out of 4 His_6-hTPC1 cells.

4.4 Discussion

The data presented in this chapter provide strong evidence in support of the view that that TPC2 constitutes, at least in part, an NAADP receptor that releases Ca^{2+} from lysosome-related acidic organelles that can trigger further Ca^{2+} release from the ER by CICR.

4.4.1 Two-pore channel subtype 2 is specifically targeted to lysosomes in HEK293 cells.

Examination of the cellular distribution of TPCs revealed that TPC2 co-localises with the lysosome markers LAMP2 and LysoTracker, but not with markers of early endosomes, late endosomes, mitochondria, Golgi apparatus, or the ER. In marked contrast, TPC1 and TPC3 showed little or no co-localisation with lysosomes or TPC2, but instead appeared to be targeted to endosomes and other unidentified organelles. Therefore, all mammalian TPCs are expressed intracellularly on the membranes of endolysosomes, with TPC2 specifically targeted to lysosomes. The presence of all 3 TPC subtypes on the membranes of intracellular endolysosomal Ca^{2+} stores is consistent with the vacuolar localisation of plant TPC1 (Peiter *et al.*, 2005) and also with the suggestion of Ishibashi *et al.,* that mammalian TPCs may exhibit an intracellular membrane localisation (Ishibashi *et al.*, 2000). Importantly, the cellular distribution of TPCs and particularly TPC2 is consistent with the view that NAADP receptors are localised to lysosome-related acidic organelles and that NAADP selectively releases Ca^{2+} from these stores (Brailoiu *et al.*, 2006; Brailoiu *et al.*, 2005; Churchill *et al.*, 2002; Kinnear *et al.*, 2004; Macgregor *et al.*, 2007; Yamasaki *et al.*, 2004; Zhang *et al.*, 2006a). Due to its absence in primates and some rodent genomes (e.g. mouse and rat), TPC3 was excluded from consideration at the level of the expression system used. However, the specific endolysosomal location of all 3 TPCs and in particular the lysosomal distribution of TPC2 suggested that TPCs may be ideal candidate NAADP receptors.

4.4.2 NAADP binds to two-pore channel subtype 2 with two affinities

In membranes prepared from HEK293 cells and HA-hTPC2 cells a ligand competition assay showed that the over-expression of HA-hTPC2 in HEK293 cells resulted in a 3-fold increase in the maximal specific binding of [^{32}P]NAADP. Such an increase in the maximal specific binding is indicative of NAADP binding to hTPC2 and thus further supports the view that TPC2 may act as an NAADP receptor. Furthermore, competitive [^{32}P]NAADP displacement assays using membranes from HA-hTPC2 cells revealed that TPC2 exhibits two binding sites for NAADP, one with a high affinity and one with a low affinity. Furthermore, paired studies on mouse

liver, which were identified as exhibiting the highest expression levels of TPC2 across all mammalian tissues studied thus far, revealed a similar binding curve. Thus, K_d values of ~5 nM and ~7 μM were obtained with membranes isolated from hTPC2 expressing cells compared with ~7 nM and ~5 μM with membranes from mouse liver. The high affinity (5 nM) binding site is consistent with the binding affinity reported in pancreatic β-cells, heart and brain preparations (Bak *et al.*, 2001; Masgrau *et al.*, 2003; Patel *et al.*, 2000b). Moreover, the presence of 2 binding sites (~130 nM and ~12 μM) has also been observed in previous studies on MIN6 cells. In marked contrast, membranes derived from hTPC2 expressing HEK293 cells showed only low-affinity binding of NADP (K_d value of ~10 μM). This low affinity is also consistent with previous reports using rabbit heart and in sea urchin egg preparations (Bak *et al.*, 2001; Patel *et al.*, 2000a) though it is important to note that the binding of NADP to TPC2 may be due to the molecules similarity to NAADP or may be due to contamination of NADP preparations with trace amounts of NAADP (Lee *et al.*, 1995). The presence of high and low affinity binding sites for NAADP has been suggested to underpin the bell-shaped concentration-response curve to NAADP by conferring homologous desensitisation (Berg *et al.*, 2000; Cancela *et al.*, 1999; Masgrau *et al.*, 2003). This proposed model predicts that occupancy of the high affinity binding site would confer activation of the NAADP receptor / Ca^{2+} release channel, whereas occupancy of the low affinity binding site would confer inactivation of the Ca^{2+} release mechanism.

The increased maximal specific binding observed in HEK293 cells due to over-expression of hTPC2 together with the similar binding affinities observed in mouse liver and other mammalian cell types, further suggests that TPC2 may be the putative NAADP receptor. By contrast TRPML1, although expressed on lysosome membranes, does not appear to bind NAADP in NRK cells (Pryor *et al.*, 2006). The NAADP-binding properties of TPC2 therefore represent an important distinction between this protein channel and other proposed targets of NAADP. Though unlikely, this does not exclude the possibility that accessory proteins may be required for appropriate NAADP / TPC2 interaction, although such an interaction would require a very close coupling in order to maintain the binding properties of TPC2 shown above.

4.4.3 NAADP-mediated Ca^{2+} mobilisation via two-pore channel subtype 2 exhibits a bell-shaped concentration-response curve

Intracellular dialysis of 10 nM NAADP into HA-hTPC2 expressing cells evoked global Ca^{2+} transients that were biphasic in nature, reminiscent of NAADP-evoked Ca^{2+} signals observed in PASMCs in which global Ca^{2+} waves are preceded by spatially restricted Ca^{2+} bursts (Boittin *et al.*, 2002). No such Ca^{2+} transients were observed in hTPC2 expressing cells when NAADP was omitted from the pipette solution, nor when the concentration of NAADP was reduced to 100 pM. Furthermore, in wild-type HEK293 cells, 10 nM NAADP failed to evoke global Ca^{2+} transients and 1 μM NAADP only induced small, spatially restricted Ca^{2+} transients in 3 out of 5 cells. These findings suggest that stable over-expression of hTPC2 confers global Ca^{2+}transients in response to 10 nM NAADP, and that the threshold for initiation of Ca^{2+} signalling via hTPC2 is in the nanomolar concentration range. This is entirely consistent with both the high affinity binding site detected in membranes prepared from hTPC2 expressing cells and with the threshold for NAADP-mediated Ca^{2+} signals in PASMCs (Boittin *et al.*, 2002).

NAADP also evoked global Ca^{2+} transients at concentrations of 1 μM and 100 μM. In marked contrast, however, 1 mM NAADP failed to evoke any identifiable Ca^{2+} signal in hTPC2 expressing cells, despite the fact that all cells exhibited Ca^{2+} transients in response to CCh, which mediates Ca^{2+} release via IP_3 (van Koppen *et al.*, 2001). Thus, at high (mM) concentrations NAADP appears to desensitise TPC2 without affecting Ca^{2+} release via IP_3Rs i.e. observed desensitisation is homologous. Furthermore, the inhibitory effect of high concentrations of NAADP indicates that in hTPC2 expressing cells, NAADP-mediated Ca^{2+} release exhibits a bell-shaped concentration-response curve consistent with other mammalian cells (Berg *et al.*, 2000; Cancela *et al.*, 1999; Masgrau *et al.*, 2003). That low concentrations (nM) of NAADP activates TPC2 whereas high concentrations (mM) are inhibitory is also consistent with the 2 binding affinities for NAADP that are exhibited by hTPC2. Thus, it is likely that a high affinity binding site, occupied at ~10 nM NAADP, confers channel activation, whereas when the low affinity binding site, occupied at NAADP concentrations ≥1 mM, confers inactivation / desensitisation.

4.4.4 Two-pore channel subtype 2 expression is knocked down by shRNA in HEK293 cells stably over-expressing two-pore channel subtype 2

Transfection with shRNA against hTPC2 was used in order to confirm that the Ca^{2+} transients observed in hTPC2 expressing cells in response to NAADP were entirely dependent on over-expression of hTPC2. Western blot and immunocytochemistry confirmed successful knockdown of hTPC2. Although the transfection efficiency was not complete (~70%), transfected cells were successfully identified using an RFP reporter, and in cells expressing this reporter the density of HA-hTPC2 labelling was reduced by approximately 8-fold. All cells that exhibited mRFP fluorescence as a result of shRNA transfection failed to respond to intracellular dialysis of 10 nM NAADP. In marked contrast, the Ca^{2+} transient in response to the application of 1 mM CCh remained unaffected. Furthermore, intracellular dialysis of NAADP into hTPC2 expressing cells that had been transfected with scrambled shRNA evoked global Ca^{2+} transients that were similar to those observed in control cells. I can conclude, therefore, that NAADP mediates Ca^{2+} signals via hTPC2.

4.4.5 NAADP mobilises Ca^{2+} via two-pore channel subtype 2 from lysosome-related acidic organelles

Pre-incubation of hTPC2 expressing cells with thapsigargin (1 μM) resulted in the inhibition of global Ca^{2+} transients and revealed smaller, spatially restricted Ca^{2+} transients. The effect of thapsigargin on NAADP-mediated Ca^{2+} release in hTPC2 expressing cells suggests that the initiation of Ca^{2+} signals does not require a functional ER store, but that a functional ER store is required for subsequent amplification of initial NAADP-induced Ca^{2+} signals into a global Ca^{2+} transient. This partial inhibition of the total Ca^{2+} release is reminiscent of the inhibition of the NAADP-mediated global Ca^{2+} wave but not spatially restricted Ca^{2+} bursts in PASMC by thapsigargin (Boittin *et al.*, 2002) and dantrolene (Chapter 3). The partial inhibition of NAADP-mediated Ca^{2+} signalling in hTPC2 expressing cells by thapsigargin is therefore consistent with the view that NAADP initiates Ca^{2+} signals via a two-pool mechanism in sea urchin eggs and PASMCs, whereby NAADP initially releases Ca^{2+} from a thapsigargin-insensitive Ca^{2+} store that is then amplified by CICR from the S / ER (Boittin *et al.*, 2002; Churchill *et al.*, 2001a). Furthermore,

given the fact that HEK293 cells do not express high levels of RyRs (Aoyama *et al.*, 2004), amplification is most likely to occur by CICR via the activation of IP_3Rs, and this was confirmed by the fact that heparin, like thapsigargin, blocked only the amplification of local NAADP-dependent Ca^{2+} signals into global Ca^{2+} waves. That NAADP-mediated Ca^{2+} release is amplified by CICR via IP_3Rs is consistent with previous reports (Berg *et al.*, 2000; Cancela *et al.*, 1999; Churchill *et al.*, 2000). Furthermore, that IP_3Rs may form junctional complexes is consistent with a recent study that demonstrated that IP_3R2, present in the ER, may form tight complexes with adenylyl cyclase subtype 6 present on the plasma membrane (Tovey *et al.*, 2008).

When the above is taken together with the fact that only localised Ca^{2+} transients were observed in response to relatively high concentrations (1 micromolar) NAADP in wild-type HEK293 cells, this suggests that the expression level of endogenous TPC2 in HEK293 cells may not be sufficient for effective coupling between TPC2 and the ER. This could be explained by the spatial distribution of lysosome-related Ca^{2+} stores in HEK293 cells, which may form "loose junctions" with the ER such that the Ca^{2+} released via endogenous TPC is not sufficient to breach the threshold for CICR via IP_3Rs.

That TPC2 releases Ca^{2+} from lysosome-related stores in response to NAADP was confirmed using the V-H^+-ATPase inhibitor bafilomycin A1, which is thought to deplete lysosome-related acidic organelles of Ca^{2+} by collapsing the proton gradient (Christensen *et al.*, 2002; Churchill *et al.*, 2002). Pre-incubation of HA-hTPC2 expressing cells with bafilomycin A1 abolished both phases of the NAADP-mediated Ca^{2+} transient, unlike thapsigargin and heparin. This therefore suggests that NAADP mobilises Ca^{2+} from a lysosomal store in hTPC2 expressing cells and in a manner dependent on hTPC2. This is consistent with the specific targeting of TPC2 to lysosomes, as indicated by co-localisation of hTPC2 with the lysosome markers LAMP2 and LysoTracker. This is entirely consistent with the concept that NAADP mobilises Ca^{2+} from lysosome-related acidic organelles in a number of cell types including sea urchin eggs, neuronal cell lines (PC12), coronary artery SMCs, cerebral cortex neurons, PASMCs and ventricular myocytes (Brailoiu *et al.*, 2006; Brailoiu *et al.*, 2005; Churchill *et al.*, 2002; Kinnear *et al.*, 2004; Macgregor *et al.*, 2007; Yamasaki *et al.*, 2004; Zhang *et al.*, 2006a).

Importantly, bafilomycin did not inhibit the Ca^{2+} transient evoked by CCh. Therefore, bafilomycin is without effect on Ca^{2+} release from the ER via IP_3Rs in

HEK293 cells. Thus, it would appear that in hTPC2 expressing cells, NAADP mobilises Ca^{2+} from a lysosome-related Ca^{2+} store which is then amplified into a global Ca^{2+} transient by CICR via IP_3Rs present on the ER.

4.4.6 NAADP evokes Ca^{2+} bursts via two-pore channel subtype 1

A potential role for TPC1 in NAADP-mediated Ca^{2+} signalling was also identified. Thus, in hTPC1 expressing cells, NAADP evoked small, spatially restricted Ca^{2+} release events. However, unlike hTPC2 expressing cells, no global signals were observed. This is consistent with the restricted distribution of TPC1 compared to TPC2, and, for that matter, with the distribution of the endosomes to which hTPC1 appears to be specifically targeted. Therefore, it would appear that activation of endosome-bound TPC1 by NAADP results in the release of Ca^{2+} that is insufficient to initiate CICR via IP_3Rs. This could be due to the absence of significant coupling between endosomes and IP_3R rich regions of the ER. However, the endosomal localisation of TPC1 together with the NAADP-evoked Ca^{2+} release in hTPC1 expressing cells suggests that TPC1 may be activated directly by NAADP and thus TPC1 may also contribute to NAADP-dependent Ca^{2+} signalling. Thus, TPCs may represent a family of NAADP receptors, although further investigation will be required to confirm whether or not this is the case.

4.4.7 Two-pore channel subtype 2 is a molecular target of NAADP

In summary, the results presented in this chapter provide compelling evidence in support of TPC2 as a molecular target of NAADP. Over-expression of TPC2 in HEK293 cells confers sensitivity to NAADP, such that intracellular dialysis of 10 nM NAADP elicited a global Ca^{2+} transient that is absent in wild-type HEK293 cells. This transient is abolished by sequence-specific knockdown of hTPC2 expression by shRNA. Furthermore, hTPC2 exhibits a bell-shaped concentration-response curve to NAADP consistent with observations of NAADP-mediated Ca^{2+} signalling in other mammalian cells (Berg *et al.*, 2000; Cancela *et al.*, 1999; Masgrau *et al.*, 2003). Importantly, NAADP-evoked Ca^{2+} transients in HA-hTPC2 expressing cells were abolished by pre-incubation with bafilomycin whereas pre-incubation with thapsigargin resulted in the inhibition of the second but not the first phase of Ca^{2+}

release evoked by NAADP. This is consistent with the lysosomal distribution of TPC2 and with previous reports of NAADP-mediated Ca^{2+} signalling via a 2-pool mechanism (Boittin *et al.*, 2002; Churchill *et al.*, 2001a; Kinnear *et al.*, 2004). These data show that TPC2 exhibits the characteristics observed with respect to native mammalian NAADP receptors and thus TPC2 likely forms NAADP receptors that release Ca^{2+} from lysosome-related acidic organelles. Furthermore, TPCs may represent a family of NAADP receptors as indicated by the fact that TPC1 also underpins NAADP-mediated Ca^{2+} signals (Brailoiu *et al.*, 2009).

Chapter 5: NAADP elicits Ca^{2+} release via two-pore channels in rat pulmonary arterial smooth muscle cells

5.1 Introduction

The results presented in Chapter 3 show that in pulmonary arterial smooth muscle cells (PASMCs) lysosomes form junctional complexes with regions of the sarcoplasmic reticulum (SR) that contain a high density of ryanodine receptor subtype 3 (RyR3) to comprise a trigger zone for Ca^{2+} signalling by NAADP. This model proposes that NAADP acts on a putative NAADP receptor to release a Ca^{2+} burst from lysosome-related organelles. Thereafter these Ca^{2+} bursts are amplified in an all-or-none manner by Ca^{2+}-induced Ca^{2+} release (CICR) from the SR via RyR3, with a resultant propagating Ca^{2+} wave likely carried away from the trigger zone by recruitment of RyR2 by CICR.

Further to this, in Chapter 4 I have provided compelling evidence to suggest that two-pore channels (TPCs) may represent a family of NAADP receptors. In particular, human TPC2 (hTPC2) was shown to be specifically targeted to the membranes of lysosomes and when over-expressed in HEK293 cells these channels bound [^{32}P]NAADP with 2 affinities, consistent with previous reports of NAADP binding to both sea urchin egg and mammalian NAADP receptors (Bak *et al.*, 2001; Billington *et al.*, 2000; Masgrau *et al.*, 2003; Patel, 2004; Patel *et al.*, 2000b). Using HEK293 cells over-expressing hTPC2 I also showed that TPC2 underpins NAADP-mediated Ca^{2+} release from lysosome-related organelles. An initial phase of Ca^{2+} release from acidic stores was clearly amplified by CICR from the ER via IP_3Rs resulting in a biphasic response to NAADP reminiscent of the two-pool mechanism of NAADP-mediated Ca^{2+} signalling in sea urchin egg and PASMCs (Boittin *et al.*, 2002; Churchill *et al.*, 2001a). In marked contrast, NAADP evoked localised Ca^{2+} transients in HEK293 cells over-expressing hTPC1, which did not appear to be amplified into global Ca^{2+} transients by CICR from the ER. Moreover, in contrast to hTPC2, immunofluorescence studies revealed that TPC1 appears to be targeted to endosomal

membranes which exhibit a more spatially restricted distribution than does TPC2 / lysosomes. It therefore seems likely that NAADP also acts on hTPC1 to mobilise Ca^{2+} from endosomes. Thus, it would appear that there is insufficient coupling between TPC1 / endosomes and the ER to support the generation of global Ca^{2+} waves through amplification by CICR from the ER. Therefore, these results indicated that all TPCs may represent a family of NAADP receptors, but that TPC2 is likely of primary importance to the regulation of primary cell function (e.g. smooth muscle contraction) through the generation of propagating, global Ca^{2+} signals.

In order to further characterise the mechanisms underpinning NAADP-mediated Ca^{2+} release in rat PASMCs I therefore sought to determine the involvement of TPCs. Given that TPC3 is not present in primates, rats and mice, although it is present in all other mammals studied thus far. Therefore, TPC3 was excluded from further consideration.

5.2 Methods

5.2.1 RNA extraction for the analysis of two-pore channel content in pulmonary arterial smooth muscle

2nd order branches of the pulmonary artery were identified and dissected out as described previously. Arteries were cut longitudinally and the endothelium was removed by gently rubbing the luminal wall with a cotton bud. The tissue was weighed and snap frozen in liquid nitrogen and stored at -80°C until required. The sample was taken out of the -80°C freezer and TRIzol (10 μl/mg; Invitrogen Ltd., USA) was added to the frozen tissue and the tissue was homogenised using a motorised pestle. The homogenate was divided into aliquots of 1 ml in microcentrifuge tubes and left for 5 minutes at room temperature. 200 μl of chloroform was then added to each tube, mixed and incubated for 2 minutes at room temperature. The samples were then centrifuged at 12000 *g* for 15 minutes at 4 °C. The supernatant was removed and placed into a clean microcentrifuge tube. 0.5 μl of isopropanol per 1 ml of sample was added and the mixture was incubated for 10 minutes at 4 °C. The samples were centrifuged at 12000 *g* for 15 minutes at 4 °C, the

supernatant was removed and discarded and the pellet was washed with 80 % ethanol before being centrifuged at 7500 *g* for 5 minutes at 4°C. Following centrifugation, the ethanol was removed and the pellet was allowed to dry for approximately 10 minutes at room temperature. The dry pellet was resuspended in sterile pure-filtered H_2O containing a ribonuclease inhibitor RNaseOUT (Invitrogen Ltd., USA). Samples were stored at -80°C until required.

5.2.2 Examination of two-pore channel subtype 2 expression in pulmonary arterial smooth muscle by RT-PCR

Reverse transcription was performed in a 200 µl PCR tube containing the following 6 µg of RNA, 1 µl of oligo dT primer and made up to 10 µl with pure-filtered H_2O. The mixture was heated at 70 °C for 5 minutes and then placed on ice for 5 minutes. Following this, the following was added to the reaction mixture: 7 µl pure-filtered H_2O, 0.5 µl RNasin, 5 µl RT buffer, deoxynucleotide trisphosphate mixture (dNTPs; 10 mM) and 1 µl Moloney Murine Leukaemia Virus (MMLV) reverse transcriptase. The reaction mixture was placed in a PCR thermal cycler and heated at 40 °C for 10 minutes, 42 °C for 3 hours, 70 °C for 10 minutes. The cDNA was stored at -20 °C until required.

Polymerase chain reaction was carried out in a 200 µl thin walled PCR tube containing the following mixture: 0.3 µl cDNA, 1 µl of each sense/antisense primer (Table 5.1), 0.2 mM each dNTP, 1.5 mM $MgCl_2$, 0.125 µl Taq polymerase and made up to a final volume of 25 µl with 1 x PCR buffer. The reaction mixture was placed in a PCR thermal cycler (Applied Biosystems) and the following programme was run: 95 °C for 4 minutes followed by 35 cycles of 95 °C for 1 minutes, 54 °C for 1 minute, and 72 °C for 1 minute. Following the 35 cycles the tube was maintained at 72 °C for 10 minutes. The PCR products were then separated on a 2 % agarose gel. 2 g agarose was mixed with 1 ml 100 x Tris Acetate EDTA (TAE) buffer and made up to a final volume of 100 ml with pure filtered H_2O. The mixture was heated until the agarose was dissolved and then allowed to cool. 10 µl SYBR Safe gel stain (Invitrogen) was added and the mixture poured into a taped mould, a comb was inserted and the gel allowed to set for approximately 40 minutes. The comb was removed and the mould was placed into the gel tank containing 1 x TAE. 10 µl of

PCR product (1 μg/ml) was mixed with 2 μl of loading buffer before being loaded onto the gel. In one outer well 2 μl Trackit 1 kb DNA ladder (Invitrogen) was mixed with 18 μl TAE (1 x) and 2 μl loading buffer and loaded onto the gel. The gel was run for 2 minutes at 230 V, followed by approximately 40 minutes at 130 V. The gel was imaged using a Synagene Bio imaging system (Synagene, Synoptics, UK).

Gene	Sense Primer Sequence	Antisense Primer Sequence
TPC2	TGGAGAACTTTCTCCAC	TCACCTGCACAGATGCAAG
TRP6	GCATTCACAACAGTTGAGGA	GGAAAACCACAATTTGGCCCTTGC
TRP7	GCTGTCCATCTTCGTGGCCTCCTTC	AGAAAATGACCATGAACTTGAAGAT
G3PDH	TCCTGCACCACCAACTGCTTAGC	CACCACCCTGTTGCTGTAGC

Table 5.1. Sense and antisense primer sequence for each probe used in reverse transcription polymerase chain reaction studies

Primers of the above sequences correspond to two-pore channel subtype 2 (TPC2), canonical transient receptor potential (TRPC) subtypes 6 and 7, and glyceraldehyde-3-phsophate dehydrogenase (G3PDH).

5.3 Results

5.3.1 Two-pore channel subtype 2 is expressed in pulmonary arterial smooth muscle cells

Previous reports from this laboratory have shown that NAADP mobilises Ca^{2+} from a lysosome-related acidic store in rat PASMCs (Boittin *et al.*, 2002; Kinnear *et al.*, 2004). This is supported by evidence presented in chapter 3 which demonstrated that the initial NAADP-evoked Ca^{2+} burst from lysosomes is amplified by CICR from the SR via the activation of RyR3. To complete this picture I therefore sought to determine whether TPC2 underpins NAADP-mediated Ca^{2+} signalling via lysosomes in PASMCs. In order to determine whether or not TPC2 was expressed in rat PASMCs, lysates of pulmonary arteries (without adventitia or endothelium) were prepared for reverse-transcription polymerase chain reaction (RT-PCR) as described above, and amplification of message from the cDNA obtained was used to determine

whether or not TPC2 is expressed in this tissue. In Fig. 5.1 an agarose gel shows the amplification products from the cDNA obtained from the reverse transcription of RNA within rat PASMC lysates. A clear band is present in the lane corresponding to the sample containing the TPC2 primer and at the appropriate size (~170 bp). Lanes corresponding to the control primers (lane 1-3) show that samples containing the primer for canonical transient receptor potential channel (TRPC) subtype 6 and glyceraldehyde-3-phosphate dehydrogenase (G3PDH) also present clear bands at the appropriate sizes (185 bp and 524 bp respectively). TRPC7 served as a negative control and thus, no clear band was indentified in the lane corresponding to this primer. Therefore, TPC2 is expressed in rat PASMCs, consistent with the proposed ubiquitous expression of TPC2 across all mammalian species and tissues, as discussed in Chapter 4.

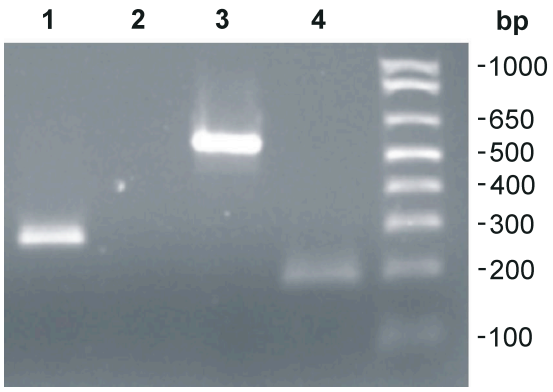

Fig. 5.1. Two-pore channel subtype 2 is expressed in rat pulmonary arterial smooth muscle cells

RT-PCR amplification (35 cycles) of TPC2 cDNA derived from PASMC lysates. Lane 4 shows a clear band corresponding to TPC2 expression. Lanes 1-3 represent control lanes with lanes 1 and 2 containing transcripts for canonical transient receptor potential (TRPC) channel subtypes 6 and 7 respectively and lane 3 containing transcripts for glyceraldehyde-3-phsophate dehydrogenase (G3PDH).

5.3.2 Ned-19 displaces [^{32}P]NAADP binding in sea urchin egg homogenates and HEK293 cells stably over-expressing two-pore channel subtype 2

In order to determine whether TPC2 underpins NAADP-mediated Ca^{2+} release in PASMCs a novel, fluorescent NAADP antagonist was used. This was recently developed by Churchill and colleagues through virtual screening using a large chemical library (Naylor *et al.*, 2009). Of the candidates tested Ned-19 had a high degree of 3D overlap and proved to be the most potent inhibitor of NAADP-mediated Ca^{2+} release in a sea urchin egg homogenate high-throughput screening assay (Naylor *et al.*, 2009). Inhibition of [^{32}P]NAADP binding by Ned-19 was also shown to be

dose-dependent with an IC_{50} of 2 μM (Naylor *et al.*, 2009). Moreover, pre-incubation of both sea urchin eggs and mouse pancreatic beta cells with Ned-19 resulted in the inhibition of NAADP-evoked Ca^{2+} release (Naylor *et al.*, 2009), demonstrating that Ned-19 may be used as an effective cell permeable and selective antagonist of NAADP-mediated Ca^{2+} signalling in both mammalian and non-mammalian cells.

In chapter 4, I showed that over-expression of hTPC2 in HEK293 cells confers a 3-fold increase in the maximal binding of [^{32}P]NAADP. Therefore, in order to verify that Ned-19 would be suitable for use as an antagonist of NAADP-mediated Ca^{2+} signalling and as a fluorescent label of NAADP receptors the ability of Ned-19 to bind to TPC2 and displace NAADP was first determined. To this end, I (in collaboration with Dr. Margarida Ruas and Dr. Xiaotong Cheng) investigated whether Ned-19 displaced [^{32}P]NAADP binding to TPC2 in homogenates prepared from either HA-hTPC2 expressing cells or sea urchin eggs. Fig. 5.2 shows a ligand competition assay using membranes derived from HA-hTPC2 cells (filled circles, solid line; Appendix 3, Table 5.1) and sea urchin egg homogenates (open circles, dotted line; Appendix 3, Table 5.2). The displacement of [^{32}P]NAADP was achieved using membranes incubated with a range of Ned-19 concentrations (0.1 μM – 1 mM) prior to the addition of 0.2 nM [^{32}P]NAADP. Fig. 5.2 shows that increasing concentrations of

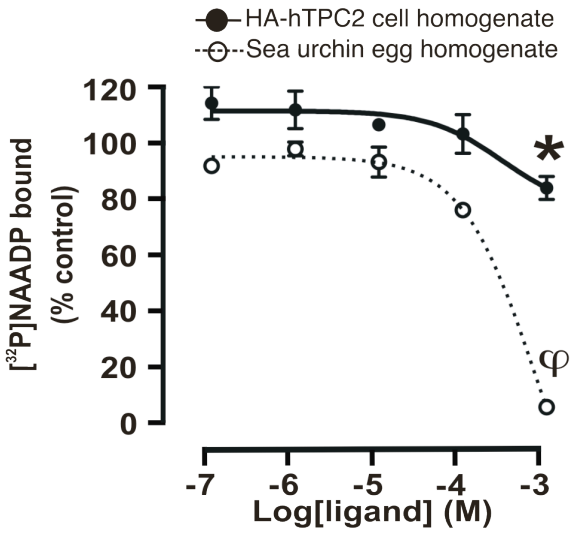

Fig. 5.2. Ned-19 inhibits [^{32}P]NAADP binding in both HA-hTPC2 cells and sea urchin eggs homogenates

0.2 nM [^{32}P]NAADP was displaced using a range of Ned-19 concentrations. Displacement of [^{32}P]NAADP binding from the total membrane prepared from HA-hTPC2 cells reveals that Ned-19 binds to TPC2 and thus displaces NAADP in both HA-hTPC2 cells (n = 3; filled circles, black line) and sea urchin egg homogenates (n = 2; open circles, dotted line). * indicates a statistically significant difference (P<0.05) when compared to the % [^{32}P]NAADP bound in the presence of 100 nM Ned-19 in HA-hTPC2 cell homogenates. φ indicates a statistically significant difference (P < 0.05) when compared to the % [^{32}P]NAADP bound in the presence of 100 nM Ned-19 in sea urchin egg homogenates.

Ned-19 displaced the binding of [^{32}P]NAADP in membranes derived from both HA-hTPC2 cells and sea urchin eggs with the half maximal inhibitory concentration (IC50) value calculated for sea urchin eggs as 702 μM. This suggests that Ned-19 binds to TPC2, displacing NAADP and is therefore consistent with Ned-19 acting as an NAADP antagonist in both mammalian and non-mammalian cells. This is also consistent with the characterisation of Ned-19 by Naylor *et al.* which, in addition to the results described above, also showed that Ned-19 does not accumulate in the lumen of acidic organelles but rather it labels NAADP receptors (Naylor *et al.*, 2009) suggesting that its inhibitory effect is specifically due to binding of the NAADP receptor. From considering Fig. 5.2 it is apparent that although there is a significant inhibition of [^{32}P]NAADP binding by Ned-19 (1 mM) in both cell-types there is variation in the potency of inhibition. This may be explained by the fact that NAADP is thought to act as a non-competitive antagonist and therefore its inhibition of [^{32}P]NAADP binding due to Ned-19 binding altering the NAADP binding site indirectly (Dr. Grant Churchill, *personal communication*). Given that the sequence homology between sea urchin egg TPCs and mammalian TPCs is <50% this may therefore explain the variation between the ability of Ned-19 to inhibit [^{32}P]NAADP binding in each cell type. Nevertheless, the displacement of [^{32}P]NAADP binding is evident in both sea urchin egg and HEK293 cells and is consistent with Ned-19 acting as a selective NAADP antagonist (Naylor *et al.*, 2009). Therefore, the use of Ned-19 is suitable for determining whether or not TPC2 underpins NAADP-mediated Ca^{2+} release in PASMCs.

5.3.3 The NAADP antagonist Ned-19 specifically labels two-pore channel subtype 2 stably expressed in HEK29 cells

To date, no specific antibody for labelling of rat TPC2 has been developed. However, Ned-19, due to it being a tryptophan derivative, is a fluorescent molecule (excitation 360 nm, emission 458 nm) (Naylor *et al.*, 2009). To circumvent the lack of specific antibodies I therefore determined whether or not the fluorescent NAADP antagonist Ned-19 could be used as a label for hTPC2, encouraged by the fact that Ned-19 displaced [^{32}P]NAADP binding to hTPC2. In this respect, it is important to note that in cells preincubated with the membrane permeable Ned-19, one would expect low levels of the antagonist to be present throughout the cytoplasm even after

washing. Therefore, in order to determine whether or not Ned-19 labels TPC2, the threshold settings for detection of fluorescence in cells incubated with Ned-19 were raised, in a stepwise manner, beyond the background level. This was used to expose those areas of the cell in which Ned-19 was most concentrated and thus reveal the distribution of Ned-19 binding sites. Fig. 5.3 shows a 3D reconstruction of a series of deconvolved Z-sections (focal depth 0.28 μm, Z step 0.2 μm) taken through a HEK293 cell stably expressing mCherry-tagged (excitation 587 nm, emission 610 nm) hTPC2 that had been pre-incubated (20 minutes) with Ned-19 (100 μM; excitation 360 nm, emission 458 nm). Panel *a* shows the distribution of mCherry-hTPC2 fluorescence labelling (red) and subsequently (*b*) shows the distribution of Ned-19 (blue) at a threshold setting of 90, which was used to remove background fluorescence. The threshold for detection of Ned-19 fluorescence was then increased beyond this initial setting such that the areas of the cell in which Ned-19 was most concentrated were revealed. This is shown in the subsequent panels in which the distribution of Ned-19 fluorescence (blue) is shown with the threshold set at (*c*) 100, (*d*) 110, and (*e*) 120. Fig. 5.3 clearly shows that, as expected for a membrane permeable pharmacological agent, Ned-19 was present throughout the cytoplasm. However, raising the fluorescence intensity threshold corresponding to Ned-19 fluorescence revealed a more spatially restricted distribution of Ned-19. That this restricted distribution was non-uniform in nature is indicative of areas in which Ned-19 is more concentrated than others. Moreover, visual comparison of these areas of Ned-19 concentration (Fig.5.3, panel *e*) with the distribution of mCherry-hTPC2 fluorescence (Fig. 5.3, panel *a*) suggests that Ned-19 concentrates in those regions of the cell that mirror regions in which clusters of mCherry-hTPC2 are specifically distributed. It would appear, therefore, that this method can be used successfully to label TPC2 in living cells. The adjustment of the thresholds for Ned-19 fluorescence beyond background levels consequently affects the apparent linear relationship between the 2 elements of labelling under study. Therefore, it is inappropriate to use the Pearson product-moment correlation coefficient to assess the degree of co-localisation. Nonetheless, in regions in which Ned-19 was most concentrated the volume of co-localisation between mCherry-TPC2 and Ned-19 accounted for 24 ± 4 % and 40 ± 7 % of the total volume of mCherry and Ned-19 labelling, respectively (*n* = 6; Appendix 3, Table 5.5). Thus, consistent with the displacement of [^{32}P]NAADP

binding by Ned-19, it would appear that Ned-19 selectively labels TPC2 in living cells.

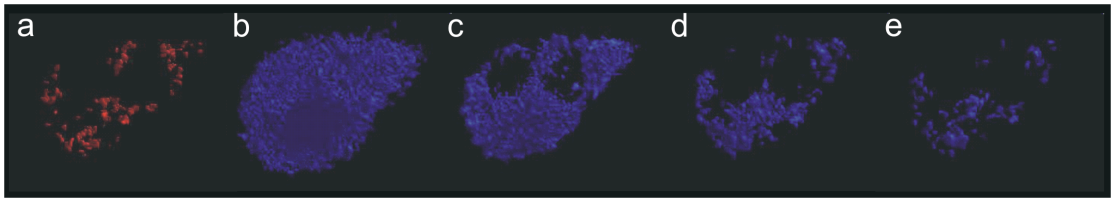

Fig. 5.3. Raising the fluorescence intensity threshold reveals regions in which Ned-19 is concentrated

An example mCherry-hTPC2 cell demonstrating that raising the fluorescence intensity threshold corresponding to Ned-19 fluorescence reveals areas in which Ned-19 is most concentrated. Panel *a* shows a 3D reconstruction of a series of deconvolved Z-sections taken through a mCherry-hTPC2 cell shown showing the distribution of mCherry-labelling of hTPC2 (red; excitation 587 nm, emission 610 nm). Panels *b-e* show 3D reconstructions of deconvolved Z-sections showing the distribution of the fluorescent NAADP antagonist Ned-19 (blue; excitation 360 nm, emission 458 nm) within the same cell and with the fluorescence intensity threshold set at an increasingly higher level: *b*, 90; *c*, 100; *d*, 110; *e*, 120.

5.3.4 Ned-19 exhibits a high degree of concentration at the surface of LysoTracker labelled acidic organelles

To confirm that Ned-19 binds to hTPC2 targeted to lysosome-related organelles, I performed an additional series of experiments on HEK293 cells expressing mCherry-tagged hTPC2. In this instance cells were co-labelled with LysoTracker Green. Fig. 5.4A shows a 3D reconstruction of a series of deconvolved Z-sections (focal depth 0.28 μm, Z step 0.2 μm) taken through a HEK293 cell stably expressing mCherry-tagged hTPC2 (excitation 587 nm, emission 610 nm) that had been pre-incubated (40 minutes) with LysoTracker Green (200 nM; excitation 504 nm, emission 511 nm). Panel A*a* shows a transmitted light image of the cell under study and subsequently shows the distribution of (*b*) LysoTracker Green fluorescent labelling (green), (*c*) mCherry-hTPC2 fluorescent labelling (red), (*d*) a merged image of (*b)* and (*c).* Panel (*e*) reveals the areas of co-localisation (yellow) between mCherry-hTPC2 and LysoTracker Green labelling. These images, strongly suggest that TPC2 is targeted to the membranes of acidic organelles in mCherry-hTPC2 cells.

This is supported by the fact that the volume of co-localisation between mCherry-TPC2 and LysoTracker Green accounted for 26 ± 5 % and 24 ± 6 % of the total volume of mCherry and LysoTracker Green labelling, respectively (n = 6; Appendix 3, Table 5.3). Furthermore, the Pearson product-moment correlation coefficient value for mCherry-hTPC2 and LysoTracker Green labelling was 0.30 ± 0.06 (n = 6; Appendix 3, Table 5.4), illustrating that there is a linear correlation between mCherry-hTPC2 and LysoTracker Green, despite the fact that LysoTracker Green labels the lumen of acidic stores while mCherry-hTPC2 is expressed on the cytoplasmic surface of lysosomes.

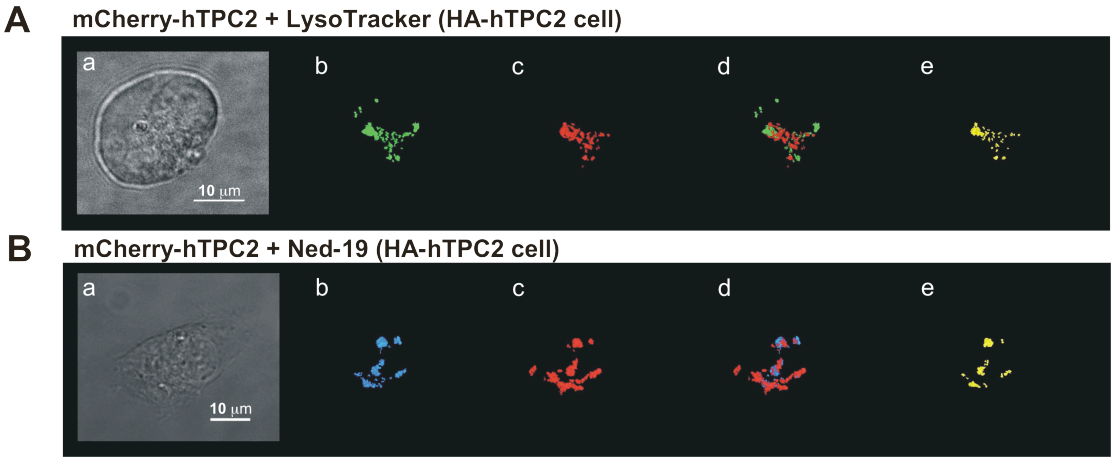

Fig. 5.4. TPC2 is labelled by Ned-19 in HEK293 stably expressing mCherry-hTPC2

Example cells showing the degree of co-localisation between mCherry-tagged hTPC2 (excitation 587 nm, emission 610 nm) and either **A**, LysoTracker Green (excitation 504 nm, emission 511 nm) or **B** Ned-19 (excitation 360 nm, emission 458 nm). In each case: Panel *a* shows a transmitted light image of the isolated mCherry-hTPC2 cell imaged; Panel *b* shows a 3D reconstruction of a series of deconvolved Z-sections taken through the cell shown in panel *a* showing the distribution of either **A**, LysoTracker Green labelling (green) or **B**, regions in which Ned-19 (blue) was most concentrated; Panel *c* shows a 3D reconstruction of deconvolved Z-sections showing the distribution of mCherry-tagged (red) hTPC2; Panel *d* shows a merged image of both panels *b* and *c*; Panel *e* is a 3D reconstruction showing individual volumes of co-localisation (yellow) between hTPC2 and either **A**, LysoTracker Green or **B**, regions in which Ned-19 was most concentrated.

Given the strong degree of co-localisation between mCherry-hTPC2 and both LysoTracker and Ned-19, one would expect a similar degree of co-localisation between Ned-19 and LysoTracker. Indeed, Fig. 5.5 shows a 3D reconstruction of a series of deconvolved Z-sections (focal depth 0.28 μm, Z step 0.2 μm) taken through

a HEK293 cell stably expressing HA-tagged hTPC2. Panel *a* shows a transmitted light image of the cell under study and panel *b* shows regions in which Ned-19 was most concentrated (blue) whereas panel *c* shows the distribution of LysoTracker Red (red). Panel *d* shows the merged image of panels *b* and *c*, and panel *e* shows the volumes represented by co-localisation (yellow) between Ned-19 and LysoTracker Red. Consideration of these images strongly suggests that Ned-19 co-localises with acidic organelles labelled with LysoTracker Red. Furthermore, in regions in which Ned-19 was most concentrated the volume of co-localisation between LysoTracker Red and Ned-19 accounted for 34 ± 7 % and 33 ± 11 % of the total volume of LysoTracker Red and Ned-19 labelling, respectively (n = 4; Appendix 3, Table 5.6). As TPC2 is present on the membranes of such organelles and shares a similar degree of co-localisation with LysoTracker Red it seems likely that Ned-19 labels TPC2, and that TPC2 is targeted to lysosomal membranes.

Given these findings I concluded that Ned-19 could be successfully used to label TPC2 in other wild-type cells, such as PASMCs.

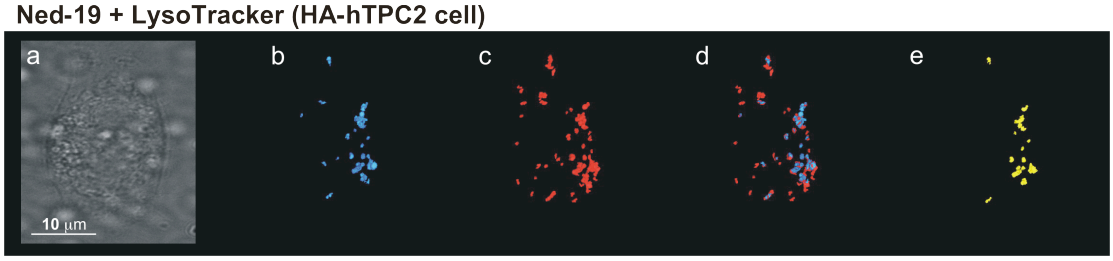

Fig. 5.5. TPC2 is labelled by Ned-19 and co-localises with lysosomes in HEK293 cells stably expressing HA-hTPC

Example cell showing the degree of co-localisation between Ned-19 labelled TPC2 and (excitation 360 nm, emission 458 nm) and LysoTracker Red (excitation 577 nm, emission 590 nm) in an HA-hTPC2 cell. Panel *a* shows a transmitted light image of the isolated cell imaged; Panel *b* shows a 3D reconstruction of a series of deconvolved Z-sections taken through the cell shown in panel *a* showing regions of the cell in which Ned-19 was most concentrated (blue); Panel *c* shows a 3D reconstruction of deconvolved Z-sections showing the distribution of LysoTracker Red labelling (red); Panel *d* shows a 3D representation of LysoTracker Red labelling and concentrated areas of Ned-19 (red and blue respectively); Panel *e* is a 3D reconstruction showing regions of co-localisation (yellow) between Ned-19 labelling and LysoTracker Red labelled organelles.

5.3.5 Ned-19 labelling concentrates on LysoTracker labelled organelles in pulmonary arterial smooth muscle cells

To establish whether Ned-19 binds to TPC2 / lysosomes in rat PASMCs I performed a series of fluorescent imaging experiments similar to those described above. Fig. 5.6 shows a transmitted light image of an isolated rat PASMC under study. Panel *b* shows regions of the cell in which Ned-19 was most concentrated (blue) whereas panel *c* shows the distribution of LysoTracker Red (red). Panel *d* shows the merged image of panels *b* and *c*, and panel *e* shows the areas of LysoTracker Red and Ned-19 co-localisation (yellow). Fig. 5.6 reveals that in PASMCs there is clear co-localisation between areas of high Ned-19 concentration and clusters of acidic organelles, consistent with observations made in HA-hTPC2 expressing cells (Fig. 5.5).

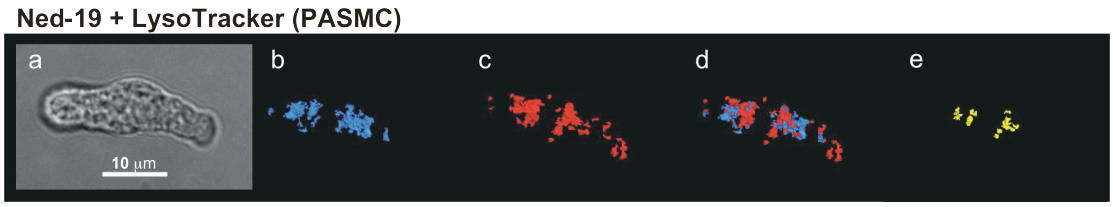

Fig. 5.6. TPC2 is labelled by Ned-19 and co-localises with lysosomes in pulmonary arterial smooth muscle cells

Example cell showing the degree of co-localisation between Ned-19 labelled TPC2 and (excitation 360 nm, emission 458 nm) and LysoTracker Red (excitation 577 nm, emission 590 nm) in an isolated PASMC. Panel *a* shows a transmitted light image of the isolated cell imaged; Panel *b* shows a 3D reconstruction of a series of deconvolved Z-sections taken through the cell shown in panel *a* showing regions of the cell in which Ned-19 was most concentrated (blue); Panel *c* shows a 3D reconstruction of deconvolved Z-sections showing the distribution of LysoTracker Red labelling (red); Panel *d* shows a 3D representation of LysoTracker Red labelling and concentrated areas of Ned-19 (red and blue respectively); Panel *e* is a 3D reconstruction showing regions of co-localisation (yellow) between Ned-19 labelling and LysoTracker Red labelled organelles.

In regions in which Ned-19 was most concentrated the volume of co-localisation between LysoTracker Red and Ned-19 accounted for 39 ± 12 % and 20 ± 1 % of the total volume of LysoTracker and Ned-19 labelling, respectively (n = 4; Appendix 3, Table 5.7). Given the strong degree of co-localisation between Ned-19, LysoTracker Red / Green labelled acidic stores and mCherry-tagged hTPC2 in

HEK293 cells these images strongly suggest that Ned-19 binds to and thus fluorescently labels TPC2 in PASMCs. This is consistent with the finding that Ned-19 displaces [^{32}P]NAADP binding from hTPC2 (Fig. 5.2).

5.3.6 Ned-19 blocks NAADP-mediated Ca^{2+} transients in HEK293 cells stably over-expressing two-pore channel subtype 2

From the above it is clear that: (1) Ned-19 displaces [^{32}P]NAADP binding to membranes from both sea urchin egg homogenates and from HEK293 cells that stably over-express HA-hTPC2; (2) Ned-19 selectively labels LysoTracker labelled acidic organelles in HEK293 cells and mCherry-tagged hTPC2 stably over-expressed in HEK293 cells. I therefore sought to determine whether or not Ned-19 blocked Ca^{2+} signalling via hTPC2 (stably over-expressed in HEK293 cells), which I have previously shown to be a pre-requisite for NAADP-mediated Ca^{2+} release in HEK293 cells that stably over-expressed hTPC2.

In order to achieve this, NAADP (10 nM) was applied intracellularly into HEK293 cells stably over-expressing HA-hTPC2, by dialysis from a patch pipette in the whole-cell configuration of the patch-clamp technique and under voltage-clamp conditions (V = -40 mV). The resultant changes in the intracellular Ca^{2+} concentration were reported by the Fura-2 fluorescence ratio (F_{340}/F_{380}) as described previously. Fig. 5.7A shows an exemplar record of the Ca^{2+} transient triggered by the intracellular dialysis of 10 nM NAADP. The upper panel shows a series of pseudocolour images of the cell in question, which are representative of the F_{340}/F_{380} ratio recorded at the time points labelled on the corresponding record of the F_{340}/F_{380} ratio against time (lower panel). This record shows clearly, that a global Ca^{2+} transient is triggered in response to 10 nM NAADP with a peak change in the F_{340}/F_{380} ratio of 0.92 ± 0.14 (n = 44; Appendix 3, Table 5.8). In marked contrast, Fig. 5.7B shows that no such response was observed following pre-incubation (20 minutes) of cells with 100 μM Ned-19, with a peak change in the F_{340}/F_{380} ratio measuring only 0.08 ± 0.03 (n = 5; P < 0.05; Appendix 3, Table 5.9). However, pre-incubation with 100 μM Ned-19 did not inhibit Ca^{2+} transients evoked by the application of 1 mM carbachol (CCh) the change in the F_{340}/F_{380} ratio measuring 2.19 ± 0.14 in the absence of Ned-19 (n = 7; Appendix 3, Table 5.10) and 2.04 ± 0.45

following pre-incubation (20 minutes) with 100 μM Ned-19 (*n* = 5; Appendix 3, Table 5.11).

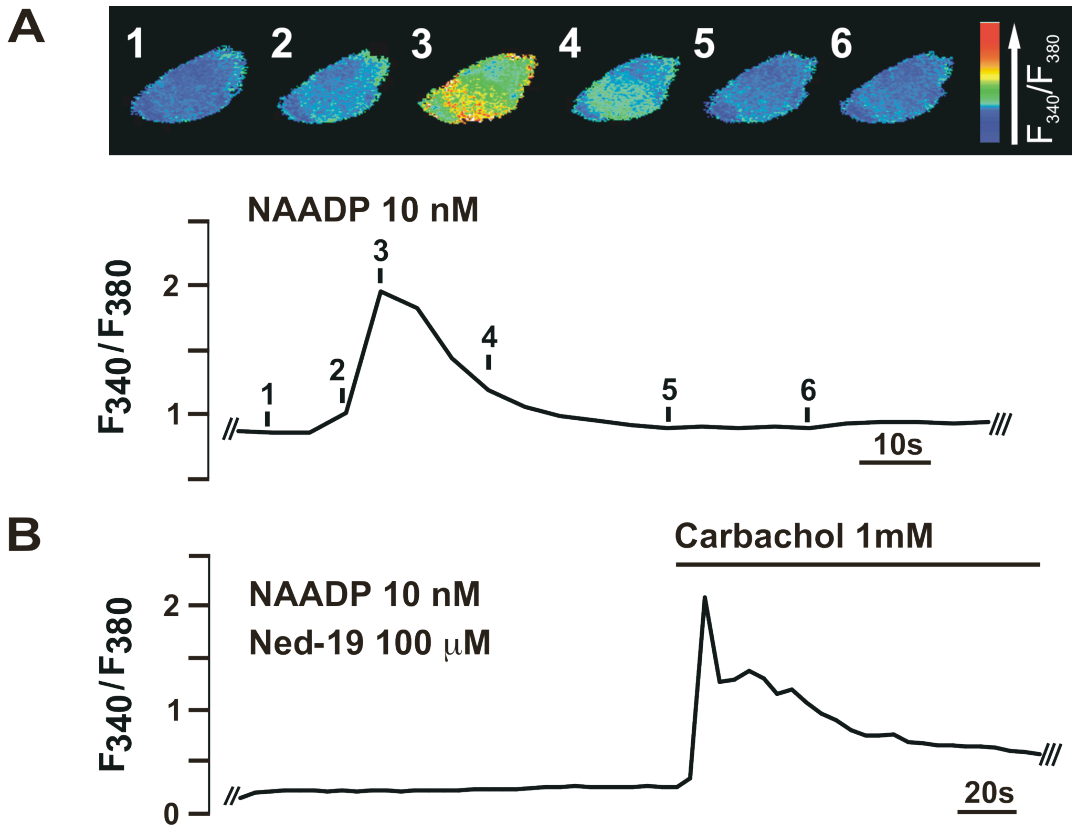

Fig. 5.7. Ned-19 blocks NAADP-mediated but not IP_3-mediated Ca^{2+} release in HA-hTPC2 cells
A Top panel, series of pseudocolour images of the Fura-2 fluorescence ratio (F_{340}/F_{380}) recorded in a HA-hTPC2 cell during the intracellular dialysis of 10 nM NAADP. NAADP evokes a global Ca^{2+} transient. Bottom panel, corresponding record of the F_{340}/F_{380} ratio against time for the cell imaged in the top panel. For this, and the subsequent record, access to the cytoplasm via the formation of the whole-cell configuration is indicated by the two bars at the beginning of the record, and the loss of a GΩ seal is indicated at the end of the record by three bars. **B** Record of the F_{340}/F_{380} ratio against time recorded in a HA-hTPC2 cell pre-incubated (20 min) with 100 μM Ned-19 during the intracellular dialysis of 10 nM NAADP. As no Ca^{2+} transient was observed 1 mM carbachol (CCh) was added towards the end of the record.

That Ned-19 selectively blocks Ca^{2+} signalling in response to NAADP is clearly shown by the bar chart in Fig. 5.8. These data suggest therefore, that the activation by NAADP of Ca^{2+} release via hTPC2 was selectively blocked by Ned-19, and that this was not a consequence of blocking the subsequent amplification of a given Ca^{2+} signal by CICR from the ER via IP_3Rs. This is clear from the fact that IP_3R-

dependent Ca^{2+} release (evoked by CCh) from the ER remained unaffected in the presence of Ned-19. Therefore, consistent with both the binding and immunofluorescence data, Ned-19 appears to act as a selective antagonist of NAADP at hTPC2.

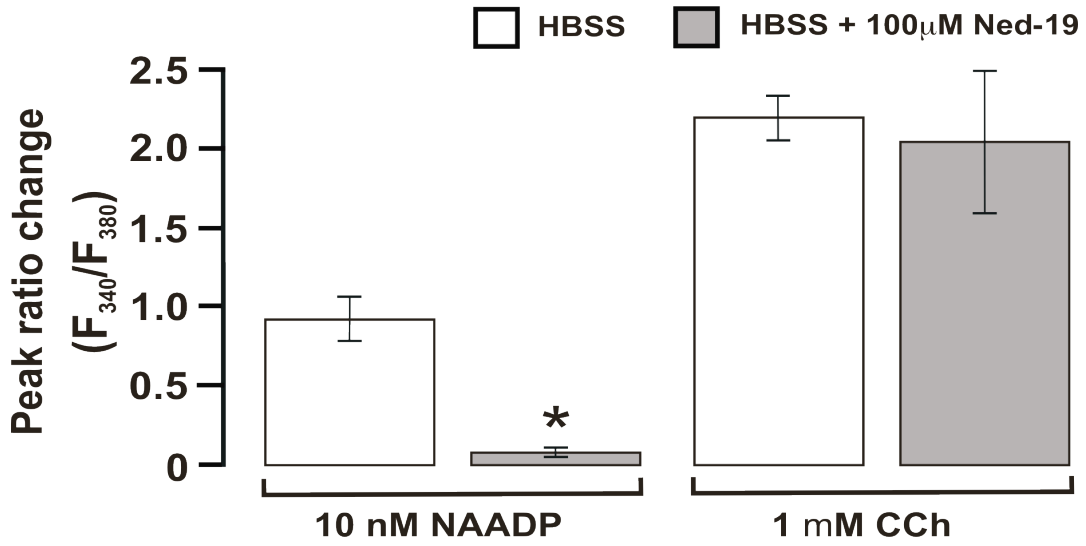

Fig. 5.8. Ned-19 inhibits the global Ca^{2+} release in response to NAADP but not carbachol in HA-hTPC2 cells

Bar chart showing the peak change in the Fura-2 fluorescence ratio (mean ± S.E.M.) recorded in HA-hTPC2 cells in response to either the intracellular dialysis of 10 nM NAADP or extracellular application of 1 mM carbachol (CCh). The responses to NAADP and CCh were recorded in either the absence (white box; NAADP n = 44; CCh n = 7) or presence of 100 μM Ned-19 (grey box; NAADP n = 5; CCh n = 5). * indicates a statistically significant difference ($P < 0.05$) when compared to the peak change in fluorescence ratio in response to 10 nM NAADP in the absence of 100 μM Ned-19.

5.3.7 Ned-19 blocks NAADP-mediated Ca^{2+} transients in pulmonary arterial smooth muscle cells

Having established that Ned-19 binds to hTPC2 and subsequently inhibits NAADP-mediated Ca^{2+} release via hTPC2, Ned-19 was used to determine whether TPC2 functions as a NAADP receptor in PASMCs. The effect of Ned-19 on Ca^{2+} transients evoked by the intracellular dialysis of NAADP (10 nM) from a patch pipette was studied in the whole-cell configuration of the patch clamp technique and under current clamp conditions (I = 0), with changes in the intracellular Ca^{2+} concentration reported by the Fura-2 fluorescence ratio (F_{340}/F_{380}). An exemplar

record is shown in Fig. 5.9A. The upper panel shows a series of pseudocolour images of the Fura-2 fluorescence ratio recorded in an isolated PASMC during the intracellular dialysis of 10 nM NAADP, with the record of the Fura-2 fluorescence ratio against time shown in the lower panel. Intracellular dialysis of 10 nM NAADP induced global Ca^{2+} waves that resulted in a mean increase in the mean Fura-2 fluorescence ratio of 0.91 ± 0.20 (n = 5; Appendix 3, Table 5.12). In marked contrast, Fig. 5.9B shows that no such transient was evoked by 10 nM NAADP following pre-incubation of PASMCs with Ned-19 100 μM, with the maximal change (non-transient) in the Fura-2 fluorescence ratio measuring only 0.13 ± 0.06 (n = 5; P < 0.05; Appendix 3, Table 5.13). Significantly, neither spatially restricted Ca^{2+} bursts, nor global Ca^{2+} waves were observed. Importantly, however, Ned-19 was without effect on Ca^{2+} transients evoked by the application of 2.5 mM caffeine in the same cells (Fig. 5.9B). Indeed, Fig. 5.10 shows that there was no significant difference in the peak increase in the F_{340}/F_{380} ratio triggered by extracellular application of caffeine (2.5 mM) in either the absence of Ned-19 (1.73 ± 0.18; n = 7; Appendix 3, Table 5.15) or following pre-incubation (20 minutes) with 100 μM Ned-19 (1.11 ± 0.31; n = 3; Appendix 3, Table 5.16). Thus, Ned-19 does not block SR Ca^{2+} release via RyRs nor, therefore, the ability of PASMCs to amplify any NAADP-dependent Ca^{2+} bursts from lysosomes by CICR from the SR via RyRs. In contrast to the effect of RyR inhibition with dantrolene (Chapter 3), however, Ned-19 abolished NAADP-induced Ca^{2+} signals and therefore blocked NAADP-dependent Ca^{2+} bursts, as does depletion of acidic Ca^{2+} stores with bafilomycin A1 (Kinnear *et al.*, 2004). These findings are consistent, therefore, with the view that Ned-19 blocks NAADP-dependent Ca^{2+} release from lysosomes via TPCs without affecting RyR-dependent Ca^{2+} release from the SR. Moreover, Fig. 5.9C shows that intracellular dialysis of 1 μM IP_3 induced global Ca^{2+} transients in PASMCs in the presence of 100 μM Ned-19, resulting in a mean increase in the Fura-2 fluorescence ratio of 1.02 ± 0.41 (n = 4; Appendix 3, Table 5.14). Thus, IP_3R-dependent Ca^{2+} release from the SR in PASMCs would also appear to be unaffected by Ned-19.

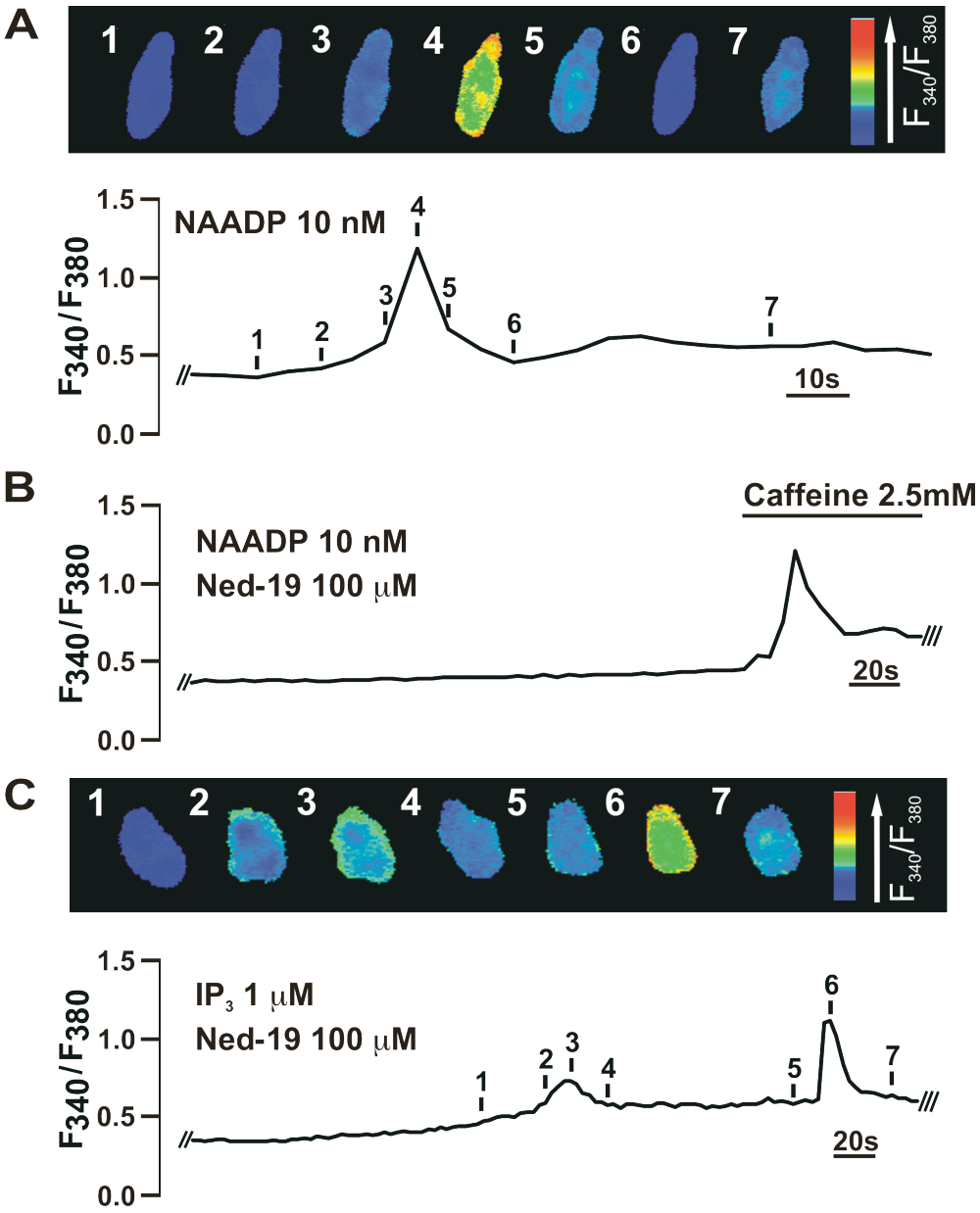

Fig. 5.9. Ned-19 blocks NAADP-mediated but not IP_3-mediated Ca^{2+} release in pulmonary arterial smooth muscle cells

A Top panel, series of pseudocolour images of the Fura-2 fluorescence ratio (F_{340}/F_{380}) recorded in a PASMC during the intracellular dialysis of 10 nM NAADP. Bottom panel, corresponding record of the F_{340}/F_{380} ratio against time for the cell imaged in the top panel. For this, and the subsequent records, access to the cytoplasm via the formation of the whole-cell configuration is indicated by the two bars at the beginning of the record, and the loss of a GΩ seal is indicated at the end of the record by three bars. **B** Record of the F_{340}/F_{380} ratio against time recorded in a PASMC pre-incubated (20 min) with 100 μM Ned-19 during the intracellular dialysis of 10 nM NAADP. As no Ca^{2+} transient was observed 2.5 mM caffeine was added towards the end of the record. **C** Top panel, series of pseudocolour images of the F_{340}/F_{380} ratio recorded in a PASMC pre-incubated (20 min) with Ned-19 (100 μM) during the intracellular dialysis of 1 μM IP_3. Bottom panel, corresponding record of the F_{340}/F_{380} ratio against time for the cell imaged in the top panel.

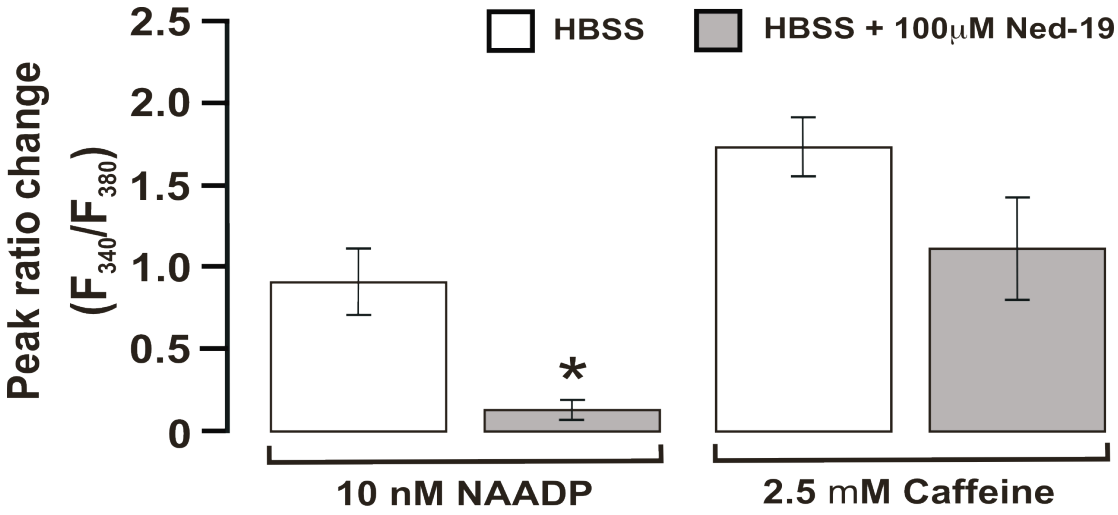

Fig. 5.10. Ned-19 inhibits the global Ca^{2+} release in response to NAADP but not caffeine in pulmonary arterial smooth muscle cells

Bar chart showing the peak change in the Fura-2 fluorescence ratio (mean ± S.E.M.) recorded in PASMCs in response to either the intracellular dialysis of 10 nM NAADP or extracellular application of 2.5 mM caffeine. The responses to NAADP and caffeine were recorded in either the absence (white box; NAADP n = 5; caffeine n = 7) or presence of 100 μM Ned-19 (grey box; NAADP n = 5; caffeine n = 3). * indicates a statistically significant difference ($P < 0.05$) when compared to the peak change in fluorescence ratio in response to 10 nM NAADP in the absence of 100 μM Ned-19.

5.4 Discussion

5.4.1 Two-pore channel subtype 2 is present in pulmonary arterial smooth muscle cells and is targeted by the selective NAADP antagonist Ned-19

The results presented in chapter 4 suggest that NAADP mediates Ca^{2+} release via TPC2 in HEK293 cells that stably over-express TPC2. Consistent with this proposal, in this chapter RT-PCR analysis revealed that TPC2 is expressed in rat PASMC, which is an important observation given that NAADP-dependent Ca^{2+} release from lysosome-related stores is observed in rat PASMCs (Boittin *et al.*, 2002; Kinnear *et al.*, 2004).

Over-expression of hTPC2 in HEK293 cells resulted in a 3-fold increase in the maximal binding of [^{32}P]NAADP when compared to wild-type HEK293 cells (Chapter 4), and therefore TPC2 represents an NAADP receptor. Thus, the

observation that the NAADP antagonist Ned-19 was found to displace 0.2 nM [^{32}P]NAADP binding to TPC2 from membranes enriched with hTPC2, and from membranes derived from sea urchin egg homogenates provides further confirmation that: (1) TPC2 is an NAADP receptor and (2) Ned-19 is an NAADP antagonist and / or inhibitor of NAADP-dependent Ca^{2+} signalling via TPC2. It is worth noting, however, that Ned-19 is thought to act as a non-competitive antagonist and therefore its inhibition of [^{32}P]NAADP binding may not be due to competitive displacement of NAADP but rather due to Ned-19 binding altering the NAADP binding site indirectly (Dr. Grant Churchill, *personal communication*). This may explain why Ned-19 appeared less effective at reversing NAADP binding to HA-hTPC2 membranes than it was in reversing binding to sea urchin egg membranes, as the sequence homology between sea urchin egg TPCs and mammalian TPCs is <50%. Nonetheless, the displacement of [^{32}P]NAADP binding is consistent with Ned-19 acting as a selective antagonist of NAADP-mediated Ca^{2+} signalling in both mammalian and non-mammalian cells (Naylor *et al.*, 2009).

As mentioned above, to date there are no specific antibodies raised against rat TPCs. Therefore, in lieu of specific antibodies I exploited the useful fluorescent property of Ned-19 to demonstrate that TPCs are targeted to acidic stores in rat PASMCs. In doing this, I first considered that the concentration of a given ligand within a solution that does not contain a receptor for said ligand (e.g. the cytoplasm) is uniform due to diffusion that conforms to Brownian motion. However, this situation changes over time if a receptor for the ligand is present within the solution, due to ligand-receptor interactions. At equilibrium, the number of ligand binding events equals the number of dissociation events and therefore there are multiple interactions per second per receptor. Such interactions will affect the normal pattern of diffusion, with a distribution bias towards the receptor binding sites. Therefore, as a result of multiple binding and dissociations a local concentration gradient will become established, with the concentration of the ligand (e.g. Ned-19) decreasing as the distance from the receptor (e.g. TPCs) increases. Moreover, this local concentration gradient would be exaggerated when receptors are clustered, due to the diffusional distance between binding sites being reduced. Thus, if Ned-19 binds to TPCs / NAADP receptors one would expect it to concentrate in regions of the cell proximal to clusters of TPCs on endo / lysosome membranes. It seemed likely, therefore, that I could identify TPC binding sites by increasing the intensity threshold

setting for detection with respect to Ned-19 fluorescence, beyond that required for removal of background fluorescence. In this way, I considered it likely that I could obtain 3D reconstructions of cells in which only those regions within the cell in which Ned-19 was most concentrated were visible. Consistent with this view, examination of the cellular distribution of TPC2 in HEK293 cells that stably over-expressed mCherry-tagged hTPC2 revealed that TPC2 co-localises with LysoTracker labelled lysosomes, and furthermore, that hTPC2 and LysoTracker labelled acidic stores, respectively, co-localised with areas of the cell in which Ned-19 was most concentrated. It is reasonable to conclude, therefore, that Ned-19 binds lysosome-targeted TPC2 and can thus be used to label TPC2 and thereby the membranes of lysosome-related organelles in all cell types. With this in mind, I examined the cellular distribution of Ned-19 labelling in acutely isolated rat PASMCs. This revealed that areas of the cell in which Ned-19 was most concentrated co-localised with clusters of LysoTracker-labelled lysosomes. Together these results support the view that TPC2 is present in PASMCs, is localised to lysosomal membranes and, of particular importance, is targeted by the selective NAADP antagonist Ned-19.

5.4.2 Ned-19 inhibits NAADP-mediated Ca^{2+} release in both HEK293 cells that stably over-express two-pore channel subtype 2 and pulmonary arterial smooth muscle cells

As described in chapter 4, intracellular dialysis of 10 nM NAADP into HEK293 cells that stably over-express hTPC2 evoked global Ca^{2+} transients that were biphasic in nature. Pre-incubation (20 minutes) of hTPC2 expressing HEK293 cells with Ned-19 abolished both phases of the NAADP-induced Ca^{2+} transient. This block of both phases was reminiscent of the effect of depletion of acidic Ca^{2+} stores with the vacuolar proton pump inhibitor bafilomycin A1 (see Chapter 4) and thus suggests that Ned-19 blocks NAADP-evoked Ca^{2+} release from lysosomes. The fact that Ned-19 was without effect on Ca^{2+} signals induced by carbachol (IP_3) confirms that this is likely the case, rather than the observed block being due to attenuation by Ned-19 of the amplification of lysosomal Ca^{2+} signals by CICR from the ER. This is consistent with the fluorescent labelling of hTPC2 by Ned-19 and with the displacement of [^{32}P]NAADP binding to hTPC2 by Ned-19. Given that HEK293 cells do not express high levels of RyRs (Aoyama *et al.*, 2004) it is therefore unlikely that Ned-19 is

exhibiting its inhibitory effect via interaction with RyRs. Therefore, these data show that Ned-19 targets TPC2 and thus selectively inhibits NAADP-mediated Ca^{2+} release in HEK293 cells.

Intracellular dialysis of 10 nM NAADP into isolated PASMCs evoked global Ca^{2+} waves that were again biphasic in nature, as a result of Ca^{2+} bursts from lysosome-related stores being subsequently amplified by CICR from the SR via RyRs (Boittin *et al.*, 2002; Churchill *et al.*, 2001a; Kinnear *et al.*, 2004). Consistent with my observations on HEK293 cells expressing TPC2, Ned-19 blocked both NAADP-mediated Ca^{2+} bursts and global Ca^{2+} waves in PASMCs, again consistent with the effect of depleting acidic Ca^{2+} stores with bafilomycin A1 on Ca^{2+} signalling by NAADP in this cell type (Kinnear *et al.*, 2004). When taken together with the co-localisation of Ned-19 and LysoTracker fluorescence, these findings strongly suggest that TPCs are present on endo / lysosomal membranes in PASMCs and that Ned-19 blocks NAADP-dependent Ca^{2+} release via these channels in PASMCs. Importantly, I also found Ned-19 to be without effect on Ca^{2+} release by either intracellular dialysis of IP_3 or extracellular application of caffeine (RyR activation) in isolated PASMCs. Thus, in PASMCs IP_3R- and RyR-dependent Ca^{2+} release pathways remained unaffected in the presence of Ned-19 and, therefore, the ability of the SR to amplify any Ca^{2+} burst remained intact. Importantly, this conclusion is consistent with the original characterisation of Ned-19 which demonstrated that pre-incubation of both pancreatic acinar cells and sea urchin eggs with Ned-19 inhibited NAADP-mediated Ca^{2+} release (Naylor *et al.*, 2009).

That TPC2 and not TPC1 mediates global Ca^{2+} signals in response to NAADP in PASMCs, seems likely given the inability of TPC1 / endosomes to couple to the ER via CICR in HEK293 cells. Furthermore, previous studies have shown that the cathepsin C substrate glycyl-L-phenylalanine 2-napthylamide (GPN) specifically disrupts lysosomal Ca^{2+} stores via osmotic lysis and, subsequently, blocks the generation of Ca^{2+} signals in response to NAADP (Berg *et al.*, 1994; Churchill *et al.*, 2002). Importantly, cathepsin C is not present in endosomes and, therefore, GPN does not disrupt endosomal Ca^{2+} stores. Thus, it would appear that NAADP-dependent Ca^{2+} release via TPC1, endogenously expressed in wild-type cells, may be insufficient to generate clearly defined and measureable (with methods employed) local Ca^{2+} signals (Berg *et al.*, 1994; Churchill *et al.*, 2002).

I conclude, therefore, that TPCs are expressed in PASMCs, are targeted to acidic stores and underpin NAADP-induced Ca^{2+} release from acidic, lysosome-related Ca^{2+} stores in this cell type. However, further experiments are required to confirm TPC2 and not TPC1 underpin global Ca^{2+} signals by NAADP in PASMCs.

Chapter 6: General Discussion

Since its discovery in 1987 (Clapper *et al.*, 1987) NAADP has been shown to mobilise Ca^{2+} in a wide variety of organisms including invertebrates, vertebrates and plants (Albrieux *et al.*, 1998; Berg *et al.*, 2000; Cancela *et al.*, 1999; Chini *et al.*, 1995a; Chini *et al.*, 1995b; Mojzisova *et al.*, 2001; Navazio *et al.*, 2000; Santella *et al.*, 2000; Zhang *et al.*, 2006a) and has been described as the most potent Ca^{2+}-mobilising molecule identified to date (Galione *et al.*, 2009). Given the broad range of species that exhibit NAADP-dependent Ca^{2+} signalling, it is clear that this Ca^{2+}-mobilising second messenger plays an important role in cellular Ca^{2+} homeostasis. Yet despite this, the molecular identity of the NAADP receptor has, until now remained elusive.

Recently the transient receptor potential channel mucolipin 1 (TRPML1) which is a lysosome-bound channel, was proposed to function as a NAADP receptor (Zhang *et al.*, 2008). However, in normal rat kidney cells (NRK) over-expression of TRPML1 failed to increase NAADP binding (Pryor *et al.*, 2006). Other groups have also suggested that the primary function of TRPML1 is to act as either a Fe^{2+} (Dong *et al.*, 2008) or a H^{+} release channel (Soyombo *et al.*, 2006). Further evidence contrary to the view that TRPML1 is an NAADP receptor comes from the finding that the antibody used by Zhang *et al*., to label / block TRPML1 would appear to label elements within TRPML1 null cells suggesting that the antibody is non-selective (Prof. Antony Galione, *personal correspondence*). NAADP has also been proposed to act directly on ryanodine receptors (RyRs) to release Ca^{2+} (Dammermann *et al.*, 2005; Hohenegger *et al.*, 2002). However, RyR antagonists such as ryanodine, procaine and ruthenium red failed to abolish NAADP-dependent Ca^{2+} signalling in both mammalian and non-mammalian cells (Boittin *et al.*, 2002; Chini *et al.*, 1995a; Lee *et al.*, 1995). Moreover, RyR1 and RyR2 reconstituted into lipid bilayers did not appear to be activated by NAADP (Copello *et al.*, 2001). Therefore, there is significant evidence to suggest that NAADP does not directly activate either TRPML1 or RyRs but acts on a discrete receptor. In 2000 the two-pore channel subtype 1 (TPC1) was first cloned and identified as a novel two-domain channel with an unknown function (Ishibashi *et al.*, 2000). In this thesis I have provided evidence in support of the view that TPCs represent a family of NAADP receptors

6.1 Two-pore channels in relation to other cation channels

Two-pore channels (TPCs) are novel members of the voltage-gated cation channel superfamily. Examination of their primary sequence revealed a predicted structure consisting of 12 transmembrane (TM) regions that are divided into 2 homologous domains of 6 TM regions each (S1-S6). Importantly, and characteristic of members of this superfamily, TPCs contain a re-entrant P-loop between S5 and S6 of each domain. This basic 6-TM unit is representative of all members within the voltage-gated ion channel superfamily, from the single domain channels such as transient receptor potential channels (TRPs) and the cation channel of spermatozoa (CatSpers), to the 4 repeat domain of the pore-forming subunit of voltage-gated Ca^{2+} channels (Ca_v) (Yu *et al.*, 2005). Of the voltage-gated cation channel superfamily members, TPCs share the greatest homology with Ca_v and voltage-gated Na^+ channels. TPCs are also closely related to CatSpers and some TRPs albeit to a lesser extent than either Na_v or Ca_v. This is particularly intriguing given that single domain channels such as TRPs form tetramers whereas only 1 of the 4-repeat domain containing α-subunit of Ca_v is required for the formation of a functional pore. This has led others to propose that TPCs channels function as dimers with the 4 P-loops (2 from each monomer) coming together in order to form the central pore (Zong *et al.*, 2009). Given the similarity to both TRPs and Ca_v and the conserved 6-TM organisation found in each protein, TPCs are purported to be evolutionary intermediates resulting from 2 rounds of duplication from a common 6 TM, single domain protein to the 4-fold symmetry of 24 TM channels such as Ca_v and Na_v (Anderson *et al.*, 2001; Ishibashi *et al.*, 2000).

Further support for the view that TPCs may be intermediary steps is taken from the finding that the 3 animal TPC subtypes (TPC1, TPC2 and TPC3) and plant TPC1 are expressed in a wide variety of species in both plant and animal kingdoms. This suggests that they represent an ancient gene family. However, it is important to note that TPC3 appears to be absent in primates and rodents such as mice and rats. Furthermore, species such as honeybees and silkworms contain only TPC1 encoding genes (*TPCN*1) whereas *C. elegans* and *D. melanogaster* do not appear to contain any sequence encoding TPCs. Conversely, sequences for *TPCN*1 and *TPCN3* but not *TPCN*2 are found in choanoflagellates. Consideration of the species distribution of

TPCs suggests that although the genes encoding TPCs appear to be from an ancient gene family, the absence of 1 or more TPC subtypes (including a complete absence of TPCs) from a number of species would indicate that TPCs represent an important ion channel family that may not be essential for cell survival.

6.2 NAADP mobilises Ca^{2+} via two-pore channels that are targeted to lysosome-related organelles

Examination of the cellular distribution of TPCs revealed that TPC2 is targeted to the membranes of lysosomes but not those of early or late endosomes, Golgi apparatus, mitochondria or the ER. Conversely, TPC1 and TPC3 showed little or no co-localisation with either lysosomal membrane markers and TPC2, but appeared to be primarily targeted to the membranes of endosomes in addition to other unidentified vesicular organelles. Clearly, all mammalian TPCs are expressed on the membranes of endolysosomes, which is consistent with the targeting of plant TPC1 to the membranes of vacuoles (Peiter *et al.*, 2005). Given that NAADP releases Ca^{2+} from acidic lysosome-related organelles (Churchill *et al.*, 2002; Kinnear *et al.*, 2004; Yamasaki *et al.*, 2004; Zhang *et al.*, 2004) and that NAADP-mediated Ca^{2+} release is inhibited by both L-type Ca^{2+} channel agonists and antagonists (phenylalkylamines and dihydropyridines) (Genazzani *et al.*, 1996a; Genazzani *et al.*, 1997) the structure and localisation of TPCs and TPC2 in particular, naturally led me to investigate whether or not TPCs represent NAADP receptors.

Consistent with a role for TPCs in NAADP-dependent Ca^{2+} signalling, HEK293 cells that stably over-expressed TPC2 were used to provide, via cell lysates, membranes enriched with TPC2 upon which NAADP was found to bind at two sites, a high and low affinity site with K_d values of ~5 nM and ~7 μM, respectively. This is consistent with the view that NAADP receptors exhibit high and low affinity binding sites that are proposed to underpin the bell-shaped concentration-response curve to NAADP. The high affinity site has been suggested to mediate activation, while the low affinity binding site may confer homologous desensitisation of the receptor (Berg *et al.*, 2000; Cancela *et al.*, 1999; Masgrau *et al.*, 2003).

In HEK293 cells stably over-expressing TPC2 NAADP elicited a biphasic global Ca^{2+} transient which was abolished by depletion of lysosomal Ca^{2+} stores with the vacuolar H^{+}-ATPase inhibitor bafilomycin A1 or when cells were preincubated with shRNA against TPC2. Moreover, the NAADP antagonist Ned-19, which was shown to fluorescently label TPC2 on the lysosomal membrane, selectively blocked NAADP-mediated Ca^{2+} signalling in HEK293 cells. Together these findings suggest that TPC2 underpins NAADP-mediated Ca^{2+} release from lysosomes. Consistent with the two site binding model, I further demonstrated that NAADP-dependent Ca^{2+} signalling via TPC2 exhibited an approximate activation threshold of 10 nM NAADP whereas no response was observed when the concentration of NAADP was increased to 1 mM suggesting significant desensitisation of the channel. This characteristic bell-shaped concentration-response curve has been observed in other mammalian preparations (Berg *et al.*, 2000; Cancela *et al.*, 1999; Masgrau *et al.*, 2003) and homologous desensitisation is also observed in sea urchin eggs (Aarhus *et al.*, 1996; Dickinson *et al.*, 2003; Genazzani *et al.*, 1996a). However, in sea urchin egg a distinction with respect to the desensitisation mechanism is apparent where low sub-threshold concentrations of NAADP desensitise / inactivate the receptor to subsequent activation by maximal NAADP concentrations (Aarhus *et al.*, 1996; Dickinson *et al.*, 2003; Genazzani *et al.*, 1996a). Given that sea urchin eggs express all 3 TPC subtypes whereas only TPC1 and TPC2 are present in human cells, the difference in the mechanisms of homologous desensitisation / inactivation between the cell types may be due to the variation in the individual properties of each TPC subtype which, for TPC1 and TPC3 remain to be determined.

As mentioned above, TPC1 appears to be primarily targeted to the membranes of endosomes which likely represent a smaller Ca^{2+} store. This is consistent with the spatially restricted Ca^{2+} release in response to NAADP in HEK293 cells stably over-expressing TPC1. It would appear, therefore that NAADP mobilises Ca^{2+} via TPC2 and TPC1 from lysosomes and most likely endosomes respectively. It is therefore probable that TPCs may represent a family of NAADP receptors each with a unique cellular distribution conferred by the organelles to which they are targeted, and this raises the possibility that each TPC may confer a degree of versatility to NAADP-mediated Ca^{2+} signalling. Yet more complexity is possible when one considers the fact that both lysosomes and endosomes are mobile within the cytoplasm (Herman *et al.*, 1984; Prekeris *et al.*, 1999; Taunton, 2001) and may utilise actin filaments and

myosin motors to direct trafficking (DePina *et al.*, 1999). Therefore, the targeted movement of these acidic, releasable Ca^{2+} stores may play an important role in region-specific, NAADP-dependent cellular functions such as neurite outgrowth (Brailoiu *et al.*, 2005).

6.3 Functional significance of two-pore channels

6.3.1 Two-pore channels and lysosomal function

Lysosomes are traditionally considered to function as sites of cellular degradation of macromolecules (Dell'Angelica *et al.*, 2000). Given that NAADP-mediated Ca^{2+} release also evokes an alkalinisation of the lysososmal intralumenal pH (Morgan *et al.*, 2007), Ca^{2+} release by NAADP via TPC2 may critically alter the intraluminal pH and thus affect the optimal functioning of hydrolytic lysosomal enzymes such as glucocerebrosidase which degrades glucocerebroside. This enzyme exhibits a marked drop in function at pH ≥5 (van Weely *et al.*, 1993). TPC2-dependent Ca^{2+} signalling may therefore regulate the degradation of macromolecules such as glucocerbroside, with TPC-dependent Ca^{2+} release potentially leading to accumulation of molecules such as glucocerbrosidase. The dysfunction of such signalling may lead to the development of a number of diseases affecting lysosomes (see below).

Lysosomes also play a significant role in the process of autophagy in which cytoplasmic constituents including organelles such as mitochondria are wrapped by a membrane to form autophagosomes that fuse with lysosomes and thus deliver their cargo for subsequent degradation. The organelles are subsequently degraded by lysosomal hydrolases (Marino *et al.*, 2004). Autophagy allows the recycling of damaged organelles and is involved in programmed cell death and consequently the development of cancer is associated with reduced autophagy in malignant cells (Gozuacik *et al.*, 2004; Marino *et al.*, 2004). Furthermore, low lysosomal enzyme activities have been observed in vesicles obtained from liver carcinomas (Gozuacik *et al.*, 2004). This suggests that, as mentioned above, NAADP-dependent Ca^{2+} signalling from lysosomes via TPC2 may affect the optimal functioning conditions of

lysosomal enzymes and thus regulate the process of autophagy. Moreover, bafilomycin inhibits autophagosome-lysosome fusion and intriguingly, this block is believed to be an indirect result of the bafilomycin-induced acidification defect (Klionsky *et al.*, 2008). As inhibition of vacuolar H^+-ATPase by bafilomycin which depletes lysosome-related Ca^{2+} stores and subsequently inhibits of NAADP-mediated Ca^{2+} release (Churchill *et al.*, 2002; Kinnear *et al.*, 2004), TPC2 may also underpin, in part, autophagosome-lysosome fusion.

In HEK293 cells over-expressing hTPC2, but not wild-type HEK293 cells, I observed an element of mechanosensitivity (Fig. 6.1). NAADP-mediated Ca^{2+} release via TPCs may therefore also be involved in mechanotransduction signalling such as that observed in mammalian hair cells, although further investigations are required in order to address a potential role for TPCs in this process.

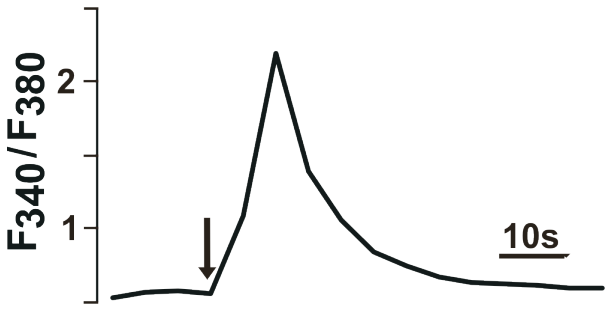

Fig. 6.1. Mechanosensitive response in HEK293 cell over-expressing HA-hTPC2

Record of the Fura-2 fluorescence ratio against time showing the effect of mechanical stimulation using a patch pipette (indicated on the record with a black arrow) in a HEK293 cell over-expressing HA-hTPC2 using the tip of a patch pipette.

It also worth noting that due to their similarity to Ca_v and Na_v, TPCs may be gated by other stimuli such as voltage in addition to NAADP. Indeed, lysosomes contain a number of ion channels such as Cl^- and Na^+ channels (Carrithers *et al.*, 2007; Suzuki *et al.*, 2006) which, together with the electrogenic vacuolar proton pump (Van Dyke, 1996), may contribute to the development of a potential difference across the lysosomal membrane. Changes in lysosomal membrane potential may therefore regulate the gating properties of TPCs. However the voltage-sensing S4 region of both Na_v or Ca_v contain a greater number of conserved positively charged residues (5-9) (Keynes *et al.*, 1999) than observed in TPCs (3-4) suggesting that TPCs may be weakly voltage-dependent if at all.

6.3.2 Two-pore channels and endosomal function

Endosomes are critically involved in the sorting of endocytosed membrane-bound proteins which may then be recycled to the plasma membrane via recycling endosomes or trafficked through the endolysosome system to lysosomes. This trafficking requires multiple membrane fusion events that are dependent on Ca^{2+} release for the effective formation of the SNARE complex (Holroyd *et al.*, 1999; Peters *et al.*, 1998; Pryor *et al.*, 2000). This process requires intracellular Ca^{2+} as, for example, buffering of intracellular Ca^{2+} with EGTA has been shown to inhibit enodocytic protein transport from the ER to Golgi apparatus (Beckers *et al.*, 1989) and increasing the Ca^{2+} concentration has been shown to increase fusion events observed in an *in vitro* assay (Mayorga *et al.*, 1994). Thus, transport of proteins between endolysosomes, Golgi apparatus, and plasma membrane via endosomes may be dependent on the spatially restricted Ca^{2+} release evoked by NAADP acting on TPC1. Such a Ca^{2+} release mechanism via TPC1 may allow the cell to elicit spatially restricted intracellular Ca^{2+} release without triggering a global Ca^{2+} transient. It is therefore possible that cells exhibiting high levels of endosomal protein trafficking may express greater levels of TPC1 than TPC2. This, together with the fact that endolysosomes are mobile organelles may allow cells to specifically target NAADP-sensitive stores to regions of the cell according to the specific function required.

6.3.3 Two-pore channels and recycling endosome function

Internalisation and transport of various plasma membrane bound receptors such as G-protein coupled receptors occurs via the endocytic pathway. Once internalised the receptors are sorted via endosomes and are either down-regulated by transportation to lysosomes or are resensitised by dephosphorylation and recycled to the membrane via recycling endosomes. This process is considered not only to regulate the number of receptors present on the plasma membrane, but may also transport the active ligand-receptor complex and thus propagate their respective signalling cascades (Sadowski *et al.*, 2009; von Zastrow *et al.*, 2007). Endosomes, may therefore deliver active ligand-receptor signalling complexes to specific locations within the cell (Sadowski *et al.*, 2009). NAADP-mediated Ca^{2+} signalling via TPCs on endosomal membranes may therefore contribute to the regulation of GPCR

signalling pathways by determining which of the divergent pathways the internalized receptor follows and / or by indirectly controlling the length of time the receptor spends intracellularly via the regulation of membrane fusion. For example in the human cervical cancer cell line (HeLa) bafilomycin abolishes transport of receptors to lysosomes but not recycling to the plasma membrane (Baravalle *et al.*, 2005). Conversely, bafilomycin reduced the rate of receptor recycling in Chinese hamster ovary (CHO) derived cell lines (Johnson *et al.*, 1993; Presley *et al.*, 1997; Sadowski *et al.*, 2009). The effect of bafilomycin suggests that NAADP-mediated Ca^{2+} release via TPCs may, in part, determine the pathway of internalisation of receptors. That the effect of bafilomycin on these divergent pathways varied according to the cell type used, suggests that this may be due to the relative expression of each TPC subtype in each cell type.

One consideration with respect to the absence of TPCs such as TPC3 in some mammalian species is that their functional role may have been lost due to the development of other channels that render the subtype functionally redundant. For example, the TRP melastatin subfamily type 2 (TRPM2) channel is established as a plasma membrane Ca^{2+} release channel that is activated by adenosine diphosphoribose (ADPR) and may be weakly gated by cADPR and NAADP (Beck *et al.*, 2006; Lange *et al.*, 2008). Recently, Penner and colleagues have shown that TRPM2 acts as a Ca^{2+} release channel that is targeted to LAMP1-labelled lysosome-related organelles as well as the plasma membrane in mouse pancreatic β-cells (Lange *et al.*, 2009). Given that TRPM2 would appear to have diverged at a later date than TPCs (Yu *et al.*, 2005) it is plausible, therefore, that during the process of endocytic recycling from the plasma membrane this, or an as yet unidentified channel, may have exhibited similar functions to TPC3 thus rendering the latter channel redundant within some species.

6.3.4 Two-pore channels and the function of lysosome-related acidic organelles

TPCs may also play an important role in the functioning of lysosome-related organelles such as melanosomes which are responsible for the delivery of melanin to keratinocytes (Bhatnagar *et al.*, 1993). Melanosome-keratinocyte interaction triggers a transient rise in intracellular Ca^{2+} concentration within the keratinocyte which in turn evokes melanosome-dependent melanin transfer. This Ca^{2+} rise is due to the

release of Ca^{2+} from intracellular stores and is unresponsive to further stimulation for up to 2 hours (Joshi *et al.*, 2007). This is reminiscent of the sperm-induced, NAADP-dependent cortical Ca^{2+} flash in sea urchin eggs that is then desensitised to further activation by NAADP (Churchill *et al.*, 2003). Thus a particular TPC subtype(s) may be involved in some of the mechanisms that underpin pigmentation. Consistent with this proposal, 2 coding variants in the *TPCN2* gene are associated with determining blonde versus brown hair colour in a Europeans (Sulem *et al.*, 2008).

6.3.5 Possible function of TPC desensitisation / inactivation

I have shown that, consistent with a number of other mammalian cell types (Berg *et al.*, 2000; Cancela *et al.*, 1999; Masgrau *et al.*, 2003), TPC2 exhibits a bell-shaped concentration-response curve in response to NAADP. Given the fact that, unlike RyR- and IP_3R-dependent Ca^{2+} release, NAADP-mediated Ca^{2+} release is insensitive to changes in cytoplasmic Ca^{2+} concentration (Chini *et al.*, 1996; Genazzani *et al.*, 1997), the inactivation of TPC2 at high concentrations of NAADP may provide a negative feedback mechanism. This may contribute to cessation of signalling by agonists that evoke NAADP-mediated Ca^{2+} signalling such as glucose. For example, the glucose transporter in pancreatic β-cells does not exhibit desensitisation and therefore inactivation of TPCs may function as a downstream negative feedback mechanism for glucose-evoked Ca^{2+} release in pancreatic β-cells (Patel, 2003). Excessive production of NAADP, evoked by glucose, would therefore result in the desensitisation of TPC2 and thus effectively inactivate further channel opening. It is important to note that the desensitisation / inactivation properties of TPC1 and TPC3 remain to be determined and therefore any variation between the subtypes and their respective expression levels may, in part, explain the discrepancy between the inactivation mechanisms observed in sea urchin eggs and mammalian preparations (Aarhus *et al.*, 1996; Berg *et al.*, 2000; Cancela *et al.*, 1999; Genazzani *et al.*, 1996a; Masgrau *et al.*, 2003).

The proposed mechanism of homologous desensitisation may allow the cell to utilise this property in order to exhibit a degree of spatiotemporal memory of previous messenger-specific Ca^{2+} release events. It is quite possible that such "spatiotemporal" controls could play a significant role in a variety of cellular processes. For example,

during fertilisation in sea urchin eggs, upon sperm / egg contact NAADP triggers a cortical Ca^{2+} flash (Churchill *et al.*, 2003). Here desensitisation of TPCs could be vital to the production of an exclusive signalling event, with desensitisation ensuring that it is not repeated within a given time period. This prolonged period of desensitisation following intracellular Ca^{2+} release has also been observed in keratinocytes following melanosome-mediated delivery of melanin (Joshi *et al.*, 2007). Though the role of NAADP in this process has not been investigated, the observed inactivation may be as a result of the inactivation characteristic of NAADP-mediated Ca^{2+} release via TPCs. Therefore, desensitisation / inactivation of TPCs would avoid further and potentially detrimental membrane fusion.

6.3.6 Significance of two-pore channel-dependent Ca^{2+} signalling in disease

Lysosomal storage diseases (LSDs) are caused by the dysfunction of lysosomal enzymes, lysosome-associated proteins involved in lysosomal biogenesis, or enzyme activation / targeting (Parkinson-Lawrence *et al.*, 2006). One of the more common LSDs is Gaucher disease, which is caused by reduced activity of lysosomal glucocerebrosidase. This aberrant function of glucocerebrosidase results in the accumulation of glucosylceramide transforming the cell into a Gaucher cell (Zhao *et al.*, 2002). Interestingly the L-type Ca^{2+} channel blockers diltiazem and verapamil have been shown to partially restore glucocerebrosidase function in Gaucher disease patient-derived fibroblasts (Mu *et al.*, 2008). This finding is particularly interesting given that NAADP-mediated Ca^{2+} release is inhibited by L-type Ca^{2+} channel blockers and agonists (Bak *et al.*, 1999; Genazzani *et al.*, 1996a; Genazzani *et al.*, 1997). These findings, together with the fact that NAADP-mediated Ca^{2+} release alters the intraluminal pH of acidic stores (Morgan *et al.*, 2007) suggests that TPC2 may be involved in regulating the optimal functional conditions for lysosomal enzymes as proposed above (pH), and may therefore be responsible for some of the mechanisms implicated in LSDs such as altering the operating conditions of glucocerebrosidase.

Another common example of LSDs is Niemann-Pick disease which is characterised by defects in the activity of sphingolipid degrading enzymes resulting in the excessive lysosomal storage of sphingolipids (Sturley *et al.*, 2004). Niemann-Pick

disease type A and B (NPA and NPB) occur due to mutations in the enzyme acid sphingomyelinase (SMase) structural gene whereas Niemann-Pick disease type C1 (NPC1) is due to defective cholesterol transport from the lysosome with a secondary defect in SMase activity. Dysfunctional SMase results in the accumulation of unesterified cholesterol in perinuclear lysosomes (Sturley *et al.*, 2004). In addition to defective hydrolysis of sphingolipids, LSDs such as NPC1 may occur due to defective transport of sphingolipids through the endocytic compartments (Marks *et al.*, 2002). As mentioned above endocytic transport of molecules such as sphingolipids requires a number of endosomal / lysosomal membrane fusion events which, in turn, are dependent upon Ca^{2+} release from the acidic stores (Piper *et al.*, 2004). Consistent with this, recent evidence suggests that dysfunctional Ca^{2+} homeostasis precedes the excessive sphingosine storage associated with NPC1 (Lloyd-Evans *et al.*, 2008). As a result, NAADP-mediated Ca^{2+} release was reduced by ~70% in NPC1 mutant cells (Lloyd-Evans *et al.*, 2008). Thus, TPCs may be involved in Niemann-Pick disease either via the alkalinisation of lysosomes, leading to dysfunctional SMase activity, or via defective endosomal transport / membrane fusion.

A further implication of the finding that NAADP mobilises Ca^{2+} via TPCs concerns an autosomal recessive nonsyndrommic deafness locus DFNB63. This locus has been linked with chromosome 11q (Khan *et al.*, 2007) which also contains the gene encoding human TPC2 (*TPCN2*). However, sequencing of the coding regions for the 13 candidate genes including TPCN2 from an affected individual showed that there was no disease-causing mutations (Kalay *et al.*, 2007). Nevertheless, given that audio abnormalities have been recognised as a symptom of a number of LSDs including Pompe disease, Gaucher disease and Hunter syndrome (Campbell *et al.*, 2003; Kamphoven *et al.*, 2004; Peck, 1984) the involvement of TPC2 in these diseases cannot be excluded. Moreover, a disruption in the mechanotransduction apparatus of hair cells has been linked to a number of mouse models of deafness (Grant *et al.*, 2007). This is intriguing given the possible role of TPC2 in mechanotransduction mentioned above.

6.4 Junctional coupling of NAADP-mediated Ca^{2+} signalling via two-pore channels

In HEK293 cells stably over-expressing HA-hTPC2, NAADP evoked biphasic Ca^{2+} transients that are consistent with the 2-pool mechanism of NAADP-mediated Ca^{2+} release shown previously in both pulmonary arterial smooth muscle cells (PASMCs) and sea urchin eggs (Churchill *et al.*, 2001a; Kinnear *et al.*, 2004). I further showed that the initial phase of NAADP-evoked Ca^{2+} release was from lysosomes via TPC2, which was then amplified into a global Ca^{2+} transient by subsequent amplification by Ca^{2+}-induced Ca^{2+} release (CICR) from the ER via the progressive recruitment of IP_3Rs (Fig. 6.2). That NAADP mobilises Ca^{2+} from a lysosome-related store is consistent with the cellular distribution of TPCs and with previous reports from a number of cell types (Brailoiu *et al.*, 2006; Brailoiu *et al.*, 2005; Churchill *et al.*, 2002; Kinnear *et al.*, 2004; Macgregor *et al.*, 2007; Yamasaki *et al.*, 2004; Zhang *et al.*, 2006a). Furthermore, amplification of NAADP mediated Ca^{2+} signalling by CICR from the S / ER has been proposed and demonstrated in a number of previous studies (Berg *et al.*, 2000; Boittin *et al.*, 2002; Brailoiu *et al.*, 2003; Cancela *et al.*, 1999; Churchill *et al.*, 2001a; Churchill *et al.*, 2000; Macgregor *et al.*, 2007). However, it is important to note that in wild-type HEK293 cells NAADP evoked spatially restricted Ca^{2+} release that failed to propagate into a global Ca^{2+} transient suggesting that the endogenous expression level of TPC2 may not be sufficient for effective coupling between lysosomal Ca^{2+} release and the ER. This absence of amplification may be explained by the formation of "loose junctions" between lysosomes and the ER in wild-type HEK293 cells. This is in marked contrast to the data presented in Chapter 3 and by Kinnear and colleagues showing that PASMCs lysosomes form "tight junctions" with the SR (Kinnear *et al.*, 2004). As mentioned above, in HEK293 cells stably over-expressing TPC1, NAADP evoked spatially restricted Ca^{2+} transients that failed to propagate into a global Ca^{2+} transient. This may be indicative of a lower Ca^{2+} content in endosomes compared to lysosomes and / or that endosomes do not form junctional complexes with the ER in HEK293 cells. Therefore, the distribution and cell-specific organisation of organellar junctions may serve to determine the functional effects of NAADP-mediated Ca^{2+} signalling.

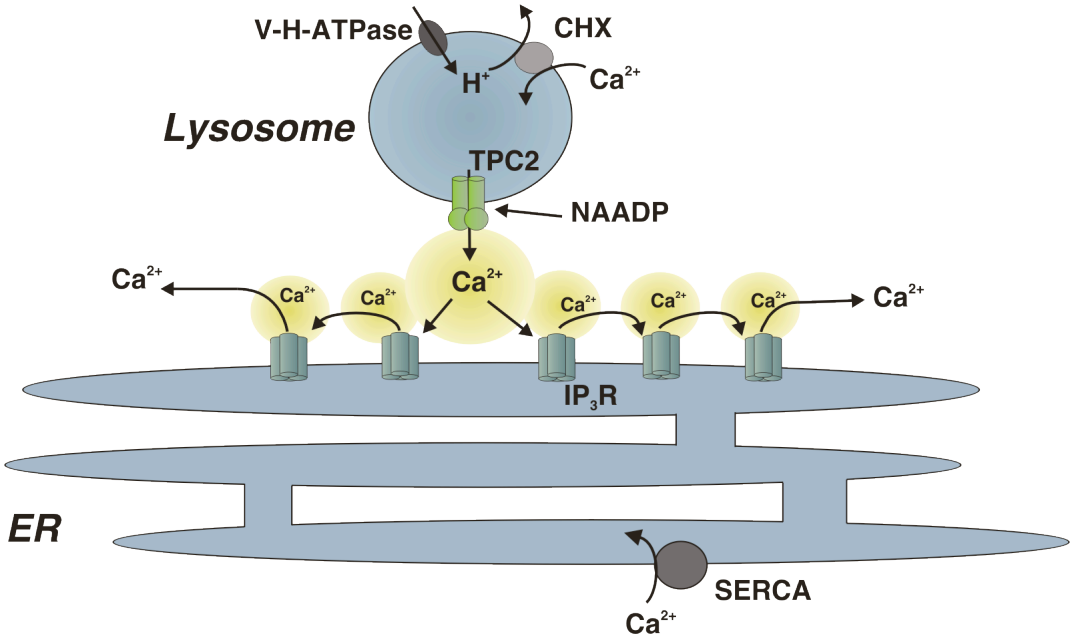

Fig. 6.2. Schematic representation of the amplification of NAADP-evoked Ca^{2+} release from lysosome-related acidic organelles in HEK293 cells

NAADP evokes spatially restricted Ca^{2+} release from lysosome-related acidic organelles via TPC2 which are then amplified via Ca^{2+}-induced Ca^{2+}-release (CICR) from the endoplasmic reticulum (ER) via proximal IP_3Rs. Lysosomes are thought to sequester Ca^{2+} via the action of the vacuolar proton pump (V-H-ATPase) coupled to a Ca^{2+} / H^+ exchanger (CHX) whereas the ER sequesters Ca^{2+} via the sarco / endoplasmic reticulum ATPase (SERCA) pump.

6.4.1 Ca^{2+} release via two-pore channels generate elementary Ca^{2+} signals that may be amplified by coupling to the sarco / endoplasmic reticulum

One consideration with respect to the coupling efficiency between NAADP-evoked Ca^{2+} release and the S / ER is that endolysosomes represent small, discreet Ca^{2+} storage vesicles with the amount of Ca^{2+} released determined by the luminal Ca^{2+} concentration and size of a given vesicle. As NAADP receptors are not sensitive to changes in cytoplasmic Ca^{2+} concentration (Chini *et al.*, 1996; Gerasimenko *et al.*, 2003) the Ca^{2+} transients developed are not regenerative and therefore comprise scattered local Ca^{2+} release events. Consequently, clustering in time and space of the acidic stores may be required in order to breach a given threshold for CICR from the S / ER. This may be analogous to the neuromuscular junction whereby each synaptic vesicle delivers quanta of neurotransmitter that, if a given number are released, is sufficient to breach a given threshold and evoke a post-synaptic potential in an all-or-

none manner. Thus, the varying size of individual endolysosomes and the number of vesicles present in any given cluster, may contribute in part to the different sizes and types of elementary Ca^{2+} signals (e.g. blips, puffs, sparks) described during stimulus-evoked Ca^{2+} transients in a number of cell types (Bootman *et al.*, 1997). However, these events may also be independent of TPCs and due to the recruitment of RyRs or IP_3Rs alone and therefore further investigation is required in order to determine a role for TPCs in these elementary Ca^{2+} signalling events.

The proximity of the S / ER store to the NAADP-sensitive acidic organelle may also determine the efficiency of coupling. For example, in PASMCs a subpopulation of lysosomes appear to be in close apposition to RyRs in the SR and thus may form a "trigger zone" for Ca^{2+} signalling by NAADP (Kinnear *et al.*, 2004). These junctional complexes would allow for the amplification and propagation of Ca^{2+} signals evoked by NAADP. Conversely, loose coupling between endolysosomes and the ER may be required to regulate a number of processes in a manner that does not require exclusive coupling. Indeed, IP_3Rs are present on the ER and Golgi apparatus, which are critically involved in the post-translation modification and trafficking of proteins. As the luminal Ca^{2+} concentration of the ER regulates a number of molecular chaperones (Burdakov *et al.*, 2005), coupling of NAADP-mediated Ca^{2+} release from endolysosomes to IP_3Rs may therefore modulate post-translational protein processing. This may not require a tight junction and as such, loose coupling may be sufficient to modulate a number of receptors on both organelles. However, whether or not TPC2 and IP_3Rs form close junctional complexes within HEK293 cells remains to be determined.

6.4.2 Coupling efficiency may be determined by the receptor subtype present on the sarco / endoplasmic reticulum

The subtype of receptor present on the S / ER may also confer a degree of functional versatility with respect to TPC-dependent Ca^{2+} signalling. For example, all 3 IP_3R subtypes exhibit biphasic regulation by cytoplasmic Ca^{2+} though with different sensitivities (Boehning *et al.*, 2000; Iino, 1990; Missiaen *et al.*, 1998; Miyakawa *et al.*, 1999; Taylor *et al.*, 2002). Therefore the relative expression of each IP_3R subtype in different cell types and / or their cellular distribution may also determine the coupling efficiency between endolysosome stores and the S / ER. As both IP_3 and

Ca^{2+} are required for IP_3R channel opening the basal IP_3 concentration in the region of the junctional complex will also regulate the coupling efficiency especially when one considers that IP_3R subtypes exhibit different affinities for IP_3 (Miyakawa *et al.*, 1999). Therefore the cellular distribution of phospholipase C which generates IP_3 may also prove decisive in determining the relative threshold for CICR in a given region of the cell. Furthermore, IP_3Rs have been shown to aggregate and form clusters upon exposure to low concentrations of IP_3 (Taufiq Ur *et al.*, 2009). Clustering caused a decrease in the open probability and the mean opening time, though this inhibition may be reversed by an increase in the cytoplasmic Ca^{2+} concentration (Taufiq Ur *et al.*, 2009). If endolysosomes were to form junctional complexes with such clusters, then NAADP-evoked Ca^{2+} release may serve to remove the cluster-induced inhibition resulting in an increased open probability and simultaneous opening of clustered IP_3Rs (Taufiq Ur *et al.*, 2009). This in turn would ensure that once the threshold for CICR via IP_3R has been breached, the propagation of the resultant Ca^{2+} wave would be less likely to fail. The subtype of IP_3R in the junctional complex and the local IP_3 concentration may therefore determine the spatiotemporal pattern of NAADP-mediated Ca^{2+} signalling.

6.4.3 Targeted coupling may determine agonist-specific signalling

In PASMCs and HEK293 cells the NAADP antagonist Ned-19 specifically blocked Ca^{2+} signalling by NAADP but not that of caffeine, carbachol and IP_3. It is clear, therefore, that signalling by some stimuli may occur independently of the NAADP / TPC pathway. For example, in pancreatic acinar cells cholecystokinin (CCK) may evoke Ca^{2+} oscillations in an NAADP-dependent manner, whereas Ca^{2+} oscillations evoked by bombesin or acetylcholine may occur independently of NAADP (Burdakov *et al.*, 2000; Cancela, 2001; Yamasaki *et al.*, 2004). Consistent with this, a transient increase in NAADP production is evoked by CCK but not acetylcholine (Yamasaki *et al.*, 2005). One particular advantage of TPC-independent Ca^{2+} release is that these signalling pathways may be regulated in a manner that does not alter the endolysosomal function discussed above.

Conversely, the NAADP / TPC pathway may also function independently of ER coupling. For example, in pancreatic β-cells NAADP production and subsequent Ca^{2+} release from lysosome-related organelles is triggered by extracellular glucose

which, together with Ca^{2+} influx results in insulin secretion (Masgrau *et al.*, 2003; Yamasaki *et al.*, 2004). It is likely, therefore, that spatially restricted Ca^{2+} signals from acidic stores may gate Ca^{2+}-activated cation channels located on the plasma membrane which may lead to membrane depolarisation and subsequent Ca^{2+} influx via voltage-gated Ca^{2+} channels. This is demonstrated in β-cells obtained from TPC2 null mice, in which the NAADP-evoked cation current is absent (Prof. Antony Galione, *Personal Correspondence*). However, it is important to note that NAADP-induced Ca^{2+} signals by NAADP may also be amplified by CICR from the ER via IP_3Rs in response to insulin (Johnson *et al.*, 2002), or via RyRs which may be involved in glucagon-like peptide 1 evoked Ca^{2+} signals (Kim *et al.*, 2008). Thus, the targeting of these acidic Ca^{2+} stores to regions of the cell such as the sub-plasmalemmal region may prove decisive in determining the coupling and resultant characteristics of stimulus-specific NAADP-evoked Ca^{2+} transients (Fig. 6.3).

The mobile nature of endolysosomes would also allow TPC-containing organelles to be targeted to regions such as the leading edge of the motile cell. For example, NAADP has been shown to potentiate neurite outgrowth (Brailoiu *et al.*, 2005) a process that requires the development of actin rich filopodia (Mattila *et al.*, 2008). The formation of these processes via actin polymerisation in a number of cell types such as vascular smooth muscle can be regulated by changes in cytoplasmic Ca^{2+} concentration (Gerthoffer, 2007). NAADP-mediated Ca^{2+} release via TPCs proximal to the sites of actin polymerisation may therefore regulate the formation of filopodia. Consistent with this proposal, bafilomycin has been shown to significantly reduce motility in mouse fibroblasts (Thomsen *et al.*, 1999). Should TPC-dependent Ca^{2+} release regulate processes such as cell motility then this will further demonstrate the versatility conferred by the targeted coupling of NAADP-sensitive endolysosomal stores.

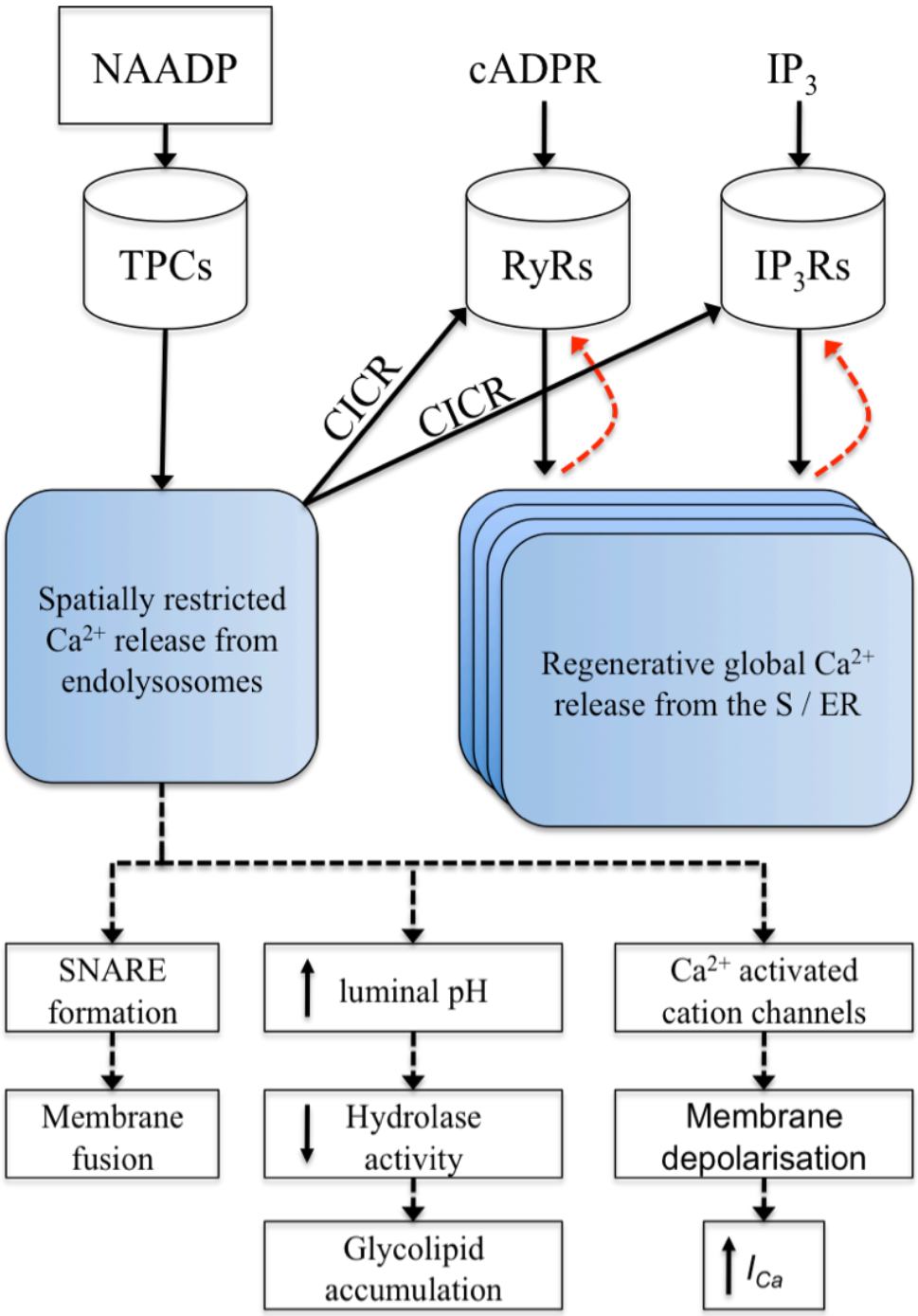

Fig. 6.3. The potential role of two-pore channels in Ca^{2+} signalling

Schematic chart showing the potential Ca^{2+}-dependent pathways regulated by NAADP. The red dashed arrows indicate potential regenerative feedback loops implicated in IP_3R- and RyR-dependent Ca^{2+} signalling. The black dashed arrows indicate some of the potential functions that NAADP-evoked elementary Ca^{2+} signals may regulate. S / ER, sarco / endoplasmic reticulum; CICR, Ca^{2+}-induced Ca^{2+}-release; SNARE, soluble NSF attachment protein (SNAP) receptor; I_{Ca}, plasma membrane Ca^{2+} current.

6.4.4 Two-pore channel subtype 2 and ryanodine receptor subtype 3 comprise a trigger zone for Ca^{2+} signalling by NAADP in pulmonary arterial smooth muscle cells

It is clear that the versatility of coupling of NAADP-sensitive lysosome-related Ca^{2+} stores to various Ca^{2+} sensitive channels, and in particular those capable of mediating CICR, is important in determining the functional properties particular to a given cell. One such example of dynamic coupling is the role of NAADP-mediated Ca^{2+} release in pulmonary arterial smooth muscle cells (PASMCs). Previously, NAADP has been shown to evoke global Ca^{2+} waves via a two-pool system in PASMCs (Boittin *et al.*, 2002; Kinnear *et al.*, 2004). Consistent with a role for TPCs in NAADP-mediated Ca^{2+} release, TPC2 is expressed in this cell type. I have also shown that TPC2 was fluorescently labelled by the NAADP antagonist Ned-19 and that this channel is targeted to the membranes of lysosomes in both PASMCs and HEK293 cells. This, together with the fact that Ned-19 selectively inhibited NAADP-mediated Ca^{2+} release in both cell types suggests that TPC2 likely represents the NAADP receptor in PASMCs. In PASMCs, NAADP is thought to produce spatially restricted Ca^{2+} bursts from lysosomes which are amplified in an all-or-none manner by CICR from the SR via RyRs (Boittin *et al.*, 2002; Kinnear *et al.*, 2004). This is supported by the finding that lysosomes closely associate with RyRs to form a trigger zone for Ca^{2+} signalling by NAADP (Kinnear *et al.*, 2004). I have shown that RyR3 was the predominant RyR subtype in the perinuclear region of PASMCs, which was also the region in which the greatest density of lysosomal labelling was observed. Consistent with this, lysosomes appeared to preferentially co-localise with RyR3 in the perinuclear region. As discussed previously, consideration of the sensitivity to CICR, the maximum gain in response to Ca^{2+}, and the sensitivity to inactivation by Ca^{2+} of each RyR subtype would suggest that RyR3 is well suited to the role in this initial all-or-none manner of amplification of NAADP-evoked Ca^{2+} bursts. Briefly, the estimated half maximal activation (EC_{50}) with respect to Ca^{2+} is ~250 nM and ~400 nM for RyR2 and RyR3, respectively (Chen *et al.*, 1997b; Li *et al.*, 2001) suggesting that RyR3 may confer a higher "margin of safety" with respect to CICR. The observed open probability (P_o) versus cytoplasmic Ca^{2+} concentration curves show that RyR3 exhibits a greater increase in the P_o (0-1) than does RyR2 (0-0.9) and RyR1 (0-0.2) (Chen *et al.*, 1997b; Li *et al.*, 2001). RyR3 also exhibits less sensitivity

to inactivation by Ca^{2+} than does RyR2 (IC_{50} ~3 mM and ~2 mM respectively) and markedly less than does RyR1 (complete inactivation observed at 1 mM) (Chen *et al.*, 1997b; Li *et al.*, 2001). Furthermore, both the marked decline in the density of RyR3 labelling outside the perinuclear region, together with the fact that RyR2 appears to be the predominant subtype within the extra-perinuclear region suggest that RyR2 plays a role in propagating the global Ca^{2+} wave beyond the lysosome-SR junctions. In marked contrast to both RyR2 and RyR3, the distribution of RyR1 was uniform throughout the cell. Nevertheless, RyR1 appeared to be the predominant subtype within the subplasmalemmal region, suggesting that this subtype may play an important role in the regulation of Ca^{2+}-sensitive ion channels in the plasma membrane.

The tight lysosome-SR coupling observed in PASMCs may determine functions specific to this cell type such as, for example hypoxic pulmonary vasoconstriction (HPV). HPV is a property of pulmonary arteries that allows blood to be redirected in order to maximise ventilation-perfusion matching. However, this property can prove damaging in certain circumstances, whereby global, chronic HPV can lead to the development of pulmonary hypertension. Upon exposure to hypoxic conditions pulmonary arteries exhibit an initial transient constriction (Phase 1) and a slow tonic constriction (Phase 2) (Dipp *et al.*, 2001b). It is generally accepted that Ca^{2+} release from the SR via RyRs underpins both Phases 1 and 2 (Evans *et al.*, 2002; Evans *et al.*, 2005; Ward *et al.*, 2009). Importantly, the cADPR antagonist 8-bromo-cADPR appeared to block Phase 2 in an all-or-none manner which suggests that HPV may exhibit a "margin of safety" with respect to cADPR-dependent Ca^{2+} release (Dipp *et al.*, 2001a). This "margin of safety" could be conferred by the components of the lysosome-SR junction and in particular the high threshold for CICR exhibited by RyR3. cADPR is an endogenous regulator of RyRs and may also activate RyRs directly, or facilitate CICR via RyRs (Meszaros *et al.*, 1993; Tanaka *et al.*, 1995). Therefore, cADPR may sensitise RyR3 and RyR2 to activation by Ca^{2+} and thus determine the CICR threshold. Such a role for cADPR has been demonstrated in cardiac myocytes, in which cADPR was shown to increase the depolarisation-induced contraction of myocytes due to sensitising RyR2 to CICR (Cui *et al.*, 1999). Thus, in PASMCs, cADPR may sensitise RyRs to activation by Ca^{2+} and subsequently increase the probability of NAADP-mediated Ca^{2+} bursts being amplified by CICR from the SR via RyRs (Fig. 6.4). 8-bromo-cADPR may therefore exhibit its all-or-

none block by competitive antagonism of cADPR and consequently the threshold for CICR would be increased. In the presence of 8-bromo-cADPR, Ca^{2+} release into the trigger zone via TPC2 may not be sufficient to breach the raised threshold for CICR. TPC2 dependent Ca^{2+} signalling via the lysosome-SR junction may therefore play a critical role in HPV. Consistent with this proposal, pulmonary hypertension is one of the pathological effects of lysosomal storage diseases such as Gaucher and Pompe's disease (Elstein *et al.*, 1998; Jmoudiak *et al.*, 2005; Noori *et al.*, 2002) which, as mentioned above, may be underpinned by dysfunctional NAADP-signalling via TPCs. Therefore, further investigation into Ca^{2+} signalling by NAADP via TPCs is required in order to better understand the mechanisms underpinning diverse spatiotemporal patterns of intracellular Ca^{2+} signalling and how these may determine cell type-specific function.

In summary, the experiments described within this thesis provide compelling evidence to suggest that two-pore channels represent a family of NAADP-gated Ca^{2+}-releasable receptors. These channels underpin localised Ca^{2+} signals in response to NAADP that, dependent on the cell and TPC subtype, may or may not couple to Ca^{2+} release channels present on the S / ER to evoke regenerative, global Ca^{2+} waves. TPCs are targeted to the membranes of endolysosomes and thus my data may shed new light on the potential functions of the organelles with respect to intracellular Ca^{2+} signalling.

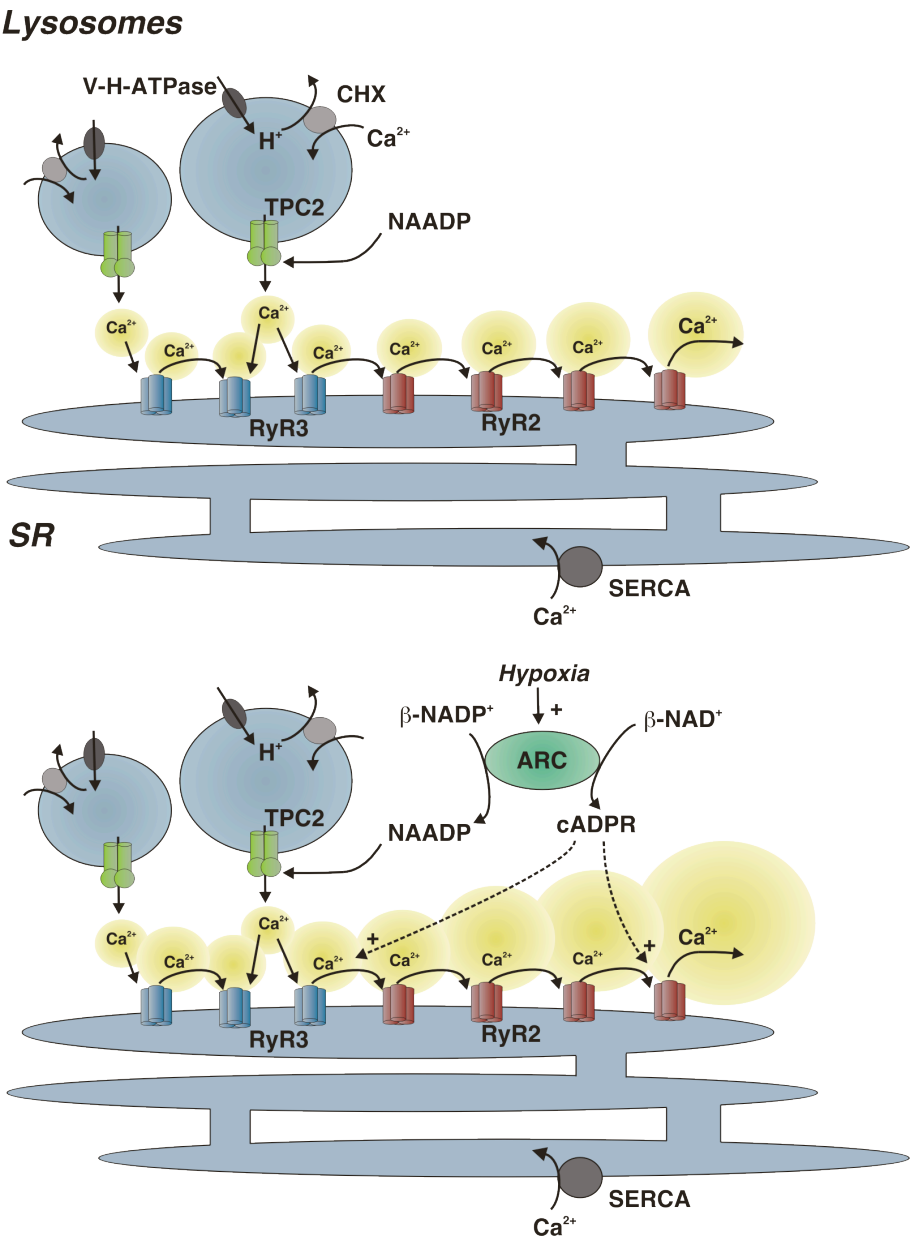

Fig. 6.4. Lysosomes preferentially co-localise with ryanodine receptor subtype 3 to comprise a trigger zone for Ca^{2+} signalling by NAADP in pulmonary arterial smooth muscle cells

Top panel, schematic diagram showing the proposed mechanism of amplification of NAADP-mediated Ca^{2+} bursts by Ca^{2+}-induced Ca^{2+} release from the sarcoplasmic reticulum (SR). Lower panel, schematic diagram representing the potential role for cADPR and NAADP in mediating hypoxic pulmonary vasoconstriction. The dashed arrows indicate how cADPR may sensitise ryanodine receptors (RyR) to activation by Ca^{2+}. NAADP mobilises Ca^{2+} from lysosomes via TPC2 which are then amplified via Ca^{2+}-induced Ca^{2+}-release (CICR) from the sarcoplasmic reticulum (SR) via proximal RyRs. Lysosomes are thought to sequester Ca^{2+} via the action of the vacuolar proton pump (V-H-ATPase) coupled to a Ca^{2+} / H^{+} exchanger (CHX). ADP ribosyl cyclase, ARC; sarco / endoplasmic reticulum ATPase, SERCA pump.

Chapter 7: Future Directions / Experiments

7.1 Are all two-pore channel subtypes NAADP receptors?

The results presented in my thesis show that NAADP evokes Ca^{2+} release via both TPC1 and TPC2 and suggest, therefore, that TPCs represent a family of NAADP receptors. However, experiments with respect to TPC1 were limited to identification of the organelles to which this subtype is targeted (endosomes) and preliminary Ca^{2+} imaging experiments. These studies were not supported by binding data, pharmacological intervention to determine the site of Ca^{2+} release (e.g. depletion of acidic stores with bafilomycin A1) or shRNA experiments; although Brailoiu and co-workers have provided data which appear to show that TPC1 knockdown attenuates Ca^{2+} signalling in response to NAADP in SKBR3 cells that had been transiently transfected with TPC1 and that Ca^{2+} released via TPC1 is derived from acidic Ca^{2+} stores (Brailoiu *et al.*, 2009). In addition to TPC1 and TPC2, TPC3 is also expressed in many animal species, but we have only thus far determined the organelles to which TPC3 is primarily targeted (endosomes). Therefore, an important direction for future investigations would be to determine whether or not all three animal TPCs comprise a family of NAADP receptors.

Using similar techniques to those I have described in this thesis with respect to my studies on TPC2, I propose the following investigations on TPC1 and TPC3:

1. Does over-expression of human TPC1 and chicken TPC3, respectively, increase the maximal binding of [^{32}P]NAADP to membranes derived from HEK293 cells?
2. Does stable over-expression of TPC1 and TPC3, respectively, in HEK293 cells confer Ca^{2+} transients in response to NAADP that are distinct from those observed in wild-type HEK293 cells? This could be confirmed by knockdown of TPC1 and TPC3 using sequence specific shRNA against TPC1 and TPC3, as I have done with respect to TPC2.
3. Are NAADP-induced Ca^{2+} signals via TPC1 and TPC3 blocked following depletion of acidic stores with bafilomycin A1? If so are they

resistant to osmotic lysis of lysosomes with glycyl-L-phenylalanine (GPN), as would be expected if TPC1 and TPC3 are targeted to endosomes (which do not contain cathepsin C) and not lysosomes.

4. Are NAADP-induced Ca^{2+} signals via TPC1 and / or TPC3 amplified by Ca^{2+}-induced Ca^{2+} release from the ER via IP_3Rs, as is the case with TPC2? As before this could be determined by studying the effect on the observed signals of depleting ER Ca^{2+} stores by thapsigargin and by blocking IP_3Rs with heparin.

7.2 Are either of the three ryanodine receptor subtypes NAADP receptors?

One major controversy that remains despite my demonstrating that TPCs act as NAADP receptors is the suggestion that in T-cells and skeletal muscle, that ryanodine receptor subtype 1 (RyR1) may act as an NAADP-activated release channel (Dammermann *et al.*, 2005; Guse, 2009; Hohenegger *et al.*, 2002). This also raises the question of RyR2 and RyR3 acting as NAADP receptors. Because HEK293 cells, as discussed previously, express little or no RyR1, RyR2 or RyR3 and insufficient levels of either TPC1, TPC2 or TPC3 to support significant Ca^{2+} signalling in response to NAADP, these cells offer the perfect model system to address this issue. I would therefore determine by intracellular dialysis of NAADP, whether or not NAADP induces release from ER stores in HEK293 cells that stably over-express RyR1, RyR2 or RyR3.

7.3 Is the antagonism of NAADP-mediated Ca^{2+} signalling by Ned-19 two-pore channel subtype-selective?

In order to use Ned-19 for further characterisation of NAADP-mediated Ca^{2+} signalling via TPCs it is important to determine whether or not Ned-19 inhibits [^{32}P]NAADP to, and NAADP-evoked Ca^{2+} release via all three TPC subtypes. This is particularly important given that in mammalian cells Ned-19 appears to be a non-competitive antagonist of NAADP binding (Dr. Grant Churchill, *personal communication*). Thus, Ned-19 appears to inhibit NAADP binding to TPC2 by

interacting with a site distinct from the NAADP-binding site. Moreover, the sequence homology between TPC1, TPC2 and TPC3 is less than 30%. Therefore, there remains the possibility that Ned-19 may bind to a site that is exclusive to TPC2 i.e. Ned-19 may show selectivity for one TPC subtype over another. I would therefore examine further the effect of Ned-19 in the following manner:

1. Does Ned-19 displace [^{32}P]NAADP binding to membranes derived from HEK293 cells that stably over-express TPC1, TPC2 and TPC3, respectively?
2. Does Ned-19 block NAADP-dependent Ca^{2+} signalling via TPC1, TPC2 and TPC3, respectively, when stably over-expressed in HEK293 cells.

7.4 Do voltage-gated Ca^{2+} channel agonists and antagonists block NAADP-dependent Ca^{2+} signalling via two-pore channels?

Early studies on Ca^{2+} signalling by NAADP in sea urchin egg homogenates demonstrated that voltage-gated Ca^{2+} channel (VGCC) antagonists (both dihydropyridine and phenylalkylamines), the VGCC agonist BAYK8644 and SKF96365 were shown to block NAADP evoked Ca^{2+} release (Genazzani *et al.*, 1996a; Genazzani *et al.*, 1997). I would therefore plan to determine whether or not these agents block NAADP-dependent signalling via TPC1, TPC2 and TPC3, respectively, stably expressed in HEK293 cells. In this way, I would also determine whether or not any of these agents show selectivity for one or other of the three TPC subtypes. If any of the VGCC antagonists block TPCs, this may also explain some of the anomalous therapeutic effects of VGCC antagonists such as nimodipine (e.g. subarachnoid haemorrhage, migraine, cluster headache) (Solomon, 1989; Tomassoni *et al.*, 2008). It is also possible that VGCC antagonists may mediate some of their anti-hypertensive effects via block of TPCs, because Saida and van Breemen showed that VGCCs mediate vasodilation partly by inhibiting intracellular Ca^{2+} release (Saida *et al.*, 1983).

7.5 Does two-pore channel subtype 2 tightly couple to inositol 1,4,5-trisphosphate receptors in HEK293 cells?

Within both pulmonary arterial smooth muscle cells (PASMCs) and HEK293 cells expressing HA-hTPC2, NAADP appeared to evoke global Ca^{2+} transients via a 2-pool mechanism. However the precise mechanism underpinning this biphasic response differed slightly between the two cell types. In both cell types NAADP mobilises Ca^{2+} from lysosome-related organelles. In PASMCs this initial phase of Ca^{2+} release is amplified by Ca^{2+}-induced Ca^{2+} release (CICR) from the sarcoplasmic reticulum (SR) via RyRs (Boittin *et al.*, 2002; Kinnear *et al.*, 2004) (Chapter 3). On the other hand, in HA-hTPC2 expressing cells Ca^{2+} release from lysosomes via TPC2 appears to be amplified by CICR from the endoplasmic reticulum (ER) via inositol 1,4,5-trisphosphate receptors (IP_3Rs) (Chapter 4). Significantly, I have shown that in PASMCs RyR3 in particular is preferentially targeted to the junctional complex that exists between lysosomes and the SR (Chapter 3). The initial amplification stage of NAADP-mediated Ca^{2+} bursts is therefore subtype-specific. Given that all 3 IP_3R subtypes are expressed in human cells, albeit with varying levels of expression (Taylor *et al.*, 1999; Tovey *et al.*, 2008; Wojcikiewicz, 1995), and that each IP_3R subtype exhibit different sensitivities to Ca^{2+} (Bootman *et al.*, 1999; Yule, 2001), TPC2 may form a tight association with a specific IP_3R subtype to comprise a trigger zone for Ca^{2+} signalling by NAADP in HEK293 cells. Alternatively, a Ca^{2+}-regulated phospholipase C (PLC) subtype (e.g. PLCδ) may also be involved and generate IP_3 in response to the initial phase of Ca^{2+} release via TPC2; this too could comprise, in part, a trigger zone. I would therefore investigate any potential role of IP_3Rs and PLC in the following manner:

- Firstly the expression of all 3 IP_3R subtypes and Ca^{2+}-regulated PLC subtypes within HEK293 cells must be verified via RT-PCR, Western blot and / or immunocytochemical analysis of HA-hTPC2 expressing HEK293 cells. Using shRNA and the PLC antagonist U73122 (heparin has already been shown to block CICR via the ER in response to NAADP-evoked Ca^{2+} release via TPC2) the role of each of these components in mediating Ca^{2+} signalling by NAADP could be determined using intracellular dialysis of NAADP.

- Using the sequence specific antibodies, where available, HEK293 cells over-expressing mCherry-tagged hTPC2 (mCherry-hTPC2 cells) can be used in immunocytochemical analysis in order to determine the degree of co-localisation between mCherry-tagged hTPC2 and each IP_3R / PLC subtype. This would indicate whether TPC2 preferentially co-localised with a specific IP_3R and / or PLC subtype as described for RyRs in Chapter 3. Immunogold labelling and electron microscopy could then be used to determine the junctional space between lysosome clusters and the ER. If the junctional space was <100 nm it would constitute a tight junctional association, if any larger one would conclude that only loose junctions were in place.

7.6 Does two-pore channel subtype 2 and ryanodine receptor subtype 3 co-localise in pulmonary arterial smooth muscle cells?

In this thesis I have shown that αIgp120-labelled lysosomes preferentially co-localised with RyR3 in the perinuclear region of PASMCs (Chapter 3). I have also shown that Ned-19 labelled TPC2 co-localised with LysoTracker labelled lysosomes in PASMCs (Chapter 5). Therefore, in order to further confirm that RyR3 and TPC2 comprise a trigger zone for NAADP-mediated Ca^{2+} signalling in PASMCs it is important to determine the degree of co-localisation between these 2 elements.

- Now that the NAADP receptor has been identified, sequence specific antibodies are being developed specifically against human, rat and mouse TPCs. In the future these may be used along with anti-RyR3 antibodies to co-label these proteins within isolated PASMCs. The degree of co-localisation between RyR3 and TPC2 may then be analysed using the volumetric analysis described previously. Immunogold labelling and electron microscopy could also be used to determine the junctional space between TPC2 / lysosomes and RyR3 / SR within the proposed trigger zone for signalling by NAADP

- The contribution of both RyR3 and TPC2 towards NAADP-mediated Ca^{2+} signalling may then be verified using sequence specific shRNA against each

element. However, transfection and long-term incubation (> 48 h) of acutely isolated PASMCs may prove problematic. Therefore, a cultured cell-line may be used such as human pulmonary artery smooth muscle cells (hPASMCs; TCS Cellworks, UK). These cells are viable for ~15 population doublings and may therefore be suitable for shRNA transfection. In order to use these cells their response to intracellular dialysis of 10 nM NAADP must first be characterised and compared to those of acutely isolated rat PASMCs. Secondly, co-localisation between TPC2 and RyR3 within hPASMCs must also be determined.

7.7 Determination of a structural protein within the trigger zone

Given that lysosomal clusters, likely a subpopulation of lysosomes, are held in close association with the sections of the SR containing a high density of RyR3 in PASMCs (Kinnear *et al.*, 2004) a structural protein may exist that holds both TPC2 / lysosomes and RyR3 / SR in a junctional complex.

Homer proteins are structural scaffolds that play an important role in Ca^{2+} signalling. There are 3 identified homer genes encoding proteins Homer1 (including 3 transcripts 1a, 1b and 1c), Homer2 and Homer3 (Worley *et al.*, 2007). With the exception of Homer1a which has a short C-terminal domain, homer proteins are comprised of an N-terminal EVH1 domain with a 200 amino acid C-terminus containing a coiled coil domain and 2 leucine zippers. Interaction of the coiled coil domains allow Homer proteins to form tetramers (Worley *et al.*, 2007). The Homer protein subtypes exhibit different cellular distributions which is exemplified in pancreatic acinar cells whereby Homer1 and Homer2 were exclusively localised to the apical pole whereas Homer3 was located to the basal pole (Shin *et al.*, 2003). Moreover, depletion of Homer2 expression did not appear to affect IP_3-dependent Ca^{2+} signalling suggesting that it was involved in forming Ca^{2+} signalling complexes with Ca^{2+} release channels other than with IP_3Rs (Shin *et al.*, 2003). Given that Homers have been shown to bind to RyRs in both cardiac and skeletal muscle cells (Ward *et al.*, 2004; Westhoff *et al.*, 2003) together with the fact that the NAADP-sensitive lysosome-related Ca^{2+} store is also located in the apical pole of pancreatic acinar cells (Cancela *et al.*, 2002; Yamasaki *et al.*, 2004) a structural role for Homer1

and / or Homer2 in NAADP-mediated Ca^{2+} signalling in PASMCs should be examined.

In cardiac muscle, skeletal muscle, smooth muscle and neurons, there exists close associations between the plasma membrane and the S / ER called junctional membrane complexes (JMCs) which couple RyRs and voltage-gated Ca^{2+} channels (Yamazaki *et al.*, 2009). However, co-expression of RyRs and voltage-gated Ca^{2+} channels in cells from a cultured cell line did not result in the formation of JMCs, suggesting that an additional protein is required for the maintenance of such a coupling (Takekura *et al.*, 1995). This protein was later identified as a member of the junctophilins (JPs), a novel family of structural proteins (Takeshima *et al.*, 2000). There are 4 mammalian JP subtypes (JP1-4) which all express multiple MORN (membrane occupation and recognition nexus) sequences in the N-terminal region and a single transmembrane segment in the C-terminal that spans the S / ER membrane (Yamazaki *et al.*, 2009). JP1 is predominantly expressed in skeletal muscle, whereas JP3 and JP4 are exclusively expressed in the brain. Conversely, JP2 appears to have a broader distribution of expression, with mRNA detected in cardiac, skeletal and smooth muscle tissue (Takeshima *et al.*, 2000). Given that JPs are able to effectively anchor two membrane-bound Ca^{2+} channels in close proximity, there may be an intracellular JMC-like association between lysosome-bound TPC2 and the SR-bound RyR3 that is maintained by a JP subtype. Indeed, within cardiomyocytes, JPs are responsible for holding the components of the JMC at a gap of approximately 12 nm (Takeshima *et al.*, 2000) which is consistent with a role for JPs in maintaining an intracellular junction. As JP2 is expressed within smooth muscle, a structural role for JP2 in linking RyR3 and TPC2 should also be investigated.

7.8 Investigation into cooperative Ca^{2+} signalling between cADPR and NAADP

Given the tight coupling between lysosomes and RyRs present on the SR in PASMCs (Kinnear *et al.*, 2004) it has been proposed that NAADP and cADPR may act in concert to provide further flexibility to the mechanisms regulating NAADP-mediated Ca^{2+} signalling (Evans *et al.*, 2005). Furthermore, it was also suggested that as cADPR may sensitise RyRs to subsequent activation by Ca^{2+}, cADPR may help to

determine the threshold for amplification of NAADP-evoked Ca^{2+} bursts by CICR via RyRs (Evans *et al.*, 2005). Thus a series of Ca^{2+} imaging experiments are required to answer the following questions:

1. Do basal cADPR levels 'prime' RyRs by lowering the threshold for CICR? This may be achieved by pre-incubating acutely isolated PASMCs with the cell-permeable cADPR antagonist 8-bromo-cADPR, prior to intracellular dialysis of NAADP (10 nM). The resultant global Ca^{2+} wave may then be compared to those evoked in the absence of 8-bromo-cADPR.

2. Does an increase in intracellular cADPR concentration lower still further the threshold for CICR and facilitate the generation of regenerative Ca^{2+} waves. A range of cADPR concentrations could be infused into PASMCs in conjunction with a set concentration of NAADP. The resultant global Ca^{2+} waves can then be analysed and compared to those observed in response to NAADP alone. Global Ca^{2+} waves may be analysed for variations in their duration, amplitude, and frequency.

7.9 Investigation into the role of two-pore channels in vascular function

In Chapter 5 of this thesis I have identified the expression of TPC2 in PASMCs and the heart. TPCs may therefore play an important role in regulating cardiovascular function. Given that *Tpc2* knockout (KO) mice have been generated, this would allow one to study the effect of TPC2 expression on heart rate and blood pressure *in-vivo* via radio telemetry or a pressure recording sensor combined with an occluding tail cuff. One could also use *in-situ* organ perfusion to determine any the effects of TPC2 expression on the heart such as the contractile force. Small vessel myography could be used to measure the vascular reactivity and basal tone of arterial rings from wild-type and *Tpc2* KO mice could also be compared to determine the effect of TPC2 expression in these processes.

7.10 Investigation into the role of NAADP-mediated Ca^{2+} signalling in lysosomal storage diseases

7.10.1 Functional investigation into the role of two-pore channels in endosomal membrane fusion in Niemann-Pick disease type C1

A whole-cell endosomal-lysosomal membrane fusion assay in NPC1-mutant CHO cells has been previously developed (Lloyd-Evans *et al.*, 2008). Briefly, cells seeded onto coverslips are incubated with the endosomal fusion marker Oregon green-labelled avidin and with a lysosomal marker biotin-dextran. Membrane fusion is subsequently monitored via fluorescence microscopy by measuring the increase in Oregon green-avidin fluorescence upon binding to biotin-dextran (Lloyd-Evans *et al.*, 2008).

Alternatively, in a cell free system, PC12 cells are harvested and washed with internalization medium containing dextran conjugated with either Alexa-488 or Alexa-594 fluorescent dyes. Fluorescently labelled dextran is commonly used as a probe for endosomes (Lencer *et al.*, 1990). After internalization of the fluorophore-labelled dextran cells are homogenised and centrifuged before collecting the postnuclear supernatant (PNS). The Alexa-488 containing PNS and the Alexa-594 containing PNS are mixed and incubated for a set time. The reaction is stopped by chilling on ice and the fused enzymes are enriched by Nycodenz density gradient centrifugation and then adsorbed onto coverslips. Fluorescence microscopy is then used to determine the degree of co-localisation between the two fluorescent dyes thus giving an indication of the level of endosomal fusion (Brandhorst *et al.*, 2006).

Therefore these techniques could be utilised firstly with HA-hTPC2 and His_6-hTPC1 cells to determine the role of NAADP in endosomal-lysosomal membrane fusion. These cells may be incubated with: (1) Ned-19, (2) repeated applications of membrane-permeable NAADP-AM (Parkesh *et al.*, 2008), repeated applications of NAADP-AM in the presence of Ned-19. Analysis of the degree of fusion in each of these conditions would thus suggest whether or not NAADP is involved in such fusion events and moreover, whether NAADP elicits an increase in fusion events via a particular TPC subtype.

If NAADP-mediated Ca^{2+} release does promote endosomal-lysosomal fusion, then these experiments may be repeated with NPC1-mutant CHO cells to determine whether application of NAADP-AM promotes fusion events and, in part, reverses the NPC1 phenotype.

7.10.2 Functional investigation into the role of NAADP-mediated Ca^{2+} release in Gaucher disease

In Gaucher disease type II fibroblast cell line (GM07968) Kelly and colleagues found that nifedipine, verapamil and diltiazem partially recovered glucocerebroside activity (Mu *et al.*, 2008). Given that Gaucher disease is a lysosome storage disease and TPC2 is specifically targeted to lysosomes, TPC2 gating could alter the luminal pH by releasing Ca^{2+} from lysosomes (Morgan *et al.*, 2007). If VGCC antagonists do indeed block TPC2, VGCC antagonists could possible mediate their corrective effects by blocking TPC2 and thereby adjusting luminal pH to a range that benefits glucocerebrosidase activity. Using the methods outlined in this thesis, this possibility could be investigated.

Chapter 8: References

Aarhus, R, Dickey, DM, Graeff, RM, Gee, KR, Walseth, TF, Lee, HC (1996) Activation and inactivation of Ca2+ release by NAADP+. *J Biol Chem* **271**(15)**:** 8513-8516.

Aarhus, R, Graeff, RM, Dickey, DM, Walseth, TF, Lee, HC (1995) ADP-ribosyl cyclase and CD38 catalyze the synthesis of a calcium-mobilizing metabolite from NADP. *J Biol Chem* **270**(51)**:** 30327-30333.

Albrieux, M, Lee, HC, Villaz, M (1998) Calcium signaling by cyclic ADP-ribose, NAADP, and inositol trisphosphate are involved in distinct functions in ascidian oocytes. *J Biol Chem* **273**(23)**:** 14566-14574.

Amiri, H, Schultz, G, Schaefer, M (2003) FRET-based analysis of TRPC subunit stoichiometry. *Cell Calcium* **33**(5-6)**:** 463-470.

Anderson, PA, Greenberg, RM (2001) Phylogeny of ion channels: clues to structure and function. *Comp Biochem Physiol B Biochem Mol Biol* **129**(1)**:** 17-28.

Aoyama, M, Yamada, A, Wang, J, Ohya, S, Furuzono, S, Goto, T, Hotta, S, Ito, Y, Matsubara, T, Shimokata, K, Chen, SR, Imaizumi, Y, Nakayama, S (2004) Requirement of ryanodine receptors for pacemaker Ca2+ activity in ICC and HEK293 cells. *J Cell Sci* **117**(Pt 13)**:** 2813-2825.

Asahi, M, Kurzydlowski, K, Tada, M, MacLennan, DH (2002) Sarcolipin inhibits polymerization of phospholamban to induce superinhibition of sarco(endo)plasmic reticulum Ca2+-ATPases (SERCAs). *J Biol Chem* **277**(30)**:** 26725-26728.

Asahi, M, Sugita, Y, Kurzydlowski, K, De Leon, S, Tada, M, Toyoshima, C, MacLennan, DH (2003) Sarcolipin regulates sarco(endo)plasmic reticulum Ca2+-ATPase (SERCA) by binding to transmembrane helices alone or in association with phospholamban. *Proc Natl Acad Sci U S A* **100**(9)**:** 5040-5045.

Bahring, R, Milligan, CJ, Vardanyan, V, Engeland, B, Young, BA, Dannenberg, J, Waldschutz, R, Edwards, JP, Wray, D, Pongs, O (2001) Coupling of voltage-dependent potassium channel inactivation and oxidoreductase active site of Kvbeta subunits. *J Biol Chem* **276**(25)**:** 22923-22929.

Bak, J, Billington, RA, Timar, G, Dutton, AC, Genazzani, AA (2001) NAADP receptors are present and functional in the heart. *Curr Biol* **11**(12)**:** 987-990.

Bak, J, White, P, Timar, G, Missiaen, L, Genazzani, AA, Galione, A (1999) Nicotinic acid adenine dinucleotide phosphate triggers Ca2+ release from brain microsomes. *Curr Biol* **9**(14)**:** 751-754.

Baksh, S, Michalak, M (1991) Expression of calreticulin in Escherichia coli and identification of its Ca2+ binding domains. *J Biol Chem* **266**(32)**:** 21458-21465.

Baravalle, G, Schober, D, Huber, M, Bayer, N, Murphy, RF, Fuchs, R (2005) Transferrin recycling and dextran transport to lysosomes is differentially affected by bafilomycin, nocodazole, and low temperature. *Cell Tissue Res* **320**(1)**:** 99-113.

Beck, A, Kolisek, M, Bagley, LA, Fleig, A, Penner, R (2006) Nicotinic acid adenine dinucleotide phosphate and cyclic ADP-ribose regulate TRPM2 channels in T lymphocytes. *FASEB J* **20**(7)**:** 962-964.

Beckers, CJ, Balch, WE (1989) Calcium and GTP: essential components in vesicular trafficking between the endoplasmic reticulum and Golgi apparatus. *J Cell Biol* **108**(4)**:** 1245-1256.

Behne, MJ, Tu, CL, Aronchik, I, Epstein, E, Bench, G, Bikle, DD, Pozzan, T, Mauro, TM (2003) Human keratinocyte ATP2C1 localizes to the Golgi and controls Golgi Ca2+ stores. *J Invest Dermatol* **121**(4)**:** 688-694.

Benham, CD, Tsien, RW (1987) A novel receptor-operated Ca2+-permeable channel activated by ATP in smooth muscle. *Nature* **328**(6127)**:** 275-278.

Berg, I, Potter, BV, Mayr, GW, Guse, AH (2000) Nicotinic acid adenine dinucleotide phosphate (NAADP(+)) is an essential regulator of T-lymphocyte Ca(2+)-signaling. *J Cell Biol* **150**(3)**:** 581-588.

Berg, TO, Stromhaug, E, Lovdal, T, Seglen, O, Berg, T (1994) Use of glycyl-L-phenylalanine 2-naphthylamide, a lysosome-disrupting cathepsin C substrate, to distinguish between lysosomes and prelysosomal endocytic vacuoles. *Biochem J* **300 (Pt 1):** 229-236.

Bernardi, P (1999) Mitochondrial transport of cations: channels, exchangers, and permeability transition. *Physiol Rev* **79**(4)**:** 1127-1155.

Berridge, G, Dickinson, G, Parrington, J, Galione, A, Patel, S (2002) Solubilization of receptors for the novel Ca2+-mobilizing messenger, nicotinic acid adenine dinucleotide phosphate. *J Biol Chem* **277**(46)**:** 43717-43723.

Berridge, MJ (1982) 5-Hydroxytryptamine stimulation of phosphatidylinositol hydrolysis and calcium signalling in the blowfly salivary gland. *Cell Calcium* **3**(4-5)**:** 385-397.

Berridge, MJ, Lipp, P, Bootman, MD (2000) The versatility and universality of calcium signalling. *Nat Rev Mol Cell Biol* **1**(1)**:** 11-21.

Bers, DM (2002) Cardiac excitation-contraction coupling. *Nature* **415**(6868)**:** 198-205.

Bhatnagar, V, Anjaiah, S, Puri, N, Darshanam, BN, Ramaiah, A (1993) pH of melanosomes of B 16 murine melanoma is acidic: its physiological importance in the regulation of melanin biosynthesis. *Arch Biochem Biophys* **307**(1)**:** 183-192.

Bichet, D, Haass, FA, Jan, LY (2003) Merging functional studies with structures of inward-rectifier K(+) channels. *Nat Rev Neurosci* **4**(12)**:** 957-967.

Billington, RA, Genazzani, AA (2000) Characterization of NAADP(+) binding in sea urchin eggs. *Biochem Biophys Res Commun* **276**(1)**:** 112-116.

Blackman, JG, Ginsborg, BL, House, CR (1979) On the effect of ionophoretically applied dopamine on salivary gland cells of Nauphoeta cinerea. *J Physiol* **287:** 67-80.

Blaustein, MP, Lederer, WJ (1999) Sodium/calcium exchange: its physiological implications. *Physiol Rev* **79**(3)**:** 763-854.

Blondel, O, Takeda, J, Janssen, H, Seino, S, Bell, GI (1993) Sequence and functional characterization of a third inositol trisphosphate receptor subtype, IP3R-3, expressed in pancreatic islets, kidney, gastrointestinal tract, and other tissues. *J Biol Chem* **268**(15)**:** 11356-11363.

Boehning, D, Joseph, SK (2000) Functional properties of recombinant type I and type III inositol 1, 4,5-trisphosphate receptor isoforms expressed in COS-7 cells. *J Biol Chem* **275**(28)**:** 21492-21499.

Boittin, FX, Dipp, M, Kinnear, NP, Galione, A, Evans, AM (2003) Vasodilation by the calcium-mobilizing messenger cyclic ADP-ribose. *J Biol Chem* **278**(11)**:** 9602-9608.

Boittin, FX, Galione, A, Evans, AM (2002) Nicotinic acid adenine dinucleotide phosphate mediates Ca2+ signals and contraction in arterial smooth muscle via a two-pool mechanism. *Circ Res* **91**(12)**:** 1168-1175.

Bolton, TB (1979) Mechanisms of action of transmitters and other substances on smooth muscle. *Physiol Rev* **59**(3)**:** 606-718.

Bootman, M, Niggli, E, Berridge, M, Lipp, P (1997) Imaging the hierarchical Ca2+ signalling system in HeLa cells. *J Physiol* **499 (Pt 2):** 307-314.

Bootman, MD, Lipp, P (1999) Ringing changes to the 'bell-shaped curve'. *Curr Biol* **9**(23)**:** R876-878.

Bradford, MM (1976) A rapid and sensitive method for the quantitation of microgram quantities of protein utilizing the principle of protein-dye binding. *Anal Biochem* **72:** 248-254.

Brailoiu, E, Churamani, D, Cai, X, Schrlau, MG, Brailoiu, GC, Gao, X, Hooper, R, Boulware, MJ, Dun, NJ, Marchant, JS, Patel, S (2009) Essential requirement for two-pore channel 1 in NAADP-mediated calcium signaling. *J Cell Biol* **186**(2)**:** 201-209.

Brailoiu, E, Churamani, D, Pandey, V, Brailoiu, GC, Tuluc, F, Patel, S, Dun, NJ (2006) Messenger-specific role for nicotinic acid adenine dinucleotide phosphate in neuronal differentiation. *J Biol Chem* **281**(23)**:** 15923-15928.

Brailoiu, E, Hoard, JL, Filipeanu, CM, Brailoiu, GC, Dun, SL, Patel, S, Dun, NJ (2005) Nicotinic acid adenine dinucleotide phosphate potentiates neurite outgrowth. *J Biol Chem* **280**(7)**:** 5646-5650.

Brailoiu, E, Patel, S, Dun, NJ (2003) Modulation of spontaneous transmitter release from the frog neuromuscular junction by interacting intracellular Ca(2+) stores: critical role for nicotinic acid-adenine dinucleotide phosphate (NAADP). *Biochem J* **373**(Pt 2)**:** 313-318.

Brandhorst, D, Zwilling, D, Rizzoli, SO, Lippert, U, Lang, T, Jahn, R (2006) Homotypic fusion of early endosomes: SNAREs do not determine fusion specificity. *Proc Natl Acad Sci U S A* **103**(8)**:** 2701-2706.

Bruzzone, S, Guida, L, Zocchi, E, Franco, L, De Flora, A (2001) Connexin 43 hemi channels mediate Ca2+-regulated transmembrane NAD+ fluxes in intact cells. *FASEB J* **15**(1)**:** 10-12.

Bultynck, G, Rossi, D, Callewaert, G, Missiaen, L, Sorrentino, V, Parys, JB, De Smedt, H (2001) The conserved sites for the FK506-binding proteins in ryanodine receptors and inositol 1,4,5-trisphosphate receptors are structurally and functionally different. *J Biol Chem* **276**(50)**:** 47715-47724.

Buntinas, L, Gunter, KK, Sparagna, GC, Gunter, TE (2001) The rapid mode of calcium uptake into heart mitochondria (RaM): comparison to RaM in liver mitochondria. *Biochim Biophys Acta* **1504**(2-3)**:** 248-261.

Burdakov, D, Galione, A (2000) Two neuropeptides recruit different messenger pathways to evoke Ca2+ signals in the same cell. *Curr Biol* **10**(16)**:** 993-996.

Burdakov, D, Petersen, OH, Verkhratsky, A (2005) Intraluminal calcium as a primary regulator of endoplasmic reticulum function. *Cell Calcium* **38**(3-4)**:** 303-310.

Campbell, PE, Harris, CM, Sirimanna, T, Vellodi, A (2003) A model of neuronopathic Gaucher disease. *J Inherit Metab Dis* **26**(7)**:** 629-639.

Cancela, JM (2001) Specific Ca2+ signaling evoked by cholecystokinin and acetylcholine: the roles of NAADP, cADPR, and IP3. *Annu Rev Physiol* **63:** 99-117.

Cancela, JM, Churchill, GC, Galione, A (1999) Coordination of agonist-induced Ca2+-signalling patterns by NAADP in pancreatic acinar cells. *Nature* **398**(6722)**:** 74-76.

Cancela, JM, Gerasimenko, OV, Gerasimenko, JV, Tepikin, AV, Petersen, OH (2000) Two different but converging messenger pathways to intracellular Ca(2+) release: the roles of nicotinic acid adenine dinucleotide phosphate, cyclic ADP-ribose and inositol trisphosphate. *EMBO J* **19**(11)**:** 2549-2557.

Cancela, JM, Van Coppenolle, F, Galione, A, Tepikin, AV, Petersen, OH (2002) Transformation of local Ca2+ spikes to global Ca2+ transients: the combinatorial roles of multiple Ca2+ releasing messengers. *EMBO J* **21**(5)**:** 909-919.

Caputo, A, Caci, E, Ferrera, L, Pedemonte, N, Barsanti, C, Sondo, E, Pfeffer, U, Ravazzolo, R, Zegarra-Moran, O, Galietta, LJ (2008) TMEM16A, a membrane protein associated with calcium-dependent chloride channel activity. *Science* **322**(5901)**:** 590-594.

Carnell, L, Moore, HP (1994) Transport via the regulated secretory pathway in semi-intact PC12 cells: role of intra-cisternal calcium and pH in the transport and sorting of secretogranin II. *J Cell Biol* **127**(3)**:** 693-705.

Carrithers, MD, Dib-Hajj, S, Carrithers, LM, Tokmoulina, G, Pypaert, M, Jonas, EA, Waxman, SG (2007) Expression of the voltage-gated sodium channel NaV1.5 in the macrophage late endosome regulates endosomal acidification. *J Immunol* **178**(12)**:** 7822-7832.

Caterina, MJ, Schumacher, MA, Tominaga, M, Rosen, TA, Levine, JD, Julius, D (1997) The capsaicin receptor: a heat-activated ion channel in the pain pathway. *Nature* **389**(6653)**:** 816-824.

Catterall, WA (2000) From ionic currents to molecular mechanisms: the structure and function of voltage-gated sodium channels. *Neuron* **26**(1)**:** 13-25.

Catterall, WA, Goldin, AL, Waxman, SG (2005) International Union of Pharmacology. XLVII. Nomenclature and structure-function relationships of voltage-gated sodium channels. *Pharmacol Rev* **57**(4)**:** 397-409.

Catterall, WA, Striessnig, J, Snutch, TP, Perez-Reyes, E (2003) International Union of Pharmacology. XL. Compendium of voltage-gated ion channels: calcium channels. *Pharmacol Rev* **55**(4)**:** 579-581.

Chen, SR, Leong, P, Imredy, JP, Bartlett, C, Zhang, L, MacLennan, DH (1997a) Single-channel properties of the recombinant skeletal muscle Ca2+ release channel (ryanodine receptor). *Biophys J* **73**(4)**:** 1904-1912.

Chen, SR, Li, X, Ebisawa, K, Zhang, L (1997b) Functional characterization of the recombinant type 3 Ca2+ release channel (ryanodine receptor) expressed in HEK293 cells. *J Biol Chem* **272**(39)**:** 24234-24246.

Chini, EN, Beers, KW, Dousa, TP (1995a) Nicotinate adenine dinucleotide phosphate (NAADP) triggers a specific calcium release system in sea urchin eggs. *J Biol Chem* **270**(7)**:** 3216-3223.

Chini, EN, Chini, CC, Kato, I, Takasawa, S, Okamoto, H (2002) CD38 is the major enzyme responsible for synthesis of nicotinic acid-adenine dinucleotide phosphate in mammalian tissues. *Biochem J* **362**(Pt 1)**:** 125-130.

Chini, EN, Dousa, TP (1995b) Enzymatic synthesis and degradation of nicotinate adenine dinucleotide phosphate (NAADP), a Ca(2+)-releasing agonist, in rat tissues. *Biochem Biophys Res Commun* **209**(1)**:** 167-174.

Chini, EN, Dousa, TP (1996) Nicotinate-adenine dinucleotide phosphate-induced Ca(2+)-release does not behave as a Ca(2+)-induced Ca(2+)-release system. *Biochem J* **316 (Pt 3):** 709-711.

Chini, EN, Nagamune, K, Wetzel, DM, Sibley, LD (2005) Evidence that the cADPR signalling pathway controls calcium-mediated microneme secretion in Toxoplasma gondii. *Biochem J* **389**(Pt 2)**:** 269-277.

Christensen, KA, Myers, JT, Swanson, JA (2002) pH-dependent regulation of lysosomal calcium in macrophages. *J Cell Sci* **115**(Pt 3)**:** 599-607.

Churchill, GC, Galione, A (2001a) NAADP induces Ca2+ oscillations via a two-pool mechanism by priming IP3- and cADPR-sensitive Ca2+ stores. *EMBO J* **20**(11)**:** 2666-2671.

Churchill, GC, Galione, A (2001b) Prolonged inactivation of nicotinic acid adenine dinucleotide phosphate-induced Ca2+ release mediates a spatiotemporal Ca2+ memory. *J Biol Chem* **276**(14)**:** 11223-11225.

Churchill, GC, Galione, A (2000) Spatial control of Ca2+ signaling by nicotinic acid adenine dinucleotide phosphate diffusion and gradients. *J Biol Chem* **275**(49)**:** 38687-38692.

Churchill, GC, O'Neill, JS, Masgrau, R, Patel, S, Thomas, JM, Genazzani, AA, Galione, A (2003) Sperm deliver a new second messenger: NAADP. *Curr Biol* **13**(2)**:** 125-128.

Churchill, GC, Okada, Y, Thomas, JM, Genazzani, AA, Patel, S, Galione, A (2002) NAADP mobilizes Ca(2+) from reserve granules, lysosome-related organelles, in sea urchin eggs. *Cell* **111**(5)**:** 703-708.

Clapham, DE, Julius, D, Montell, C, Schultz, G (2005) International Union of Pharmacology. XLIX. Nomenclature and structure-function relationships of transient receptor potential channels. *Pharmacol Rev* **57**(4)**:** 427-450.

Clapper, DL, Walseth, TF, Dargie, PJ, Lee, HC (1987) Pyridine nucleotide metabolites stimulate calcium release from sea urchin egg microsomes desensitized to inositol trisphosphate. *J Biol Chem* **262**(20)**:** 9561-9568.

Collado-Hilly, M, Coquil, JF (2009) Ins(1,4,5)P3 receptor type 1 associates with AKAP9 (AKAP450 variant) and protein kinase A type IIbeta in the Golgi apparatus in cerebellar granule cells. *Biol Cell* **101**(8)**:** 469-480.

Copello, JA, Qi, Y, Jeyakumar, LH, Ogunbunmi, E, Fleischer, S (2001) Lack of effect of cADP-ribose and NAADP on the activity of skeletal muscle and heart ryanodine receptors. *Cell Calcium* **30**(4)**:** 269-284.

Cox, DH, Aldrich, RW (2000) Role of the beta1 subunit in large-conductance Ca(2+)-activated K(+) channel gating energetics. Mechanisms of enhanced Ca(2+) sensitivity. *J Gen Physiol* **116**(3)**:** 411-432.

Cui, Y, Galione, A, Terrar, DA (1999) Effects of photoreleased cADP-ribose on calcium transients and calcium sparks in myocytes isolated from guinea-pig and rat ventricle. *Biochem J* **342 (Pt 2):** 269-273.

Dammermann, W, Guse, AH (2005) Functional ryanodine receptor expression is required for NAADP-mediated local Ca2+ signaling in T-lymphocytes. *J Biol Chem* **280**(22)**:** 21394-21399.

David, G, Barrett, JN, Barrett, EF (1998) Evidence that mitochondria buffer physiological Ca2+ loads in lizard motor nerve terminals. *J Physiol* **509 (Pt 1):** 59-65.

Davis, LC, Morgan, AJ, Ruas, M, Wong, JL, Graeff, RM, Poustka, AJ, Lee, HC, Wessel, GM, Parrington, J, Galione, A (2008) Ca(2+) signaling occurs via second messenger release from intraorganelle synthesis sites. *Curr Biol* **18**(20)**:** 1612-1618.

De Flora, A, Franco, L, Guida, L, Bruzzone, S, Usai, C, Zocchi, E (2000) Topology of CD38. *Chem Immunol* **75:** 79-98.

DeHaven, WI, Jones, BF, Petranka, JG, Smyth, JT, Tomita, T, Bird, GS, Putney, JW, Jr. (2009) TRPC channels function independently of STIM1 and Orai1. *J Physiol* **587**(Pt 10)**:** 2275-2298.

Dell'Angelica, EC, Mullins, C, Caplan, S, Bonifacino, JS (2000) Lysosome-related organelles. *FASEB J* **14**(10)**:** 1265-1278.

DePina, AS, Langford, GM (1999) Vesicle transport: the role of actin filaments and myosin motors. *Microsc Res Tech* **47**(2)**:** 93-106.

Di Leva, F, Domi, T, Fedrizzi, L, Lim, D, Carafoli, E (2008) The plasma membrane Ca2+ ATPase of animal cells: structure, function and regulation. *Arch Biochem Biophys* **476**(1)**:** 65-74.

Dickinson, GD, Patel, S (2003) Modulation of NAADP (nicotinic acid-adenine dinucleotide phosphate) receptors by K+ ions: evidence for multiple NAADP receptor conformations. *Biochem J* **375**(Pt 3)**:** 805-812.

Dipp, M, Evans, AM (2001a) Cyclic ADP-ribose is the primary trigger for hypoxic pulmonary vasoconstriction in the rat lung in situ. *Circ Res* **89**(1)**:** 77-83.

Dipp, M, Nye, PC, Evans, AM (2001b) Hypoxic release of calcium from the sarcoplasmic reticulum of pulmonary artery smooth muscle. *Am J Physiol Lung Cell Mol Physiol* **281**(2)**:** L318-325.

Dode, L, Andersen, JP, Vanoevelen, J, Raeymaekers, L, Missiaen, L, Vilsen, B, Wuytack, F (2006) Dissection of the functional differences between human secretory pathway Ca2+/Mn2+-ATPase (SPCA) 1 and 2 isoenzymes by steady-state and transient kinetic analyses. *J Biol Chem* **281**(6)**:** 3182-3189.

Dolman, NJ, Gerasimenko, JV, Gerasimenko, OV, Voronina, SG, Petersen, OH, Tepikin, AV (2005) Stable Golgi-mitochondria complexes and formation of Golgi Ca(2+) gradients in pancreatic acinar cells. *J Biol Chem* **280**(16)**:** 15794-15799.

Dolmetsch, RE, Xu, K, Lewis, RS (1998) Calcium oscillations increase the efficiency and specificity of gene expression. *Nature* **392**(6679)**:** 933-936.

Dolphin, AC (2006) A short history of voltage-gated calcium channels. *Br J Pharmacol* **147 Suppl 1:** S56-62.

Dong, XP, Cheng, X, Mills, E, Delling, M, Wang, F, Kurz, T, Xu, H (2008) The type IV mucolipidosis-associated protein TRPML1 is an endolysosomal iron release channel. *Nature* **455**(7215)**:** 992-996.

Duchen, MR (2000) Mitochondria and calcium: from cell signalling to cell death. *J Physiol* **529 Pt 1:** 57-68.

Elstein, D, Klutstein, MW, Lahad, A, Abrahamov, A, Hadas-Halpern, I, Zimran, A (1998) Echocardiographic assessment of pulmonary hypertension in Gaucher's disease. *Lancet* **351**(9115)**:** 1544-1546.

Endo, M, Tanaka, M, Ogawa, Y (1970) Calcium induced release of calcium from the sarcoplasmic reticulum of skinned skeletal muscle fibres. *Nature* **228**(5266)**:** 34-36.

Ertel, EA, Campbell, KP, Harpold, MM, Hofmann, F, Mori, Y, Perez-Reyes, E, Schwartz, A, Snutch, TP, Tanabe, T, Birnbaumer, L, Tsien, RW, Catterall, WA (2000) Nomenclature of voltage-gated calcium channels. *Neuron* **25**(3)**:** 533-535.

Eustice, DC, Wilhelm, JM (1984) Mechanisms of action of aminoglycoside antibiotics in eucaryotic protein synthesis. *Antimicrob Agents Chemother* **26**(1)**:** 53-60.

Evans, AM, Dipp, M (2002) Hypoxic pulmonary vasoconstriction: cyclic adenosine diphosphate-ribose, smooth muscle Ca(2+) stores and the endothelium. *Respir Physiol Neurobiol* **132**(1)**:** 3-15.

Evans, AM, Wyatt, CN, Kinnear, NP, Clark, JH, Blanco, EA (2005) Pyridine nucleotides and calcium signalling in arterial smooth muscle: from cell physiology to pharmacology. *Pharmacol Ther* **107**(3)**:** 286-313.

Falcon-Perez, JM, Nazarian, R, Sabatti, C, Dell'Angelica, EC (2005) Distribution and dynamics of Lamp1-containing endocytic organelles in fibroblasts deficient in BLOC-3. *J Cell Sci* **118**(Pt 22)**:** 5243-5255.

Fasolato, C, Zottini, M, Clementi, E, Zacchetti, D, Meldolesi, J, Pozzan, T (1991) Intracellular Ca2+ pools in PC12 cells. Three intracellular pools are distinguished by their turnover and mechanisms of Ca2+ accumulation, storage, and release. *J Biol Chem* **266**(30)**:** 20159-20167.

Feske, S, Gwack, Y, Prakriya, M, Srikanth, S, Puppel, SH, Tanasa, B, Hogan, PG, Lewis, RS, Daly, M, Rao, A (2006) A mutation in Orai1 causes immune deficiency by abrogating CRAC channel function. *Nature* **441**(7090)**:** 179-185.

Fill, M, Copello, JA (2002) Ryanodine receptor calcium release channels. *Physiol Rev* **82**(4)**:** 893-922.

Fire, A, Xu, S, Montgomery, MK, Kostas, SA, Driver, SE, Mello, CC (1998) Potent and specific genetic interference by double-stranded RNA in Caenorhabditis elegans. *Nature* **391**(6669)**:** 806-811.

Fox, AP, Nowycky, MC, Tsien, RW (1987a) Kinetic and pharmacological properties distinguishing three types of calcium currents in chick sensory neurones. *J Physiol* **394:** 149-172.

Fox, AP, Nowycky, MC, Tsien, RW (1987b) Single-channel recordings of three types of calcium channels in chick sensory neurones. *J Physiol* **394:** 173-200.

Furuichi, T, Cunningham, KW, Muto, S (2001) A putative two pore channel AtTPC1 mediates Ca(2+) flux in Arabidopsis leaf cells. *Plant Cell Physiol* **42**(9)**:** 900-905.

Galione, A, Evans, AM, Ma, J, Parrington, J, Arredouani, A, Cheng, X, Zhu, MX (2009) The acid test: the discovery of two-pore channels (TPCs) as NAADP-gated endolysosomal Ca(2+) release channels. *Pflugers Arch* **458**(5)**:** 869-876.

Galione, A, Lee, HC, Busa, WB (1991) Ca(2+)-induced Ca2+ release in sea urchin egg homogenates: modulation by cyclic ADP-ribose. *Science* **253**(5024)**:** 1143-1146.

Galione, A, Ruas, M (2005) NAADP receptors. *Cell Calcium* **38**(3-4)**:** 273-280.

Genazzani, AA, Empson, RM, Galione, A (1996a) Unique inactivation properties of NAADP-sensitive Ca2+ release. *J Biol Chem* **271**(20)**:** 11599-11602.

Genazzani, AA, Galione, A (1996b) Nicotinic acid-adenine dinucleotide phosphate mobilizes Ca2+ from a thapsigargin-insensitive pool. *Biochem J* **315 (Pt 3):** 721-725.

Genazzani, AA, Mezna, M, Dickey, DM, Michelangeli, F, Walseth, TF, Galione, A (1997) Pharmacological properties of the Ca2+-release mechanism sensitive to NAADP in the sea urchin egg. *Br J Pharmacol* **121**(7)**:** 1489-1495.

Gerasimenko, JV, Maruyama, Y, Yano, K, Dolman, NJ, Tepikin, AV, Petersen, OH, Gerasimenko, OV (2003) NAADP mobilizes Ca2+ from a thapsigargin-sensitive store in the nuclear envelope by activating ryanodine receptors. *J Cell Biol* **163**(2)**:** 271-282.

Gerasimenko, JV, Tepikin, AV, Petersen, OH, Gerasimenko, OV (1998) Calcium uptake via endocytosis with rapid release from acidifying endosomes. *Curr Biol* **8**(24)**:** 1335-1338.

Gerthoffer, WT (2007) Mechanisms of vascular smooth muscle cell migration. *Circ Res* **100**(5)**:** 607-621.

Ginsborg, BL, House, CR, Mitchell, MR (1980a) A calcium-readmission response recorded from Nauphoeta salivary gland acinar cells. *J Physiol* **304:** 437-447.

Ginsborg, BL, House, CR, Mitchell, MR (1980b) On the role of calcium in the electrical responses of cockroach salivary gland cells to dopamine. *J Physiol* **303:** 325-335.

Gozuacik, D, Kimchi, A (2004) Autophagy as a cell death and tumor suppressor mechanism. *Oncogene* **23**(16)**:** 2891-2906.

Gramolini, AO, Kislinger, T, Asahi, M, Li, W, Emili, A, MacLennan, DH (2004) Sarcolipin retention in the endoplasmic reticulum depends on its C-terminal RSYQY sequence and its interaction with sarco(endo)plasmic Ca(2+)-ATPases. *Proc Natl Acad Sci U S A* **101**(48)**:** 16807-16812.

Grant, L, Fuchs, PA (2007) Auditory transduction in the mouse. *Pflugers Arch* **454**(5)**:** 793-804.

Grayson, TH, Haddock, RE, Murray, TP, Wojcikiewicz, RJ, Hill, CE (2004) Inositol 1,4,5-trisphosphate receptor subtypes are differentially distributed between smooth muscle and endothelial layers of rat arteries. *Cell Calcium* **36**(6)**:** 447-458.

Grynkiewicz, G, Poenie, M, Tsien, RY (1985) A new generation of Ca2+ indicators with greatly improved fluorescence properties. *J Biol Chem* **260**(6)**:** 3440-3450.

Gunter, TE, Yule, DI, Gunter, KK, Eliseev, RA, Salter, JD (2004) Calcium and mitochondria. *FEBS Lett* **567**(1)**:** 96-102.

Guse, AH (2009) Second messenger signaling: multiple receptors for NAADP. *Curr Biol* **19**(13)**:** R521-523.

Gutman, GA, Chandy, KG, Grissmer, S, Lazdunski, M, McKinnon, D, Pardo, LA, Robertson, GA, Rudy, B, Sanguinetti, MC, Stuhmer, W, Wang, X (2005) International Union of Pharmacology. LIII. Nomenclature and molecular relationships of voltage-gated potassium channels. *Pharmacol Rev* **57**(4)**:** 473-508.

Haller, T, Volkl, H, Deetjen, P, Dietl, P (1996) The lysosomal Ca2+ pool in MDCK cells can be released by ins(1,4,5)P3-dependent hormones or thapsigargin but does not activate store-operated Ca2+ entry. *Biochem J* **319 (Pt 3):** 909-912.

Hamill, OP, Marty, A, Neher, E, Sakmann, B, Sigworth, FJ (1981) Improved patch-clamp techniques for high-resolution current recording from cells and cell-free membrane patches. *Pflugers Arch* **391**(2)**:** 85-100.

Hamilton, SL (2005) Ryanodine receptors. *Cell Calcium* **38**(3-4)**:** 253-260.

Hawkins, PT, Stephens, L, Downes, CP (1986) Rapid formation of inositol 1,3,4,5-tetrakisphosphate and inositol 1,3,4-trisphosphate in rat parotid glands may both result indirectly from receptor-stimulated release of inositol 1,4,5-trisphosphate from phosphatidylinositol 4,5-bisphosphate. *Biochem J* **238**(2)**:** 507-516.

Hellmich, MR, Strumwasser, F (1991) Purification and characterization of a molluscan egg-specific NADase, a second-messenger enzyme. *Cell Regul* **2**(3)**:** 193-202.

Herman, B, Albertini, DF (1984) A time-lapse video image intensification analysis of cytoplasmic organelle movements during endosome translocation. *J Cell Biol* **98**(2)**:** 565-576.

Hewavitharana, T, Deng, X, Soboloff, J, Gill, DL (2007) Role of STIM and Orai proteins in the store-operated calcium signaling pathway. *Cell Calcium* **42**(2)**:** 173-182.

Higashida, H (1997) ADP-ribosyl cyclase coupled with receptors via G proteins. *FEBS Lett* **418**(3)**:** 355-356.

Hilden, SA, Madias, NE (1989) H+/Ca2+ exchange in rabbit renal cortical endosomes. *J Membr Biol* **112**(2)**:** 131-138.

Hirata, Y, Kimura, N, Sato, K, Ohsugi, Y, Takasawa, S, Okamoto, H, Ishikawa, J, Kaisho, T, Ishihara, K, Hirano, T (1994) ADP ribosyl cyclase activity of a novel bone marrow stromal cell surface molecule, BST-1. *FEBS Lett* **356**(2-3)**:** 244-248.

Hofmann, F, James, P, Vorherr, T, Carafoli, E (1993) The C-terminal domain of the plasma membrane Ca2+ pump contains three high affinity Ca2+ binding sites. *J Biol Chem* **268**(14)**:** 10252-10259.

Hofmann, T, Obukhov, AG, Schaefer, M, Harteneck, C, Gudermann, T, Schultz, G (1999) Direct activation of human TRPC6 and TRPC3 channels by diacylglycerol. *Nature* **397**(6716)**:** 259-263.

Hohenegger, M, Suko, J, Gscheidlinger, R, Drobny, H, Zidar, A (2002) Nicotinic acid-adenine dinucleotide phosphate activates the skeletal muscle ryanodine receptor. *Biochem J* **367**(Pt 2)**:** 423-431.

Holroyd, C, Kistner, U, Annaert, W, Jahn, R (1999) Fusion of endosomes involved in synaptic vesicle recycling. *Mol Biol Cell* **10**(9)**:** 3035-3044.

Horrigan, FT, Aldrich, RW (2002) Coupling between voltage sensor activation, Ca2+ binding and channel opening in large conductance (BK) potassium channels. *J Gen Physiol* **120**(3)**:** 267-305.

Hoth, M, Penner, R (1992) Depletion of intracellular calcium stores activates a calcium current in mast cells. *Nature* **355**(6358)**:** 353-356.

Howard, M, Grimaldi, JC, Bazan, JF, Lund, FE, Santos-Argumedo, L, Parkhouse, RM, Walseth, TF, Lee, HC (1993) Formation and hydrolysis of cyclic ADP-ribose catalyzed by lymphocyte antigen CD38. *Science* **262**(5136)**:** 1056-1059.

Hudmon, A, Schulman, H, Kim, J, Maltez, JM, Tsien, RW, Pitt, GS (2005) CaMKII tethers to L-type Ca2+ channels, establishing a local and dedicated integrator of Ca2+ signals for facilitation. *J Cell Biol* **171**(3)**:** 537-547.

Hwang, J, Kim, YY, Huh, S, Shim, J, Park, C, Kimm, K, Choi, DK, Park, TK, Kim, S (2005) The time-dependent serial gene response to Zeocin treatment involves caspase-dependent apoptosis in HeLa cells. *Microbiol Immunol* **49**(4)**:** 331-342.

Iino, M (1990) Biphasic Ca2+ dependence of inositol 1,4,5-trisphosphate-induced Ca release in smooth muscle cells of the guinea pig taenia caeci. *J Gen Physiol* **95**(6)**:** 1103-1122.

Ishibashi, K, Suzuki, M, Imai, M (2000) Molecular cloning of a novel form (two-repeat) protein related to voltage-gated sodium and calcium channels. *Biochem Biophys Res Commun* **270**(2)**:** 370-376.

Iwamoto, T, Uehara, A, Imanaga, I, Shigekawa, M (2000) The Na+/Ca2+ exchanger NCX1 has oppositely oriented reentrant loop domains that contain conserved aspartic acids whose mutation alters its apparent Ca2+ affinity. *J Biol Chem* **275**(49)**:** 38571-38580.

Jadot, M, Colmant, C, Wattiaux-De Coninck, S, Wattiaux, R (1984) Intralysosomal hydrolysis of glycyl-L-phenylalanine 2-naphthylamide. *Biochem J* **219**(3)**:** 965-970.

Jeyakumar, LH, Ballester, L, Cheng, DS, McIntyre, JO, Chang, P, Olivey, HE, Rollins-Smith, L, Barnett, JV, Murray, K, Xin, HB, Fleischer, S (2001) FKBP binding characteristics of cardiac microsomes from diverse vertebrates. *Biochem Biophys Res Commun* **281**(4)**:** 979-986.

Jeyakumar, LH, Copello, JA, O'Malley, AM, Wu, GM, Grassucci, R, Wagenknecht, T, Fleischer, S (1998) Purification and characterization of ryanodine receptor 3 from mammalian tissue. *J Biol Chem* **273**(26)**:** 16011-16020.

Jmoudiak, M, Futerman, AH (2005) Gaucher disease: pathological mechanisms and modern management. *Br J Haematol* **129**(2)**:** 178-188.

Johnson, JD, Misler, S (2002) Nicotinic acid-adenine dinucleotide phosphate-sensitive calcium stores initiate insulin signaling in human beta cells. *Proc Natl Acad Sci U S A* **99**(22)**:** 14566-14571.

Johnson, LS, Dunn, KW, Pytowski, B, McGraw, TE (1993) Endosome acidification and receptor trafficking: bafilomycin A1 slows receptor externalization by a mechanism involving the receptor's internalization motif. *Mol Biol Cell* **4**(12)**:** 1251-1266.

Jones, SW (2003) Calcium channels: unanswered questions. *J Bioenerg Biomembr* **35**(6)**:** 461-475.

Joshi, PG, Nair, N, Begum, G, Joshi, NB, Sinkar, VP, Vora, S (2007) Melanocyte-keratinocyte interaction induces calcium signalling and melanin transfer to keratinocytes. *Pigment Cell Res* **20**(5)**:** 380-384.

Jouaville, LS, Pinton, P, Bastianutto, C, Rutter, GA, Rizzuto, R (1999) Regulation of mitochondrial ATP synthesis by calcium: evidence for a long-term metabolic priming. *Proc Natl Acad Sci U S A* **96**(24)**:** 13807-13812.

Juhaszova, M, Blaustein, MP (1997) Distinct distribution of different Na+ pump alpha subunit isoforms in plasmalemma. Physiological implications. *Ann N Y Acad Sci* **834:** 524-536.

Kalay, E, Caylan, R, Kiroglu, AF, Yasar, T, Collin, RW, Heister, JG, Oostrik, J, Cremers, CW, Brunner, HG, Karaguzel, A, Kremer, H (2007) A novel locus for autosomal recessive nonsyndromic hearing impairment, DFNB63, maps to chromosome 11q13.2-q13.4. *J Mol Med* **85**(4)**:** 397-404.

Kamp, TJ, Hell, JW (2000) Regulation of cardiac L-type calcium channels by protein kinase A and protein kinase C. *Circ Res* **87**(12)**:** 1095-1102.

Kamphoven, JH, de Ruiter, MM, Winkel, LP, Van den Hout, HM, Bijman, J, De Zeeuw, CI, Hoeve, HL, Van Zanten, BA, Van der Ploeg, AT, Reuser, AJ (2004) Hearing loss in infantile Pompe's disease and determination of underlying pathology in the knockout mouse. *Neurobiol Dis* **16**(1)**:** 14-20.

Kanatani, I, Ikai, T, Okazaki, A, Jo, J, Yamamoto, M, Imamura, M, Kanematsu, A, Yamamoto, S, Ito, N, Ogawa, O, Tabata, Y (2006) Efficient gene transfer by pullulan-spermine occurs through both clathrin- and raft/caveolae-dependent mechanisms. *J Control Release* **116**(1)**:** 75-82.

Katan, M (2005) New insights into the families of PLC enzymes: looking back and going forward. *Biochem J* **391**(Pt 3)**:** e7-9.

Kawano, T, Kadono, T, Fumoto, K, Lapeyrie, F, Kuse, M, Isobe, M, Furuichi, T, Muto, S (2004) Aluminum as a specific inhibitor of plant TPC1 Ca2+ channels. *Biochem Biophys Res Commun* **324**(1)**:** 40-45.

Kedei, N, Szabo, T, Lile, JD, Treanor, JJ, Olah, Z, Iadarola, MJ, Blumberg, PM (2001) Analysis of the native quaternary structure of vanilloid receptor 1. *J Biol Chem* **276**(30)**:** 28613-28619.

Keef, KD, Hume, JR, Zhong, J (2001) Regulation of cardiac and smooth muscle Ca(2+) channels (Ca(V)1.2a,b) by protein kinases. *Am J Physiol Cell Physiol* **281**(6)**:** C1743-1756.

Keynes, RD, Elinder, F (1999) The screw-helical voltage gating of ion channels. *Proc Biol Sci* **266**(1421)**:** 843-852.

Khan, SY, Riazuddin, S, Tariq, M, Anwar, S, Shabbir, MI, Riazuddin, SA, Khan, SN, Husnain, T, Ahmed, ZM, Friedman, TB (2007) Autosomal recessive nonsyndromic deafness locus DFNB63 at chromosome 11q13.2-q13.3. *Hum Genet* **120**(6)**:** 789-793.

Kim, BJ, Park, KH, Yim, CY, Takasawa, S, Okamoto, H, Im, MJ, Kim, UH (2008) Generation of nicotinic acid adenine dinucleotide phosphate and cyclic ADP-ribose by glucagon-like peptide-1 evokes Ca2+ signal that is essential for insulin secretion in mouse pancreatic islets. *Diabetes* **57**(4)**:** 868-878.

Kimura, Y, Kurzydlowski, K, Tada, M, MacLennan, DH (1997) Phospholamban inhibitory function is activated by depolymerization. *J Biol Chem* **272**(24)**:** 15061-15064.

Kinnear, NP, Boittin, FX, Thomas, JM, Galione, A, Evans, AM (2004) Lysosome-sarcoplasmic reticulum junctions. A trigger zone for calcium signaling by nicotinic acid adenine dinucleotide phosphate and endothelin-1. *J Biol Chem* **279**(52)**:** 54319-54326.

Klionsky, DJ, Elazar, Z, Seglen, PO, Rubinsztein, DC (2008) Does bafilomycin A1 block the fusion of autophagosomes with lysosomes? *Autophagy* **4**(7)**:** 849-950.

Kontani, K, Nishina, H, Ohoka, Y, Takahashi, K, Katada, T (1993) NAD glycohydrolase specifically induced by retinoic acid in human leukemic HL-60 cells. Identification of the NAD glycohydrolase as leukocyte cell surface antigen CD38. *J Biol Chem* **268**(23)**:** 16895-16898.

Korovkina, VP, England, SK (2002) Molecular diversity of vascular potassium channel isoforms. *Clin Exp Pharmacol Physiol* **29**(4)**:** 317-323.

Koshiyama, H, Lee, HC, Tashjian, AH, Jr. (1991) Novel mechanism of intracellular calcium release in pituitary cells. *J Biol Chem* **266**(26)**:** 16985-16988.

Kubo, Y, Adelman, JP, Clapham, DE, Jan, LY, Karschin, A, Kurachi, Y, Lazdunski, M, Nichols, CG, Seino, S, Vandenberg, CA (2005) International Union of Pharmacology. LIV. Nomenclature and molecular relationships of inwardly rectifying potassium channels. *Pharmacol Rev* **57**(4)**:** 509-526.

Kuo, TH, Wang, KK, Carlock, L, Diglio, C, Tsang, W (1991) Phorbol ester induces both gene expression and phosphorylation of the plasma membrane Ca2+ pump. *J Biol Chem* **266**(4)**:** 2520-2525.

Kuruma, A, Hartzell, HC (2000) Bimodal control of a Ca(2+)-activated Cl(-) channel by different Ca(2+) signals. *J Gen Physiol* **115**(1)**:** 59-80.

Lamont, C, Vial, C, Evans, RJ, Wier, WG (2006) P2X1 receptors mediate sympathetic postjunctional Ca2+ transients in mesenteric small arteries. *Am J Physiol Heart Circ Physiol* **291**(6)**:** H3106-3113.

Lange, I, Penner, R, Fleig, A, Beck, A (2008) Synergistic regulation of endogenous TRPM2 channels by adenine dinucleotides in primary human neutrophils. *Cell Calcium* **44**(6)**:** 604-615.

Lange, I, Yamamoto, S, Partida-Sanchez, S, Mori, Y, Fleig, A, Penner, R (2009) TRPM2 functions as a lysosomal Ca2+-release channel in beta cells. *Sci Signal* **2**(71)**:** ra23.

Langhorst, MF, Schwarzmann, N, Guse, AH (2004) Ca2+ release via ryanodine receptors and Ca2+ entry: major mechanisms in NAADP-mediated Ca2+ signaling in T-lymphocytes. *Cell Signal* **16**(11)**:** 1283-1289.

Lee, HC (1999) A unified mechanism of enzymatic synthesis of two calcium messengers: cyclic ADP-ribose and NAADP. *Biol Chem* **380**(7-8)**:** 785-793.

Lee, HC (2000) Enzymatic functions and structures of CD38 and homologs. *Chem Immunol* **75:** 39-59.

Lee, HC (1993) Potentiation of calcium- and caffeine-induced calcium release by cyclic ADP-ribose. *J Biol Chem* **268**(1)**:** 293-299.

Lee, HC, Aarhus, R (1995) A derivative of NADP mobilizes calcium stores insensitive to inositol trisphosphate and cyclic ADP-ribose. *J Biol Chem* **270**(5)**:** 2152-2157.

Lee, HC, Aarhus, R (1991) ADP-ribosyl cyclase: an enzyme that cyclizes NAD+ into a calcium-mobilizing metabolite. *Cell Regul* **2**(3)**:** 203-209.

Lee, HC, Aarhus, R (2000) Functional visualization of the separate but interacting calcium stores sensitive to NAADP and cyclic ADP-ribose. *J Cell Sci* **113 Pt 24:** 4413-4420.

Lee, HC, Aarhus, R (1993) Wide distribution of an enzyme that catalyzes the hydrolysis of cyclic ADP-ribose. *Biochim Biophys Acta* **1164**(1)**:** 68-74.

Lee, HC, Walseth, TF, Bratt, GT, Hayes, RN, Clapper, DL (1989) Structural determination of a cyclic metabolite of NAD+ with intracellular Ca2+-mobilizing activity. *J Biol Chem* **264**(3)**:** 1608-1615.

Lencer, WI, Weyer, P, Verkman, AS, Ausiello, DA, Brown, D (1990) FITC-dextran as a probe for endosome function and localization in kidney. *Am J Physiol* **258**(2 Pt 1)**:** C309-317.

Lesh, RE, Marks, AR, Somlyo, AV, Fleischer, S, Somlyo, AP (1993) Anti-ryanodine receptor antibody binding sites in vascular and endocardial endothelium. *Circ Res* **72**(2)**:** 481-488.

Lewis, AM, Masgrau, R, Vasudevan, SR, Yamasaki, M, O'Neill, JS, Garnham, C, James, K, Macdonald, A, Ziegler, M, Galione, A, Churchill, GC (2007) Refinement

of a radioreceptor binding assay for nicotinic acid adenine dinucleotide phosphate. *Anal Biochem* **371**(1)**:** 26-36.

Lewis, V, Green, SA, Marsh, M, Vihko, P, Helenius, A, Mellman, I (1985) Glycoproteins of the lysosomal membrane. *J Cell Biol* **100**(6)**:** 1839-1847.

Li, P, Chen, SR (2001) Molecular basis of Ca(2)+ activation of the mouse cardiac Ca(2)+ release channel (ryanodine receptor). *J Gen Physiol* **118**(1)**:** 33-44.

Liao, Y, Erxleben, C, Yildirim, E, Abramowitz, J, Armstrong, DL, Birnbaumer, L (2007) Orai proteins interact with TRPC channels and confer responsiveness to store depletion. *Proc Natl Acad Sci U S A* **104**(11)**:** 4682-4687.

Lievremont, JP, Bird, GS, Putney, JW, Jr. (2004) Canonical transient receptor potential TRPC7 can function as both a receptor- and store-operated channel in HEK-293 cells. *Am J Physiol Cell Physiol* **287**(6)**:** C1709-1716.

Liman, ER, Tytgat, J, Hess, P (1992) Subunit stoichiometry of a mammalian K+ channel determined by construction of multimeric cDNAs. *Neuron* **9**(5)**:** 861-871.

Lin, P, Yao, Y, Hofmeister, R, Tsien, RY, Farquhar, MG (1999) Overexpression of CALNUC (nucleobindin) increases agonist and thapsigargin releasable Ca2+ storage in the Golgi. *J Cell Biol* **145**(2)**:** 279-289.

Liou, J, Kim, ML, Heo, WD, Jones, JT, Myers, JW, Ferrell, JE, Jr., Meyer, T (2005) STIM is a Ca2+ sensor essential for Ca2+-store-depletion-triggered Ca2+ influx. *Curr Biol* **15**(13)**:** 1235-1241.

Lloyd-Evans, E, Morgan, AJ, He, X, Smith, DA, Elliot-Smith, E, Sillence, DJ, Churchill, GC, Schuchman, EH, Galione, A, Platt, FM (2008) Niemann-Pick disease type C1 is a sphingosine storage disease that causes deregulation of lysosomal calcium. *Nat Med* **14**(11)**:** 1247-1255.

Lopatin, AN, Makhina, EN, Nichols, CG (1994) Potassium channel block by cytoplasmic polyamines as the mechanism of intrinsic rectification. *Nature* **372**(6504)**:** 366-369.

Lytton, J (2007) Na+/Ca2+ exchangers: three mammalian gene families control Ca2+ transport. *Biochem J* **406**(3)**:** 365-382.

Lytton, J, Westlin, M, Burk, SE, Shull, GE, MacLennan, DH (1992) Functional comparisons between isoforms of the sarcoplasmic or endoplasmic reticulum family of calcium pumps. *J Biol Chem* **267**(20)**:** 14483-14489.

Lytton, J, Westlin, M, Hanley, MR (1991) Thapsigargin inhibits the sarcoplasmic or endoplasmic reticulum Ca-ATPase family of calcium pumps. *J Biol Chem* **266**(26)**:** 17067-17071.

Macgregor, A, Yamasaki, M, Rakovic, S, Sanders, L, Parkesh, R, Churchill, GC, Galione, A, Terrar, DA (2007) NAADP controls cross-talk between distinct Ca2+ stores in the heart. *J Biol Chem* **282**(20)**:** 15302-15311.

Mackenzie, L, Roderick, HL, Berridge, MJ, Conway, SJ, Bootman, MD (2004) The spatial pattern of atrial cardiomyocyte calcium signalling modulates contraction. *J Cell Sci* **117**(Pt 26)**:** 6327-6337.

MacKinnon, R (1991) Determination of the subunit stoichiometry of a voltage-activated potassium channel. *Nature* **350**(6315)**:** 232-235.

MacLennan, DH, Abu-Abed, M, Kang, C (2002) Structure-function relationships in Ca(2+) cycling proteins. *J Mol Cell Cardiol* **34**(8)**:** 897-918.

Majerus, PW, Connolly, TM, Bansal, VS, Inhorn, RC, Ross, TS, Lips, DL (1988) Inositol phosphates: synthesis and degradation. *J Biol Chem* **263**(7)**:** 3051-3054.

Marchant, JS, Taylor, CW (1997) Cooperative activation of IP3 receptors by sequential binding of IP3 and Ca2+ safeguards against spontaneous activity. *Curr Biol* **7**(7)**:** 510-518.

Marino, G, Lopez-Otin, C (2004) Autophagy: molecular mechanisms, physiological functions and relevance in human pathology. *Cell Mol Life Sci* **61**(12)**:** 1439-1454.

Marks, DL, Pagano, RE (2002) Endocytosis and sorting of glycosphingolipids in sphingolipid storage disease. *Trends Cell Biol* **12**(12)**:** 605-613.

Martinez-Azorin, F (2004) Cyclopiazonic acid reduces the coupling factor of the Ca2+-ATPase acting on Ca2+ binding. *FEBS Lett* **576**(1-2)**:** 73-76.

Masgrau, R, Churchill, GC, Morgan, AJ, Ashcroft, SJ, Galione, A (2003) NAADP: a new second messenger for glucose-induced Ca2+ responses in clonal pancreatic beta cells. *Curr Biol* **13**(3)**:** 247-251.

Matsuda, H, Saigusa, A, Irisawa, H (1987) Ohmic conductance through the inwardly rectifying K channel and blocking by internal Mg2+. *Nature* **325**(7000)**:** 156-159.

Matsushita, M, Tanaka, S, Nakamura, N, Inoue, H, Kanazawa, H (2004) A novel kinesin-like protein, KIF1Bbeta3 is involved in the movement of lysosomes to the cell periphery in non-neuronal cells. *Traffic* **5**(3)**:** 140-151.

Mattila, PK, Lappalainen, P (2008) Filopodia: molecular architecture and cellular functions. *Nat Rev Mol Cell Biol* **9**(6)**:** 446-454.

Mayorga, LS, Beron, W, Sarrouf, MN, Colombo, MI, Creutz, C, Stahl, PD (1994) Calcium-dependent fusion among endosomes. *J Biol Chem* **269**(49)**:** 30927-30934.

McHugh, D, Sharp, EM, Scheuer, T, Catterall, WA (2000) Inhibition of cardiac L-type calcium channels by protein kinase C phosphorylation of two sites in the N-terminal domain. *Proc Natl Acad Sci U S A* **97**(22)**:** 12334-12338.

Meszaros, LG, Bak, J, Chu, A (1993) Cyclic ADP-ribose as an endogenous regulator of the non-skeletal type ryanodine receptor Ca2+ channel. *Nature* **364**(6432)**:** 76-79.

Michalak, M, Corbett, EF, Mesaeli, N, Nakamura, K, Opas, M (1999) Calreticulin: one protein, one gene, many functions. *Biochem J* **344 Pt 2:** 281-292.

Michalak, M, Milner, RE, Burns, K, Opas, M (1992) Calreticulin. *Biochem J* **285 (Pt 3):** 681-692.

Michikawa, T, Hamanaka, H, Otsu, H, Yamamoto, A, Miyawaki, A, Furuichi, T, Tashiro, Y, Mikoshiba, K (1994) Transmembrane topology and sites of N-glycosylation of inositol 1,4,5-trisphosphate receptor. *J Biol Chem* **269**(12)**:** 9184-9189.

Mignery, GA, Sudhof, TC (1990) The ligand binding site and transduction mechanism in the inositol-1,4,5-triphosphate receptor. *EMBO J* **9**(12)**:** 3893-3898.

Missiaen, L, Parys, JB, Sienaert, I, Maes, K, Kunzelmann, K, Takahashi, M, Tanzawa, K, De Smedt, H (1998) Functional properties of the type-3 InsP3 receptor in 16HBE14o- bronchial mucosal cells. *J Biol Chem* **273**(15)**:** 8983-8986.

Mitchell, KJ, Lai, FA, Rutter, GA (2003) Ryanodine receptor type I and nicotinic acid adenine dinucleotide phosphate receptors mediate Ca2+ release from insulin-containing vesicles in living pancreatic beta-cells (MIN6). *J Biol Chem* **278**(13)**:** 11057-11064.

Miyakawa, T, Maeda, A, Yamazawa, T, Hirose, K, Kurosaki, T, Iino, M (1999) Encoding of Ca2+ signals by differential expression of IP3 receptor subtypes. *EMBO J* **18**(5)**:** 1303-1308.

Mojzisova, A, Krizanova, O, Zacikova, L, Kominkova, V, Ondrias, K (2001) Effect of nicotinic acid adenine dinucleotide phosphate on ryanodine calcium release channel in heart. *Pflugers Arch* **441**(5)**:** 674-677.

Montell, C (2005) The TRP superfamily of cation channels. *Sci STKE* **2005**(272)**:** re3.

Morgan, AJ, Galione, A (2007) NAADP induces pH changes in the lumen of acidic Ca2+ stores. *Biochem J* **402**(2)**:** 301-310.

Mu, TW, Fowler, DM, Kelly, JW (2008) Partial restoration of mutant enzyme homeostasis in three distinct lysosomal storage disease cell lines by altering calcium homeostasis. *PLoS Biol* **6**(2)**:** e26.

Navazio, L, Bewell, MA, Siddiqua, A, Dickinson, GD, Galione, A, Sanders, D (2000) Calcium release from the endoplasmic reticulum of higher plants elicited by the NADP metabolite nicotinic acid adenine dinucleotide phosphate. *Proc Natl Acad Sci U S A* **97**(15)**:** 8693-8698.

Naylor, E, Arredouani, A, Vasudevan, SR, Lewis, AM, Parkesh, R, Mizote, A, Rosen, D, Thomas, JM, Izumi, M, Ganesan, A, Galione, A, Churchill, GC (2009) Identification of a chemical probe for NAADP by virtual screening. *Nat Chem Biol* **5**(4)**:** 220-226.

Neylon, CB, Richards, SM, Larsen, MA, Agrotis, A, Bobik, A (1995) Multiple types of ryanodine receptor/Ca2+ release channels are expressed in vascular smooth muscle. *Biochem Biophys Res Commun* **215**(3)**:** 814-821.

Noguchi, N, Takasawa, S, Nata, K, Tohgo, A, Kato, I, Ikehata, F, Yonekura, H, Okamoto, H (1997) Cyclic ADP-ribose binds to FK506-binding protein 12.6 to release Ca2+ from islet microsomes. *J Biol Chem* **272**(6)**:** 3133-3136.

Nohmi, M, Kuba, K, Hua, SY (1991) Ultraviolet light activates blocking actions of dantrolene on intracellular Ca2+ release in bullfrog sympathetic neurones. *J Biol Chem* **266**(33)**:** 22254-22259.

Noori, S, Acherman, R, Siassi, B, Luna, C, Ebrahimi, M, Pavlova, Z, Ramanathan, R (2002) A rare presentation of Pompe disease with massive hypertrophic cardiomyopathy at birth. *J Perinat Med* **30**(6)**:** 517-521.

Oda, K (1992) Calcium depletion blocks proteolytic cleavages of plasma protein precursors which occur at the Golgi and/or trans-Golgi network. Possible involvement of Ca(2+)-dependent Golgi endoproteases. *J Biol Chem* **267**(24)**:** 17465-17471.

Okamura, Y, Nishino, A, Murata, Y, Nakajo, K, Iwasaki, H, Ohtsuka, Y, Tanaka-Kunishima, M, Takahashi, N, Hara, Y, Yoshida, T, Nishida, M, Okado, H, Watari, H, Meinertzhagen, IA, Satoh, N, Takahashi, K, Satou, Y, Okada, Y, Mori, Y (2005) Comprehensive analysis of the ascidian genome reveals novel insights into the molecular evolution of ion channel genes. *Physiol Genomics* **22**(3)**:** 269-282.

Orth, P, Weimer, A, Kaul, G, Kohn, D, Cucchiarini, M, Madry, H (2008) Analysis of novel nonviral gene transfer systems for gene delivery to cells of the musculoskeletal system. *Mol Biotechnol* **38**(2)**:** 137-144.

Ostwald, TJ, MacLennan, DH (1974) Isolation of a high affinity calcium-binding protein from sarcoplasmic reticulum. *J Biol Chem* **249**(3)**:** 974-979.

Pacaud, P, Loirand, G, Mironneau, C, Mironneau, J (1989) Noradrenaline activates a calcium-activated chloride conductance and increases the voltage-dependent calcium current in cultured single cells of rat portal vein. *Br J Pharmacol* **97**(1)**:** 139-146.

Panfoli, I, Burlando, B, Viarengo, A (1999) Cyclic ADP-ribose-dependent Ca2+ release is modulated by free [Ca2+] in the scallop sarcoplasmic reticulum. *Biochem Biophys Res Commun* **257**(1)**:** 57-62.

Park, MK, Tepikin, AV, Petersen, OH (2002) What can we learn about cell signalling by combining optical imaging and patch clamp techniques? *Pflugers Arch* **444**(3)**:** 305-316.

Park, WS, Ko, JH, Kim, N, Son, YK, Kang, SH, Warda, M, Jung, ID, Park, YM, Han, J (2007a) Increased inhibition of inward rectifier K+ channels by angiotensin II in small-diameter coronary artery of isoproterenol-induced hypertrophied model. *Arterioscler Thromb Vasc Biol* **27**(8)**:** 1768-1775.

Park, WS, Son, YK, Kim, N, Ko, JH, Kang, SH, Warda, M, Earm, YE, Jung, ID, Park, YM, Han, J (2007b) Acute hypoxia induces vasodilation and increases coronary blood flow by activating inward rectifier K(+) channels. *Pflugers Arch* **454**(6)**:** 1023-1030.

Parkesh, R, Lewis, AM, Aley, PK, Arredouani, A, Rossi, S, Tavares, R, Vasudevan, SR, Rosen, D, Galione, A, Dowden, J, Churchill, GC (2008) Cell-permeant NAADP: a novel chemical tool enabling the study of Ca2+ signalling in intact cells. *Cell Calcium* **43**(6)**:** 531-538.

Parkinson-Lawrence, E, Fuller, M, Hopwood, JJ, Meikle, PJ, Brooks, DA (2006) Immunochemistry of lysosomal storage disorders. *Clin Chem* **52**(9)**:** 1660-1668.

Patel, S (2003) NAADP on the up in pancreatic beta cells-a sweet message? *Bioessays* **25**(5)**:** 430-433.

Patel, S (2004) NAADP-induced Ca2+ release -- a new signalling pathway. *Biol Cell* **96**(1)**:** 19-28.

Patel, S, Churchill, GC, Galione, A (2000a) Unique kinetics of nicotinic acid-adenine dinucleotide phosphate (NAADP) binding enhance the sensitivity of NAADP receptors for their ligand. *Biochem J* **352 Pt 3:** 725-729.

Patel, S, Churchill, GC, Sharp, T, Galione, A (2000b) Widespread distribution of binding sites for the novel Ca2+-mobilizing messenger, nicotinic acid adenine dinucleotide phosphate, in the brain. *J Biol Chem* **275**(47)**:** 36495-36497.

Pawelczyk, T (1999) Isozymes delta of phosphoinositide-specific phospholipase C. *Acta Biochim Pol* **46**(1)**:** 91-98.

Peck, JE (1984) Hearing loss in Hunter's syndrome--mucopolysaccharidosis II. *Ear Hear* **5**(4)**:** 243-246.

Peier, AM, Moqrich, A, Hergarden, AC, Reeve, AJ, Andersson, DA, Story, GM, Earley, TJ, Dragoni, I, McIntyre, P, Bevan, S, Patapoutian, A (2002) A TRP channel that senses cold stimuli and menthol. *Cell* **108**(5)**:** 705-715.

Peinelt, C, Vig, M, Koomoa, DL, Beck, A, Nadler, MJ, Koblan-Huberson, M, Lis, A, Fleig, A, Penner, R, Kinet, JP (2006) Amplification of CRAC current by STIM1 and CRACM1 (Orai1). *Nat Cell Biol* **8**(7)**:** 771-773.

Peiter, E, Maathuis, FJ, Mills, LN, Knight, H, Pelloux, J, Hetherington, AM, Sanders, D (2005) The vacuolar Ca2+-activated channel TPC1 regulates germination and stomatal movement. *Nature* **434**(7031)**:** 404-408.

Penna, A, Demuro, A, Yeromin, AV, Zhang, SL, Safrina, O, Parker, I, Cahalan, MD (2008) The CRAC channel consists of a tetramer formed by Stim-induced dimerization of Orai dimers. *Nature* **456**(7218)**:** 116-120.

Peters, C, Mayer, A (1998) Ca2+/calmodulin signals the completion of docking and triggers a late step of vacuole fusion. *Nature* **396**(6711)**:** 575-580.

Pezzati, R, Bossi, M, Podini, P, Meldolesi, J, Grohovaz, F (1997) High-resolution calcium mapping of the endoplasmic reticulum-Golgi-exocytic membrane system. Electron energy loss imaging analysis of quick frozen-freeze dried PC12 cells. *Mol Biol Cell* **8**(8)**:** 1501-1512.

Piper, RC, Luzio, JP (2004) CUPpling calcium to lysosomal biogenesis. *Trends Cell Biol* **14**(9)**:** 471-473.

Poburko, D, Kuo, KH, Dai, J, Lee, CH, van Breemen, C (2004) Organellar junctions promote targeted Ca2+ signaling in smooth muscle: why two membranes are better than one. *Trends Pharmacol Sci* **25**(1)**:** 8-15.

Polgar, L, Halasz, P (1982) Current problems in mechanistic studies of serine and cysteine proteinases. *Biochem J* **207**(1)**:** 1-10.

Porat, A, Elazar, Z (2000) Regulation of intra-Golgi membrane transport by calcium. *J Biol Chem* **275**(38)**:** 29233-29237.

Preiano, BS, Guerini, D, Carafoli, E (1996) Expression and functional characterization of isoforms 4 of the plasma membrane calcium pump. *Biochemistry* **35**(24)**:** 7946-7953.

Prekeris, R, Foletti, DL, Scheller, RH (1999) Dynamics of tubulovesicular recycling endosomes in hippocampal neurons. *J Neurosci* **19**(23)**:** 10324-10337.

Prentki, M, Glennon, MC, Thomas, AP, Morris, RL, Matschinsky, FM, Corkey, BE (1988) Cell-specific patterns of oscillating free Ca2+ in carbamylcholine-stimulated insulinoma cells. *J Biol Chem* **263**(23)**:** 11044-11047.

Presley, JF, Mayor, S, McGraw, TE, Dunn, KW, Maxfield, FR (1997) Bafilomycin A1 treatment retards transferrin receptor recycling more than bulk membrane recycling. *J Biol Chem* **272**(21)**:** 13929-13936.

Pryor, PR, Mullock, BM, Bright, NA, Gray, SR, Luzio, JP (2000) The role of intraorganellar Ca(2+) in late endosome-lysosome heterotypic fusion and in the reformation of lysosomes from hybrid organelles. *J Cell Biol* **149**(5)**:** 1053-1062.

Pryor, PR, Reimann, F, Gribble, FM, Luzio, JP (2006) Mucolipin-1 is a lysosomal membrane protein required for intracellular lactosylceramide traffic. *Traffic* **7**(10)**:** 1388-1398.

Pusch, M, Neher, E (1988) Rates of diffusional exchange between small cells and a measuring patch pipette. *Pflugers Arch* **411**(2)**:** 204-211.

Putney, JW, Jr. (1986) A model for receptor-regulated calcium entry. *Cell Calcium* **7**(1)**:** 1-12.

Quednau, BD, Nicoll, DA, Philipson, KD (2004) The sodium/calcium exchanger family-SLC8. *Pflugers Arch* **447**(5)**:** 543-548.

Randall, A, Tsien, RW (1995) Pharmacological dissection of multiple types of Ca2+ channel currents in rat cerebellar granule neurons. *J Neurosci* **15**(4)**:** 2995-3012.

Ranf, S, Wunnenberg, P, Lee, J, Becker, D, Dunkel, M, Hedrich, R, Scheel, D, Dietrich, P (2008) Loss of the vacuolar cation channel, AtTPC1, does not impair Ca2+ signals induced by abiotic and biotic stresses. *Plant J* **53**(2)**:** 287-299.

Rao, RN, Allen, NE, Hobbs, JN, Jr., Alborn, WE, Jr., Kirst, HA, Paschal, JW (1983) Genetic and enzymatic basis of hygromycin B resistance in Escherichia coli. *Antimicrob Agents Chemother* **24**(5)**:** 689-695.

Reaves, BJ, Bright, NA, Mullock, BM, Luzio, JP (1996) The effect of wortmannin on the localisation of lysosomal type I integral membrane glycoproteins suggests a role for phosphoinositide 3-kinase activity in regulating membrane traffic late in the endocytic pathway. *J Cell Sci* **109 (Pt 4):** 749-762.

Rebecchi, MJ, Pentyala, SN (2000) Structure, function, and control of phosphoinositide-specific phospholipase C. *Physiol Rev* **80**(4)**:** 1291-1335.

Reddy, BS, Sondhi, SM, Lown, JW (1999) Synthetic DNA minor groove-binding drugs. *Pharmacol Ther* **84**(1)**:** 1-111.

Rizzuto, R, Pozzan, T (2006) Microdomains of intracellular Ca2+: molecular determinants and functional consequences. *Physiol Rev* **86**(1)**:** 369-408.

Robb-Gaspers, LD, Burnett, P, Rutter, GA, Denton, RM, Rizzuto, R, Thomas, AP (1998) Integrating cytosolic calcium signals into mitochondrial metabolic responses. *EMBO J* **17**(17)**:** 4987-5000.

Rojas, P, Surroca, A, Orellana, A, Wolff, D (2000) Kinetic characterization of calcium uptake by the rat liver Golgi apparatus. *Cell Biol Int* **24**(4)**:** 229-233.

Rudolf, R, Mongillo, M, Magalhaes, PJ, Pozzan, T (2004) In vivo monitoring of Ca(2+) uptake into mitochondria of mouse skeletal muscle during contraction. *J Cell Biol* **166**(4)**:** 527-536.

Rusinko, N, Lee, HC (1989) Widespread occurrence in animal tissues of an enzyme catalyzing the conversion of NAD+ into a cyclic metabolite with intracellular Ca2+-mobilizing activity. *J Biol Chem* **264**(20)**:** 11725-11731.

Sadowski, L, Pilecka, I, Miaczynska, M (2009) Signaling from endosomes: location makes a difference. *Exp Cell Res* **315**(9)**:** 1601-1609.

Saida, K, van Breemen, C (1983) Mechanism of Ca++ antagonist-induced vasodilation. Intracellular actions. *Circ Res* **52**(2)**:** 137-142.

Saleh, S, Yeung, SY, Prestwich, S, Pucovsky, V, Greenwood, I (2005) Electrophysiological and molecular identification of voltage-gated sodium channels in murine vascular myocytes. *J Physiol* **568**(Pt 1)**:** 155-169.

Sansom, MS, Shrivastava, IH, Bright, JN, Tate, J, Capener, CE, Biggin, PC (2002) Potassium channels: structures, models, simulations. *Biochim Biophys Acta* **1565**(2)**:** 294-307.

Santella, L, Kyozuka, K, Genazzani, AA, De Riso, L, Carafoli, E (2000) Nicotinic acid adenine dinucleotide phosphate-induced Ca(2+) release. Interactions among distinct Ca(2+) mobilizing mechanisms in starfish oocytes. *J Biol Chem* **275**(12)**:** 8301-8306.

Schroder, F, Klein, G, Fiedler, B, Bastein, M, Schnasse, N, Hillmer, A, Ames, S, Gambaryan, S, Drexler, H, Walter, U, Lohmann, SM, Wollert, KC (2003) Single L-type Ca(2+) channel regulation by cGMP-dependent protein kinase type I in adult cardiomyocytes from PKG I transgenic mice. *Cardiovasc Res* **60**(2)**:** 268-277.

Schumacher, MA, Rivard, AF, Bachinger, HP, Adelman, JP (2001) Structure of the gating domain of a Ca2+-activated K+ channel complexed with Ca2+/calmodulin. *Nature* **410**(6832)**:** 1120-1124.

Schwarzmann, N, Kunerth, S, Weber, K, Mayr, GW, Guse, AH (2002) Knock-down of the type 3 ryanodine receptor impairs sustained Ca2+ signaling via the T cell receptor/CD3 complex. *J Biol Chem* **277**(52)**:** 50636-50642.

Shin, DM, Dehoff, M, Luo, X, Kang, SH, Tu, J, Nayak, SK, Ross, EM, Worley, PF, Muallem, S (2003) Homer 2 tunes G protein-coupled receptors stimulus intensity by regulating RGS proteins and PLCbeta GAP activities. *J Cell Biol* **162**(2)**:** 293-303.

Solomon, GD (1989) Verapamil in migraine prophylaxis--a five-year review. *Headache* **29**(7)**:** 425-427.

Soyombo, AA, Tjon-Kon-Sang, S, Rbaibi, Y, Bashllari, E, Bisceglia, J, Muallem, S, Kiselyov, K (2006) TRP-ML1 regulates lysosomal pH and acidic lysosomal lipid hydrolytic activity. *J Biol Chem* **281**(11)**:** 7294-7301.

Sparagna, GC, Gunter, KK, Sheu, SS, Gunter, TE (1995) Mitochondrial calcium uptake from physiological-type pulses of calcium. A description of the rapid uptake mode. *J Biol Chem* **270**(46)**:** 27510-27515.

Srinivas, SP, Ong, A, Goon, L, Bonanno, JA (2002) Lysosomal Ca(2+) stores in bovine corneal endothelium. *Invest Ophthalmol Vis Sci* **43**(7)**:** 2341-2350.

States, DJ, Walseth, TF, Lee, HC (1992) Similarities in amino acid sequences of Aplysia ADP-ribosyl cyclase and human lymphocyte antigen CD38. *Trends Biochem Sci* **17**(12)**:** 495.

Story, GM, Peier, AM, Reeve, AJ, Eid, SR, Mosbacher, J, Hricik, TR, Earley, TJ, Hergarden, AC, Andersson, DA, Hwang, SW, McIntyre, P, Jegla, T, Bevan, S, Patapoutian, A (2003) ANKTM1, a TRP-like channel expressed in nociceptive neurons, is activated by cold temperatures. *Cell* **112**(6)**:** 819-829.

Streb, H, Irvine, RF, Berridge, MJ, Schulz, I (1983) Release of Ca2+ from a nonmitochondrial intracellular store in pancreatic acinar cells by inositol-1,4,5-trisphosphate. *Nature* **306**(5938)**:** 67-69.

Strehler, EE, Zacharias, DA (2001) Role of alternative splicing in generating isoform diversity among plasma membrane calcium pumps. *Physiol Rev* **81**(1)**:** 21-50.

Sturley, SL, Patterson, MC, Balch, W, Liscum, L (2004) The pathophysiology and mechanisms of NP-C disease. *Biochim Biophys Acta* **1685**(1-3)**:** 83-87.

Sugaya, E, Onozuka (1978) Intracellular calcium: its release from granules during bursting activity in snail neurons. *Science* **202**(4373)**:** 1195-1197.

Sulem, P, Gudbjartsson, DF, Stacey, SN, Helgason, A, Rafnar, T, Jakobsdottir, M, Steinberg, S, Gudjonsson, SA, Palsson, A, Thorleifsson, G, Palsson, S, Sigurgeirsson, B, Thorisdottir, K, Ragnarsson, R, Benediktsdottir, KR, Aben, KK, Vermeulen, SH, Goldstein, AM, Tucker, MA, Kiemeney, LA, Olafsson, JH, Gulcher, J, Kong, A, Thorsteinsdottir, U, Stefansson, K (2008) Two newly identified genetic determinants of pigmentation in Europeans. *Nat Genet* **40**(7)**:** 835-837.

Sun, L, Adebanjo, OA, Koval, A, Anandatheerthavarada, HK, Iqbal, J, Wu, XY, Moonga, BS, Wu, XB, Biswas, G, Bevis, PJ, Kumegawa, M, Epstein, S, Huang, CL, Avadhani, NG, Abe, E, Zaidi, M (2002) A novel mechanism for coupling cellular intermediary metabolism to cytosolic Ca2+ signaling via CD38/ADP-ribosyl cyclase, a putative intracellular NAD+ sensor. *FASEB J* **16**(3)**:** 302-314.

Surroca, A, Wolff, D (2000) Inositol 1,4,5-trisphosphate but not ryanodine-receptor agonists induces calcium release from rat liver Golgi apparatus membrane vesicles. *J Membr Biol* **177**(3)**:** 243-249.

Suzuki, M, Morita, T, Iwamoto, T (2006) Diversity of Cl(-) channels. *Cell Mol Life Sci* **63**(1)**:** 12-24.

Syyong, HT, Poburko, D, Fameli, N, van Breemen, C (2007) ATP promotes NCX-reversal in aortic smooth muscle cells by DAG-activated Na+ entry. *Biochem Biophys Res Commun* **357**(4)**:** 1177-1182.

Takahashi, A, Camacho, P, Lechleiter, JD, Herman, B (1999) Measurement of intracellular calcium. *Physiol Rev* **79**(4)**:** 1089-1125.

Takahashi, M, Seagar, MJ, Jones, JF, Reber, BF, Catterall, WA (1987) Subunit structure of dihydropyridine-sensitive calcium channels from skeletal muscle. *Proc Natl Acad Sci U S A* **84**(15)**:** 5478-5482.

Takazawa, K, Lemos, M, Delvaux, A, Lejeune, C, Dumont, JE, Erneux, C (1990) Rat brain inositol 1,4,5-trisphosphate 3-kinase. Ca2(+)-sensitivity, purification and antibody production. *Biochem J* **268**(1)**:** 213-217.

Takekura, H, Takeshima, H, Nishimura, S, Takahashi, M, Tanabe, T, Flockerzi, V, Hofmann, F, Franzini-Armstrong, C (1995) Co-expression in CHO cells of two muscle proteins involved in excitation-contraction coupling. *J Muscle Res Cell Motil* **16**(5)**:** 465-480.

Takeshima, H, Komazaki, S, Nishi, M, Iino, M, Kangawa, K (2000) Junctophilins: a novel family of junctional membrane complex proteins. *Mol Cell* **6**(1)**:** 11-22.

Tanaka, Y, Meera, P, Song, M, Knaus, HG, Toro, L (1997) Molecular constituents of maxi KCa channels in human coronary smooth muscle: predominant alpha + beta subunit complexes. *J Physiol* **502 (Pt 3):** 545-557.

Tanaka, Y, Tashjian, AH, Jr. (1995) Calmodulin is a selective mediator of Ca(2+)-induced Ca2+ release via the ryanodine receptor-like Ca2+ channel triggered by cyclic ADP-ribose. *Proc Natl Acad Sci U S A* **92**(8)**:** 3244-3248.

Tang, WX, Chen, YF, Zou, AP, Campbell, WB, Li, PL (2002) Role of FKBP12.6 in cADPR-induced activation of reconstituted ryanodine receptors from arterial smooth muscle. *Am J Physiol Heart Circ Physiol* **282**(4)**:** H1304-1310.

Taufiq Ur, R, Skupin, A, Falcke, M, Taylor, CW (2009) Clustering of InsP3 receptors by InsP3 retunes their regulation by InsP3 and Ca2+. *Nature* **458**(7238)**:** 655-659.

Taunton, J (2001) Actin filament nucleation by endosomes, lysosomes and secretory vesicles. *Curr Opin Cell Biol* **13**(1)**:** 85-91.

Taylor, CW, Genazzani, AA, Morris, SA (1999) Expression of inositol trisphosphate receptors. *Cell Calcium* **26**(6)**:** 237-251.

Taylor, CW, Laude, AJ (2002) IP3 receptors and their regulation by calmodulin and cytosolic Ca2+. *Cell Calcium* **32**(5-6)**:** 321-334.

Tewari, K, Simard, JM (1997) Sodium nitroprusside and cGMP decrease Ca2+ channel availability in basilar artery smooth muscle cells. *Pflugers Arch* **433**(3)**:** 304-311.

Thebault, S, Zholos, A, Enfissi, A, Slomianny, C, Dewailly, E, Roudbaraki, M, Parys, J, Prevarskaya, N (2005) Receptor-operated Ca2+ entry mediated by TRPC3/TRPC6 proteins in rat prostate smooth muscle (PS1) cell line. *J Cell Physiol* **204**(1)**:** 320-328.

Thomas, JM, Masgrau, R, Churchill, GC, Galione, A (2001) Pharmacological characterization of the putative cADP-ribose receptor. *Biochem J* **359**(Pt 2)**:** 451-457.

Thomas, P, Smart, TG (2005) HEK293 cell line: a vehicle for the expression of recombinant proteins. *J Pharmacol Toxicol Methods* **51**(3)**:** 187-200.

Thomas, RC (2009) The plasma membrane calcium ATPase (PMCA) of neurones is electroneutral and exchanges 2 H+ for each Ca2+ or Ba2+ ion extruded. *J Physiol* **587**(Pt 2)**:** 315-327.

Thomsen, P, Rudenko, O, Berezin, V, Norrild, B (1999) The HPV-16 E5 oncogene and bafilomycin A(1) influence cell motility. *Biochim Biophys Acta* **1452**(3)**:** 285-295.

Tinel, H, Cancela, JM, Mogami, H, Gerasimenko, JV, Gerasimenko, OV, Tepikin, AV, Petersen, OH (1999) Active mitochondria surrounding the pancreatic acinar granule region prevent spreading of inositol trisphosphate-evoked local cytosolic Ca(2+) signals. *EMBO J* **18**(18)**:** 4999-5008.

Tomassoni, D, Lanari, A, Silvestrelli, G, Traini, E, Amenta, F (2008) Nimodipine and its use in cerebrovascular disease: evidence from recent preclinical and controlled clinical studies. *Clin Exp Hypertens* **30**(8)**:** 744-766.

Tovey, SC, Dedos, SG, Taylor, EJ, Church, JE, Taylor, CW (2008) Selective coupling of type 6 adenylyl cyclase with type 2 IP3 receptors mediates direct sensitization of IP3 receptors by cAMP. *J Cell Biol* **183**(2)**:** 297-311.

Traaseth, NJ, Ha, KN, Verardi, R, Shi, L, Buffy, JJ, Masterson, LR, Veglia, G (2008) Structural and dynamic basis of phospholamban and sarcolipin inhibition of Ca(2+)-ATPase. *Biochemistry* **47**(1)**:** 3-13.

Tsien, RY (1980) New calcium indicators and buffers with high selectivity against magnesium and protons: design, synthesis, and properties of prototype structures. *Biochemistry* **19**(11)**:** 2396-2404.

Van Breemen, C, Aaronson, P, Loutzenhiser, R (1978) Sodium-calcium interactions in mammalian smooth muscle. *Pharmacol Rev* **30**(2)**:** 167-208.

Van Dyke, RW (1996) Acidification of lysosomes and endosomes. *Subcell Biochem* **27:** 331-360.

van Koppen, CJ, Meyer zu Heringdorf, D, Alemany, R, Jakobs, KH (2001) Sphingosine kinase-mediated calcium signaling by muscarinic acetylcholine receptors. *Life Sci* **68**(22-23)**:** 2535-2540.

van Weely, S, van den Berg, M, Barranger, JA, Sa Miranda, MC, Tager, JM, Aerts, JM (1993) Role of pH in determining the cell-type-specific residual activity of glucocerebrosidase in type 1 Gaucher disease. *J Clin Invest* **91**(3)**:** 1167-1175.

Vangheluwe, P, Schuermans, M, Zador, E, Waelkens, E, Raeymaekers, L, Wuytack, F (2005) Sarcolipin and phospholamban mRNA and protein expression in cardiac and skeletal muscle of different species. *Biochem J* **389**(Pt 1)**:** 151-159.

Vanoevelen, J, Raeymaekers, L, Parys, JB, De Smedt, H, Van Baelen, K, Callewaert, G, Wuytack, F, Missiaen, L (2004) Inositol trisphosphate producing agonists do not

mobilize the thapsigargin-insensitive part of the endoplasmic-reticulum and Golgi Ca2+ store. *Cell Calcium* **35**(2)**:** 115-121.

Vasudevan, SR, Galione, A, Churchill, GC (2008) Sperm express a Ca2+-regulated NAADP synthase. *Biochem J* **411**(1)**:** 63-70.

Verboomen, H, Wuytack, F, Van den Bosch, L, Mertens, L, Casteels, R (1994) The functional importance of the extreme C-terminal tail in the gene 2 organellar Ca(2+)-transport ATPase (SERCA2a/b). *Biochem J* **303 (Pt 3):** 979-984.

Voeltz, GK, Rolls, MM, Rapoport, TA (2002) Structural organization of the endoplasmic reticulum. *EMBO Rep* **3**(10)**:** 944-950.

Volpe, P, Martini, A, Furlan, S, Meldolesi, J (1994) Calsequestrin is a component of smooth muscles: the skeletal- and cardiac-muscle isoforms are both present, although in highly variable amounts and ratios. *Biochem J* **301 (Pt 2):** 465-469.

von Zastrow, M, Sorkin, A (2007) Signaling on the endocytic pathway. *Curr Opin Cell Biol* **19**(4)**:** 436-445.

Wagman, GH, Testa, RT, Marquez, JA, Weinstein, MJ (1974) Antibiotic G-418, a new Micromonospora-produced aminoglycoside with activity against protozoa and helminths: fermentation, isolation, and preliminary characterization. *Antimicrob Agents Chemother* **6**(2)**:** 144-149.

Walseth, TF, Aarhus, R, Kerr, JA, Lee, HC (1993) Identification of cyclic ADP-ribose-binding proteins by photoaffinity labeling. *J Biol Chem* **268**(35)**:** 26686-26691.

Walseth, TF, Aarhus, R, Zeleznikar, RJ, Jr., Lee, HC (1991) Determination of endogenous levels of cyclic ADP-ribose in rat tissues. *Biochim Biophys Acta* **1094**(1)**:** 113-120.

Wang, S, Trumble, WR, Liao, H, Wesson, CR, Dunker, AK, Kang, CH (1998) Crystal structure of calsequestrin from rabbit skeletal muscle sarcoplasmic reticulum. *Nat Struct Biol* **5**(6)**:** 476-483.

Wang, YX, Zheng, YM, Mei, QB, Wang, QS, Collier, ML, Fleischer, S, Xin, HB, Kotlikoff, MI (2004) FKBP12.6 and cADPR regulation of Ca2+ release in smooth muscle cells. *Am J Physiol Cell Physiol* **286**(3)**:** C538-546.

Ward, CW, Feng, W, Tu, J, Pessah, IN, Worley, PK, Schneider, MF (2004) Homer protein increases activation of Ca2+ sparks in permeabilized skeletal muscle. *J Biol Chem* **279**(7)**:** 5781-5787.

Ward, JP, McMurtry, IF (2009) Mechanisms of hypoxic pulmonary vasoconstriction and their roles in pulmonary hypertension: new findings for an old problem. *Curr Opin Pharmacol* **9**(3)**:** 287-296.

Wegener, AD, Simmerman, HK, Lindemann, JP, Jones, LR (1989) Phospholamban phosphorylation in intact ventricles. Phosphorylation of serine 16 and threonine 17 in response to beta-adrenergic stimulation. *J Biol Chem* **264**(19)**:** 11468-11474.

Wei, AD, Gutman, GA, Aldrich, R, Chandy, KG, Grissmer, S, Wulff, H (2005) International Union of Pharmacology. LII. Nomenclature and molecular relationships of calcium-activated potassium channels. *Pharmacol Rev* **57**(4)**:** 463-472.

Wei, Y, Chen, J, Rosas, G, Tompkins, DA, Holt, PA, Rao, R (2000) Phenotypic screening of mutations in Pmr1, the yeast secretory pathway Ca2+/Mn2+-ATPase, reveals residues critical for ion selectivity and transport. *J Biol Chem* **275**(31)**:** 23927-23932.

Westhoff, JH, Hwang, SY, Duncan, RS, Ozawa, F, Volpe, P, Inokuchi, K, Koulen, P (2003) Vesl/Homer proteins regulate ryanodine receptor type 2 function and intracellular calcium signaling. *Cell Calcium* **34**(3)**:** 261-269.

White, AM, Watson, SP, Galione, A (1993) Cyclic ADP-ribose-induced Ca2+ release from rat brain microsomes. *FEBS Lett* **318**(3)**:** 259-263.

Wiederanders, B (2003) Structure-function relationships in class CA1 cysteine peptidase propeptides. *Acta Biochim Pol* **50**(3)**:** 691-713.

Wojcikiewicz, RJ (1995) Type I, II, and III inositol 1,4,5-trisphosphate receptors are unequally susceptible to down-regulation and are expressed in markedly different proportions in different cell types. *J Biol Chem* **270**(19)**:** 11678-11683.

Wojcikiewicz, RJ, Luo, SG (1998) Differences among type I, II, and III inositol-1,4,5-trisphosphate receptors in ligand-binding affinity influence the sensitivity of calcium stores to inositol-1,4,5-trisphosphate. *Mol Pharmacol* **53**(4)**:** 656-662.

Woo, JS, Kim do, H, Allen, PD, Lee, EH (2008) TRPC3-interacting triadic proteins in skeletal muscle. *Biochem J* **411**(2)**:** 399-405.

Worley, PF, Zeng, W, Huang, G, Kim, JY, Shin, DM, Kim, MS, Yuan, JP, Kiselyov, K, Muallem, S (2007) Homer proteins in Ca2+ signaling by excitable and non-excitable cells. *Cell Calcium* **42**(4-5)**:** 363-371.

Wray, D (2004) The roles of intracellular regions in the activation of voltage-dependent potassium channels. *Eur Biophys J* **33**(3)**:** 194-200.

Wray, S, Burdyga, T, Noble, K (2005) Calcium signalling in smooth muscle. *Cell Calcium* **38**(3-4)**:** 397-407.

Xu, X, Rials, SJ, Wu, Y, Marinchak, RA, Kowey, PR (1999) The properties of the inward rectifier potassium currents in rabbit coronary arterial smooth muscle cells. *Pflugers Arch* **438**(2)**:** 187-194.

Yagi, T, Boyden, PA (2002) Protein tyrosine kinases and L-type Ca2+ currents in cells that have survived in epicardial border zone of canine infarcted heart. *J Cardiovasc Pharmacol* **40**(5)**:** 669-677.

Yagodin, S, Pivovarova, NB, Andrews, SB, Sattelle, DB (1999) Functional characterization of thapsigargin and agonist-insensitive acidic Ca2+ stores in Drosophila melanogaster S2 cell lines. *Cell Calcium* **25**(6)**:** 429-438.

Yalcintepe, L, Albeniz, I, Adin-Cinar, S, Tiryaki, D, Bermek, E, Graeff, RM, Lee, HC (2005) Nuclear CD38 in retinoic acid-induced HL-60 cells. *Exp Cell Res* **303**(1)**:** 14-21.

Yamasaki, M, Masgrau, R, Morgan, AJ, Churchill, GC, Patel, S, Ashcroft, SJ, Galione, A (2004) Organelle selection determines agonist-specific Ca2+ signals in pancreatic acinar and beta cells. *J Biol Chem* **279**(8)**:** 7234-7240.

Yamasaki, M, Thomas, JM, Churchill, GC, Garnham, C, Lewis, AM, Cancela, JM, Patel, S, Galione, A (2005) Role of NAADP and cADPR in the induction and maintenance of agonist-evoked Ca2+ spiking in mouse pancreatic acinar cells. *Curr Biol* **15**(9)**:** 874-878.

Yamazaki, D, Yamazaki, T, Takeshima, H (2009) New molecular components supporting ryanodine receptor-mediated Ca(2+) release: Roles of junctophilin and TRIC channel in embryonic cardiomyocytes. *Pharmacol Ther* **121**(3)**:** 265-272.

Yang, J, Ellinor, PT, Sather, WA, Zhang, JF, Tsien, RW (1993) Molecular determinants of Ca2+ selectivity and ion permeation in L-type Ca2+ channels. *Nature* **366**(6451)**:** 158-161.

Yang, XR, Lin, MJ, Yip, KP, Jeyakumar, LH, Fleischer, S, Leung, GP, Sham, JS (2005) Multiple ryanodine receptor subtypes and heterogeneous ryanodine receptor-gated Ca2+ stores in pulmonary arterial smooth muscle cells. *Am J Physiol Lung Cell Mol Physiol* **289**(2)**:** L338-348.

Yang, YD, Cho, H, Koo, JY, Tak, MH, Cho, Y, Shim, WS, Park, SP, Lee, J, Lee, B, Kim, BM, Raouf, R, Shin, YK, Oh, U (2008) TMEM16A confers receptor-activated calcium-dependent chloride conductance. *Nature* **455**(7217)**:** 1210-1215.

Yu, FH, Catterall, WA (2003) Overview of the voltage-gated sodium channel family. *Genome Biol* **4**(3)**:** 207.

Yu, FH, Yarov-Yarovoy, V, Gutman, GA, Catterall, WA (2005) Overview of molecular relationships in the voltage-gated ion channel superfamily. *Pharmacol Rev* **57**(4)**:** 387-395.

Yu, X, Carroll, S, Rigaud, JL, Inesi, G (1993) H+ countertransport and electrogenicity of the sarcoplasmic reticulum Ca2+ pump in reconstituted proteoliposomes. *Biophys J* **64**(4)**:** 1232-1242.

Yule, DI (2001) Subtype-specific regulation of inositol 1,4,5-trisphosphate receptors: controlling calcium signals in time and space. *J Gen Physiol* **117**(5)**:** 431-434.

Yusufi, AN, Cheng, J, Thompson, MA, Burnett, JC, Grande, JP (2002) Differential mechanisms of Ca(2+) release from vascular smooth muscle cell microsomes. *Exp Biol Med (Maywood)* **227**(1)**:** 36-44.

Yusufi, AN, Cheng, J, Thompson, MA, Dousa, TP, Warner, GM, Walker, HJ, Grande, JP (2001) cADP-ribose/ryanodine channel/Ca2+-release signal transduction pathway in mesangial cells. *Am J Physiol Renal Physiol* **281**(1)**:** F91-F102.

Zeng, XH, Xia, XM, Lingle, CJ (2005) Divalent cation sensitivity of BK channel activation supports the existence of three distinct binding sites. *J Gen Physiol* **125**(3)**:** 273-286.

Zhang, F, Jin, S, Yi, F, Li, PL (2008) TRP-ML1 Functions as a Lysosomal NAADP-Sensitive Ca(2+) Release Channel in Coronary Arterial Myocytes. *J Cell Mol Med*.

Zhang, F, Zhang, G, Zhang, AY, Koeberl, MJ, Wallander, E, Li, PL (2006a) Production of NAADP and its role in Ca2+ mobilization associated with lysosomes in coronary arterial myocytes. *Am J Physiol Heart Circ Physiol* **291**(1)**:** H274-282.

Zhang, S, Remillard, CV, Fantozzi, I, Yuan, JX (2004) ATP-induced mitogenesis is mediated by cyclic AMP response element-binding protein-enhanced TRPC4 expression and activity in human pulmonary artery smooth muscle cells. *Am J Physiol Cell Physiol* **287**(5)**:** C1192-1201.

Zhang, S, Yuan, JX, Barrett, KE, Dong, H (2005) Role of Na+/Ca2+ exchange in regulating cytosolic Ca2+ in cultured human pulmonary artery smooth muscle cells. *Am J Physiol Cell Physiol* **288**(2)**:** C245-252.

Zhang, SL, Yeromin, AV, Zhang, XH, Yu, Y, Safrina, O, Penna, A, Roos, J, Stauderman, KA, Cahalan, MD (2006b) Genome-wide RNAi screen of Ca(2+) influx identifies genes that regulate Ca(2+) release-activated Ca(2+) channel activity. *Proc Natl Acad Sci U S A* **103**(24)**:** 9357-9362.

Zhang, Y, Hoon, MA, Chandrashekar, J, Mueller, KL, Cook, B, Wu, D, Zuker, CS, Ryba, NJ (2003) Coding of sweet, bitter, and umami tastes: different receptor cells sharing similar signaling pathways. *Cell* **112**(3)**:** 293-301.

Zhao, F, Li, P, Chen, SR, Louis, CF, Fruen, BR (2001) Dantrolene inhibition of ryanodine receptor Ca2+ release channels. Molecular mechanism and isoform selectivity. *J Biol Chem* **276**(17)**:** 13810-13816.

Zhao, H, Grabowski, GA (2002) Gaucher disease: Perspectives on a prototype lysosomal disease. *Cell Mol Life Sci* **59**(4)**:** 694-707.

Zong, X, Schieder, M, Cuny, H, Fenske, S, Gruner, C, Rotzer, K, Griesbeck, O, Harz, H, Biel, M, Wahl-Schott, C (2009) The two-pore channel TPCN2 mediates NAADP-dependent Ca(2+)-release from lysosomal stores. *Pflugers Arch* **458**(5)**:** 891-899.

Zuhlke, RD, Pitt, GS, Deisseroth, K, Tsien, RW, Reuter, H (1999) Calmodulin supports both inactivation and facilitation of L-type calcium channels. *Nature* **399**(6732)**:** 159-162.

Appendix 1:

Results tables for Chapter 3:

	Total cell volume (μm^3)	Perinuclear region volume (μm^3)	Extra-perinuclear region volume (μm^3)	Sub-plasmalemmal region volume (μm^3)
	2089.31	570.75	616.57	901.99
	927.2	253.72	225.44	368.13
	1507.29	453.68	316.91	662.69
	4206.95	1237.26	751.28	2218.41
	729.16	192.94	171.92	329.92
	1879.62	616.13	494.84	768.65
	1701.72	460.13	715.44	513.17
	2208.73	554.25	1017.2	637.28
	1075.34	321.68	215.95	491.53
	868.45	211.19	236.17	369.82
	1472.71	438.72	455.17	633.47
	1366.61	283.73	401.6	641.56
	741.59	178.63	210.36	285.09
	1429.76	282.09	458.06	514.44
	2551.58	1131.17	425.68	958.68
	1959.04	840.18	318.82	652.62
	2076.69	758.86	411.12	801.96
	1688.99	719.56	354.95	569.38
	1030.88	305.05	274.4	373.02
	847.31	179.9	168.57	438.5
	1687.92	350.39	427.51	798.98
	850.3	204.88	289.56	302.79
	649.95	191.17	152.61	227.2
	830.59	197.49	217.92	359.14
	2300.8	584.03	555.19	1071.32
	1090.41	309.18	275.59	444.15
	846.87	266.9	178.52	376.58
	2073.08	649.4	83.35	540.33
	2215.08	950.76	590.71	626.81
	1934.38	948.97	300.32	642.8
	1557.8	750.38	313.7	443.05
	1542.94	498.46	387.95	554.32
	665.34	247.43	89.77	272.12
	922.2	278.46	187.01	395.83
	1018.23	329.04	239.9	381.91
Mean	1501.28	478.47	358.00	587.65
S.E.M.	122.83	48.68	34.13	59.05

Table 3.1. Measurements of the volume occupied by the 3 regions of the divided cell for all the isolated pulmonary arterial smooth muscle cells analysed

	Volume of lysosomal labelling (μm^3)	Total cell volume (μm^3)	Density of lysosmal labelling (μm^3 per μm^3)
	26.14	2089.31	0.013
	10.6	927.2	0.011
	8.68	1507.29	0.006
	34.78	4206.95	0.008
	23.59	729.16	0.032
	34.68	1879.62	0.018
	28.53	1701.72	0.017
	31.5	2208.73	0.014
	31.04	1075.34	0.029
	34.73	868.45	0.040
	42.52	1472.71	0.029
	33.9	1366.61	0.025
	24.87	741.59	0.034
	29.73	1429.76	0.021
	33.15	2551.58	0.013
	24.46	1959.04	0.012
	29.13	2076.69	0.014
	21.28	1688.99	0.013
	17.72	1030.88	0.017
	20.62	847.31	0.024
	36.24	1687.92	0.021
	20.69	850.3	0.024
	14.49	649.95	0.022
	16.36	830.59	0.020
	31.58	2300.8	0.014
	29.77	1090.41	0.027
	22.68	846.87	0.027
	22.43	2073.08	0.011
	38.1	2215.08	0.017
	35.64	1934.38	0.018
	51.51	1557.8	0.033
	46.93	1542.94	0.030
	14.57	665.34	0.022
	24.53	922.2	0.027
	22.63	1018.23	0.022
Mean	27.71	1501.28	0.021
S.E.M.	1.63	122.83	0.001

Table 3.2. Measurements of the density of αIgp120 labelling within the whole cell volume of isolated pulmonary arterial smooth muscle cells

	Volume of perinuclear lysosomal labelling (μm^3)	Mean volume of individual labelling within the perinuclear region (μm^3)	Perinuclear region volume (μm^3)	Density of perinuclear lysosomal labelling (μm^3 per μm^3)
	8.73	0.42	570.75	0.015
	3.76	0.58	253.72	0.015
	3.08	0.55	453.68	0.007
	15.15	0.33	1237.26	0.012
	11.12	0.93	192.94	0.058
	10.04	0.42	616.13	0.016
	9.55	0.40	460.13	0.021
	13.86	0.43	554.25	0.025
	19.88	0.30	321.68	0.062
	13.3	1.02	211.19	0.063
	20.79	0.54	438.72	0.047
	16.05	0.68	283.73	0.057
	6.59	0.51	178.63	0.037
	16.57	0.67	282.09	0.059
	17.12	0.63	1131.17	0.015
	22.6	1.50	840.18	0.027
	19.36	0.82	758.86	0.026
	12.64	0.47	719.56	0.018
	12.72	0.67	305.05	0.042
	12.31	0.34	179.9	0.068
	16.49	0.72	350.39	0.047
	12.84	0.61	204.88	0.063
	11.51	0.96	191.17	0.060
	8.01	0.73	197.49	0.041
	20.15	0.64	584.03	0.035
	16.18	0.87	309.18	0.050
	14.31	0.59	266.9	0.054
	16.54	0.85	649.4	0.026
	24.61	1.51	950.76	0.026
	25.72	0.83	948.97	0.027
	47.77	1.90	750.38	0.064
	17.71	1.13	498.46	0.036
	11.36	0.95	247.43	0.046
	12.5	1.04	278.46	0.045
	16.92	1.21	329.04	0.051
Mean	15.37	0.76	478.47	0.039
S.E.M.	1.30	0.06	48.68	0.003

Table 3.3. Measurements of the mean volume of individual αIgp120 labelling and the density of αIgp120 labelling within the perinuclear region of isolated pulmonary arterial smooth muscle cells

	Volume of extra-perinuclear lysosomal labelling (μm^3)	Mean volume of individual labelling within the extra-perinuclear region (μm^3)	Extra-perinuclear region volume (μm^3)	Density of extra-perinuclear lysosomal labelling (μm^3 per μm^3)
	7.98	0.43	616.57	0.013
	0.85	0.22	225.44	0.004
	2.6	0.21	316.91	0.008
	9.97	0.30	751.28	0.013
	8.36	1.19	171.92	0.049
	9.83	0.41	494.84	0.020
	2.35	0.90	715.44	0.003
	6.75	0.29	1017.2	0.007
	2.7	0.23	215.95	0.013
	11.66	2.92	236.17	0.049
	15.34	0.72	455.17	0.034
	12.56	0.59	401.6	0.031
	14.21	1.80	210.36	0.068
	7.36	0.33	458.06	0.016
	5.28	0.55	425.68	0.012
	1.09	0.52	318.82	0.003
	6.16	0.44	411.12	0.015
	3.91	0.33	354.95	0.011
	3.28	0.27	274.4	0.012
	5.24	0.35	168.57	0.031
	7.65	0.48	427.51	0.018
	5.17	0.78	289.56	0.018
	2.35	0.39	152.61	0.015
	7.05	1.01	217.92	0.032
	4.27	0.27	555.19	0.008
	10.8	0.78	275.59	0.039
	2.87	0.47	178.52	0.016
	1.73	0.57	83.35	0.002
	10	1.13	590.71	0.017
	5.9	0.40	300.32	0.019
	2.55	0.58	313.7	0.008
	8.57	0.73	387.95	0.022
	0.77	0.19	89.77	0.009
	6.62	0.60	187.01	0.035
	3.61	0.40	239.9	0.015
Mean	6.21	0.62	358.00	0.020
S.E.M.	0.65	0.09	34.13	0.003

Table 3.4. Measurements of the mean volume of individual αIgp120 labelling and the density of αIgp120 labelling within the extra-perinuclear region of isolated pulmonary arterial smooth muscle cells

	Volume of sub-plasmalemmal lysosomal labelling (μm^3)	Mean volume of individual labelling within the sub-plasmalemmal region (μm^3)	Sub-plasmalemmal region volume (μm^3)	Density of sub-plasmalemmal lysosomal labelling (μm^3 per μm^3)
	9.43	0.31	901.99	0.010
	2.15	0.21	368.13	0.006
	3.00	0.22	662.69	0.005
	7.52	0.27	2218.41	0.003
	4.11	0.22	329.92	0.012
	13.19	0.27	768.65	0.017
	15.46	0.24	513.17	0.030
	9.09	0.32	637.28	0.014
	8.28	0.21	491.53	0.017
	9.77	0.51	369.82	0.026
	3.72	0.19	633.47	0.006
	4.33	0.24	641.56	0.007
	3.94	0.26	285.09	0.014
	4.75	0.25	514.44	0.009
	8.47	0.52	958.68	0.009
	0.77	0.25	652.62	0.001
	3.30	0.37	801.96	0.004
	3.26	0.24	569.38	0.006
	1.53	0.17	373.02	0.004
	1.99	0.18	438.5	0.005
	11.08	0.62	798.98	0.014
	1.36	0.19	302.79	0.004
	0.63	0.21	227.2	0.003
	1.15	0.19	359.14	0.003
	6.10	0.21	1071.32	0.006
	2.79	0.28	444.15	0.006
	5.46	0.27	376.58	0.015
	3.61	0.56	540.33	0.007
	2.86	0.43	626.81	0.005
	3.44	0.28	642.8	0.005
	1.19	0.30	443.05	0.003
	20.46	0.90	554.32	0.037
	2.00	0.22	272.12	0.007
	4.69	0.36	395.83	0.012
	1.76	0.25	381.91	0.005
Mean	5.33	0.31	587.65	0.010
S.E.M.	0.76	0.03	59.05	0.001

Table 3.5. Measurements of the mean volume of individual αIgp120 labelling and the density of αIgp120 labelling within the sub-plasmalemmal region of isolated pulmonary arterial smooth muscle cells

	% of total lysosomal labelling represented by the perinuclear region	% of total lysosomal labelling represented by the extra-perinuclear region	% of total lysosomal labelling represented by the sub-plasmalemmal region	% of whole cell volume represented by the perinuclear region	% of whole cell volume represented by the extra-perinuclear region	% of whole cell volume represented by the sub-plasmalemmal region
	33.4	30.5	36.1	27.3	29.5	43.2
	35.5	8.0	20.3	27.4	24.3	39.7
	35.5	30.0	34.6	30.1	21.0	44.0
	43.6	28.7	21.6	29.4	17.9	52.7
	47.1	35.4	17.4	26.5	23.6	45.2
	29.0	28.3	38.0	32.8	26.3	40.9
	33.5	8.2	54.2	27.0	42.0	30.2
	44.0	21.4	28.9	25.1	46.1	28.9
	64.0	8.7	26.7	29.9	20.1	45.7
	38.3	33.6	28.1	24.3	27.2	42.6
	48.9	36.1	8.7	29.8	30.9	43.0
	47.3	37.1	12.8	20.8	29.4	46.9
	26.5	57.1	15.8	24.1	28.4	38.4
	55.7	24.8	16.0	19.7	32.0	36.0
	51.6	15.9	25.6	44.3	16.7	37.6
	92.4	4.5	3.1	42.9	16.3	33.3
	66.5	21.1	11.3	36.5	19.8	38.6
	59.4	18.4	15.3	42.6	21.0	33.7
	71.8	18.5	8.6	29.6	26.6	36.2
	59.7	25.4	9.7	21.2	19.9	51.8
	45.5	21.1	30.6	20.8	25.3	47.3
	62.1	25.0	6.6	24.1	34.1	35.6
	79.4	16.2	4.3	29.4	23.5	35.0
	49.0	43.1	7.0	23.8	26.2	43.2
	63.8	13.5	19.3	25.4	24.1	46.6
	54.4	36.3	9.4	28.4	25.3	40.7
	63.1	12.7	24.1	31.5	21.1	44.5
	73.7	7.7	16.1	31.3	4.0	26.1
	64.6	26.2	7.5	42.9	26.7	28.3
	72.2	16.6	9.7	49.1	15.5	33.2
	92.7	5.0	2.3	48.2	20.1	28.4
	37.7	18.3	43.6	32.3	25.1	35.9
	78.0	5.3	13.7	37.2	13.5	40.9
	51.0	27.0	19.1	30.2	20.3	42.9
	74.8	16.0	7.8	32.3	23.6	37.5
Mean	55.6	22.3	18.7	30.8	24.2	39.3
S.E.M.	2.9	2.0	2.1	1.3	1.3	1.1

Table 3.6. Measurements of the total αIgp120 labelling and the total cell volume represented by each region of sub-divided isolated pulmonary arterial smooth muscle cells

	Volume of RyR1 labelling (μm^3)	Total cell volume (μm^3)	Density of RyR1 labelling (μm^3 per μm^3)
	47.78	2089.31	0.023
	19.2	847.29	0.023
	28.39	1430.7	0.020
	77.61	4206.95	0.018
	34.41	729.16	0.047
	64.48	1879.62	0.034
	64.22	1701.72	0.038
	70.07	2208.73	0.032
	55.83	1075.34	0.052
	27.49	868.45	0.032
	38.06	822.47	0.046
Mean	47.96	1623.61	0.033
S.E.M.	5.94	305.36	0.004

Table 3.7. Measurements of the density of RyR1 labelling within the whole cell volume of isolated pulmonary arterial smooth muscle cells

	Volume of perinuclear RyR1 labelling (μm^3)	Mean volume of individual labelling within the perinuclear region (μm^3)	Perinuclear region volume (μm^3)	Density of perinuclear RyR1 labelling (μm^3 per μm^3)
	13.54	1.03	570.75	0.024
	6	0.67	253.72	0.024
	3.93	0.56	449.64	0.009
	23.06	0.56	1237.26	0.019
	13.52	0.65	192.94	0.070
	26.6	1.34	616.13	0.043
	7.55	0.93	460.13	0.016
	31.97	3.61	554.25	0.058
	23.53	1.05	321.68	0.073
	8.85	0.49	211.19	0.042
	15.62	0.58	217.24	0.072
Mean	15.83	1.04	462.27	0.041
S.E.M.	2.79	0.27	90.63	0.007

Table 3.8. Measurements of the mean volume of individual RyR1 labelling and the density of RyR1 labelling within the perinuclear region of isolated pulmonary arterial smooth muscle cells

	Volume of extra-perinuclear RyR1 labelling (μm^3)	Mean volume of individual labelling within the extra-perinuclear region (μm^3)	Extra-perinuclear region volume (μm^3)	Density of extra-perinuclear RyR1 labelling (μm^3 per μm^3)
	6.52	0.31	616.57	0.011
	4.45	0.74	225.44	0.020
	3.87	0.35	312.49	0.012
	22.52	0.51	751.28	0.030
	2.87	0.26	171.92	0.017
	14.03	1.11	494.84	0.028
	8.13	0.45	715.44	0.011
	12.64	2.72	1017.2	0.012
	13.19	0.27	215.95	0.061
	6.55	0.47	236.17	0.028
	7.99	0.61	181.18	0.044
Mean	9.34	0.71	448.95	0.025
S.E.M.	1.75	0.21	86.98	0.005

Table 3.9. Measurements of the mean volume of individual RyR1 labelling and the density of RyR1 labelling within the extra-perinuclear region of isolated pulmonary arterial smooth muscle cells

	Volume of sub-plasmalemmal RyR1 labelling (μm^3)	Mean volume of individual labelling within the sub-plasmalemmal region (μm^3)	Sub-plasmalemmal region volume (μm^3)	Density of sub-plasmalemmal RyR1 labelling (μm^3 per μm^3)
	20.7	0.63	901.99	0.023
	6.87	0.32	368.13	0.019
	18.52	0.37	668.57	0.028
	28.62	0.4	2218.41	0.013
	14.19	0.43	329.92	0.043
	16.33	0.48	768.65	0.021
	36.73	1.27	513.17	0.072
	16.57	0.33	637.28	0.026
	14.88	0.55	491.53	0.030
	11.81	0.59	369.82	0.032
	12.97	0.46	393.09	0.033
Mean	18.02	0.53	696.41	0.031
S.E.M.	2.50	0.08	161.94	0.005

Table 3.10. Measurements of the mean volume of individual RyR1 labelling and the density of RyR1 labelling within the sub-plasmalemmal region of isolated pulmonary arterial smooth muscle cells

	Volume of RyR2 labelling (μm^3)	Total cell volume (μm^3)	Density of RyR2 labelling (μm^3 per μm^3)
	64.61	1472.71	0.044
	53.54	1366.61	0.039
	45.39	741.59	0.061
	58.83	1429.76	0.041
	44.3	2551.58	0.017
	36.47	1959.04	0.019
	36.07	2076.69	0.017
	52.13	1688.99	0.031
	24.56	1030.88	0.024
	35.47	847.31	0.042
	31.48	1687.92	0.019
	24.82	850.3	0.029
	14.42	649.95	0.022
	44.45	830.59	0.054
Mean	40.47	1370.28	0.033
S.E.M.	3.78	154.10	0.004

Table 3.11. Measurements of the mean volume of individual RyR2 labelling and the density of RyR2 labelling within the whole cell volume of isolated pulmonary arterial smooth muscle cells

	Volume of perinuclear RyR2 labelling (μm^3)	Mean volume of individual labelling within the perinuclear region (μm^3)	Perinuclear region volume (μm^3)	Density of perinuclear RyR2 labelling (μm^3 per μm^3)
	15.01	1.23	438.72	0.034
	10.45	0.49	283.75	0.037
	21.61	2.30	178.63	0.121
	12.16	0.64	282.09	0.043
	5.33	0.40	1131.17	0.005
	13.14	0.63	840.18	0.016
	10.98	0.49	758.86	0.014
	24.05	1.33	719.56	0.033
	8.58	0.57	305.05	0.028
	11.54	1.15	179.9	0.064
	10.38	0.74	350.39	0.030
	4.44	0.74	204.88	0.022
	7.63	0.85	191.17	0.040
	10.71	1.96	197.49	0.054
Mean	11.86	0.97	432.99	0.039
S.E.M.	1.46	0.15	81.35	0.008

Table 3.12. Measurements of the mean volume of individual RyR2 labelling and the density of RyR2 labelling within the perinuclear region of isolated pulmonary arterial smooth muscle cells

	Volume of extra-perinuclear RyR2 labelling (μm^3)	Mean volume of individual labelling within the extra-perinuclear region (μm^3)	Extra-perinuclear region volume (μm^3)	Density of extra-perinuclear RyR2 labelling (μm^3 per μm^3)
	47.12	2.55	455.17	0.104
	32.48	1.91	401.6	0.081
	22.36	4.24	210.36	0.106
	35.27	1.21	458.06	0.077
	30.76	2.30	425.68	0.072
	5.42	0.45	318.82	0.017
	17.27	0.62	411.12	0.042
	9.25	0.36	354.95	0.026
	13.77	0.63	274.4	0.050
	17.61	2.52	168.57	0.104
	13.64	0.59	427.51	0.032
	18.33	1.41	289.56	0.063
	4.96	0.99	152.61	0.033
	23.56	2.62	217.92	0.108
Mean	20.84	1.60	326.17	0.065
S.E.M.	3.23	0.30	28.91	0.009

Table 3.13. Measurements of the mean volume of individual RyR2 labelling and the density of RyR2 labelling within the extra-perinuclear region of isolated pulmonary arterial smooth muscle cells

	Volume of sub-plasmalemmal RyR2 labelling (μm^3)	Mean volume of individual labelling within the sub-plasmalemmal region (μm^3)	Sub-plasmalemmal region volume (μm^3)	Density of sub-plasmalemmal RyR2 labelling (μm^3 per μm^3)
	2.23	0.36	633.47	0.004
	10.23	0.38	641.56	0.016
	0.79	0.27	285.09	0.003
	10.93	0.27	514.44	0.021
	7.94	0.47	958.68	0.008
	9.77	0.41	652.62	0.015
	4.00	0.48	801.96	0.005
	12.97	0.56	569.38	0.023
	2.21	0.37	373.02	0.006
	5.66	0.81	438.5	0.013
	7.21	0.38	798.98	0.009
	2.05	0.34	302.79	0.007
	1.65	0.32	227.2	0.007
	5.18	1.04	359.14	0.014
Mean	5.92	0.46	539.77	0.011
S.E.M.	1.06	0.06	59.03	0.002

Table 3.14. Measurements of the mean volume of individual RyR2 labelling and the density of RyR2 labelling within the sub-plasmalemmal region of isolated pulmonary arterial smooth muscle cells

	Volume of RyR3 labelling (μm^3)	Total cell volume (μm^3)	Density of RyR3 labelling (μm^3 per μm^3)
	66.94	2300.8	0.029
	37.66	1090.41	0.035
	29.8	846.87	0.035
	33.43	2073.08	0.016
	72.06	2215.08	0.033
	37.3	1934.38	0.019
	39.2	1557.8	0.025
	60.67	1542.94	0.039
	33.24	665.34	0.050
	29.61	922.2	0.032
	28.3	1018.23	0.028
Mean	42.56	1469.74	0.031
S.E.M.	4.82	178.93	0.003

Table 3.15. Measurements of the density of RyR3 labelling within the whole cell volume of isolated pulmonary arterial smooth muscle cells

	Volume of perinuclear RyR3 labelling (μm^3)	Mean volume of individual labelling within the perinuclear region (μm^3)	Perinuclear region volume (μm^3)	Density of perinuclear RyR3 labelling (μm^3 per μm^3)
	61.80	4.74	584.03	0.106
	23.10	1.54	309.18	0.075
	22.51	2.23	266.9	0.084
	24.67	1.37	649.4	0.038
	48.57	1.37	950.76	0.051
	38.36	3.00	948.97	0.040
	30.63	1.03	750.38	0.041
	48.37	3.35	498.46	0.097
	26.19	2.18	247.43	0.106
	20.97	2.62	278.46	0.075
	27.12	3.01	329.04	0.082
Mean	33.84	2.40	528.46	0.072
S.E.M.	4.09	0.33	80.95	0.008

Table 3.16. Measurements of the mean volume of individual RyR3 labelling and the density of RyR3 labelling within the perinuclear region of isolated pulmonary arterial smooth muscle cells

	Volume of extra-perinuclear RyR3 labelling (μm^3)	Mean volume of individual labelling within the extra-perinuclear region (μm^3)	Extra-perinuclear region volume (μm^3)	Density of extra-perinuclear RyR3 labelling (μm^3 per μm^3)
	1.87	0.38	555.19	0.003
	10.56	1.29	275.59	0.038
	6.27	0.35	178.52	0.035
	1.01	0.51	883.35	0.001
	18.09	1.99	590.71	0.031
	1.79	0.45	300.32	0.006
	4.31	0.75	313.7	0.014
	2.09	0.58	387.95	0.005
	2.59	0.52	89.77	0.029
	8.58	0.86	187.01	0.046
	0.73	0.24	239.9	0.003
Mean	5.26	0.72	363.82	0.019
S.E.M.	1.61	0.15	69.35	0.005

Table 3.17. Measurements of the mean volume of individual RyR3 labelling and the density of RyR3 labelling within the extra-perinuclear region of isolated pulmonary arterial smooth muscle cells

	Volume of sub-plasmalemmal RyR3 labelling (μm^3)	Mean volume of individual labelling within the sub-plasmalemmal region (μm^3)	Sub-plasmalemmal region volume (μm^3)	Density of sub-plasmalemmal RyR3 labelling (μm^3 per μm^3)
	2.62	0.19	1071.32	0.002
	3.6	0.54	444.15	0.008
	1.02	0.34	376.58	0.003
	5.53	0.38	540.33	0.010
	1.35	0.39	626.81	0.002
	0.78	0.32	642.8	0.001
	2.92	0.22	443.05	0.007
	7.27	1.21	554.32	0.013
	1.09	1.09	272.12	0.004
	0.62	0.31	395.83	0.002
	0.45	0.23	381.91	0.001
Mean	2.48	0.47	522.66	0.005
S.E.M.	0.67	0.11	64.68	0.001

Table 3.18. Measurements of the mean volume of individual RyR3 labelling and the density of RyR3 labelling within the sub-plasmalemmal region of isolated pulmonary arterial smooth muscle cells

	Volume of co-localisation (RyR1/lysosomal labelling) (μm^3)	Total cell volume (μm^3)	Density of co-localisation (RyR1/lysosomal labelling) (μm^3 per μm^3)	Pearson correlation coefficient
	1.61	2089.31	0.0008	0.12
	1.02	927.2	0.0011	0.14
	0.13	1507.29	0.0001	0.05
	4.61	4206.95	0.0011	0.16
	3.69	729.16	0.0051	0.13
	5.85	1879.62	0.0031	0.18
	9.51	1701.72	0.0056	0.25
	7.3	2208.73	0.0033	0.20
	5.17	1075.34	0.0048	0.20
	4.84	868.45	0.0056	0.18
Mean	4.37	1719.38	0.0031	0.16
S.E.M.	0.92	322.87	0.0007	0.02

Table 3.19. Measurements of the density of co-localisation and correlation between RyR1 and αIgp120 labelling within the whole cell volume of isolated pulmonary arterial smooth muscle cells

	Volume of perinuclear co-localisation (RyR1/lysosomal labelling) (μm^3)	Mean volume of individual co-localisation within the perinuclear region (μm^3)	Perinuclear region volume (μm^3)	Density of perinuclear co-localisation (RyR1/lysosomal labelling) (μm^3 per μm^3)
	0.57	0.19	570.75	0.0010
	0.87	0.29	253.72	0.0034
	0.13	0.13	453.68	0.0003
	2.41	0.21	1237.26	0.0019
	2.65	0.44	192.94	0.0137
	1.42	0.39	616.13	0.0023
	2.37	0.26	460.13	0.0052
	4.89	0.40	554.25	0.0088
	2.99	0.30	321.68	0.0093
	2.26	0.38	211.19	0.0107
Mean	2.06	0.30	487.17	0.0057
S.E.M.	0.44	0.03	96.45	0.0015

Table 3.20. Measurements of the mean volume of individual areas of co-localisation and the density of co-localisation between RyR1 and αIgp120 labelling within the perinuclear region of isolated pulmonary arterial smooth muscle cells

	Volume of extra-perinuclear co-localisation (RyR1/lysosomal labelling) (μm^3)	Mean volume of individual co-localisation within the extra-perinuclear region (μm^3)	Extra-perinuclear region volume (μm^3)	Density of extra-perinuclear co-localisation (RyR1/lysosomal labelling) (μm^3 per μm^3)
	0.15	0.14	616.57	0.0002
	0	0.00	225.44	0.0000
	0	0.00	316.91	0.0000
	1.60	0.40	751.28	0.0021
	0.57	0.29	171.92	0.0033
	2.94	0.25	494.84	0.0059
	1.19	0.78	715.44	0.0017
	0.75	0.32	1017.2	0.0007
	0.90	0.23	215.95	0.0042
	2.17	0.31	236.17	0.0092
Mean	1.03	0.27	476.17	0.0027
S.E.M.	0.31	0.07	91.40	0.0009

Table 3.21. Measurements of the mean volume of individual areas of co-localisation and the density of co-localisation between RyR1 and αIgp120 labelling within the extra-perinuclear region of isolated pulmonary arterial smooth muscle cells

	Volume of sub-plasmalemmal co-localisation (RyR1/lysosomal labelling) (μm^3)	Mean volume of individual co-localisation within the sub-plasmalemmal region (μm^3)	Sub-plasmalemmal region volume (μm^3)	Density of sub-plasmalemmal co-localisation (RyR1/lysosomal labelling) (μm^3 per μm^3)
	0.42	0.15	901.99	0.0005
	0	0.00	368.13	0.0000
	0	0.00	662.69	0.0000
	0.86	0.30	2218.41	0.0004
	0.47	0.24	329.92	0.0014
	0.56	0.19	768.65	0.0007
	0.98	0.33	513.17	0.0019
	1.34	0.20	637.28	0.0021
	1.28	0.21	491.53	0.0026
	0.41	0.41	369.82	0.0011
Mean	0.63	0.20	726.16	0.0011
S.E.M.	0.15	0.04	175.88	0.0003

Table 3.22. Measurements of the mean volume of individual areas of co-localisation and the density of co-localisation between RyR1 and αIgp labelling within the sub-plasmalemmal region of isolated pulmonary arterial smooth muscle cells

	Volume of co-localisation (RyR2/lysosomal labelling) (μm^3)	Total cell volume (μm^3)	Density of co-localisation (RyR2/lysosomal labelling) (μm^3 per μm^3)	Pearson correlation coefficient
	7.03	1472.71	0.0048	0.18
	6.81	1366.61	0.0050	0.24
	8.52	741.59	0.0115	0.25
	2.41	1429.76	0.0017	0.14
	4.13	2551.58	0.0016	0.17
	3.72	1959.04	0.0019	0.18
	2.24	2076.69	0.0011	0.09
	4.65	1688.99	0.0028	0.18
	4.14	1030.88	0.0040	0.15
	2.01	847.31	0.0024	0.19
	3.98	1687.92	0.0024	0.19
	1.53	850.3	0.0018	0.19
	1.58	649.95	0.0024	0.19
	3.09	830.59	0.0037	0.20
Mean	3.99	1370.28	0.0034	0.18
S.E.M.	0.58	154.10	0.0007	0.01

Table 3.23. Measurements of the density of co-localisation and correlation between RyR2 and αIgp120 labelling within the whole cell volume of isolated pulmonary arterial smooth muscle cells

	Volume of perinuclear co-localisation (RyR2/lysosomal labelling) (μm^3)	Mean volume of individual co-localisation within the perinuclear region (μm^3)	Perinuclear region volume (μm^3)	Density of perinuclear co-localisation (RyR2/lysosomal labelling) (μm^3 per μm^3)
	2.42	0.35	438.72	0.0055
	1.67	0.34	283.75	0.0059
	2.82	0.71	178.63	0.0158
	0.88	0.18	282.09	0.0031
	0.3	0.15	1131.17	0.0003
	3.4	0.38	840.18	0.0040
	1.9	0.35	758.86	0.0025
	3.92	0.69	719.56	0.0054
	2.74	0.39	305.05	0.0090
	1.52	0.27	179.9	0.0085
	1.92	0.38	350.39	0.0055
	1.53	0.31	204.88	0.0075
	1.14	0.38	191.17	0.0060
	2.22	0.44	197.49	0.0112
Mean	2.03	0.38	432.99	0.0064
S.E.M.	0.26	0.04	81.35	0.0010

Table 3.24. Measurements of the mean volume of individual areas of co-localisation and the density of co-localisation between RyR2 and αIgp120 labelling within the perinuclear region of isolated pulmonary arterial smooth muscle cells

	Volume of extra-perinuclear co-localisation (RyR2/lysosomal labelling) (μm^3)	Mean volume of individual co-localisation within the extra-perinuclear region (μm^3)	Extra-perinuclear region volume (μm^3)	Density of extra-perinuclear co-localisation (RyR2/lysosomal labelling) (μm^3 per μm^3)
	4.47	0.41	455.17	0.0098
	4.73	0.53	401.6	0.0118
	5.41	1.80	210.36	0.0257
	0.85	0.31	458.06	0.0019
	2.32	0.25	425.68	0.0055
	0.32	0.32	318.82	0.0010
	0.34	0.14	411.12	0.0008
	0.2	0.00	354.95	0.0006
	1.4	0.28	274.4	0.0051
	0.49	0.16	168.57	0.0029
	1.23	0.34	427.51	0.0029
	0	0.00	289.56	0.0000
	0.44	0.22	152.61	0.0029
	0.87	0.17	217.92	0.0040
Mean	1.65	0.35	326.17	0.0053
S.E.M.	0.50	0.12	28.91	0.0018

Table 3.25. Measurements of the mean volume of individual areas of co-localisation and the density of co-localisation between RyR2 and αIgp120 labelling within the extra-perinuclear region of isolated pulmonary arterial smooth muscle cells

	Volume of sub-plasmalemmal co-localisation (RyR2/lysosomal labelling) (μm^3)	Mean volume of individual co-localisation within the sub-plasmalemmal region (μm^3)	Sub-plasmalemmal region volume (μm^3)	Density of sub-plasmalemmal co-localisation (RyR2/lysosomal labelling) (μm^3 per μm^3)
	0.14	0.14	633.47	0.0002
	0.41	0.20	641.56	0.0006
	0.29	0.29	285.09	0.0010
	0.68	0.15	514.44	0.0013
	1.51	0.43	958.68	0.0016
	0	0.00	652.62	0.0000
	0	0.00	801.96	0.0000
	0.3	0.25	569.38	0.0005
	0	0.00	373.02	0.0000
	0	0.00	438.5	0.0000
	0.8	0.27	798.98	0.0010
	0	0.00	302.79	0.0000
	0	0.00	227.2	0.0000
	0.00	0.00	359.14	0.0000
Mean	0.30	0.12	539.77	0.0005
S.E.M.	0.12	0.04	59.03	0.0002

Table 3.26. Measurements of the mean volume of individual areas of co-localisation and the density of co-localisation between RyR2 and αIgp120 labelling within the sub-plasmalemmal region of isolated pulmonary arterial smooth muscle cells

	Volume of co-localisation (RyR3/lysosomal labelling) (μm^3)	Total cell volume (μm^3)	Density of co-localisation (RyR3/lysosomal labelling) (μm^3 per μm^3)	Pearson correlation coefficient
	8.31	2300.8	0.0036	**0.21**
	9.4	1090.41	0.0086	**0.27**
	3.76	846.87	0.0044	**0.26**
	3.53	2073.08	0.0017	**0.27**
	15.21	2215.08	0.0069	**0.26**
	12.13	1934.38	0.0063	**0.35**
	8.19	1557.8	0.0053	**0.33**
	5.16	1542.94	0.0033	**0.22**
	5.08	665.34	0.0076	**0.21**
	5.02	922.2	0.0054	**0.22**
	7.9	1018.23	0.0078	**0.27**
Mean	7.61	1469.74	0.0055	**0.26**
S.E.M.	1.10	178.93	0.0006	**0.01**

Table 3.27. Measurements of the density of co-localisation and correlation between RyR3 and αIgp120 labelling within the whole cell volume of isolated pulmonary arterial smooth muscle cells

	Volume of perinuclear co-localisation (RyR3/lysosomal labelling) (μm^3)	Mean volume of individual co-localisation within the perinuclear region (μm^3)	Perinuclear region volume (μm^3)	Density of perinuclear co-localisation (RyR3/lysosomal labelling) (μm^3 per μm^3)
	8.31	0.63	584.03	0.0140
	5.89	1.63	309.18	0.0190
	3.00	0.43	266.9	0.0110
	3.53	0.44	649.4	0.005
	11.44	0.61	950.76	0.0100
	11.34	0.63	948.97	0.0120
	8.03	0.46	750.38	0.0110
	3.28	0.62	498.46	0.0070
	3.33	0.83	247.43	0.0070
	3.94	0.66	278.46	0.0141
	7.75	1.94	329.04	0.0236
Mean	6.35	0.81	528.46	0.0122
S.E.M.	0.97	0.15	80.95	0.0016

Table 3.28. Measurements of the mean volume of individual areas of co-localisation and the density of co-localisation between RyR3 and αIgp120 labelling within the perinuclear region of isolated pulmonary arterial smooth muscle cells

	Volume of extra-perinuclear co-localisation (RyR3/lysosomal labelling) (μm^3)	Mean volume of individual co-localisation within the extra-perinuclear region (μm^3)	Extra-perinuclear region volume (μm^3)	Density of extra-perinuclear co-localisation (RyR3/lysosomal labelling) (μm^3 per μm^3)
	0	0.68	555.19	0.0000
	3.51	0.75	275.59	0.0130
	0.13	0.35	178.52	0.0007
	0	0.00	883.35	0.0000
	3.61	0.68	590.71	0.0060
	0.24	0.24	300.32	0.0008
	0.16	0.21	313.7	0.0005
	1.88	0.30	387.95	0.0050
	1.32	0.33	89.77	0.0050
	1.08	0.27	187.01	0.0058
	0	0.00	239.9	0.0000
Mean	1.08	0.35	363.82	0.0033
S.E.M.	0.42	0.08	69.35	0.0012

Table 3.29. Measurements of the mean volume of individual areas of co-localisation and the density of co-localisation between RyR3 and αIgp120 labelling within the extra-perinuclear region of isolated pulmonary arterial smooth muscle cells

	Volume of sub-plasmalemmal co-localisation (RyR3/lysosomal labelling) (μm^3)	Mean volume of individual co-localisation within the sub-plasmalemmal region (μm^3)	Sub-plasmalemmal region volume (μm^3)	Density of sub-plasmalemmal co-localisation (RyR3/lysosomal labelling) (μm^3 per μm^3)
	0	0.00	1071.32	0.0000
	0	0.00	444.15	0.0000
	0.63	0.11	376.58	0.0017
	0	0.00	540.33	0.0000
	0.16	0.16	626.81	0.0002
	0	0.00	642.8	0.0000
	0	0.00	443.05	0.0000
	0	0.00	554.32	0.0000
	2	0.00	272.12	0.0000
	0	0.00	395.83	0.0000
	0.15	0.15	381.91	0.0004
Mean	0.27	0.04	522.66	0.0002
S.E.M.	0.18	0.02	64.68	0.00015

Table 3.30. Measurements of the mean volume of individual areas of co-localisation and the density of co-localisation between RyR3 and αIgp120 labelling within the sub-plasmalemmal region of isolated pulmonary arterial smooth muscle cells

	% of total lysosomal labelling co-localised with RyR1 labelling	% of total lysosomal labelling co-localised with RyR2 labelling	% of total lysosomal labelling co-localised with RyR3 labelling
	6.2	16.5	26.3
	9.6	20.1	31.6
	1.5	34.3	16.6
	13.3	8.1	15.7
	15.6	12.5	39.9
	16.9	15.2	34.0
	33.3	7.7	15.9
	23.2	21.9	11.0
	16.7	23.4	34.9
	13.9	9.7	20.5
		11.0	34.9
		7.4	
		10.9	
		18.9	
Mean	15.0	15.5	25.6
S.E.M.	2.8	2.0	3.0

Table 3.31. Percentage of the total volume of αIgp120 labelling co-localised with each RyR subtype across the entire cell volume of the pulmonary arterial smooth muscle cells studied

	% of total lysosomal labelling co-localised with RyR1 labelling			% of total lysosomal labelling co-localised with RyR2 labelling			% of total lysosomal labelling co-localised with RyR3 labelling		
	Peri nuclear region	**Exxtra-peri nuclear region**	**Sub-plasma lemmal region**	**Peri nuclear region**	**Extra-peri nuclear region**	**Sub-plasma lemmal region**	**Peri nuclear region**	**Extra-peri nuclear region**	**Sub-plasma lemmal region**
	3.7	2.4	7.9	15.7	72.0	2.6	54.0	0.0	0.0
	5.6	0.0	0.0	10.8	76.2	7.7	38.2	56.5	0.0
	0.8	0.0	0.0	18.3	87.1	5.4	19.5	2.1	11.8
	15.6	25.8	16.1	5.7	13.7	12.8	22.9	0.0	0.0
	17.2	9.2	8.8	1.9	37.4	28.3	74.3	58.1	3.0
	9.2	47.3	10.5	22.1	5.2	0.0	73.6	3.9	0.0
	15.4	19.2	18.4	12.3	5.5	0.0	52.1	2.6	0.0
	31.8	12.1	25.1	25.5	3.2	5.6	21.3	30.3	0.0
	19.4	14.5	24.0	17.8	22.5	0.0	21.6	12.4	0.0
	14.7	34.9	7.7	9.9	7.9	0.0	25.6	17.4	0.0
				12.5	19.8	15.0	50.3	0.0	2.8
				9.9	0.0	0.0			
				7.4	7.1	0.0			
				14.4	14.0	0.0			
Mean	13.4	16.5	11.9	13.2	26.5	5.5	41.2	16.7	1.6
S.E.M	2.8	4.9	2.8	1.7	8.0	2.2	6.3	6.7	1.1

Table 3.32. Percentage of the total volume of αIgp120 labelling co-localised with each RyR subtype within the subdivided regions of the pulmonary arterial smooth muscle cells studied

	Cells co-labelled for RyR1 and αIgp120		Cells co-labelled for RyR2 and αIgp120		Cells co-labelled for RyR3 and αIgp120	
	Density of RyR1 labelling across the whole cell	Density of αIgp120 labelling across the whole cell	Density of RyR2 labelling across the whole cell	Density of αIgp120 labelling across the whole cell	Density of RyR3 labelling across the whole cell	Density of αIgp120 labelling across the whole cell
	0.0229	0.0125	0.0439	0.0289	0.0291	0.0140
	0.0227	0.0114	0.0392	0.0248	0.0345	0.0270
	0.0198	0.0058	0.0612	0.0335	0.0352	0.0270
	0.0184	0.0083	0.0411	0.0208	0.0161	0.0110
	0.0472	0.0324	0.0174	0.0130	0.0325	0.0170
	0.0343	0.0185	0.0186	0.0125	0.0193	0.0180
	0.0377	0.0168	0.0174	0.0140	0.0252	0.0330
	0.0317	0.0143	0.0309	0.0126	0.0393	0.0300
	0.0519	0.0289	0.0238	0.0172	0.0500	0.0219
	0.0317	0.0400	0.0420	0.0243	0.0321	0.0266
			0.0187	0.0215	0.0278	0.0222
			0.0292	0.0243	0.0310	
			0.0222	0.0223	0.0028	
			0.0535	0.0197		
Mean	0.0318	0.0189	0.0328	0.0207	0.0310	0.0225
S.E.M.	0.0036	0.0035	0.0038	0.0017	0.0028	0.0021

Table 3.33. Measurements of the density of labelling for αIgp120 and each RyR subtype within the whole cell volume of isolated pulmonary arterial smooth muscle cells

	Resting F_{340}/F_{380}	Peak F_{340}/F_{380}	Increase in F_{340}/F_{380}	% increase in F_{340}/F_{380}
	0.38	1.18	0.80	212.7
	0.36	1.58	1.22	340.0
	0.59	1.07	0.48	80.5
	0.56	1.03	0.47	83.3
	0.66	2.26	1.60	243.8
Mean	0.51	1.42	0.91	192.0
S.E.M.	0.05	0.21	0.20	45.3

Table 3.34. Record of the Fura-2 fluorescence ratio measurements taken for each experiment during the intracellular dialysis of 10 nM NAADP in pulmonary arterial smooth muscle cells
The resting F_{340}/F_{380} ratio was determined by the calculating the average F_{340}/F_{380} ratio taken at 4 time-points immediately prior to the initiation of the Ca^{2+} transient. The peak F_{340}/F_{380} ratio is the maximum F_{340}/F_{380} ratio obtained during the record. The increase in F_{340}/F_{380} ratio was determined by subtracting the peak F_{340}/F_{380} ratio from the resting F_{340}/F_{380} ratio. The percentage increase in F_{340}/F_{380} ratio was determined by dividing the increase in F_{340}/F_{380} ratio by the resting F_{340}/F_{380} ratio, and expressing this ratio as a percentage.

	Resting F_{340}/F_{380}	Peak F_{340}/F_{380}	Increase in F_{340}/F_{380}	% increase in F_{340}/F_{380}
	0.67	0.98	0.31	46.3
	0.60	0.81	0.21	34.9
	0.58	1.00	0.42	71.9
	0.47	0.70	0.23	48.9
	0.49	0.79	0.31	62.8
	0.47	0.69	0.22	46.1
Mean	0.55	0.83	0.28	51.8
S.E.M.	0.03	0.05	0.03	5.4

Table 3.35. Record of the Fura-2 fluorescence ratio measurements taken for each experiment during the intracellular dialysis of 10 nM NAADP in pulmonary arterial smooth muscle cells pre-incubated (20 mins) with 30 μM dantrolene

The resting F_{340}/F_{380} ratio was determined by the calculating the average F_{340}/F_{380} ratio taken at 4 time-points immediately prior to the initiation of the Ca^{2+} transient. The peak F_{340}/F_{380} ratio is the maximum F_{340}/F_{380} ratio obtained during the record. The increase in F_{340}/F_{380} ratio was determined by subtracting the peak F_{340}/F_{380} ratio from the resting F_{340}/F_{380} ratio. The percentage increase in F_{340}/F_{380} ratio was determined by dividing the increase in F_{340}/F_{380} ratio by the resting F_{340}/F_{380} ratio, and expressing this ratio as a percentage.

	Resting F_{340}/F_{380}	Peak F_{340}/F_{380}	Increase in F_{340}/F_{380}	% increase in F_{340}/F_{380}
	0.31	0.69	0.38	122.6
	0.51	0.94	0.43	84.3
	0.51	1.10	0.59	114.4
	0.38	0.58	0.20	52.6
	0.42	0.63	0.21	50.0
	0.43	0.63	0.20	46.5
	0.46	0.79	0.33	71.7
	0.40	0.62	0.22	55.0
	0.46	0.79	0.33	71.7
	0.42	0.66	0.24	57.1
	0.46	0.73	0.27	58.7
Mean	0.43	0.74	0.31	71.3
S.E.M.	0.02	0.05	0.04	7.8

Table 3.36. Record of the Fura-2 fluorescence ratio measurements taken for each experiment during the extracellular application of 1 μM ionomycin in pulmonary arterial smooth muscle cells

The resting F_{340}/F_{380} ratio was determined by the calculating the average F_{340}/F_{380} ratio taken at 4 time-points immediately prior to the initiation of the Ca^{2+} transient. The peak F_{340}/F_{380} ratio is the maximum F_{340}/F_{380} ratio obtained during the record. The increase in F_{340}/F_{380} ratio was determined by subtracting the peak F_{340}/F_{380} ratio from the resting F_{340}/F_{380} ratio. The percentage increase in F_{340}/F_{380} ratio was determined by dividing the increase in F_{340}/F_{380} ratio by the resting F_{340}/F_{380} ratio, and expressing this ratio as a percentage.

	Resting F_{340}/F_{380}	Peak F_{340}/F_{380}	Increase in F_{340}/F_{380}	% increase in F_{340}/F_{380}
	0.39	0.66	0.27	69.2
	0.35	0.72	0.37	105.7
	0.42	0.69	0.27	64.3
	0.39	0.67	0.28	71.8
	0.43	0.63	0.20	46.5
	0.39	0.65	0.26	66.7
	0.44	0.65	0.21	47.7
	0.43	0.86	0.43	100.0
	0.43	1.17	0.74	172.1
	0.49	0.84	0.35	71.4
	0.43	1.10	0.67	155.8
	0.48	0.71	0.23	47.9
Mean	0.42	0.78	0.36	84.9
S.E.M.	0.01	0.05	0.05	12.0

Table 3.37. Record of the Fura-2 fluorescence ratio measurements taken for each experiment during the extracellular application of 1 μM ionomycin in pulmonary arterial smooth muscle cells pre-incubated (20 mins) with 30 μM dantrolene

The resting F_{340}/F_{380} ratio was determined by the calculating the average F_{340}/F_{380} ratio taken at 4 time-points immediately prior to the initiation of the Ca^{2+} transient. The peak F_{340}/F_{380} ratio is the maximum F_{340}/F_{380} ratio obtained during the record. The increase in F_{340}/F_{380} ratio was determined by subtracting the peak F_{340}/F_{380} ratio from the resting F_{340}/F_{380} ratio. The percentage increase in F_{340}/F_{380} ratio was determined by dividing the increase in F_{340}/F_{380} ratio by the resting F_{340}/F_{380} ratio, and expressing this ratio as a percentage.

Appendix 2:

Results tables for Chapter 4:

	Volume of mCherry-hTPC2 labelling (μm^3)	Volume of LysoTracker Green labelling (μm^3)	Total cell volume (μm^3)	Density of mCherry-hTPC2 labelling (μm^3 per μm^3)	Density of LysoTracker Green labelling (μm^3 per μm^3)
	37.4	36.2	1909.6	0.0196	0.0190
	19.0	17.5	1610.2	0.0118	0.0109
	12.6	20.6	1895.2	0.0067	0.0109
	30.6	36.1	2580.2	0.0119	0.0140
	26.2	21.2	2850.1	0.0092	0.0074
	22.3	40.2	2738.1	0.0081	0.0147
Mean	24.7	28.6	2263.9	0.0112	0.0128
S.E.M.	3.6	4.0	212.7	0.0019	0.0016

Table 4.1. Measurements of mCherry-hTPC2 labelling and LysoTracker Green labelling in mCherry-hTPC2 cells

	Volume of colocalisation (μm^3)	Total cell volume (μm^3)	Density of colocalisation (μm^3 per μm^3)	Pearson correlation coefficient
	16.8	1909.6	0.0088	0.54
	4.0	1610.2	0.0025	0.28
	1.9	1895.2	0.0010	0.15
	11.6	2580.2	0.0045	0.39
	4.8	2850.1	0.0017	0.24
	4.3	2738.1	0.0016	0.20
Mean	7.2	2263.9	0.0033	0.30
S.E.M.	2.3	212.7	0.0012	0.06

Table 4.2. Measurements of the density of co-localisation and correlation between mCherry-hTPC2 and LysoTracker Green labelling in mCherry-hTPC2 cells

	Volume of LAMP2 labelling (μm^3)	Volume of HA-hTPC2 labelling (μm^3)	Total cell volume (μm^3)	Density of LAMP2 labelling (μm^3 per μm^3)	Density of HA-hTPC2 labelling (μm^3 per μm^3)
	70.3	103.3	7033.6	0.0100	0.0147
	38.8	33.4	3072.1	0.0126	0.0109
	32.8	54.7	2816.7	0.0116	0.0194
	31.8	29.5	3096.6	0.0103	0.0095
	22.8	31.9	2510.2	0.0091	0.0127
	22.5	29.7	3561.9	0.0063	0.0083
	55.6	65.0	3386.2	0.0164	0.0192
Mean	39.2	49.6	3639.6	0.0109	0.0135
S.E.M.	6.7	10.4	580.6	0.0012	0.0017

Table 4.3. Measurements of LAMP2 labelling and HA-hTPC2 labelling in fixed HA-hTPC2 cells

	Volume of colocalisation (μm^3)	Total cell volume (μm^3)	Density of colocalisation (μm^3 per μm^3)	Pearson correlation coefficient
	49.5	7033.6	0.0070	0.66
	19.1	3072.1	0.0062	0.62
	24.7	2816.7	0.0088	0.67
	16.9	3096.6	0.0055	0.61
	16.1	2510.2	0.0064	0.67
	12.7	3561.9	0.0036	0.60
	35.0	3386.2	0.0103	0.66
Mean	24.8	3639.6	0.0068	0.64
S.E.M.	5.0	580.6	0.0008	0.01

Table 4.4. Measurements of the density of co-localisation and correlation between LAMP2 and HA-hTPC2 labelling in fixed HA-hTPC2 cells

	HA-hTPC2 and LAMP2 labelling	GFP-hTPC1 and LAMP2 labelling	GFP-cTPC3 and LAMP2 labelling	GFP-hTPC1 and transferrin labelling	GFP-cTPC3 and M6PR labelling
	0.904	0.441	0.499	0.508	0.508
	0.899	0.507	0.630	0.549	0.461
	0.910	0.403	0.527	0.586	
	0.902	0.708	0.616	0.571	
	0.914	0.715	0.478	0.525	
		0.705	0.477	0.587	
		0.602		0.656	
		0.633		0.735	
		0.595			
Mean	0.906	0.590	0.538	0.590	0.485
S.E.M.	0.003	0.039	0.028	0.026	0.024

Table 4.5. Measurements of the Pearson product-moment correlation coefficient between each TPC subtype and organelle markers in fixed HEK293 cells
Note, for $n = 2$ the data are S.E.M. is expressed as a range.

	Specific binding in wild-type HEK293 cells (% of wild-type)	Specific binding in HA-hTPC2 cells (% of wild-type)
	144.3	293.0
	105.0	382.6
	50.7	338.3
Mean	100.0	338.0
S.E.M.	27.1	25.9

Table 4.6 Overall increase in specific binding between wild-type HEK293 cells and HEK293 cells stably over-expressing HA-hTPC2

Log ligand conc. (M)	Specific binding NAADP (% max)					
	1	2	3	4	Mean	SEM
-9.0	122.0	102.3	93.1	82.7	100.0	8.3
-8.5	90.5	110.3	103.0	86.5	97.6	5.5
-8.0	63.2	117.2	83.2	70.8	83.6	12.0
-7.5	95.1	82.4	62.8	63.7	76.0	7.8
-7.0	53.9	73.9	65.1	69.4	65.6	4.3
-6.5	57.5	70.6	80.5	50.0	64.6	6.8
-6.0	37.4	68.0	57.1	50.6	53.3	6.4
-5.5	16.6	50.0	61.0	48.6	44.0	9.6
-5.0	16.5	42.6	42.1	35.0	34.0	6.1
-4.5	-1.2	12.5	21.4	8.7	10.3	4.7
-4.0	-5.0	6.0	18.5	-8.0	2.9	6.0
-3.5	-9.4	7.2	23.3	-21.1	0.0	9.7
-3.0	-14.9	20.1	12.4	33.4	12.7	10.2

Table 4.7. Competitive inhibition of [^{32}P]NAADP binding by NAADP in HA-hTPC2 cell homogenates

Log ligand conc. (M)	Specific binding NADP (% max)					
	1	2	3	4	Mean	SEM
-9.0	90.3	51.2	140.1	87.7	92.3	18.2
-8.5	100.8	59.5	116.4	90.5	91.8	12.0
-8.0	111.8	62.1	123.4	95.1	98.1	13.3
-7.0	89.0	51.0	152.0	104.2	99.0	20.9
-6.5	81.0	70.3	125.6	123.2	100.0	14.2
-6.0	79.3	49.3	139.7	83.9	88.0	18.8
-5.0	48.2	-2.2	72.4	63.1	45.4	16.6
-4.5	27.1	-4.2	116.5	58.8	49.6	25.8
-4.0	34.6	-20.9	81.3	61.3	39.1	22.2
-3.0	-8.4	-31.9	11.0	29.2	0.0	13.1

Table 4.8. Competitive inhibition of [^{32}P]NAADP binding by NADP in HA-hTPC2 cell homogenates

Log ligand conc. (M)	Specific binding NAADP (% max)					Specific binding NADP (% max)				
	1	2	3	Mean	SEM	1	2	3	Mean	SEM
-12	97.1	100.4	95.3	97.6	1.5	96.4	96.6	91.8	94.9	1.6
-11	97.2	102.8	100.0	100.0	1.6	92.6	98.7	90.8	94.0	2.4
-10	96.2	99.6	94.8	96.9	1.4	96.6	97.4	95.0	96.3	0.7
-9	74.2	68.6	75.7	72.8	2.1	94.5	97.5	100.5	97.5	1.7
-8	58.5	66.0	54.7	59.7	3.3	100.5	99.9	99.6	100.0	0.3
-7	46.5	45.5	21.4	37.8	8.2	89.7	93.2	88.3	90.4	1.4
-6	25.3	36.5	41.1	34.3	4.7	58.7	53.4	56.6	56.2	1.5
-5	8.7	17.6	8.8	11.7	3.0	23.8	21.1	18.4	21.1	1.5
-4	14.5	5.8	-2.7	5.9	5.0	4.1	9.4	7.2	6.9	1.5
-3	11.7	0.0	-11.6	0.0	6.7	2.2	1.0	-3.2	0.0	1.6

Table 4.9. Competitive inhibition of [^{32}P]NAADP binding by NAADP and NADP in mouse liver homogenates

	Resting F_{340}/F_{380}	Peak F_{340}/F_{380}	Increase in F_{340}/F_{380}	% increase in F_{340}/F_{380}
	0.80	1.14	0.34	43.0
	1.02	1.95	0.94	92.0
	0.87	1.96	1.09	125.1
	0.80	3.16	2.37	297.2
	0.86	2.95	2.09	244.1
	1.24	2.28	1.03	83.2
	1.08	3.08	2.00	185.3
	1.12	3.50	2.38	212.1
	0.79	2.37	1.59	201.7
	0.89	2.82	1.93	216.1
	0.63	2.75	2.12	334.0
	0.76	3.39	2.63	346.5
	0.72	1.59	0.87	121.0
	0.76	1.89	1.13	149.5
	0.59	2.13	1.54	263.2
	0.59	2.23	1.63	274.7
	0.68	1.52	0.84	123.0
	0.70	4.72	4.02	576.9
	0.48	1.54	1.06	220.9
	0.94	1.95	1.01	108.1
	0.83	2.43	1.60	192.9
	0.52	1.49	0.98	189.5
	0.70	1.30	0.59	84.7
	0.93	1.73	0.80	85.9
	0.79	0.99	0.20	24.7
	0.49	0.55	0.05	11.1
	0.93	1.02	0.09	9.1
	0.64	0.90	0.26	40.5
	0.62	0.79	0.18	28.8
	1.01	1.08	0.06	6.2
	0.82	1.05	0.24	29.0
	0.68	0.73	0.05	8.1
	0.61	0.78	0.18	29.4
	0.77	0.93	0.16	21.1
	0.57	0.72	0.15	25.8
	0.63	0.88	0.24	38.3
	0.63	0.77	0.13	21.0
	0.69	0.83	0.14	20.6
	0.47	0.52	0.05	10.7
	0.64	0.79	0.15	23.9
	0.72	1.60	0.88	121.2
	0.47	0.56	0.08	17.3
	0.51	0.73	0.22	42.1
	1.17	1.42	0.25	21.0
Mean	0.75	1.67	0.92	120.93
S.E.M.	0.03	0.15	0.14	18.39

Table 4.10. Record of the Fura-2 fluorescence ratio measurements taken for each experiment during the intracellular dialysis of 10 nM NAADP in HA-hTPC2 cells
The resting F_{340}/F_{380} ratio was determined by the calculating the average F_{340}/F_{380} ratio taken at 4 time-points immediately prior to the initiation of the Ca^{2+} transient. When no transient was observed, the

resting F_{340}/F_{380} ratio was determined by calculating the average F_{340}/F_{380} ratio taken at 4 time-points either side of achieving the whole-cell configuration. The peak F_{340}/F_{380} ratio is the maximum F_{340}/F_{380} ratio obtained during the record. The increase in F_{340}/F_{380} ratio was determined by subtracting the peak F_{340}/F_{380} ratio from the resting F_{340}/F_{380} ratio. The percentage increase in F_{340}/F_{380} ratio was determined by dividing the increase in F_{340}/F_{380} ratio by the resting F_{340}/F_{380} ratio, and expressing this ratio as a percentage.

	Resting F_{340}/F_{380}	**Peak F_{340}/F_{380}**	**Increase in F_{340}/F_{380}**	**% increase in F_{340}/F_{380}**
	0.90	1.09	0.20	22.1
	0.81	0.86	0.05	6.3
	0.66	0.67	0.01	1.8
	0.77	1.01	0.23	30.3
	0.63	0.84	0.21	34.1
	0.60	0.70	0.11	17.6
	0.53	0.65	0.12	23.4
	0.55	0.56	0.00	0.7
	0.77	0.97	0.20	26.6
	0.66	0.74	0.08	12.4
	0.57	0.58	0.01	1.2
	0.64	0.77	0.13	19.9
	0.46	0.53	0.07	16.1
	0.51	0.65	0.14	28.3
Mean	0.65	0.76	0.11	17.20
S.E.M.	0.03	0.05	0.02	3.01

Table 4.11. Record of the Fura-2 fluorescence ratio measurements taken for each experiment during the intracellular dialysis of NAADP-free pipette solution in HA-hTPC2 cells
The resting F_{340}/F_{380} ratio was determined by calculating the average F_{340}/F_{380} ratio taken at 4 time-points either side of achieving the whole-cell configuration. The peak F_{340}/F_{380} ratio is the maximum F_{340}/F_{380} ratio obtained during the record. The increase in F_{340}/F_{380} ratio was determined by subtracting the peak F_{340}/F_{380} ratio from the resting F_{340}/F_{380} ratio. The percentage increase in F_{340}/F_{380} ratio was determined by dividing the increase in F_{340}/F_{380} ratio by the resting F_{340}/F_{380} ratio, and expressing this ratio as a percentage.

	Resting F_{340}/F_{380}	Peak F_{340}/F_{380}	Increase in F_{340}/F_{380}	% increase in F_{340}/F_{380}
	0.67	0.55	-0.12	-18.5
	0.58	0.65	0.07	12.8
	0.72	0.77	0.05	6.3
	0.73	0.96	0.23	31.5
	0.69	0.87	0.18	26.4
	0.70	0.71	0.02	2.7
	0.52	0.63	0.11	22.2
	0.59	0.63	0.04	6.8
	0.50	0.58	0.08	15.5
	0.54	0.57	0.03	4.6
	0.59	0.89	0.30	51.4
	0.67	0.88	0.20	30.3
	0.52	0.67	0.15	29.6
	0.56	0.60	0.05	8.9
	1.08	0.81	-0.26	-24.4
Mean	0.64	0.72	0.08	13.7
S.E.M.	0.04	0.03	0.04	5.0

Table 4.12. Record of the Fura-2 fluorescence ratio measurements taken for each experiment during the intracellular dialysis of 10 nM NAADP in wild-type HEK293 cells
The resting F_{340}/F_{380} ratio was determined by calculating the average F_{340}/F_{380} ratio taken at 4 time-points either side of achieving the whole-cell configuration. The peak F_{340}/F_{380} ratio is the maximum F_{340}/F_{380} ratio obtained during the record. The increase in F_{340}/F_{380} ratio was determined by subtracting the peak F_{340}/F_{380} ratio from the resting F_{340}/F_{380} ratio. The percentage increase in F_{340}/F_{380} ratio was determined by dividing the increase in F_{340}/F_{380} ratio by the resting F_{340}/F_{380} ratio, and expressing this ratio as a percentage.

	Resting F_{340}/F_{380}	Peak F_{340}/F_{380}	Increase in F_{340}/F_{380}	% increase in F_{340}/F_{380}
	0.53	0.73	0.20	38.2
	0.51	0.61	0.09	18.6
	0.41	0.53	0.12	29.9
	0.45	0.77	0.32	72.8
	0.35	0.55	0.19	54.5
Mean	0.45	0.64	0.19	42.8
S.E.M.	0.03	0.05	0.04	9.5

Table 4.13. Record of the Fura-2 fluorescence ratio measurements taken for each experiment during the intracellular dialysis of 1 μM NAADP in wild-type HEK293 cells
The resting F_{340}/F_{380} ratio was determined by the calculating the average F_{340}/F_{380} ratio taken at 4 time-points immediately prior to the initiation of the Ca^{2+} transient. When no transient was observed, the resting F_{340}/F_{380} ratio was determined by calculating the average F_{340}/F_{380} ratio taken at 4 time-points either side of achieving the whole-cell configuration. The peak F_{340}/F_{380} ratio is the maximum F_{340}/F_{380} ratio obtained during the record. The increase in F_{340}/F_{380} ratio was determined by subtracting the peak F_{340}/F_{380} ratio from the resting F_{340}/F_{380} ratio. The percentage increase in F_{340}/F_{380} ratio was determined by dividing the increase in F_{340}/F_{380} ratio by the resting F_{340}/F_{380} ratio, and expressing this ratio as a percentage.

	Resting F_{340}/F_{380}	Peak F_{340}/F_{380}	Increase in F_{340}/F_{380}	% increase in F_{340}/F_{380}
	0.40	0.47	0.07	17.0
	0.56	0.62	0.07	11.9
	0.44	0.52	0.08	19.3
	0.42	0.50	0.08	18.9
Mean	0.45	0.53	0.07	16.8
S.E.M.	0.03	0.03	0.00	1.7

Table 4.14. Record of the Fura-2 fluorescence ratio measurements taken for each experiment during the intracellular dialysis of 100 pM NAADP in HA-hTPC2 cells
The resting F_{340}/F_{380} ratio was determined by calculating the average F_{340}/F_{380} ratio taken at 4 time-points either side of achieving the whole-cell configuration. The peak F_{340}/F_{380} ratio is the maximum F_{340}/F_{380} ratio obtained during the record. The increase in F_{340}/F_{380} ratio was determined by subtracting the peak F_{340}/F_{380} ratio from the resting F_{340}/F_{380} ratio. The percentage increase in F_{340}/F_{380} ratio was determined by dividing the increase in F_{340}/F_{380} ratio by the resting F_{340}/F_{380} ratio, and expressing this ratio as a percentage.

	Resting F_{340}/F_{380}	Peak F_{340}/F_{380}	Increase in F_{340}/F_{380}	% increase in F_{340}/F_{380}
	0.34	1.13	0.79	236.4
	0.33	1.96	1.63	500.0
Mean	0.33	1.55	1.21	368.2
Range	0.00	0.42	0.42	131.8

Table 4.15. Record of the Fura-2 fluorescence ratio measurements taken for each experiment during the intracellular dialysis of 1 μM NAADP in HA-hTPC2 cells
The resting F_{340}/F_{380} ratio was determined by the calculating the average F_{340}/F_{380} ratio taken at 4 time-points immediately prior to the initiation of the Ca^{2+} transient. The peak F_{340}/F_{380} ratio is the maximum F_{340}/F_{380} ratio obtained during the record. The increase in F_{340}/F_{380} ratio was determined by subtracting the peak F_{340}/F_{380} ratio from the resting F_{340}/F_{380} ratio. The percentage increase in F_{340}/F_{380} ratio was determined by dividing the increase in F_{340}/F_{380} ratio by the resting F_{340}/F_{380} ratio, and expressing this ratio as a percentage.

	Resting F_{340}/F_{380}	Peak F_{340}/F_{380}	Increase in F_{340}/F_{380}	% increase in F_{340}/F_{380}
	0.87	4.92	4.05	464.9
	1.04	2.84	1.80	173.7
	0.54	2.74	2.20	407.2
	1.25	4.45	3.20	256.9
	1.15	3.28	2.13	185.2
	0.68	0.98	0.30	44.9
	0.62	0.76	0.13	21.1
	0.55	0.74	0.19	34.7
	0.55	0.81	0.26	47.5
	0.51	0.58	0.07	14.3
	0.54	0.56	0.03	4.7
Mean	0.75	2.06	1.31	150.5
S.E.M.	0.08	0.50	0.43	49.5

Table 4.16. Record of the Fura-2 fluorescence ratio measurements taken for each experiment during the intracellular dialysis of 100 μM NAADP in HA-hTPC2 cells
The resting F_{340}/F_{380} ratio was determined by the calculating the average F_{340}/F_{380} ratio taken at 4 time-points immediately prior to the initiation of the Ca^{2+} transient. When no transient was observed, the resting F_{340}/F_{380} ratio was determined by calculating the average F_{340}/F_{380} ratio taken at 4 time-points either side of achieving the whole-cell configuration. The peak F_{340}/F_{380} ratio is the maximum F_{340}/F_{380} ratio obtained during the record. The increase in F_{340}/F_{380} ratio was determined by subtracting the peak F_{340}/F_{380} ratio from the resting F_{340}/F_{380} ratio. The percentage increase in F_{340}/F_{380} ratio was determined by dividing the increase in F_{340}/F_{380} ratio by the resting F_{340}/F_{380} ratio, and expressing this ratio as a percentage.

	Resting F_{340}/F_{380}	Peak F_{340}/F_{380}	Increase in F_{340}/F_{380}	% increase in F_{340}/F_{380}
	0.57	0.81	0.25	43.4
	0.59	0.75	0.16	26.9
	0.55	0.68	0.13	23.9
	0.52	0.59	0.06	11.8
	0.62	0.90	0.27	44.2
	0.50	0.66	0.16	32.3
	0.60	0.86	0.26	43.7
	0.52	0.68	0.16	31.4
	0.58	0.69	0.11	18.7
	0.47	0.58	0.10	22.2
Mean	0.55	0.72	0.17	29.8
S.E.M.	0.02	0.03	0.02	3.6

Table 4.17. Record of the Fura-2 fluorescence ratio measurements taken for each experiment during the intracellular dialysis of 1 mM NAADP in HA-hTPC2 cells
The resting F_{340}/F_{380} ratio was determined by calculating the average F_{340}/F_{380} ratio taken at 4 time-points either side of achieving the whole-cell configuration. The peak F_{340}/F_{380} ratio is the maximum F_{340}/F_{380} ratio obtained during the record. The increase in F_{340}/F_{380} ratio was determined by subtracting the peak F_{340}/F_{380} ratio from the resting F_{340}/F_{380} ratio. The percentage increase in F_{340}/F_{380} ratio was determined by dividing the increase in F_{340}/F_{380} ratio by the resting F_{340}/F_{380} ratio, and expressing this ratio as a percentage.

	10 nM NAADP, time to initiation of transient (s)	1 μM NAADP, time to initiation of transient (s)	100 μM NAADP, time to initiation of transient (s)
	70	25	20
	10	20	25
	25		20
	30		10
	35		
	55		
	30		
	30		
	20		
	35		
	15		
	30		
	20		
	10		
	20		
	15		
	40		
	45		
	25		
	10		
	10		
	40		
Mean	28.18	20.00	18.75
S.E.M.	3.30	5.0	2.81

Table 4.18. Record of time taken for the initiation of a Ca^{2+} transient in HA-hTPC2 cells in response to the intracellular dialysis of NAADP

Intracellular dialysis of either 10 nM, 1 μM or 100 μM NAADP in HA-hTPC2 cells evoked global Ca^{2+} transients. When a point of initiation of these Ca^{2+} transients could be clearly determined, the delay (seconds) between the formation of the whole-cell configuration to the initiation of the Ca^{2+} transient was recorded. Note, for $n = 2$ the S.E.M. is given as the range.

	Resting F_{340}/F_{380}	Peak F_{340}/F_{380}	Increase in F_{340}/F_{380}	% increase in F_{340}/F_{380}
	0.58	0.65	0.07	12.8
	0.65	0.64	0.00	-0.2
	0.55	0.63	0.08	14.4
	0.68	0.81	0.13	18.3
	0.71	0.83	0.13	17.8
	0.74	1.02	0.29	38.8
	0.64	0.71	0.08	11.8
	0.54	0.84	0.30	56.4
	0.64	0.79	0.15	23.0
	0.57	0.75	0.18	31.0
	0.67	1.18	0.51	75.2
Mean	0.63	0.80	0.17	27.2
S.E.M.	0.02	0.05	0.04	6.6

Table 4.19. Record of the Fura-2 fluorescence ratio measurements taken for each experiment during the intracellular dialysis of 10 nM NAADP in HA-hTPC2 cells pre-incubated (45 mins) with 100 nM Bafilomycin A1

The resting F_{340}/F_{380} ratio was determined by calculating the average F_{340}/F_{380} ratio taken at 4 time-points either side of achieving the whole-cell configuration. The peak F_{340}/F_{380} ratio is the maximum F_{340}/F_{380} ratio obtained during the record. The increase in F_{340}/F_{380} ratio was determined by subtracting the peak F_{340}/F_{380} ratio from the resting F_{340}/F_{380} ratio. The percentage increase in F_{340}/F_{380} ratio was determined by dividing the increase in F_{340}/F_{380} ratio by the resting F_{340}/F_{380} ratio, and expressing this ratio as a percentage.

	Resting F_{340}/F_{380}	Peak F_{340}/F_{380}	Increase in F_{340}/F_{380}	% increase in F_{340}/F_{380}
	0.35	0.74	0.40	114.6
	0.33	0.51	0.18	54.4
	0.37	0.43	0.06	16.2
	0.52	0.65	0.14	27.2
	0.43	0.77	0.35	81.8
Mean	0.40	0.62	0.23	58.8
S.E.M.	0.03	0.07	0.06	18.0

Table 4.20. Record of the Fura-2 fluorescence ratio measurements taken for each experiment during the intracellular dialysis of 10 nM NAADP in HA-hTPC2 cells pre-incubated (30 mins) with 1 μM thapsigargin

The resting F_{340}/F_{380} ratio was determined by the calculating the average F_{340}/F_{380} ratio taken at 4 time-points immediately prior to the initiation of the Ca^{2+} transient. When no transient was observed, the resting F_{340}/F_{380} ratio was determined by calculating the average F_{340}/F_{380} ratio taken at 4 time-points either side of achieving the whole-cell configuration. The peak F_{340}/F_{380} ratio is the maximum F_{340}/F_{380} ratio obtained during the record. The increase in F_{340}/F_{380} ratio was determined by subtracting the peak F_{340}/F_{380} ratio from the resting F_{340}/F_{380} ratio. The percentage increase in F_{340}/F_{380} ratio was determined by dividing the increase in F_{340}/F_{380} ratio by the resting F_{340}/F_{380} ratio, and expressing this ratio as a percentage.

	Volume of HA-hTPC2 labelling (μm^3)	Total cell volume (μm^3)	Density of HA-hTPC2 labelling (μm^3 per μm^3)
	117.1	4056.6	0.029
	47.8	2155.0	0.022
	38.0	1039.6	0.037
	76.3	1209.2	0.063
Mean	69.8	2115.1	0.038
S.E.M.	17.7	692.1	0.009

Table 4.21. Measurements of HA-hTPC2 labelling in fixed HA-hTPC2 cells

	Volume of HA-hTPC2 labelling (μm^3)	Total cell volume (μm^3)	Density of HA-hTPC2 labelling (μm^3 per μm^3)
	24.7	1618.6	0.015
	2.2	2606.1	0.001
	0.0	2149.3	0.000
	9.8	1296.1	0.008
	0.0	1323.8	0.000
	12.0	1833.1	0.007
Mean	8.1	1804.5	0.005
S.E.M.	3.9	207.1	0.002

Table 4.22. Measurements of HA-hTPC2 labelling in fixed HA-hTPC2 cells transfected with shRNA against hTPC2

	Resting F_{340}/F_{380}	Peak F_{340}/F_{380}	Increase in F_{340}/F_{380}	% increase in F_{340}/F_{380}
	0.68	0.98	0.30	44.3
	0.94	1.26	0.32	33.9
	0.66	0.93	0.27	40.9
	0.93	1.73	0.80	85.9
	0.61	3.49	2.87	469.5
	1.01	3.36	2.35	232.7
Mean	0.80	1.96	1.15	151.2
S.E.M.	0.07	0.48	0.47	70.6

Table 4.23. Record of the Fura-2 fluorescence ratio measurements taken for each experiment during the intracellular dialysis of 10 nM NAADP in HA-hTPC2 cells transfected with scrambled shRNA

The resting F_{340}/F_{380} ratio was determined by the calculating the average F_{340}/F_{380} ratio taken at 4 time-points immediately prior to the initiation of the Ca^{2+} transient. When no transient was observed, the resting F_{340}/F_{380} ratio was determined by calculating the average F_{340}/F_{380} ratio taken at 4 time-points either side of achieving the whole-cell configuration. The peak F_{340}/F_{380} ratio is the maximum F_{340}/F_{380} ratio obtained during the record. The increase in F_{340}/F_{380} ratio was determined by subtracting the peak F_{340}/F_{380} ratio from the resting F_{340}/F_{380} ratio. The percentage increase in F_{340}/F_{380} ratio was determined by dividing the increase in F_{340}/F_{380} ratio by the resting F_{340}/F_{380} ratio, and expressing this ratio as a percentage.

	Resting F_{340}/F_{380}	Peak F_{340}/F_{380}	Increase in F_{340}/F_{380}	% increase in F_{340}/F_{380}
	0.76	0.91	0.15	20.2
	0.51	0.53	0.02	4.7
	0.54	0.64	0.10	17.9
	0.53	0.78	0.25	47.2
	0.65	0.73	0.08	11.7
	1.01	0.94	-0.07	-6.9
	1.15	1.07	-0.08	-6.9
	0.62	0.92	0.30	48.4
	0.57	0.62	0.05	8.6
	0.70	0.68	-0.01	-2.1
Mean	0.76	0.91	0.15	20.2
S.E.M.	0.51	0.53	0.02	4.7

Table 4.24. Record of the Fura-2 fluorescence ratio measurements taken for each experiment during the intracellular dialysis of 10 nM NAADP in HA-hTPC2 cells transfected with shRNA against hTPC2

The resting F_{340}/F_{380} ratio was determined by the calculating the average F_{340}/F_{380} ratio taken at 4 time-points immediately prior to the initiation of the Ca^{2+} transient. When no transient was observed, the resting F_{340}/F_{380} ratio was determined by calculating the average F_{340}/F_{380} ratio taken at 4 time-points either side of achieving the whole-cell configuration. The peak F_{340}/F_{380} ratio is the maximum F_{340}/F_{380} ratio obtained during the record. The increase in F_{340}/F_{380} ratio was determined by subtracting the peak F_{340}/F_{380} ratio from the resting F_{340}/F_{380} ratio. The percentage increase in F_{340}/F_{380} ratio was determined by dividing the increase in F_{340}/F_{380} ratio by the resting F_{340}/F_{380} ratio, and expressing this ratio as a percentage.

	Resting F_{340}/F_{380}	Peak F_{340}/F_{380}	Increase in F_{340}/F_{380}	% increase in F_{340}/F_{380}
	1.03	1.27	0.24	23.4
	0.74	1.27	0.53	70.8
	0.61	1.16	0.55	89.5
	0.47	0.55	0.08	16.5
	0.92	1.28	0.36	39.3
Mean	0.75	1.10	0.35	47.9
S.E.M.	0.10	0.14	0.09	14.0

Table 4.25. Record of the Fura-2 fluorescence ratio measurements taken for each experiment during the intracellular dialysis of 10 nM NAADP in His_6-hTPC1 cells

The resting F_{340}/F_{380} ratio was determined by the calculating the average F_{340}/F_{380} ratio taken at 4 time-points immediately prior to the initiation of the Ca^{2+} transient. When no transient was observed, the resting F_{340}/F_{380} ratio was determined by calculating the average F_{340}/F_{380} ratio taken at 4 time-points either side of achieving the whole-cell configuration. The peak F_{340}/F_{380} ratio is the maximum F_{340}/F_{380} ratio obtained during the record. The increase in F_{340}/F_{380} ratio was determined by subtracting the peak F_{340}/F_{380} ratio from the resting F_{340}/F_{380} ratio. The percentage increase in F_{340}/F_{380} ratio was determined by dividing the increase in F_{340}/F_{380} ratio by the resting F_{340}/F_{380} ratio, and expressing this ratio as a percentage.

Appendix 3:

Results tables for Chapter 5:

Ned-19 conc. (μM)	Typhoon scanner relative fluorescence units (x 10^6 units)					Percentage of radioactivity compared to control (%)				
	1	2	3	Mean	S.E.M.	1	2	3	Mean	S.E.M.
0	2.66	2.64	2.77	2.69	0.04	100	100	100	100	
0.1	3.32	2.78	3.08	3.06	0.16	124.9	105.4	111.4	113.9	5.8
1	3.33	2.71	2.95	3.00	0.18	125.3	102.9	106.5	111.5	6.7
10	2.89	2.89	2.78	2.85	0.04	109.0	109.5	100.6	106.3	1.3
100	2.96	2.94	2.39	2.76	0.19	111.4	111.6	86.5	102.9	6.9
1000	2.44	2.06	2.25	2.25	0.11	91.9	78.1	81.2	83.7	4.1

Table 5.1. Measurements of the effect of increasing concentrations of Ned-19 on the [^{32}P]NAADP radioactivity retained in HA-hTPC2 cell homogenate obtained using a storage phosphor screen and scanned using a Typhoon 9400 scanner and analyzed using ImageQuant (GE Healthcare)

Ned-19 conc. (μM)	Scintilation radioactivity count (cpm)				Percentage of radioactivity compared to control (%)			
	1	2	Mean	Range	1	2	Mean	Range
0	68247	54704	61476	6771	100.0	100.0	100.0	
0.1	62978	49705	56342	6637	92.3	90.9	91.6	0.7
1	64940	54713	59826	5114	95.2	100.0	97.6	2.4
10	59817	53744	56781	3037	87.6	98.2	92.9	5.3
100	50332	42560	46446	3886	73.7	77.8	75.8	2.0
1000	3717	2892	3304	413	5.4	5.3	5.4	0.1

Table 5.1. Measurements of the effect of increasing concentrations of Ned-19 on the [^{32}P]NAADP radioactivity retained in sea urchin egg homogenate obtained using Cerenkov scintillation counting

	Volume of mCherry-hTPC2 labelling (μm^3)	Volume of LysoTracker Green labelling (μm^3)	Total cell volume (μm^3)	Density of mCherry-hTPC2 labelling (μm^3 per μm^3)	Density of LysoTracker Green labelling (μm^3 per μm^3)
	37.4	36.2	1909.6	0.0196	0.0190
	19.0	17.5	1610.2	0.0118	0.0109
	12.6	20.6	1895.2	0.0067	0.0109
	30.6	36.1	2580.2	0.0119	0.0140
	26.2	21.2	2850.1	0.0092	0.0074
	22.3	40.2	2738.1	0.0081	0.0147
Mean	24.7	28.6	2263.9	0.0112	0.0128
S.E.M.	3.6	4.0	212.7	0.0019	0.0016

Table 5.3. Measurements of mCherry-hTPC2 labelling and LysoTracker Green labelling in mCherry-hTPC2 cells

	Volume of colocalisation (μm^3)	Total cell volume (μm^3)	Density of colocalisation (μm^3 per μm^3)	Pearson correlation coefficient
	16.8	1909.6	0.0088	0.54
	4.0	1610.2	0.0025	0.28
	1.9	1895.2	0.0010	0.15
	11.6	2580.2	0.0045	0.39
	4.8	2850.1	0.0017	0.24
	4.3	2738.1	0.0016	0.20
Mean	7.2	2263.9	0.0033	0.30
S.E.M.	2.3	212.7	0.0012	0.06

Table 5.4. Measurements of the density of co-localisation and correlation between mCherry-hTPC2 and LysoTracker Green labelling in mCherry-hTPC2 cells

	Volume of mCherry-hTPC2 labelling (μm^3)	Volume of Ned-19 labelling (μm^3)	Volume of Co-localisation (μm^3)	Percentage mCherry-hTPC2 labelling co-localised (%)	Percentage Ned-19 labelling co-localised (%)
	118.7	72.5	41.2	34.7	56.8
	73.1	15.4	8.9	12.2	57.8
	62.7	34.9	10.6	16.9	30.4
	51.1	40.8	14.9	29.2	36.5
	25.2	43.9	4.7	18.6	10.7
	55.0	39.0	17.9	32.6	46.0
Mean	64.3	41.1	16.4	24.0	39.7
S.E.M.	12.7	7.5	5.3	3.8	7.3

Table 5.5. Measurements of mCherry-hTPC2 labelling and Ned-19 labelling in mCherry-hTPC2 expressing cells

	Volume of LysoTracker Red labelling (μm^3)	Volume of Ned-19 labelling (μm^3)	Volume of Co-localisation (μm^3)	Percentage LysoTracker Red labelling co-localised (%)	Percentage Ned-19 labelling co-localised (%)
	23.8	11.3	6.4	26.7	56.4
	15.9	15.7	3.9	24.4	24.8
	10.3	68.6	5.8	55.8	8.4
	13.8	9.5	4.1	30.1	43.6
Mean	15.9	26.3	5.0	34.3	33.3
S.E.M.	2.8	14.2	0.6	7.3	10.5

Table 5.6. Measurements of LysoTracker Red labelling and Ned-19 labelling in HA-hTPC2 expressing cells

	Volume of LysoTracker Red labelling (μm^3)	Volume of Ned-19 labelling (μm^3)	Volume of Co-localisation (μm^3)	Percentage LysoTracker Red labelling co-localised (%)	Percentage Ned-19 labelling co-localised (%)
	24.4	19.2	4.2	22.0	17.3
	21.9	80.4	15.7	19.6	72.0
	5.4	8.0	1.7	21.2	31.7
	7.5	15.0	2.6	17.4	34.8
Mean	14.8	30.7	6.1	20.0	39.0
S.E.M.	4.9	16.7	3.3	1.0	11.7

Table 5.7. Measurements of LysoTracker Red labelling and Ned-19 labelling in pulmonary arterial smooth muscle cells

	Resting F_{340}/F_{380}	Peak F_{340}/F_{380}	Increase in F_{340}/F_{380}	% increase in F_{340}/F_{380}
	0.80	1.14	0.34	43.0
	1.02	1.95	0.94	92.0
	0.87	1.96	1.09	125.1
	0.80	3.16	2.37	297.2
	0.86	2.95	2.09	244.1
	1.24	2.28	1.03	83.2
	1.08	3.08	2.00	185.3
	1.12	3.50	2.38	212.1
	0.79	2.37	1.59	201.7
	0.89	2.82	1.93	216.1
	0.63	2.75	2.12	334.0
	0.76	3.39	2.63	346.5
	0.72	1.59	0.87	121.0
	0.76	1.89	1.13	149.5
	0.59	2.13	1.54	263.2
	0.59	2.23	1.63	274.7
	0.68	1.52	0.84	123.0
	0.70	4.72	4.02	576.9
	0.48	1.54	1.06	220.9
	0.94	1.95	1.01	108.1
	0.83	2.43	1.60	192.9
	0.52	1.49	0.98	189.5
	0.70	1.30	0.59	84.7
	0.93	1.73	0.80	85.9
	0.79	0.99	0.20	24.7
	0.49	0.55	0.05	11.1
	0.93	1.02	0.09	9.1
	0.64	0.90	0.26	40.5
	0.62	0.79	0.18	28.8
	1.01	1.08	0.06	6.2
	0.82	1.05	0.24	29.0
	0.68	0.73	0.05	8.1
	0.61	0.78	0.18	29.4
	0.77	0.93	0.16	21.1
	0.57	0.72	0.15	25.8
	0.63	0.88	0.24	38.3
	0.63	0.77	0.13	21.0
	0.69	0.83	0.14	20.6
	0.47	0.52	0.05	10.7
	0.64	0.79	0.15	23.9
	0.72	1.60	0.88	121.2
	0.47	0.56	0.08	17.3
	0.51	0.73	0.22	42.1
	1.17	1.42	0.25	21.0
Mean	0.75	1.67	0.92	120.93
S.E.M.	0.03	0.15	0.14	18.39

Table 5.8. Record of the Fura-2 fluorescence ratio measurements taken for each experiment during the intracellular dialysis of 10 nM NAADP in HA-hTPC2 cells

The resting F_{340}/F_{380} ratio was determined by the calculating the average F_{340}/F_{380} ratio taken at 4 time-points immediately prior to the initiation of the Ca^{2+} transient. When no transient was observed, the

resting F_{340}/F_{380} ratio was determined by calculating the average F_{340}/F_{380} ratio taken at 4 time-points either side of achieving the whole-cell configuration. The peak F_{340}/F_{380} ratio is the maximum F_{340}/F_{380} ratio obtained during the record. The increase in F_{340}/F_{380} ratio was determined by subtracting the peak F_{340}/F_{380} ratio from the resting F_{340}/F_{380} ratio. The percentage increase in F_{340}/F_{380} ratio was determined by dividing the increase in F_{340}/F_{380} ratio by the resting F_{340}/F_{380} ratio, and expressing this ratio as a percentage.

	Resting F_{340}/F_{380}	**Peak F_{340}/F_{380}**	**Increase in F_{340}/F_{380}**	**% increase in F_{340}/F_{380}**
	0.59	0.69	0.09	15.7
	0.45	0.47	0.02	4.1
	0.54	0.64	0.10	18.4
	0.76	0.80	0.04	5.2
	0.98	1.16	0.17	17.7
Mean	0.66	0.75	0.08	12.2
S.E.M.	0.09	0.12	0.03	3.1

Table 5.9. Record of the Fura-2 fluorescence ratio measurements taken for each experiment during the intracellular dialysis of 10 nM NAADP in HA-hTPC2 cells pre-incubated (20 minutes) with 100 μM Ned-19

The resting F_{340}/F_{380} ratio was determined by calculating the average F_{340}/F_{380} ratio taken at 4 time-points either side of achieving the whole-cell configuration. The peak F_{340}/F_{380} ratio is the maximum F_{340}/F_{380} ratio obtained during the record. The increase in F_{340}/F_{380} ratio was determined by subtracting the peak F_{340}/F_{380} ratio from the resting F_{340}/F_{380} ratio. The percentage increase in F_{340}/F_{380} ratio was determined by dividing the increase in F_{340}/F_{380} ratio by the resting F_{340}/F_{380} ratio, and expressing this ratio as a percentage.

	Resting F_{340}/F_{380}	**Peak F_{340}/F_{380}**	**Increase in F_{340}/F_{380}**	**% increase in F_{340}/F_{380}**
	0.65	4.38	3.73	571.7
	0.51	2.32	1.81	355.9
	0.66	1.66	0.99	149.6
	0.97	2.65	1.68	173.1
	0.95	2.96	2.01	211.8
Mean	0.75	2.79	2.04	292.4
S.E.M.	0.09	0.45	0.45	78.5

Table 5.10. Record of the Fura-2 fluorescence ratio measurements taken for each experiment during the extracellular application of 1 mM CCh

The resting F_{340}/F_{380} ratio was determined by calculating the average F_{340}/F_{380} ratio taken at 4 time-points either side of achieving the whole-cell configuration. The peak F_{340}/F_{380} ratio is the maximum F_{340}/F_{380} ratio obtained during the record. The increase in F_{340}/F_{380} ratio was determined by subtracting the peak F_{340}/F_{380} ratio from the resting F_{340}/F_{380} ratio. The percentage increase in F_{340}/F_{380} ratio was determined by dividing the increase in F_{340}/F_{380} ratio by the resting F_{340}/F_{380} ratio, and expressing this ratio as a percentage.

	Resting F_{340}/F_{380}	Peak F_{340}/F_{380}	Increase in F_{340}/F_{380}	% increase in F_{340}/F_{380}
	0.41	2.20	1.79	434.7
	0.41	2.23	1.82	441.8
	0.41	3.11	2.70	664.8
	0.40	3.05	2.64	654.5
	0.42	2.58	2.16	518.2
	0.43	2.63	2.20	509.3
	0.43	2.45	2.02	467.5
Mean	0.42	2.60	2.19	527.3
S.E.M.	0.00	0.14	0.14	36.2

Table 5.11. Record of the Fura-2 fluorescence ratio measurements taken for each experiment during the extracellular application of 1 mM CCh in HA-hTPC2 cells pre-incubated (20 minutes) with 100 μM Ned-19

The resting F_{340}/F_{380} ratio was determined by calculating the average F_{340}/F_{380} ratio taken at 4 time-points either side of achieving the whole-cell configuration. The peak F_{340}/F_{380} ratio is the maximum F_{340}/F_{380} ratio obtained during the record. The increase in F_{340}/F_{380} ratio was determined by subtracting the peak F_{340}/F_{380} ratio from the resting F_{340}/F_{380} ratio. The percentage increase in F_{340}/F_{380} ratio was determined by dividing the increase in F_{340}/F_{380} ratio by the resting F_{340}/F_{380} ratio, and expressing this ratio as a percentage.

	Resting F_{340}/F_{380}	Peak F_{340}/F_{380}	Increase in F_{340}/F_{380}	% increase in F_{340}/F_{380}
	0.38	1.18	0.80	212.7
	0.36	1.58	1.22	340.0
	0.59	1.07	0.48	80.5
	0.56	1.03	0.47	83.3
	0.66	2.26	1.60	243.8
Mean	0.51	1.42	0.91	192.0
S.E.M.	0.05	0.21	0.20	45.3

Table 5.12. Record of the Fura-2 fluorescence ratio measurements taken for each experiment during the intracellular dialysis of 10 nM NAADP in pulmonary arterial smooth muscle cells

The resting F_{340}/F_{380} ratio was determined by the calculating the average F_{340}/F_{380} ratio taken at 4 time-points immediately prior to the initiation of the Ca^{2+} transient. The peak F_{340}/F_{380} ratio is the maximum F_{340}/F_{380} ratio obtained during the record. The increase in F_{340}/F_{380} ratio was determined by subtracting the peak F_{340}/F_{380} ratio from the resting F_{340}/F_{380} ratio. The percentage increase in F_{340}/F_{380} ratio was determined by dividing the increase in F_{340}/F_{380} ratio by the resting F_{340}/F_{380} ratio, and expressing this ratio as a percentage.

	Resting F_{340}/F_{380}	Peak F_{340}/F_{380}	Increase in F_{340}/F_{380}	% increase in F_{340}/F_{380}
	0.32	0.39	0.07	22.1
	0.34	0.41	0.08	22.6
	0.35	0.66	0.32	91.6
	0.37	0.42	0.05	12.7
Mean	0.34	0.47	0.13	37.2
S.E.M.	0.01	0.06	0.06	18.3

Table 5.13. Record of the Fura-2 fluorescence ratio measurements taken for each experiment during the intracellular dialysis of 10 nM NAADP in pulmonary arterial smooth muscle cells pre-incubated (20 minutes) with 100 μM Ned-19

The resting F_{340}/F_{380} ratio was determined by the calculating the average F_{340}/F_{380} ratio taken at 4 time-points immediately prior to the initiation of the Ca^{2+} transient. When no transient was observed, the resting F_{340}/F_{380} ratio was determined by calculating the average F_{340}/F_{380} ratio taken at 4 time-points either side of achieving the whole-cell configuration. The peak F_{340}/F_{380} ratio is the maximum F_{340}/F_{380} ratio obtained during the record. The increase in F_{340}/F_{380} ratio was determined by subtracting the peak F_{340}/F_{380} ratio from the resting F_{340}/F_{380} ratio. The percentage increase in F_{340}/F_{380} ratio was determined by dividing the increase in F_{340}/F_{380} ratio by the resting F_{340}/F_{380} ratio, and expressing this ratio as a percentage.

	Resting F_{340}/F_{380}	Peak F_{340}/F_{380}	Increase in F_{340}/F_{380}	% increase in F_{340}/F_{380}
	0.43	0.76	0.33	77.2
	0.41	1.19	0.78	190.2
	0.49	1.26	0.77	157.9
	0.41	2.62	2.21	540.3
Mean	0.43	1.46	1.02	241.4
S.E.M.	0.02	0.40	0.41	102.4

Table 5.14. Record of the Fura-2 fluorescence ratio measurements taken for each experiment during the intracellular dialysis of 1 μM IP_3 in pulmonary arterial smooth muscle cells pre-incubated (20 minutes) with 100 μM Ned-19

The resting F_{340}/F_{380} ratio was determined by the calculating the average F_{340}/F_{380} ratio taken at 4 time-points immediately prior to the initiation of the Ca^{2+} transient. When no transient was observed, the resting F_{340}/F_{380} ratio was determined by calculating the average F_{340}/F_{380} ratio taken at 4 time-points either side of achieving the whole-cell configuration. The peak F_{340}/F_{380} ratio is the maximum F_{340}/F_{380} ratio obtained during the record. The increase in F_{340}/F_{380} ratio was determined by subtracting the peak F_{340}/F_{380} ratio from the resting F_{340}/F_{380} ratio. The percentage increase in F_{340}/F_{380} ratio was determined by dividing the increase in F_{340}/F_{380} ratio by the resting F_{340}/F_{380} ratio, and expressing this ratio as a percentage.

	Resting F_{340}/F_{380}	Peak F_{340}/F_{380}	Increase in F_{340}/F_{380}	% increase in F_{340}/F_{380}
	0.67	2.78	2.11	311.9
	0.53	2.89	2.36	441.0
	0.63	2.09	1.46	231.1
	0.46	1.78	1.32	289.3
	0.69	1.71	1.02	146.9
	0.73	2.58	1.85	252.6
	0.80	2.78	1.98	247.7
Mean	0.65	2.37	1.73	274.4
S.E.M.	0.04	0.19	0.18	34.0

Table 5.15. Record of the Fura-2 fluorescence ratio measurements taken for each experiment during the extracellular application of 2.5 mM caffeine in pulmonary arterial smooth muscle cells

The resting F_{340}/F_{380} ratio was determined by the calculating the average F_{340}/F_{380} ratio taken at 4 time-points immediately prior to the initiation of the Ca^{2+} transient. The peak F_{340}/F_{380} ratio is the maximum F_{340}/F_{380} ratio obtained during the record. The increase in F_{340}/F_{380} ratio was determined by subtracting the peak F_{340}/F_{380} ratio from the resting F_{340}/F_{380} ratio. The percentage increase in F_{340}/F_{380} ratio was determined by dividing the increase in F_{340}/F_{380} ratio by the resting F_{340}/F_{380} ratio, and expressing this ratio as a percentage.

	Resting F_{340}/F_{380}	Peak F_{340}/F_{380}	Increase in F_{340}/F_{380}	% increase in F_{340}/F_{380}
	0.53	1.10	0.57	107.3
	0.43	1.56	1.13	260.0
	0.59	2.23	1.64	280.7
Mean	0.52	1.63	1.11	216.0
S.E.M.	0.04	0.33	0.31	54.7

Table 5.16. Record of the Fura-2 fluorescence ratio measurements taken for each experiment during the extracellular application of 2.5 mM caffeine in pulmonary arterial smooth muscle cells pre-incubated (20 minutes) with 100 μM Ned-19

The resting F_{340}/F_{380} ratio was determined by the calculating the average F_{340}/F_{380} ratio taken at 4 time-points immediately prior to the initiation of the Ca^{2+} transient. The peak F_{340}/F_{380} ratio is the maximum F_{340}/F_{380} ratio obtained during the record. The increase in F_{340}/F_{380} ratio was determined by subtracting the peak F_{340}/F_{380} ratio from the resting F_{340}/F_{380} ratio. The percentage increase in F_{340}/F_{380} ratio was determined by dividing the increase in F_{340}/F_{380} ratio by the resting F_{340}/F_{380} ratio, and expressing this ratio as a percentage.

Appendix 4:

Publications associated with this thesis:

Peer reviewed papers

- Kinnear, N.P., Wyatt, C.N., Clark, J.H., Calcraft, P.J., Fleischer, S., Jeyakumar, L.H., Nixon G.F. and Evans, A.M. (2008) Lysosomes co-localize with ryanodine receptor subtype 3 to form a trigger zone for calcium signalling by NAADP in rat pulmonary arterial smooth muscle. *Cell Calcium* **44**, 190-201.

- Calcraft, P.J., Arredouani A., Ruas M., Pan Z., Cheng X., Hao X., Tang J., Rietdorf K., Teboul L., Chuang K.-T., Lin P., Xiao R., Wang C., Lin Y., Wyatt C.N., Parrington J., Ma J., Evans A.M., Galione A., and Zhu M.X. (2009). NAADP mobilizes calcium from acidic organelles through two-pore channels. *Nature* **459**, 596-600.

Published abstracts of poster presentations to learned societies

- Calcraft, P.J., Ogunbayo O., Ma J., Galione A., Churchill G.C., Zhu M.X., and Evans, A.M. (2008). Does nicotinic acid adenine dinucleotide phosphate elicit Ca^{2+} release via two-pore channel subtype 2 in rat arterial smooth muscle cells? *Proc. Physiol. Soc. 13,* PC18.